Source and Magma Evolution of the tuff of Elevenmile Canyon, Stillwater Range, Clan Alpine and northern Desatoya Mountains, western Nevada.

Daniel Stepner

A thesis submitted to the Faculty of Graduate and Postdoctoral Studies in partial fulfillment of the requirements for the degree of:

Master of Science

In

Earth Sciences

University of Ottawa

Abstract

The tuff of Elevenmile Canyon (TEC) is a 25.1 Ma trachydacite to rhyolite intracaldera tuff produced by the largest of 6 Oligocene overlapping calderas that, along with related plutons, constitute the Stillwater Caldera Complex, one of the largest eruptions of the Western Nevada Volcanic Field during the mid-Tertiary ignimbrite flare-up. Typically crystal-rich with a mineral assemblage of plagioclase > quartz ≅ sanidine > biotite ± hornblende and clinopyroxene, there are two discernable pumice types throughout the tuff: a lighter crystal-rich pumice and a darker, commonly aphyric pumice type. Rb-Sr and Sm-Nd isotopic compositions of pumice fragments and whole rock samples indicate an enriched mantle component ($^{87}Sr/^{86}Sr_{in}$ = 0.70495 – 0.70535, $\varepsilon Nd[t=25.1Ma]$ = -1.13 to -0.39) similar to that of coeval Cenozoic mafic lavas. Pb isotopes ($^{206}Pb/^{204}Pb_{in}$ = 19.042 – 19.168, $^{207}Pb/^{204}Pb_{in}$ = 15.557 – 15.664) fall along a tight trend between the Northern Hemisphere Reference Line (Hart 1984) and an endmember similar to local granitic units. Major and trace element modelling support a source for the TEC derived from the mixing of anatectic melts of crustal rocks with intruded mantle-derived magmas similar to a local basaltic-andesite.

Acknowledgements

First and foremost, I`d like to thank both of my supervisors for teaching me that there is always room for improvement. Thank you Brian Cousens for accepting me as a relatively unknown undergraduate with an interest in volcanoes and opening my eyes towards a shared academic interest in geochemistry. Without opportunities provided by Brian, both prior to this project and throughout, I would not be here today. Thank you to Jon O`Neil for all of your help, nearly infinite patience and careful attention to detail, without any of which this thesis would never have been completed.

Field work would not have been possible without the help of Dr. David John, Dr. Joe Colgan and Dr. Kathryn Watts with the USGS and Dr. Chris Henry with the Nevada Bureau of Mines. Each are resident experts of this area of Nevada and have all provided a wealth of knowledge, additional samples and guidance throughout. A generous thank you is also deserved of Ayesha Landon-Browne for her work as a field assistant and the additional work she performed on our shared samples.

To everyone at Carleton University and the University of Ottawa, staff, faculty members and fellow students I`d like to extend my thanks as well.

Lastly, thank you to my friends and family. Thank you to my parents, Nate and Karen Stepner, you both have gone above and beyond encouraging my interest in science and satisfying my endless curiosity. And most importantly, thank you to Shelbi Dippold; your unwavering support (and unending patience) in me served as a driving force behind my work.

Table of Contents

List of Figures

List of Tables

List of Abbreviations

CHUR	Chondritic Uniform Reservoir
HFSE	High field strength elements
LILE	Large ion lithophile elements
HAOT	High aluminium olivine tholeiite
MORB	Mid-ocean ridge basalt
NHRL	Northern Hemisphere Reference Line
OIB	Ocean island basalt
REE(s)	Rare earth element(s)
TEC	tuff of Elevenmile Canyon
WNVF	Western Nevada Volcanic Field

1.0 Introduction

The mid-Cenozoic Ignimbrite Flare-up reshaped the western half of North America during one of the largest episodes of continental volcanism known in geologic history. Recent studies have aimed to untangle the puzzle of interconnected and overlapping calderas and outflow ignimbrites with the goal of understanding how these incredible volumes of magma were produced within a continental volcanic arc setting (Best et al., 2013; Henry and John, 2013; Watts et al., 2016).

The mid-Cenozoic Ignimbrite Flare-up occurred from 45-8 million years ago (Ma) (Sawyer et al., 1994; Henry et al., 2010; Henry and John, 2013), during which over 5,000,000 km^3 of intermediate and felsic magmas were erupted in a southwestward sweep across North America. The general understanding is that in association with the rollback of the subducted Farallon plate beneath the continent, partial melts of the mantle intruded and stalled, fluxing and partially melting the continental crust (Hildreth 2004; Watts et al., 2016). These dacitic to rhyolitic magmas are generated in extremely complex environments, with a variety of igneous processes often interplaying to varying degrees (Hildreth and Moorbath, 1988; Annen and Sparks, 2002). A current model for the generation of felsic magmas in subduction-related arc systems is by the melting of continental crust as a response to the flux of basaltic magma from the mantle into the lower crust, mixing of these diverse magmas, followed by crystallization and segregation of residual liquids (Smith 1979; Hildreth 1981; Hildreth and Moorbath 1988; Annen et al., 2006; de Silva 2008). However, the degree to which processes such as fractional

crystallization or assimilation affect the evolving systems is still unclear (Best and Christiansen, 1991; Humphreys 1995; Farmer et al., 2008). The application of radiogenic isotopes comparing typical crustal rocks and coeval mafic flows can provide information about petrogenesis and the proportions of each component (mantle, crust) involved in the generation of these evolved magmas within the continental crust (Davidson 1985; Aitcheson et al., 1995; Siebel et. al., 2001)

To date, limited geochemical characterization of felsic ignimbrites has been performed in the calderas of the southwestern United States, which leaves a fundamental gap in our understanding of the petrogenetic histories of the regional systems. This study focuses on an individual large ignimbrite to better constrain processes specific to a single magmatic system. The tuff of Elevenmile Canyon (TEC), located in the Western Nevada Volcanic Field (WNVF) of western Nevada within the Basin and Range Province of the United States, was chosen as it presents an exceptional opportunity to explore changes within a volcanic package through intracaldera stratigraphy. Basin and Range extension of the region has tilted the entire volcanic sequence and exposed the entirety of the intracaldera tuff and provides ample opportunity to sample the entire sequence and monitor chemical changes throughout the eruptive package.

The aim of this work is to combine the trace element systematics and Sr, Nd and Pb isotopic systems to ascertain a likely magma source(s) and evaluate the extent of crustal interaction and contributions to the generation of magmas related to the TEC.

2.0 Tectonothermal history of the Southwestern United States

The TEC is one of many rhyolitic ash-flow tuffs that erupted during the Cenozoic Ignimbrite Flareup that swept across the southwestern portion of North America from 45-8 Ma (Henry and John, 2013; Henry et al., 2010; Sawyer et al., 1994). This idea of a distinct volcanic period in history for the Great Basin (GB) was first proposed by McKee et al., (1970), who noticed a scarcity of sedimentary rocks in the stratigraphic column combined with widespread ash flow sheets that were dated between 40 and 20 Ma. The concept was then further developed by McKee (1971) and Coney (1978) as the "Ignimbrite Flare-up", which linked voluminous rhyolitic and andesitic volcanism across the continent to the subduction of a tectonic plate (Farallon) beneath western North America. When scrutinizing such a short episode such as the TEC in a much larger geologic event, it is important to consider the full picture and therefore this section summarizes the tectonic history of the GB and provides the context linking the TEC within the much larger picture.

2.1 Subduction of Farallon Plate

Prior to the Mesozoic, a passive margin had existed between the oceanic Mezcalera plate and the western edge of Laurentia. Cordilleran subduction began as early as the late Permian (Barth and Wooden 2006), and by mid-Jurassic time the margin had evolved into a single convergent margin (Atwater 1970; Dickinson and Snyder; 1978; Mann et al., 2007) where the Mezcalera plate was being driven beneath Laurentia (Fig. 2.1). The Mezcalera plate was entirely consumed by the mid-Jurassic along an arc-continent suture now

exposed in the Sierra Nevada foothills and western Klamath Mountains (Dickinson 2006) and subsequently the leading edge of the Farallon plate began moving beneath the Pacific margin. Convergence rates at the Farallon-Laurentia margin are estimated to have reached upwards of 12 cm/yr (Decelles 2004), which may have influenced slab flattening during the late Mesozoic.

Coney and Reynolds (1977) were the first to introduce the idea that subduction of the Farallon plate shallowed from a more normal high angle geometry to one that was relatively flat during the Laramide orogeny as fast-paced subduction drove the oceanic plate beneath North America before it was able to cool and transition to a more typical dip angle (Fig. 2.2). This transition is marked by a dynamic change in magmatic expression on the continent, where initial magmatism related to the Cordilleran arc was intense along the western side of North America with the emplacement of a batholith belt and satellite plutons throughout Mesozoic. At the end of the Cretaceous, traditional Andean style arc-magmatism shifted rapidly eastward from the margin (Dickinson and Snyder 1978) with the shift to flat-slab geometry, marked by a period of magmatic quiescence (~55-75 Ma) in the western US as the slab remained in direct contact with the base of the continental lithosphere.

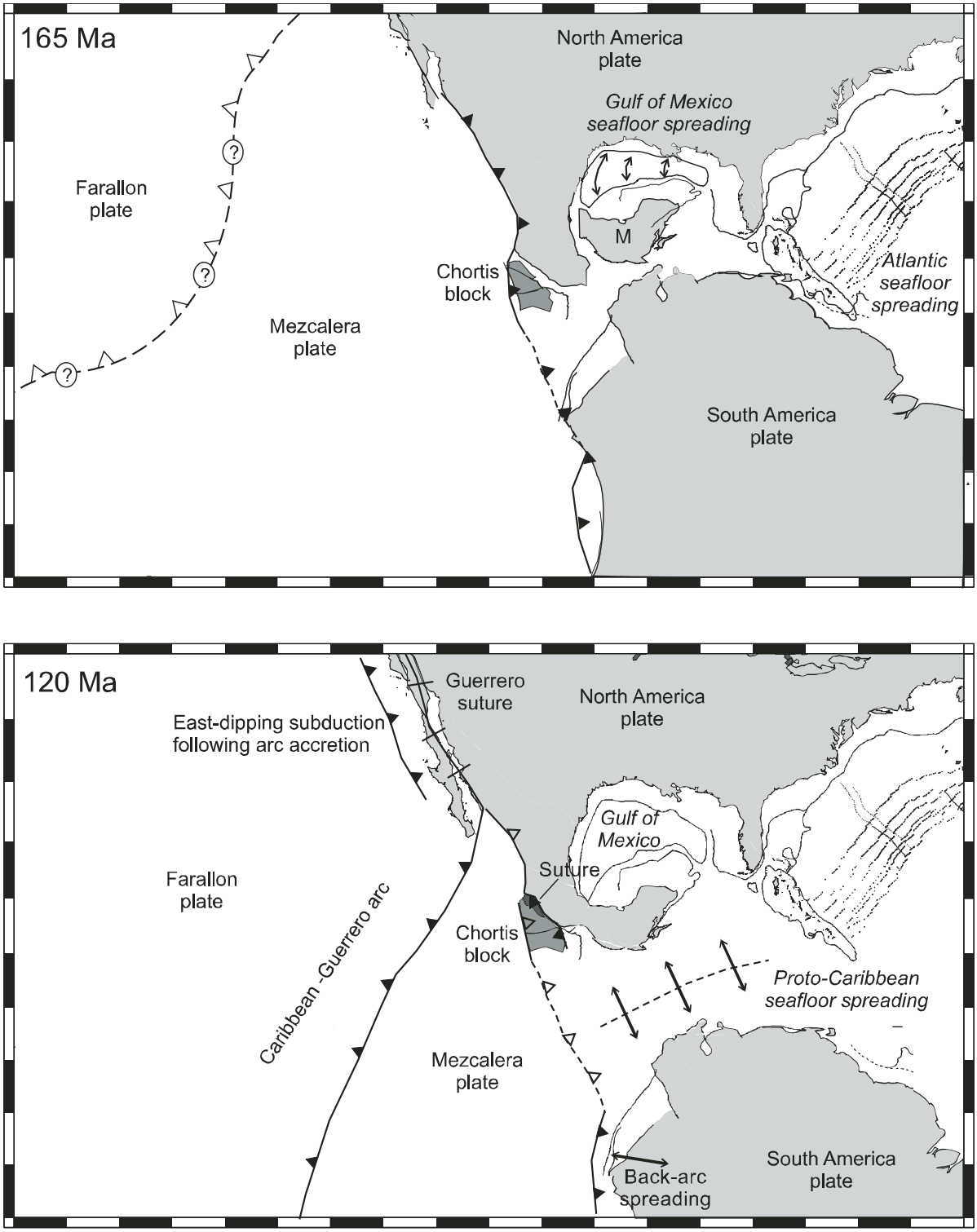

Figure 2.1 Schematic showing consumption of the Mezcalera plate beneath present day Pacific margin and transition to Farallon plate subduction. Modified from Mann (2007)

Mechanisms to explain a near horizontal subduction geometry have been expounded by multiple authors, and any combination of these processes can be invoked in a reasonable model: 1. rapid subduction of the relatively warm, buoyant young Farallon plate (Engebretson et al., 1985; Jarrard 1986; van Hunen et al., 2002), 2. a thick oceanic plate being held up by slab buoyancy (Livaccari et al., 1981; Cross and Pilger 1982), 3. entrapment of lithospheric mantle within a limited mantle wedge, thus increasing suction between the oceanic and continental plates and enhancing slab-flattening (Cadek and Fleitout 2003; O'Driscoll et al., 2009).

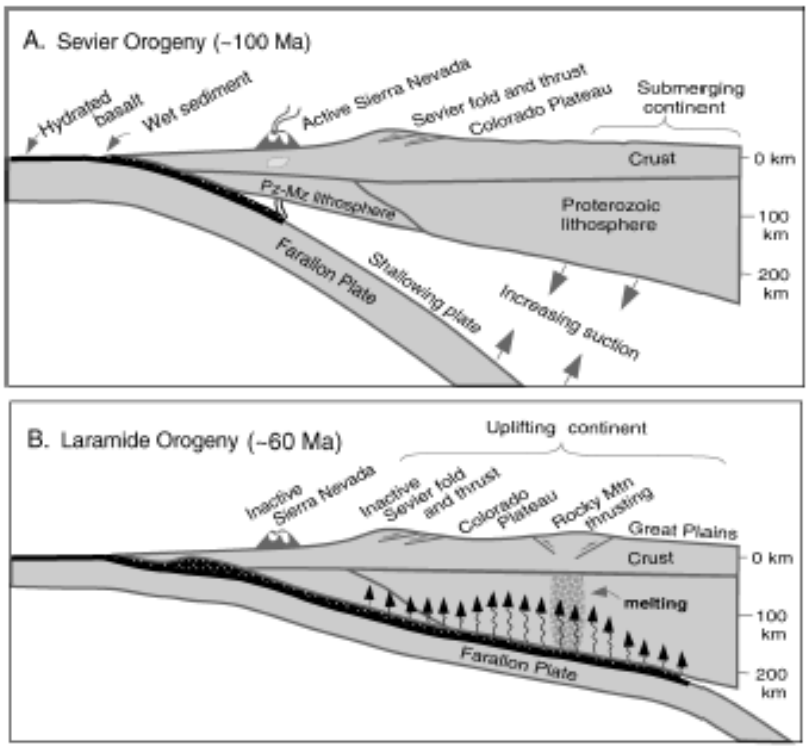

Figure 2.2 Schematic of the western margin of the United States through the late Jurassic to Cenozoic time. Showing the transition of Farallon subduction to flat-slab geometry and the raising of an altiplano as a response to thickening crust. The black arrows leaving the Farallon slab represent slab-derived fluids permeating the lithospheric mantle. After Humphreys (2009).

2.2 Crustal Thickening and Formation of the Nevadaplano

With the Farallon plate shallowing and coming into direct contact with the bottom of the North American lithosphere, resultant crustal thicknesses are estimated to have been anywhere from 40-70 km (Colgan and Henry, 2009; and references therein), leading to a hinterland with an estimated elevation of 3-4 km above sea level, similar to the modern central Andean Plateau (DeCelles 2004; DeCelles and Coogan, 2006; Snell et al., 2014). This buoyed crust was situated above tapering lithospheric mantle; total lithospheric thickness reached ~200 km beneath Colorado and Wyoming (Humphreys 2009) which thinned considerably to the SW (~140 km thick beneath the Four Corners, Lowrey et al., 2000) to a potential thickness of 0 km in southern California (Humphreys 2009). Coined by DeCelles (2004), this uplifted plateau is known as the "Nevadaplano" and is thought to be analogous to the modern Tibetan plateau or Andean Altiplano.

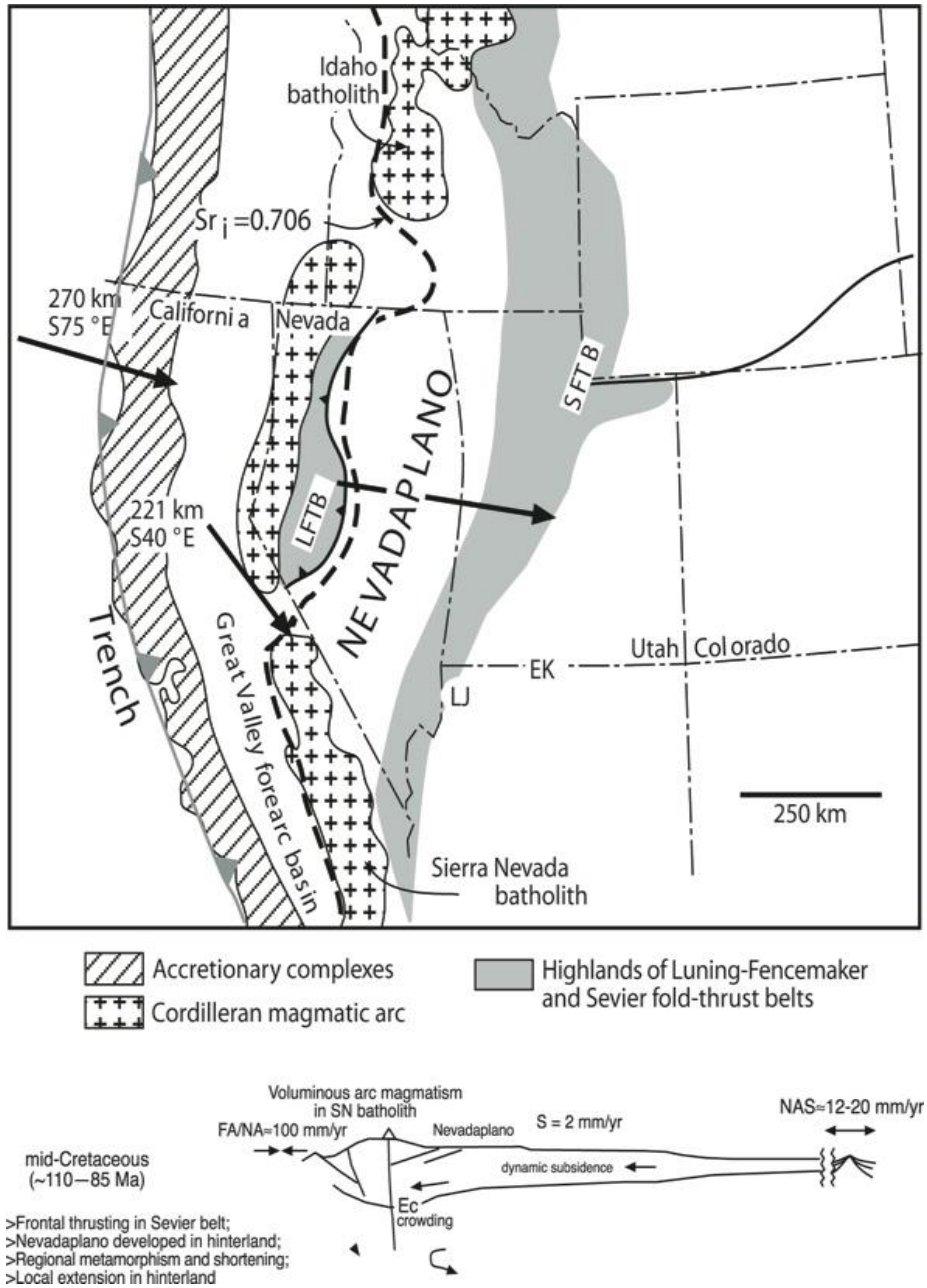

Figure 2.3 Major thrust belts of the Sevier orogeny, and extent of the Nevadaplano as interpreted from paleovalleys and drainage patterns of Eocene-Oligocene water systems in Nevada. SFTB= Sevier Fold-Thrust Belt, LFTB= Luning-Fencemaker Fold-Thrust Belt.
Modified from DeCelles (2004) and DeCelles and Coogan (2006)

Figure 2.3 shows the major thrust belts of Cordilleran thrust belts and the inferred extent of the Nevadaplano during the Mid-Cretaceous. By 60 Ma, with continued thickening during the Laramide orogeny, this plateau was the erosional highland of the western US. The rising of the Nevadaplano is often invoked as a key factor in the Cenozoic evolution of the Great Basin; as Cenozoic magmatism grew in scale, the overly thickened Nevadaplano crust provided ample opportunity for mantle-derived magmas to interact with continental crust, ponding and assembling massive composite plutons and related caldera-style volcanic eruptions. As Hodges and Walker (1992) proposed, once a maximum degree of elevation was achieved the Nevadaplano collapsed under its own gravitational stresses, adding to the geodynamic stresses involved in later Miocene extension of the GB.

2.3 Mid-Cenozoic Ignimbrite Flare-up

Cenozoic magmatism in the western United States is dominated by intermediate and rhyolitic ash flow sheets which have been the focus of many studies trying to better understand the geological complexity of the western Cordillera, due to 1) being deposited in a near horizontal plane and 2) being easily datable (Mackin, 1960). The flat-slab geometry of the Farallon plate continued until the accretion of Siletzia to North America caused subduction to transition westward to the modern day Cascadia subduction zone in Oregon and Washington around 48 Ma (Madsen et al., 2006). As subduction in the Southwest slowed considerably, the forces supporting flat-slab geometry diminished, and

the Farallon plate began sinking towards normal slab dip angles forcing the hinge line to retreat oceanward (Humphreys 2009). This transition fractured the Farallon plate into a northern Cascadia slab that transitioned quickly to a normal slab angle, and a southern Farallon slab that retained the Laramide-related flat slab geometry for a longer period of time. The near-flat subduction had allowed free-phase water to migrate from the oceanic slab upwards and, through contact, hydrate the previously refractory lithospheric mantle. As hydrous minerals such and hornblende, phlogopite, chlorite and apatite were now prevalent in this fertilized lithospheric mantle, this source now had the potential to generate large volumes of mafic magma. The tear in the Farallon plate probably occurred at the southern margin of the accreted Siletzia (Humphreys 2009), somewhere in central Oregon, and opened a slab window which began to expose the hydrated lithospheric mantle to warmer asthenospheric material (Figure 2.4). Once the slab was removed either by buckling (Humphreys 1995) or rolling-back (Dickinson 2006) (Fig. 2.4), the lithospheric mantle which had been previously hydrated by fluids from the Farallon slab was exposed to upwelling hotter asthenosphere and began to partially melt. This thermal rejuvenation of the lithospheric mantle resulted in the input of large amounts of mantle-derived magmas into the crust (Timmermans 2015) where they were able to sufficiently raise the thermal regime creating the optimum conditions for the generation of vast volumes of intermediate to evolved magmas. This was all expressed as a magmatic episode where more than 500,000 km^3 of ash-flow tuffs and 5,000,000 km^3 of intermediate to felsic lavas were deposited by predominantly caldera-forming eruptions (Johnson 1991), now referred to as the Mid-Cenozoic Ignimbrite Flare-up (McKee 1970, 1971).

Upwelling mantle created two magmatic fronts on the edges of the slab, that each separately travelled east to west across the southwest United States as the Farallon plate was floundering. The initial front began around 50-55 Ma in northern Washington and central Idaho and moved southward at a rate of about 15 km/m.y., passing through Nevada between ~45 and 20 Ma (Christiansen and Yeats 1992). At around 40 Ma, a second, southern front initiated in western Texas and Sonora and moved west-northwest at a faster rate of about 30 km/m.y. (Christensen and Yeats, 1992). Magmatism in both directions coalesced in southern Nevada around 20 Ma as shown in Figure 2.5 (Armstrong and Ward, 1991; Humphreys 1995), marking the removal of the subducted slab from the base of the North American lithosphere and a transition to mantle wedge-derived magmatism (Cousens et al., 2008). The subducted slab is presently imaged in the mantle dipping beneath northern California and northern Nevada at depths of 200-450 km (Humphreys 2009).

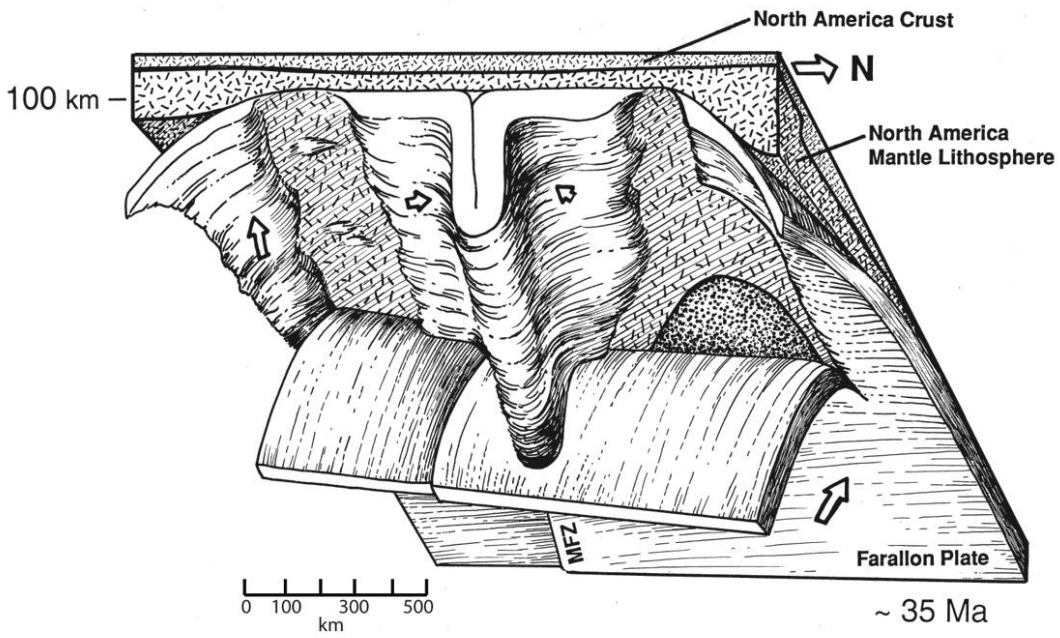

Figure 2.4 Cartoon showing the underside of the North American plate looking westwards towards the Pacific Ocean ca. 35 Ma., with the Farallon plate (dashed pattern) tearing and beginning to rollback. The accreted Siletzia is shown in the grey stippled pattern In the middle right. Figure by Humphreys (1995)

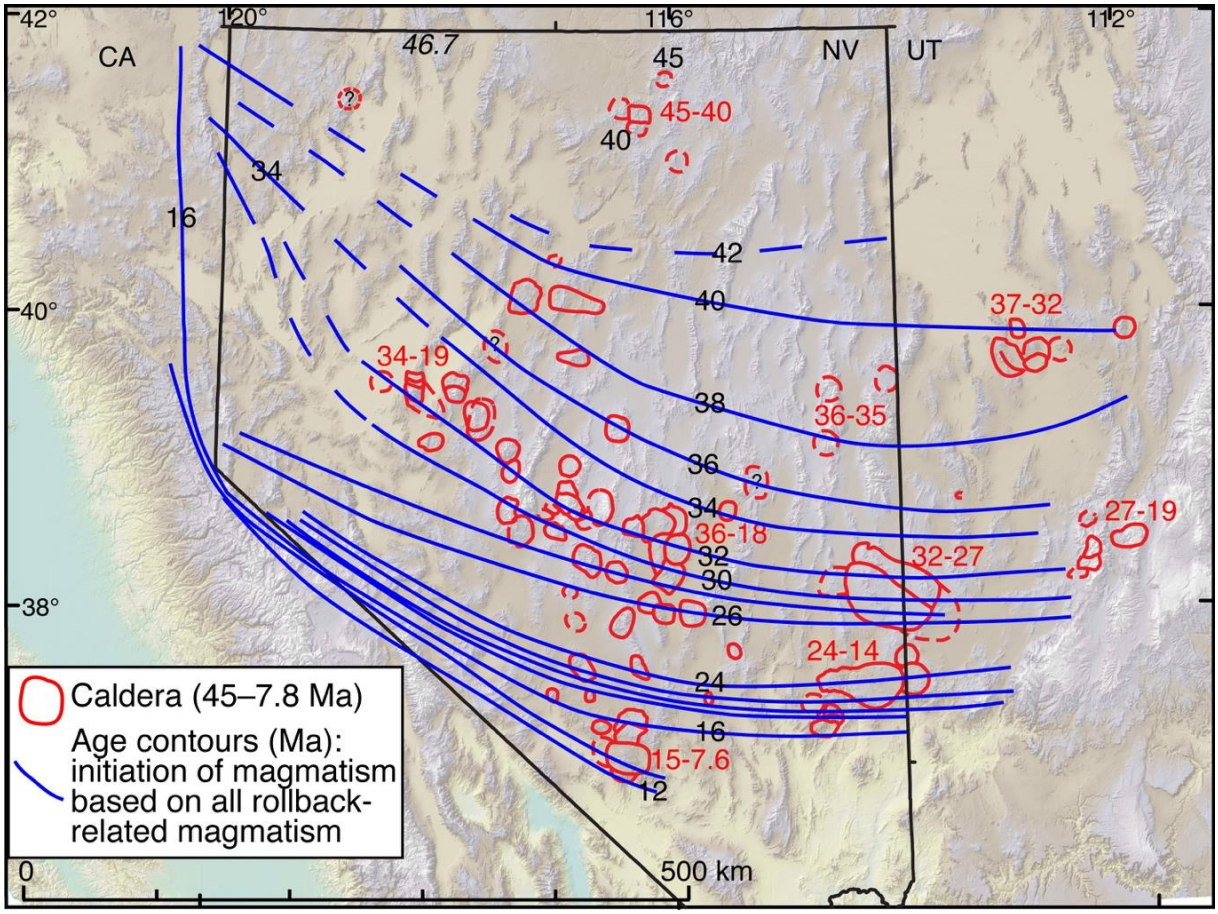

Figure 2.5 Map of western United States showing approximate ages of magmatic activity, and age contours showing the general direction of mid-Cenozoic Ignimbrite Flare-up migration (south west). After ~24 Ma magmatism shifted more westward in direction. Map provided by C. Henry (2013).

2.4 Basin and Range Extension

The Basin and Range province has often served as a type example of the horst and graben topography forming from regional extensional forces. Colloquially, the terms Great Basin and the Basin and Range Province are used interchangeably to denote North-South trending mountainous regions separated by sedimented valleys (Dickinson 2006) in the southwestern United States; however a few important distinctions should be made between these terms. The Great Basin is a hydrological term for the endorheic watershed that covers much of Nevada, Utah and Oregon, an area that drains internally with no connection to the ocean. The Great Basin is part of the much larger Basin and Range Province that spans from the Pacific Northwest to central Mexico and is a geologic province defined by faulted mountain chains and flat sediment-filled valleys which spans a stretch of almost 2500 km following the trend of the North American Cordillera. Armstrong and Ward (1991) and Colgan and Henry (2009) propose that the Basin and Range region was held together by this shrinking piece of the Farallon slab until 16-17 Ma when it finally fell away and the Basin and Range was free to collapse during rapid extension. Extension was potentially facilitated by a combination of 1) the dynamic change in stress regime with the reorganization of the San Andreas Fault system, 2) the orogenic collapse of the Nevadaplano, and/or 3) the onset of Yellowstone plume magmatism, the formation of the northern Nevada Rift, and the Columbia River igneous event, all of which added heat to the Cordilleran lithosphere and crust at ca. 17-15 Ma (Camp et al., 2015). Colgan and Henry (2009) propose a scenario in which the Pacific-North American boundary evolved to a

transform margin in the middle Miocene, which required continental extension to compensate for movement along the transform fault. As the older and stronger Sierra Nevada Block resisted deformation as it moved west with the motion of the Pacific plate, extension was accommodated by the weaker Basin and Range region to the east. The westward movement of the Sierra Nevada block would provide a space to accommodate the collapse of the previously thickened Nevadaplano, which had become unstable as the Farallon plate was removed.

Extension of the Great Basin has been separated into 2 main phases: an early stage of highly extended metamorphic core complexes (50 -100% strain), and a late stage of high angle block faulting (Parsons et al., 1996; Colgan and Henry, 2009). Compared to the later phase, the overall extent of the early phase of extension was relatively small, limited to exposure of core complexes in highly localized areas bounded by terranes that were not as strongly extended. These first core complexes are found in and above the northern part of the Great Basin, in British Columbia, Washington, Oregon and northern Nevada. Extension propagated southward, as the earliest extensional features in the southern Basin and Range were metamorphic core complexes exhumed in the southern parts of California and Arizona as well as northern Mexico during the early Oligocene.

The second phase of extension within the Great Basin began ~17 Ma, and was responsible for the distinctive basin and range topography observed today. This phase is characterized by up to 100% extension along steeply dipping normal faults resulting in domino–style tilted fault blocks (Proffett 1977; Chamberlain 1983). Using the Shoshone Range of central

Nevada as a typical example, these fault blocks have been tilted between 5 and 8 degrees (Gilluly et. al., 1965), with laboratory experiments showing up to 20 degrees of tilting possible in the upper sections (Cloos 1968). Further extension has continued to the present along the margins of the Great Basin, accommodated by local deformation within the greater Basin and Range region (Manley et al., 2000; Jones et al., 2004).

2.5 Extension-related Magmatism

Middle Miocene volcanism has a complex association with extension within the Basin and Range. Synextensional magmatism has been observed with almost every phase of Basin and Range extension including dike and sill intrusions, synextensional plutonism, ash flow tuffs, cinder cones and rhyolite and basalt flows to the extent that Gans (1987) concluded that all Cenozoic magmatism in the western United States was synextensional in nature. This view was opposed by Best and Christensen (1991), where they argue maximum extension and maximum volcanism within the Great Basin occurred in distinct time intervals. Best and Christensen believe the initial wave of magmatism was linked to the removal of the Farallon plate from beneath the continental plate, and extension only began once the plate was completely removed.

Models for the onset of magmatism are further complicated by the arrival of the Yellowstone plume around 16-17 Ma which broke through northern Nevada erupting numerous rhyolite tuffs from related calderas as well as a migrating magmatic system related to the plume tail (Geist and Richards, 1993). The arrival of a mantle plume is typically associated with both voluminous volcanism as well as broad domal uplift centered around the plume head. A volcanic maximum occurred as the Columbia River Flood Basalts were emplaced in Oregon at ~16 Ma in a back-arc, extensional environment (Camp and Hanan, 2008; Colgan and Henry 2009) that only underwent a small degree of post-eruptive extension. Linking the arrival of the Yellowstone hotspot with the beginnings of extension remains a controversial topic with multiple authors proposing variable contributions to the

commencement of extension; some authors attribute the arrival of the Yellowstone plume as a catalyst for Basin and Range extension (Camp et al., 2015), while others find large scale Basin and Range extension had commenced prior to the arrival of the Yellowstone plume (Colgan 2013) and there were only localized deformation structures as a response to the onset of Yellowstone volcanism. Colgan and Henry (2009) propose a scenario in which Basin and Range extension was triggered by reorganization of the Pacific-North American plate boundary leading to divergent motion between the plates over a large area. The previously uplifted Nevadaplano had become thermally weakened with the removal of the Farallon slab and contact with upwelling warm mantle material and was able to readily collapse, magnifying the effects of divergent plate motion and aiding rapid extension.

3.0 Applied Concepts and Theory

3.1 Models for Generating Felsic Magmas

Felsic magmas can be the result of multiple complex processes working in tandem throughout the crust to eventually produce rhyolites and granites as end-member compositions. In this section I will briefly review and discuss current models for the general petrogenesis of felsic magmas and link it to the following section with a focus on subduction settings.

It is expressed matter-of-factly that any magma is the result of partial melting of some source rock, and Hutton (1794) was the first to propose that felsic rocks were formed by the intrusion of molten material and subsequent fusion of pre-existing rocks. In the years following much progress has been made in understanding the generation of magma above subduction zones, the interactions between fluxed material from the mantle and crustal rocks, as well as the subsequent crustal anataxis that occurs (Perry and DePaolo, 1993; Annen and Sparks, 2002; de Silva 2008; Clemens 2012; Brown 2013). It is accepted that basaltic magmas are only generated by partial melting of the mantle, however given sufficient time any magma will evolve towards a felsic composition through igneous differentiation. As melts derived from any protolith have the potential to evolve into felsic magmas, pin-pointing a source for a felsic melt is particularly difficult and best approached on a case-by-case basis.

Clemens (2012) and Winter (2010) summarize the different pathways that have been proposed to explain the generation of felsic magmas, including miniscule degrees of partial

melting of the mantle, extensive crystal fractionation from a tholeiitic basalt parent, combined fractionation and contamination of a basaltic magma (assimilation fractional crystallization, AFC), or partial melting of crustal rocks. The first two of these models can be quickly discounted for wide applications; extremely small degree partial melts of the mantle would result in magmas resembling felsic melts in terms of silica content, but cannot produce the volumes of granites and rhyolites that make up the continental crust. Secondly, these low degree partial melts would have very unusual trace element characteristics and resemble the mantle isotopically to a degree that is not observed in natural granites. Extreme fractionation of a tholeiitic basalt can result in sodic magmas, granophyres and alkaline rhyolites as seen in mid-ocean ridge granites (Pearce 1996). These granites have mantle-like isotopic compositions and their sodic nature is reflective of the lack of potassium in the depleted mantle source, but there are volumetric issues to overcome if this process is a general pathway for most felsic magmas. The amount of felsic magma produced by differentiation of a basaltic melt is orders of magnitude lower than the initial volume of basalt, likely < 1%, and without some process accounting for this "missing" basalt the volume of granites/rhyolites present today cannot be explained.

The spatial relation of felsic rocks to the continents and isotopic similarities to continental crust led to a combination of crustal melting and assimilation being invoked as the main mechanisms by which felsic rocks are produced. Regardless of which of these processes (crustal melting vs. assimilation into a primitive magma) is dominant, a major material contribution must be made by either the continental crust or lithosphere to satisfy chemical and isotopic constraints common to many felsic suites. It is easy to visualize how a

hot basaltic magma would interact with the continental crust as it ascended, providing a heat source to melt country rock and assimilating both this new melt and crystal phases derived from the crustal rocks into the ascending magma body. DePaolo (1981, 1987) was the first to numerically model the process of AFC, in which a magma continuously assimilates wall rock while ongoing fractional crystallization. This process has been applied on numerous occasions to explain trace element and isotopic variation in felsic suites, and generally explains compositions lying between those of the mantle and continental crust. More recent work (Glazner 2007; Spera and Bohrson; 2001; Clemens et al., 2009, 2010) has shown that both thermodynamically and geochemically the DePaolo models are insufficient in explaining felsic magma petrogenesis. The energy consumed by assimilation would essentially quench the magma body, and the hybrid magma would be so highly crystalized it would be immobilized and unable to undergo further magmatic evolution (Clemens 2012). Furthermore, though able to explain trace element and isotopic data, AFC modelling frequently fails to correctly predict the major-element chemistry of these hybrid magmas.

The production of felsic magmas is almost certainly a multi-step process, either commencing with the fractionation of a basaltic magma or beginning with the remelting of pre-existing rocks. In arc-settings a common model begins with the production of a basaltic magma from the sub-continental lithospheric or asthenospheric mantle which intrudes the lower crust, providing both heat and volatiles to the surrounding wall-rock (Clemens 2012). Specific granites are of particular interest to petrologists, as they are attributed to the hybridization of mantle magmas with a significant degree of crustal input; I-type or igneous/infracrustal granites were first introduced by Chappell & White (1974) as

metaluminous to weakly peraluminous, sodic rocks with variable in silica content (56-77 wt. % SiO_2). As further assimilation is difficult to achieve outside the elevated thermal regime where hybridization of these endmembers can occur, the chemical composition of felsic magmas can be tied closely to the source characteristics. Many authors conclude the source is the primary control on felsic magma chemistry and secondary processes (i.e. late fractional crystallization) only contribute a secondary overlay to this inherited composition (Annen et al., 2006; Clemens and Stevens, 2012; Clemens et al., 2010). This is especially true for isotopic characteristics, as once a magma has ascended from the source, it is generally too cool to assimilate a significant fraction of wall rock, resulting in isotopic trends directly representative of source processes.

3.2 Melting, Assimilation, Storage, Homogenization Zone/Deep Crustal Hot Zone

Subduction zones are very complex tectonic environments, with dynamic processes occurring all the way from the upper continental crust through the crust-mantle transition and into the mantle wedge. Buoyant melts from the mantle wedge with variable additions from the subducting plate ascend towards Earth's surface and flux the overlying continent. Hildreth and Moorbath (1988) were the first to invoke the idea of MASH, a hot region where rising mantle-derived magmas stall at the mantle-crust boundary, partially melt the heterogeneous crustal rocks, which then are free to mix with each other. In this region, melting, assimilation, storage and homogenization (MASH) of magmas can occur simultaneously. The combination of heat and volatiles which are released from crystalizing

mantle-derived basalts initiates significant crustal melting (Annen and Sparks 2002), and large volumes of intermediate to felsic magmas can be produced with a volumetrically moderate intrusion of basalts into the lower crust. Physically this region would be a complex interweave of dikes, sills, small chambers, crystalline mush and residual rocks which can blur the distinction of the crust-mantle boundary (Hildreth and Moorbath 1988).

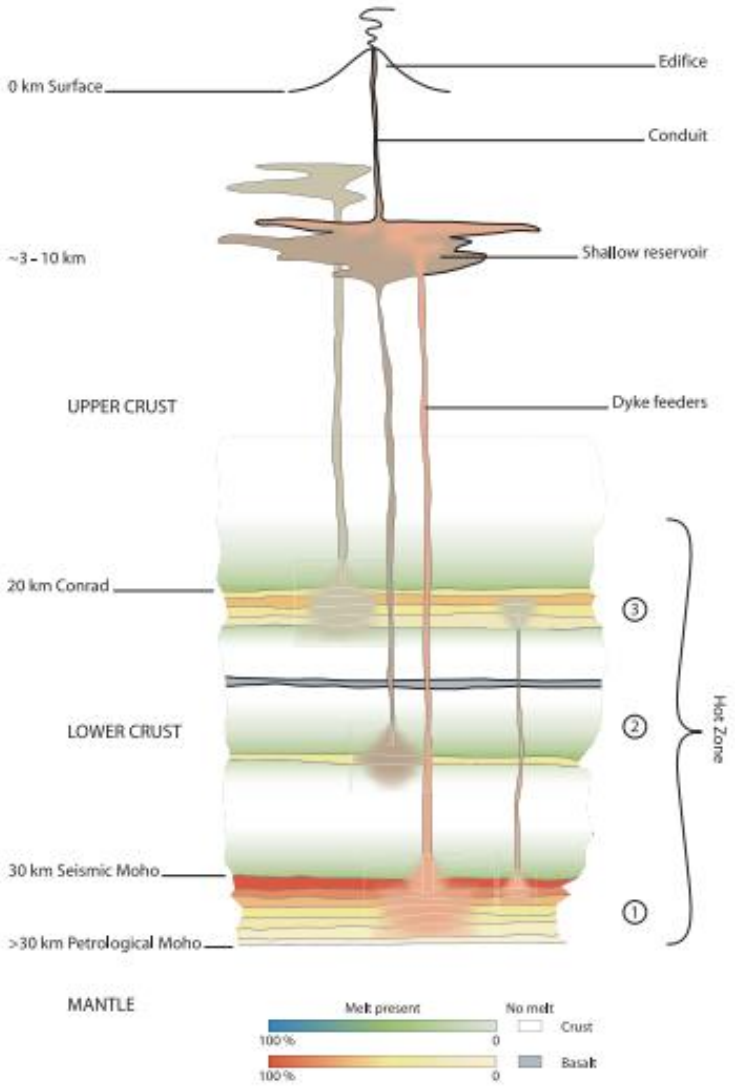

Figure 3.1 Schematic of Deep Crustal Hot Zone as envisioned by Annen et al., (2006). Mantle derived basalt is intruded as dikes and sills at various depths within the DCHZ, cooling from their intrusion temperature to that of the geotherm. As the number of sills increases the local temperature increases until subsequent basaltic intrusions can remain

partially molten. Crustal melting fractions will be dependent on the temperature of injections, number of sills emplaced and geometry in relation to the injections. Basaltic melts as well as those from crustal melting are free to mix and mingle throughout the DCHZ, prior to ascension or while ponding together in shallow reservoirs.

This hypothetical MASH model was further expanded and developed upon by Annen et al. (2006, 2008) and Solano et al. (2012) who using numerical simulations and phase equilibria constraints propose the idea of a Deep Crustal Hot Zone (DCHZ, Fig. 3.1). This DCHZ is envisioned as a region between 20-50 km depth where a mixture of partially crystalized basalt, partially molten crustal rocks and free-phase H_2O are able to comingle. Similar to the idea of basaltic underplating (Raia and Spera, 1997), successive mafic sills intrude and are emplaced in the lower crust above the mantle-crust boundary. The first sills to intrude are free to crystalize and pass heat into the surrounding rocks, and with repeated injections the region will progressively rise in temperature. The modelling shows after a period of time and depending on the rate of emplacement, the region can reach temperatures above the mafic solidus (>1000°C hydrous [Rapp and Watson, 1995], >1100°C anhydrous [Gill 2010]) and subsequent intrusions will remain partially molten allowing for the accumulation and mixing of residual melts. After sufficient heat has been provided to the pre-existing lower crust, fluid-absent crustal melting will also begin; this allows the DCHZ to generate magmas by any combination of residual melt from incomplete crystallization of the injected basalts, partial melts derived from pre-existing crustal rocks and the remelting of earlier emplaced fully crystalized intrusions. In this scenario, chemical variations in the mixed magmas are inherited from the earliest processes in the lower crust, by hybridization of a residual liquid from incomplete crystallization of the influxed basalt and a very minor

degree of crustal melting. Then, in nearly closed-system behaviour, the evolved andesite/dacite magma rises and rapidly crystalizes by degassing and conductive cooling in the upper crust and, through igneous differentiation, the magma then evolves towards a more siliceous compositions.

It should be noted that the MASH/DCHZ processes were modelled after the long-lived and relatively stationary Andean subduction zone. The sweeping volcanic front of the Ignimbrite Flare-up may have been migrating too quickly to establish the many processes intrinsic processes to a MASH/DCHZ, and instead these magmas formed as a result of shorter-term processes within the deep crust.

3.3 Introduction to Isotopes

Isotope geochemistry is a powerful tool in a geoscientist's toolbox that, amongst other capacities, allows for great resolution in determining the sources of igneous rocks. This section details the isotopic systematics for Rb-Sr, Sm-Nd and U-Th-Pb and presents the basics of applying each as source tracers.

Rb-Sr

One of the first parent-daughter pairs developed and applied by geoscientists was the rubidium (Rb) - strontium (Sr) isotopic system. Initially developed as a geochronometer, differences in chemical behaviour between the parent and daughter isotopes allowed further development as a method to identify source characteristics. Rb has two naturally

occurring isotopes, stable ^{85}Rb and the radioactive ^{87}Rb, while Sr has four isotopes ^{84}Sr, ^{86}Sr, ^{87}Sr and ^{88}Sr. ^{87}Sr is the only radiogenic isotope and is produced by the beta decay of ^{87}Rb with a half-life of ^{87}Rb ($t_{1/2}$) = 4.88 x 10^{10}y, and a decay-constant λ=1.42 x $10^{-11}y^{-1}$. By convention Sr isotopic data are reported as ^{87}Sr/^{86}Sr ratios, which is the comparison of the number of atoms of the radiogenic daughter relative to a stable, non-radiogenic isotope.

Rb has a 1+ charge and a large ionic radius making it a highly incompatible element in most igneous systems, while Sr is slightly less incompatible as a result of a smaller ionic radius and a 2+ ionic charge. These differences of chemical behavior between the parent and daughter elements can produce large variations of the Rb/Sr ratio in rocks or minerals. As time progresses, subsequent differences in ^{87}Sr/^{86}Sr are helpful in both constraining the geologic age or rocks and the timing of mantle differentiation events that produce reservoirs with measurably different isotopic compositions.

Age determinations using Rb and Sr relies on a technique known as isochron dating, which can be applied to suites of cogenetic rocks as well as different mineral phases within a single rock. The assumptions being made are that all the chosen samples are cogenetic (same age) and had the same initial isotopic ratios, in this case the same initial ^{87}Sr/^{86}Sr. As we've shown previously, the amount of a daughter isotope within a closed system is a function of the amount of time passed as well as the ratio of parent to daughter isotope in the system at the time of closure:

$$^{87}Sr/^{86}Sr_t = {}^{87}Sr/^{86}Sr_{t=0} + {}^{87}Rb/^{86}Sr * (e^{\lambda t} - 1)$$

Thus, in a suite of samples that all underwent closure at the same time, the variation in $^{87}Sr/^{86}Sr$ will only be a result of differences in the parent-daughter ratio at the time of crystallization and the time since crystallization. If all the assumptions made are correct, by plotting $^{87}Sr/^{86}Sr$ against $^{87}Rb/^{86}Sr$ a set of samples will fall on a line known as an isochron, with a slope representative of the time passed since the system closed , $m= e^{\lambda t} - 1$. By rearranging the decay equation we can solve for t:

$$t = \frac{1}{\lambda} \ln(m + 1)$$

These plots also allow for us to determine the initial isotopic ratio of the system at the time of closure, at t=0 or the y-intercept. Worth discussing is the validity of an age derived from an isochron, as a primary assumption when constructing these plots is that the suite of samples has remained isotopically closed throughout geologic time and the calculated age represents the time of crystallization for the system. In the case where the system has reopened, for example if temperatures exceed the closure temperature of the Rb-Sr system and fully rehomogenized isotopically, a mineral isochron will give the age of re-equilibration whereas a suite of whole-rock analyses will still give the initial age of crystallization. Re-equilibration is a frequent result of metamorphic events, and it is vital to understand the limitations of isochrons to correctly understanding the established geochronology. Igneous processes intrinsic to the generation or evolution of magmas, such as fractional crystallization or partial melting, will not fractionate isotopes of the same element from one another; i.e. crystallization of a mineral phase from a magma body will inherit the exact isotopic composition of the magma at the time of crystallization. With this

in mind, if an igneous system has remained closed since the time of crystallization, the isotopic composition of such a system is the sum of radiogenic ingrowth and the initial composition of the system.

Because of the differences in chemical behaviour between Rb and Sr, over geologic time the mantle and crust have evolved to measurably different $^{87}Sr/^{86}Sr$ compositions. Rubidium is more incompatible than strontium, and as a result for each differentiation event (i.e. melting of the mantle) Rb will partition into the melt to a greater degree than Sr. With time, reservoirs that are enriched in the more incompatible elements (high Rb/Sr ratio, i.e. continental crust) will evolve to higher $^{87}Sr/^{86}Sr$ ratios, and reservoirs which are depleted in incompatible elements (low Rb/Sr ratio, i.e. the mantle) will evolve to lower $^{87}Sr/^{86}Sr$ ratios (Fig. 3.2).

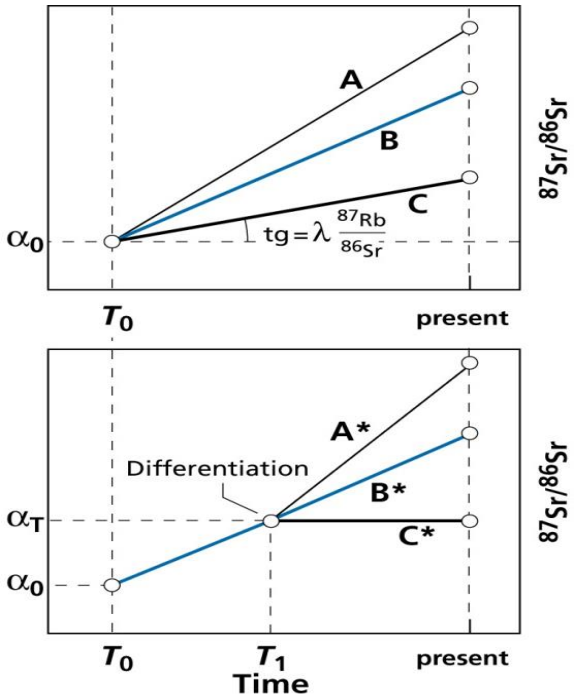

Figure 3.2 Above) The evolution of $^{87}Sr/^{86}Sr$ ratios for 3 reservoirs through time, the slope of each line is a function of Rb/Sr concentration. Enriched reservoirs (A) will have high

Rb/Sr ratios and will evolve to high $^{87}Sr/^{86}Sr$ ratios, while depleted reservoirs (C) will have low Rb/Sr ratios and in the same amount of time will evolve to lower $^{87}Sr/^{86}Sr$ ratios. Below) Differentiation of a system at time T_1, A^* is the most enriched reservoir (high Rb/Sr) and evolves to the highest $^{87}Sr/^{86}Sr$ ratio with time, B^* the same Rb/Sr ratio as the initial reservoir and evolves to the same $^{87}Sr/^{86}Sr$ ratio the undifferentiated reservoir would have with time. C^* is the depleted reservoir and in this cartoon has an Rb/Sr ratio of 0, consequently its $^{87}Sr/^{86}Sr$ ratio remains constant through time. Allègre (2008).

Sm-Nd

Samarium (Sm) and Neodymium (Nd) are rare earth elements; they are both lithophile and refractory elements. ^{143}Nd is produced from the alpha decay of ^{147}Sm with a half-life of 1.06 x 10^{11}y (λ=6.54 x $10^{-12}y^{-1}$). Neodymium is more incompatible than Sm, resulting in higher Sm/Nd ratios in incompatible trace element depleted reservoirs such as in the mantle compared to enriched reservoirs such as the crust. As a consequence, the $^{143}Nd/^{144}Nd$ ratio is higher in mantle rocks than crustal ones. The Sm-Nd system can be used for isochron dating similarly to the Rb-Sr system but given that Sm and Nd have similar chemical characteristics (both are rare earth elements having a 3+ charge and a small ionic radius), there is significantly less variation in parent-daughter ratio variations in comparison to the Rb-Sr system. It can be more difficult to get a suite of co-genetic samples with a large enough variation in the Sm/Nd ratio to get a precise age. This is especially true for young rocks given the long half-life of 106 billion years for ^{147}Sm. Also unlike Rb and Sr, Sm and Nd are relatively immobile elements and thus more resistant to post-crystallization events such as weathering and metamorphism.

By convention, Nd-isotopes are reported as a $^{143}Nd/^{144}Nd$ ratio or more commonly as epsilon Nd (εNd) values representing the measure of deviation from the Earth's chondritic $^{143}Nd/^{144}Nd$ ratio. Epsilon notation is calculated using the following equation;

$$\varepsilon NdT = \left[\frac{\frac{^{143}Nd}{^{144}Nd} T_{sample}}{\frac{^{143}Nd}{^{144}Nd} T_{CHUR}} - 1 \right] x\ 10^4$$

where CHUR represents the Chondritic Uniform Reservoir assuming a chondritic Nd isotopic composition for the bulk silicate Earth at a time T. Present-day CHUR values are $^{143}Nd/^{144}Nd$ of 0.51263, $^{147}Sm/^{144}Nd$ =0.196 (Bouvier et al., 2008). For terrestrial rocks, εNd values generally ranges from -20 to +10, with positive values representing a depleted source and negative εNd values associated with enriched sources (Fig. 3.3).

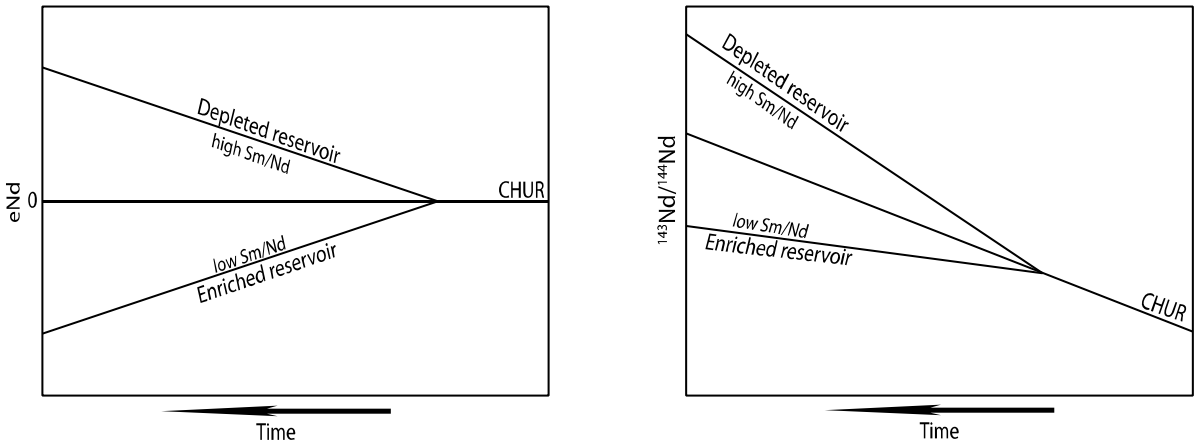

Figure 3.3 Left) Epsilon Nd evolution of an enriched and depleted reservoir through time after differentiation from Chondritic Uniform Reservoir. Right) The same differentiation event and subsequent evolution of $^{143}Nd/^{144}Nd$ for an enriched and depleted reservoir.

When Sr and Nd isotopic results are combined, they can be very useful in determining source characteristics, as the inverse relative compatibilities between parent-daughter

pairs results in great contrast between source reservoirs (Fig 3.4). The opposite chemical compatibility of parents and daughters results in mantle rocks and mantle-derived magmas with high eNd values and very low $^{87}Sr/^{86}Sr$ ratios. A spectrum of isotopic ratios can be found in modern oceanic basaltic magmas which constitutes what is considered to be the "mantle array", which begins with mid-ocean ridge basalts which are the melting products of the depleted mantle and have the highest εNd and lowest $^{87}Sr/^{86}Sr$ and evolves though oceanic island basalts representing the melting products of the enriched mantle with low εNd and near continental $^{87}Sr/^{86}Sr$ values. The continental crust is much more heterogeneous than the mantle but for the most part has high $^{87}Sr/^{86}Sr$ and low εNd.

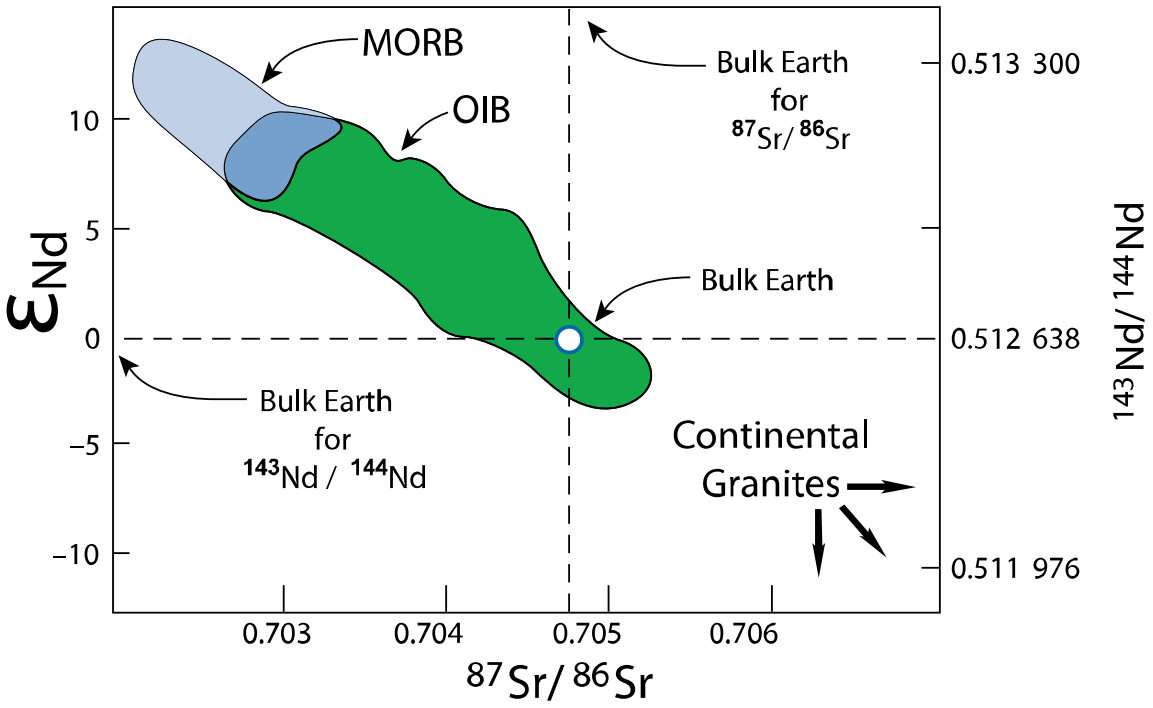

Figure 3.4 Sr vs Nd isotopic correlation for major terrestrial reservoirs. The mantle array is defined by the tight correlation between radiogenic Sr and Nd for oceanic basalts; granites plot as a broader field to the lower right of Bulk Earth on this cartoon and extend to a much

larger range of isotopic values than shown. Modified after Allègre (2008)

(Pb)-(Pb), Common Lead

Unlike the Sr and Nd isotopic systems, Pb is a relatively volatile and chalcophile element, resulting in a non-chondritic Pb isotopic composition of the bulk silicate Earth. Lead is widely distributed as a trace element throughout Earth's systems and exists as the radiogenic daughter products of 3 different parent isotopes, ^{238}U, ^{235}U and ^{232}Th, as well as a primeval Pb-component formed by nucleosynthesis. The decay of both U and Th to stable isotopes is more complicated than the previous discussed systems; the main radioactive isotopes of U and Th (^{238}U, ^{235}U and ^{232}Th) are each parents to a series of radioactive decay chains ending in stable ^{206}Pb, ^{207}Pb and ^{208}Pb, respectively, and are measured relative to the sole stable isotope ^{204}Pb.

Pb isotopes are arguably the strongest of the isotope systems discussed in this section as indicators of crustal contamination of a mantle-derived magma. U and Th are both highly incompatible elements compared to Pb and partition strongly into the continental crust, and thus crustal rocks will evolve to higher Pb isotopic ratios compared to the mantle (Fig. 3.5). Furthermore, Pb's tendency to partition to crustal rocks results in significantly higher Pb concentrations in crustal rocks when compared to mantle derived magmas. The isotopic ratio of a system in which two end-members are mixing will be controlled by the elemental concentrations of each end-member and, in the case of Pb, when mantle-derived magmas are assimilating crustal rocks the isotopic signature of the mixture quickly shifts to that of the crustal source. In situations with only a small degree of mixing the resultant isotopic signature is often completely representative of the crustal end-member (Dickin 2005).

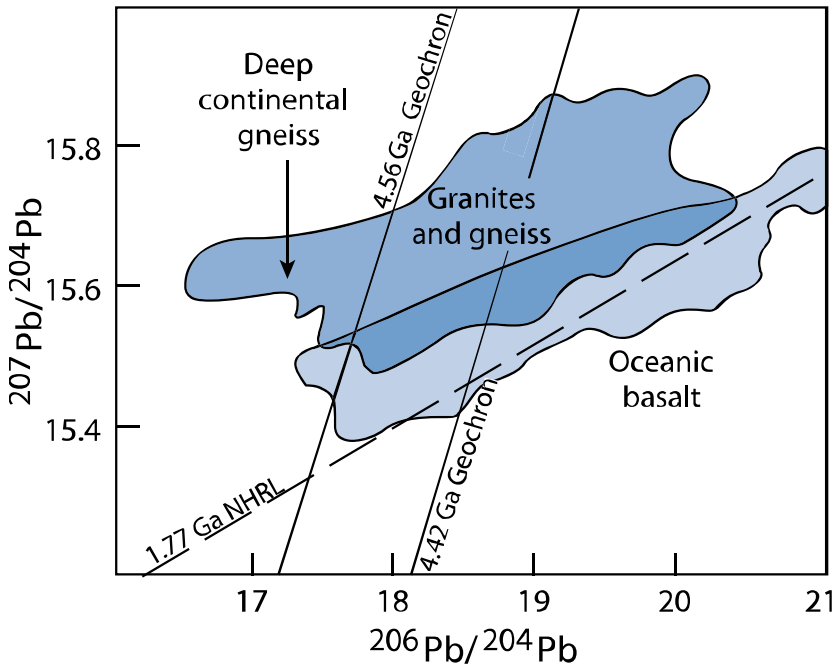

Figure 3.5 Cartoon of the major Earth domains in lead-isotope space. Notice both the continental crust and mantle basalts generally overlap in terms of $^{206}Pb/^{204}Pb$ but have differing $^{207}Pb/^{204}Pb$ compositions. For reference, there are the 4.56 and 4.42 geochrons showing the approximate evolution of Bulk Earth's lead-isotope composition over geologic time as well as the Northern Hemisphere Reference Line (NHRL, Hart 1984) which represents the isotopic evolution of the convecting mantle beneath the northern hemisphere with a slope equal to an age of 1.77 Ga. Modified after Allègre (2008).

4. Regional Geology

4.1 Geological Framework

The tuff of Elevenmile Canyon (TEC) is located within the WNVF of the southwest United States (Fig. 4.1). Originally recognized by Riehle et al., (1972) as a rhyolitic tuff sequence in the Clan Alpine Mountains, the TEC was identified as a distinct intracaldera deposit by John (1994, 1995), and the boundaries of the caldera margin have continued to expand with additional mapping in recent years. Intracaldera rocks of the TEC have now been found in 4 adjacent mountain ranges: the southern Stillwater Range, Louderback Mountains, Clan Alpine Mountains and the Desatoya Mountains, making it one of the largest calderas of the WNVF (Henry and John 2013). Significant outflow material is correlated with the TEC up to 120 km westward, reaching as far as the California-Nevada border. Estimated volumes of total erupted material are greater than 2000 km^3, predominantly as intracaldera intermediate and felsic ash-flow tuffs.

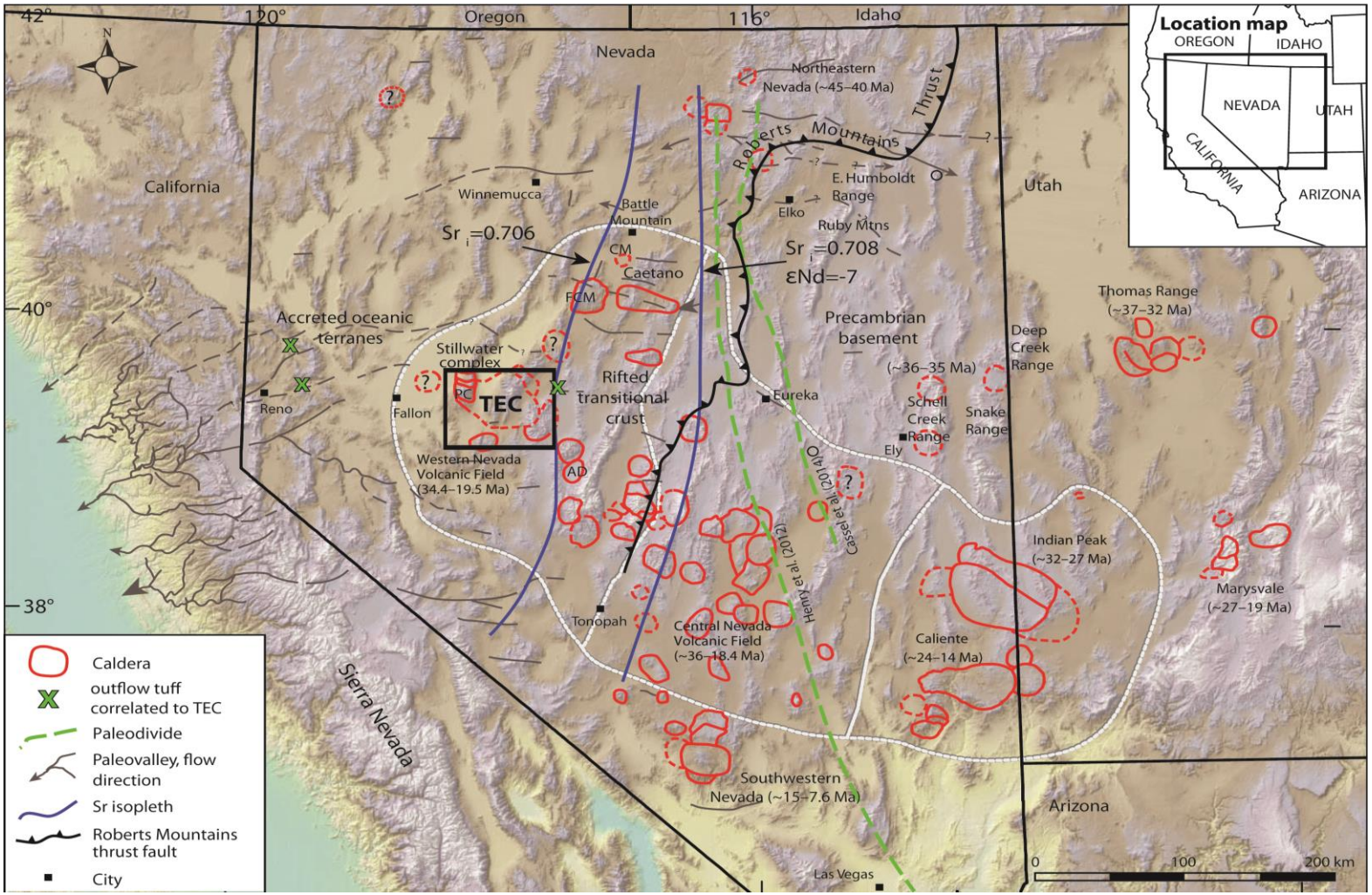

Figure 4.1 Map of the western United States centered on Nevada detailing the three major Nevada Volcanic Fields related to the Ignimbrite Flare-up. Dashed red lines denote inferred caldera margins of erupted units, and the Southern Stillwater Volcanic Complex is outlined by a bold black box. The tuff of Elevenmile Canyon is the largest of these calderas in the volcanic complex. The approximate locations of samples taken of outflow material correlate to the TEC are shown with green X's. The Sr and Nd isopleths are from Farmer and DePaolo (1983). Modified after Henry and John (2013).

4.2 Stratigraphic Relations

The Elevenmile Canyon Caldera is the largest of 5 overlapping Oligocene calderas and related plutons within the Stillwater Caldera Complex, one of the largest magmatic centres of the WNVF (Fig. 4.2). Tectonic relations were originally described by John (1995) and later studies confirmed the volcanic and plutonic chronology with geochemistry and isotopic dating (Henry and John, 2013; John et al., 2014). This summary is based on their interpretations unless otherwise noted.

The Stillwater Caldera Complex uncomformably overlies and intrudes Mesozoic basement rocks exposed in the region, including Triassic and Jurassic metasedimentary and metavolcanic rocks that are locally intruded by Late Cretaceous granites and a Late Cretaceous felsite. Cenozoic magmatism in the area began with the eruption of a thick sequence of rhyolitic lava flows, domes and densely welded tuff, forming a large dome sequence of ~30 Ma age that underlies the earliest formed caldera (Job Canyon) that was shown to be genetically separate from the southern Stillwater Caldera Complex based on geochronological and trace element differences. This volcanic sequence and the overlying Job Canyon tuff were intruded locally by the IXL pluton in the northwestern section of the field area around 28 Ma.

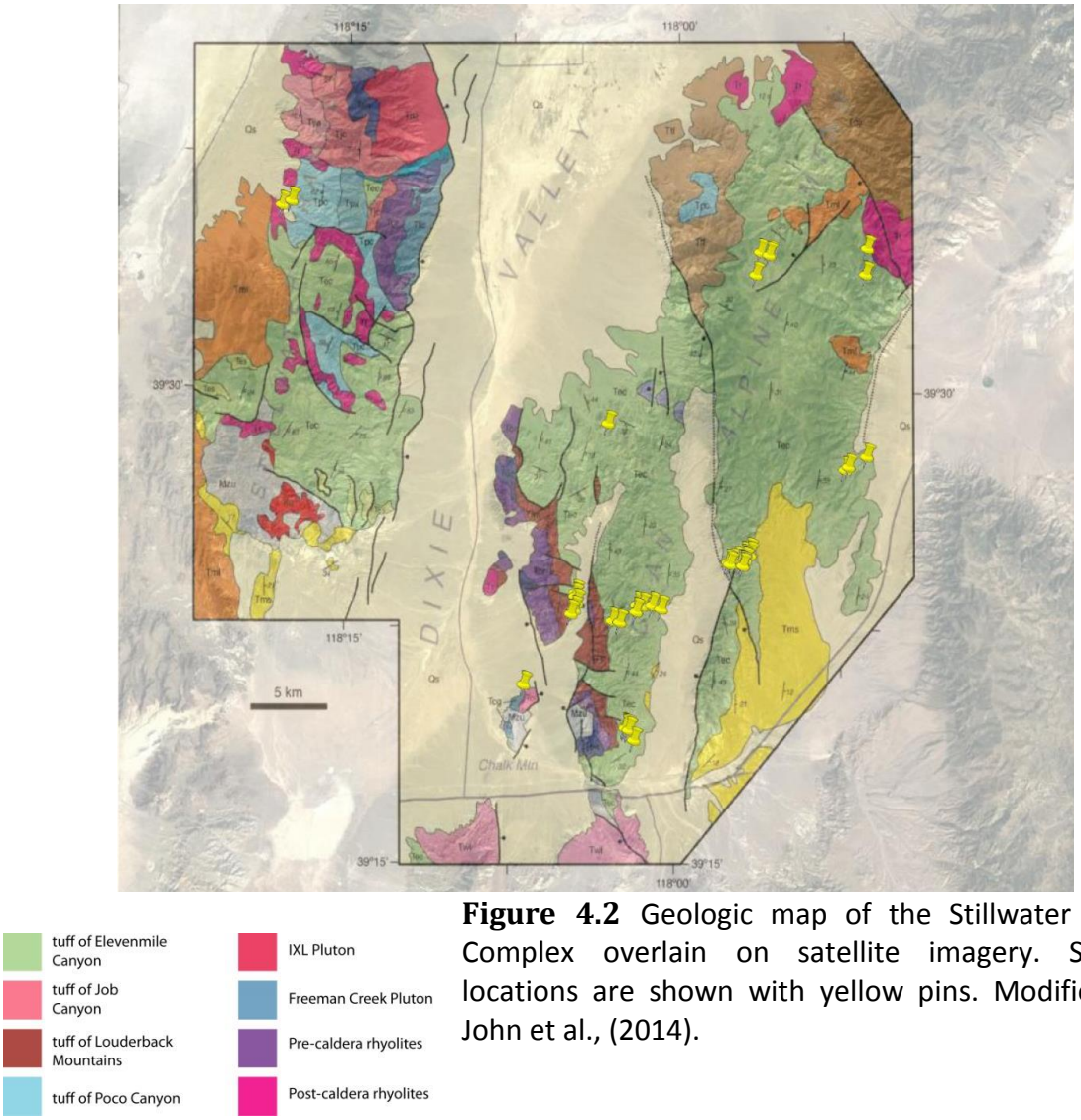

Figure 4.2 Geologic map of the Stillwater Caldera Complex overlain on satellite imagery. Sampling locations are shown with yellow pins. Modified after John et al., (2014).

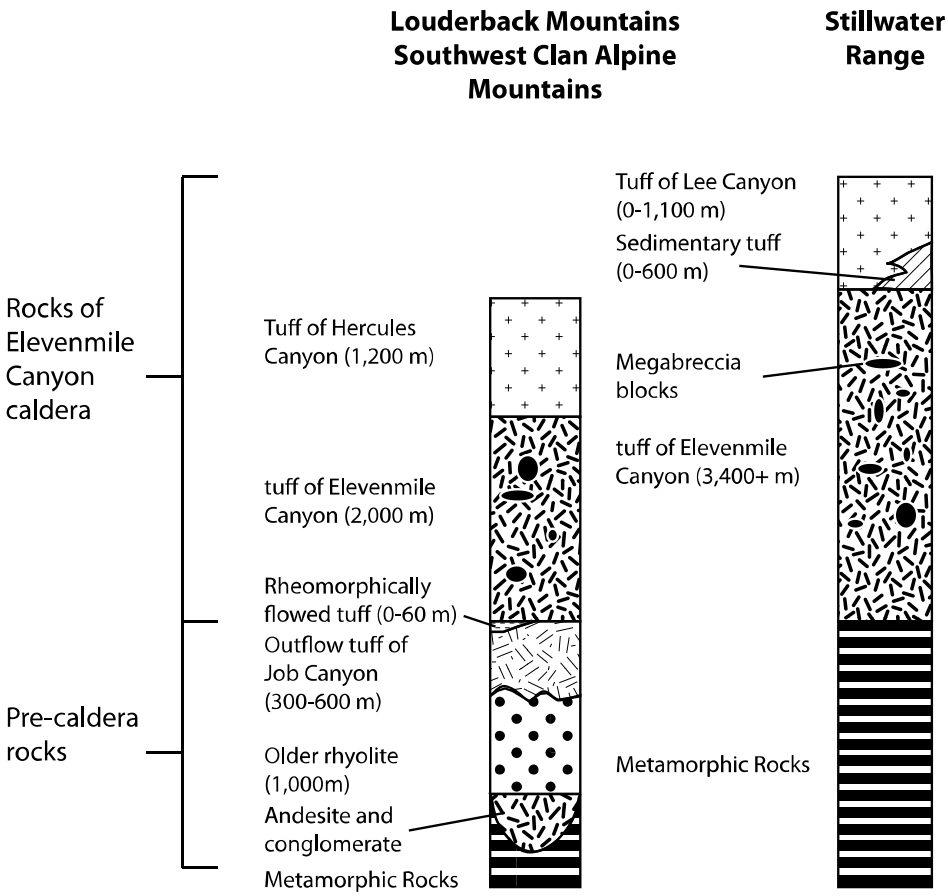

Figure 4.3 Stratigraphic column of the Elevenmile Canyon caldera in the Louderback, Southern Clan Alpine and Stillwater ranges**.** Not shown are the Poco Canyon Caldera and Louderback Mountain caldera which lie above and below the rheomorphically flowed tuff in the left column. After Henry and John (2013)

The oldest of the overlapping calderas, the Job Canyon Caldera, collapsed at about 29 Ma in the northwestern-most part of complex, depositing intracaldera tuff conformably over older dacitic to andesitic lava flows. The Job Canyon sequence is composed of ~1,500 m pre-collapse intermediate lava flows and breccias, ~2,000 m of intracaldera ash-flow tuff (tuff of Job Canyon), and an additional ~1,000 m of post-collapse breccia and sedimentary units. The caldera is composed of 2 distinct northern and southern structural blocks,

separated by a fault trace that has been since destroyed by subsequent tectonic and igneous events. This caldera event includes a widely distributed outflow tuff component that travelled predominantly to the east and southeast. Underlying the caldera is up to 1500 m of pre-collapse andesite and dacite lava flows that are commonly brecciated. The intracaldera tuff of Job Canyon is a moderately to densely welded ash-flow tuff, crystal-poor (<15% phenocrysts), and predominantly rhyolitic in composition. Phenocrysts are principally potassium feldspar and plagioclase in variable amounts, with minor quartz and trace amounts of biotite. Lithic fragments are sub-angular to sub-rounded clasts of Cenozoic andesitic and rhyolitic lava flows, and less commonly Mesozoic quartzite. Lithic proportions are as high as 50% by volume in lithic-rich parts of the tuff, most evident in the south block. Ar-Ar and K-Ar dates throughout the tuff give an eruption age of ~29 Ma (John et al., 2014), and are very tightly clustered which supports a very short eruption period (<0.5 m.y.). The tuff of Job Canyon is locally interbedded with collapse-related breccia, and is overlain by up 2500 m of intermediate lava flows and minor sedimentary sequences. Above the north block this includes dacitic and andesitic lava flows, flow breccia, shallow intrusive rocks, minor lacustrine and other sedimentary rocks, and caldera-collapse related megabreccia near the caldera wall. Intruding the north block is the IXL pluton, a weakly porphyritic granodiorite and quartz monzodiorite that is roughly coeval (~28 Ma) with the dacitic to andesitic lava flows that overlie the caldera. The southern block of the Job Canyon caldera is a composite of smaller fault blocks separated by east-west faults that were active during deposition of the intracaldera tuff. The tuff in the south block ranges in

thickness from ~2000 m at the northern margin to ~1000 m at the south end and is overlain by thinner, younger dacite and andesite lava flows that filled depressions in caldera.

After a 3 m.y. hiatus in magmatism in the area, a subsequent series of three calderas formed almost coevally between 25.1 and 25.2 Ma (Henry and John 2013, John et al., 2014). Both the Poco Canyon Caldera (~25.2 Ma) and Louderback Mountains Caldera (25.2 Ma) are nested within the Elevenmile Canyon caldera (~25.1 Ma, Fig. 4.4). In the southern Stillwater Range the Poco Canyon Caldera and the Elevenmile Canyon caldera share a common northern margin that overlaps with the tuff of Job Canyon, following the structural divide that separates northern and southern fault blocks of the Job Canyon caldera. Chronological relations between these calderas are difficult to ascertain. In Poco Canyon of the southern Stillwater range, the upper cooling unit of the tuff of Poco Canyon overlies the lower cooling unit of the TEC. However, south of Job Peak, the lower cooling unit of the tuff of Poco Canyon lies below the TEC. Field observations interpreted these as two megascopically identical cooling units within the tuff of Poco Canyon that represent distinct eruptions in time, possibly linked to the eruption of the TEC. The 2 distinct cooling units are a crystal-rich rhyolite and a high-silica rhyolite tuff, separated by a crystal-poor high-silica rhyolite tuff of uncorrelated origin, caldera-collapse breccia as well as a thick unit of the TEC. The tuff of Poco Canyon contains between 25-55% phenocrysts by volume which are principally sanidine, smoky quartz, minor plagioclase and trace amounts of biotite. The upper cooling unit also contains trace amounts of allanite as an accessory phase. Ar-Ar dating on sanidine from the tuff has given an age of ~25.2 Ma (John et al., 2014) in agreement with the Ar-Ar dates determined from associated outflow tuffs. Total

thickness of Poco Canyon caldera-related deposits is greater than 4500 m in places, with an outflow component being identified to the east and up to 180 km west of the Stillwater complex. Somewhere between the eruption of the two Poco Canyon cooling units the primary eruption of TEC rocks occurred.

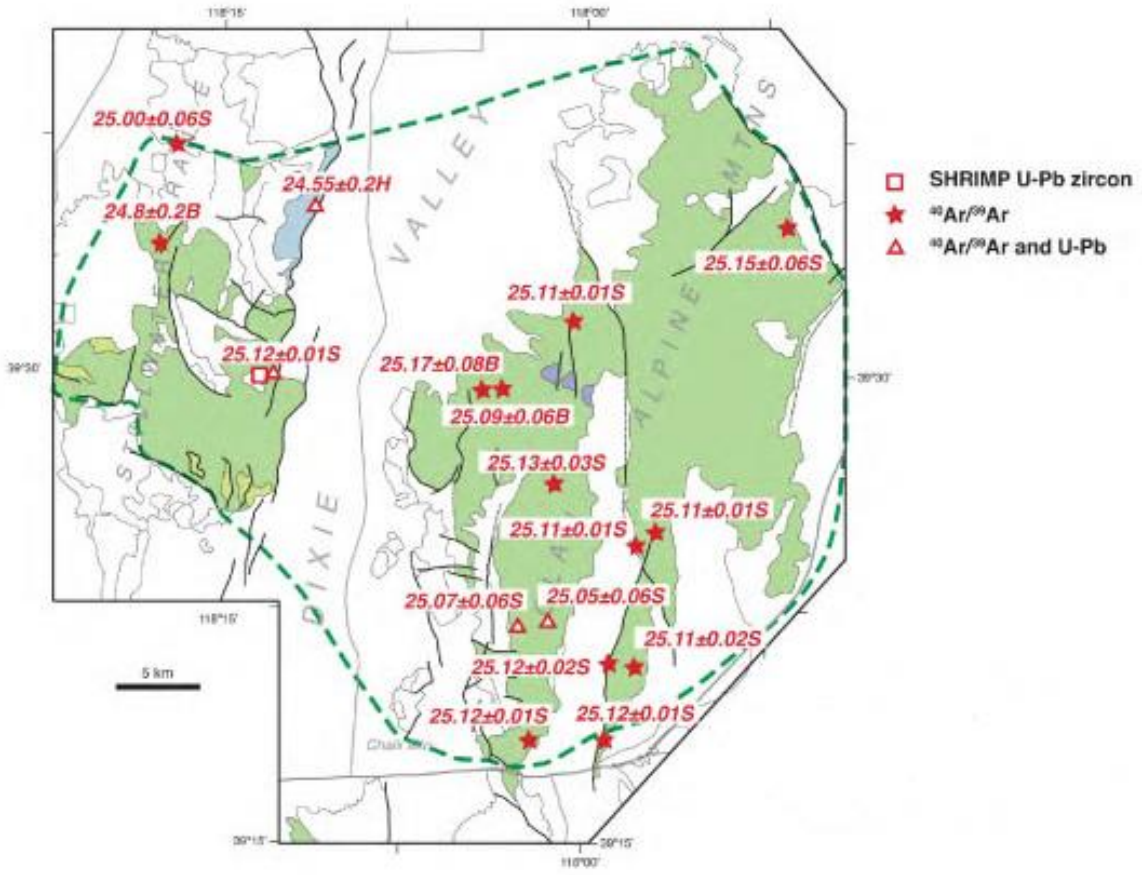

Figure 4.4 Sample locations of $^{40}Ar/^{39}Ar$ and U-Pb zircon age determinations of the TEC reported by John et al., (2014). 20 $^{40}Ar/^{39}Ar$ ages on individual sanidine grains yielded a mean age of 25.12 ± 0.01 Ma, while U-Pb zircons dates from 8 samples yielded ages between 24.98 ± 0.25 and 25.82 ± 0.28 Ma.

The TEC and tuff of Poco Canyon are linked to the Freeman Creek pluton which intrudes the central and northern two thirds of the Poco Canyon caldera and subsequently the Elevenmile Canyon caldera. As a composite pluton, it consists of an older biotite-hornblende granodiorite porphyry phase and a younger leucocratic porphyritic granite phase. Compositional variation has linked the older more mafic granodiorite to the more intermediate TEC. U-Pb and $^{40}Ar/^{39}Ar$ dating have given an age of 25.01 ± 0.15 Ma for the granodiorite phase and an age of 24.83 ± 0.20 Ma for the younger granite phase.

The last pulse of magmatism related to the Ignimbrite Flare-up within the Stillwater Caldera Complex is represented by the emplacement of the Chalk Mountain pluton (24.8 Ma) and a series of post-caldera rhyolites that range in age from 24.8-21 Ma. These include rhyolite-dacite domes (24.8-22.6 Ma) in the northwestern part of the Stillwater Caldera Complex and a silicic dike swarm (23-21 Ma) that intrudes the southern half of the region.

4.3 Extension in the Stillwater Caldera Complex

There have been two periods of Cenozoic extensional faulting that affected the caldera complex, an early period of extension that took place shortly after the eruption of the TEC and the later Great Basin extension. Initial extension occurred between 25 and 22 Ma, as evidenced by field relations between the volcaniclastic rocks and later silicic intrusions. Tilting is thought to have occurred along shallow, west dipping, curviplanar faults in the TEC (John 1992) and resulted in the north half of the caldera complex being tilted 70-90 degrees west and the south half tilted 55-75 degrees to the east. The zone of accommodation for

this change in tilt-direction is poorly understood and was masked during the subsequent phase of extension, though dikes emplaced during the early Miocene (~19.5 Ma) indicate a local north-northeast to south-southwest direction of extension that conflicts with regional early Miocene east-west stresses (John 1993). Extension occurred along north-northeast striking, high-angle, dip-slip faults with little to no later movement, supported by Middle Miocene (~14.5 – 13 Ma) lava flows to the west and southwest of Dixie Valley which show gentle tilting to the west along the north-northeast striking fault traces. Most recently the Fairview Peak/Dixie Valley earthquakes of 1954 have left fault scarps on the east side of the Stillwater Range and contributed to a total uplift of the Stillwater Range to several kilometres relative to Dixie Valley.

4.4 Field Observations

Fieldwork was conducted in April 2015 for 2 weeks. In the field, the distinguishing feature of the TEC amongst all the other volcanic rocks of the Stillwater Caldera Complex is the abundance of black argillite lithic clasts and biotite as an abundant phenocrystic phase.

Throughout almost the entire southern Stillwater Range, the TEC has undergone some degree of alteration (Fig 4.5 E) resulting in a green tinged groundmass with green-yellow-brown pumice. The altered matrix resisted significant weathering but included pumice fragments have generally begun to eroded out. In the adjacent ranges, unaltered exposures of the TEC have a light-grey or a red-brown groundmass with at least 2 separate pumice types; a light grey to very light pink phenocryst-rich pumice (Plagioclase + Quartz +

Sanidine, Fig. 4.5 C), and a darker, waxy (more hydrated?) dark pink-brown-red pumice which is significantly less crystal rich (Fig. 4.5 B). Lithic clasts are mainly the black argillites but the TEC also includes fragments of flow-banded rhyolite, grey-ashy rhyolite, and green-brown, heavily altered volcanic rock. At the outcrop and hand sample scale these fragments are often accompanied by deformation of the surrounding groundmass, and in the more altered samples the lithic fragments are surrounded by heavily weathered halos.

The TEC can be separated into 3 textural zones; a densely welded lower portion with significant deuteric alteration (Fig. 4.5 E), a middle unaltered (outside of Stillwater Range) section (Fig. 4.5 B,C) and an upper poorly welded portion that is locally interbedded with lacustrine sediments (Fig. 4.5 A). Transects of the Clan Alpine Mountains represented the best opportunity to continuously sample through close to the entire intracaldera package. Multi-tiered cliff faces were present (Fig. 4.5F) suggestive of multiple flow units but the contacts between each had been obscured by erosion. Typical weathering patterns included rounded blocks and rubble from jointed flow-units as well as sheet-like weathering of more rounded outcrops. Topping a peak in the Clan Alpine Range is a single vitrophyric unit (Fig 4.5 D) (15-CA-33) that separates 2 packages of moderately welded TEC. The vitrophyre has a mineralogy identical to the TEC with 2 types of very strongly welded fiamme: a glassy black pumice with abundant feldspar, and a crystal poor red-brown pumice. These possibly represent the white-pink and dark-pink-red pumices observed elsewhere in the TEC respectively. Directly above the vitrophyre, pumices became significantly less compressed, possibly marking the top of tuff deposition.

A)

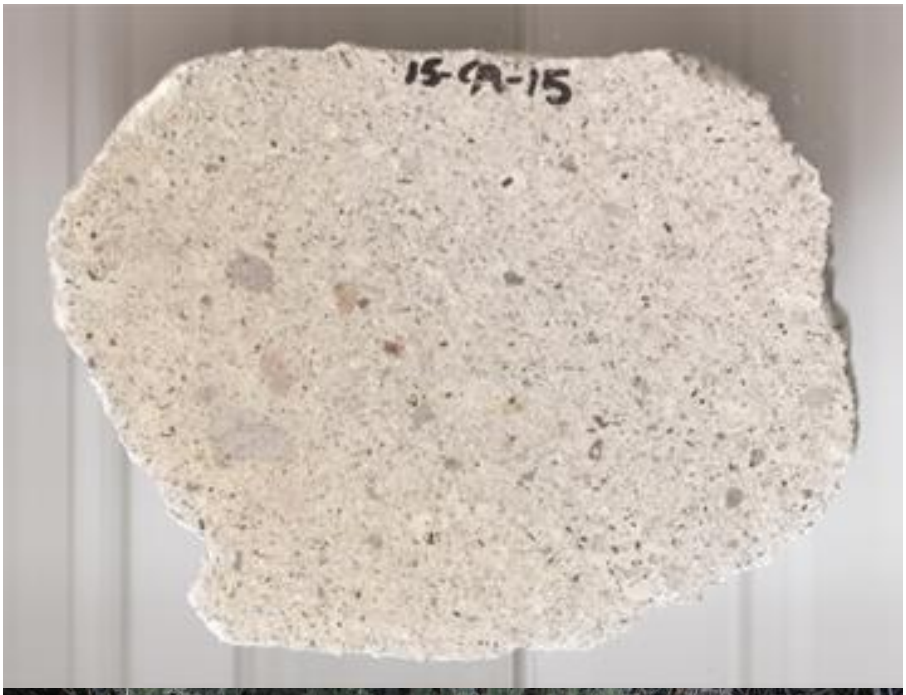

B)

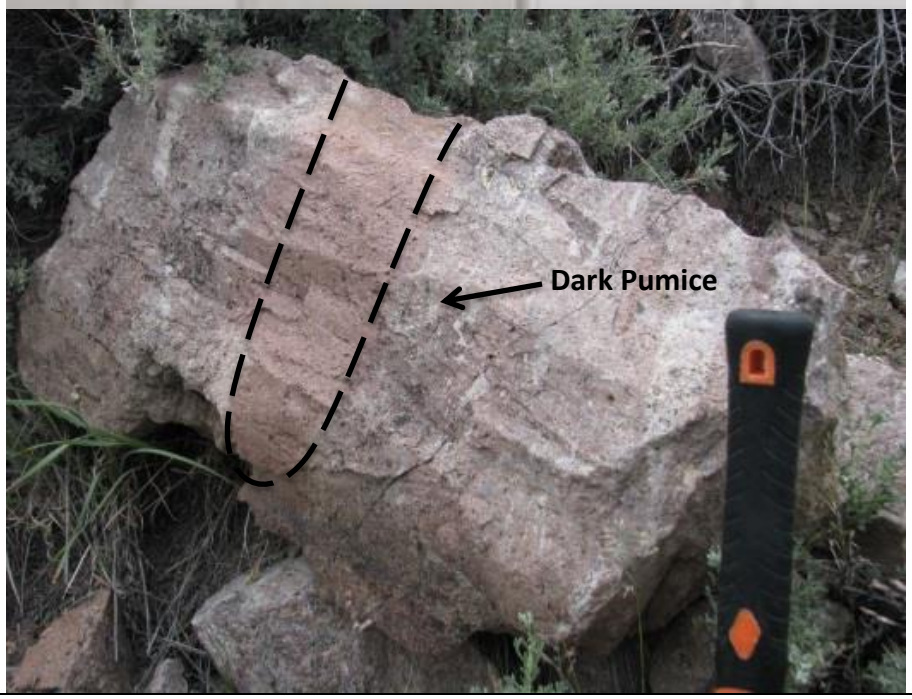

Figure 4.5 A) Hand sample of poorly-welded tuff of Elevenmile Canyon, showing 2-4 mm clasts of black argillite and slightly larger 3-5 mm clasts of a flow-banded rhyolite **B)** Pink moderately crystal-poor pumice in left third of boulder, referred to as "dark pumice"

Fig. 4.5 Cont. C) Grey crystal-rich pumice fragment in densely welded tuff, referred to as "light pumice" **D)** Contact between densely welded tuff above vitrophyric tuff

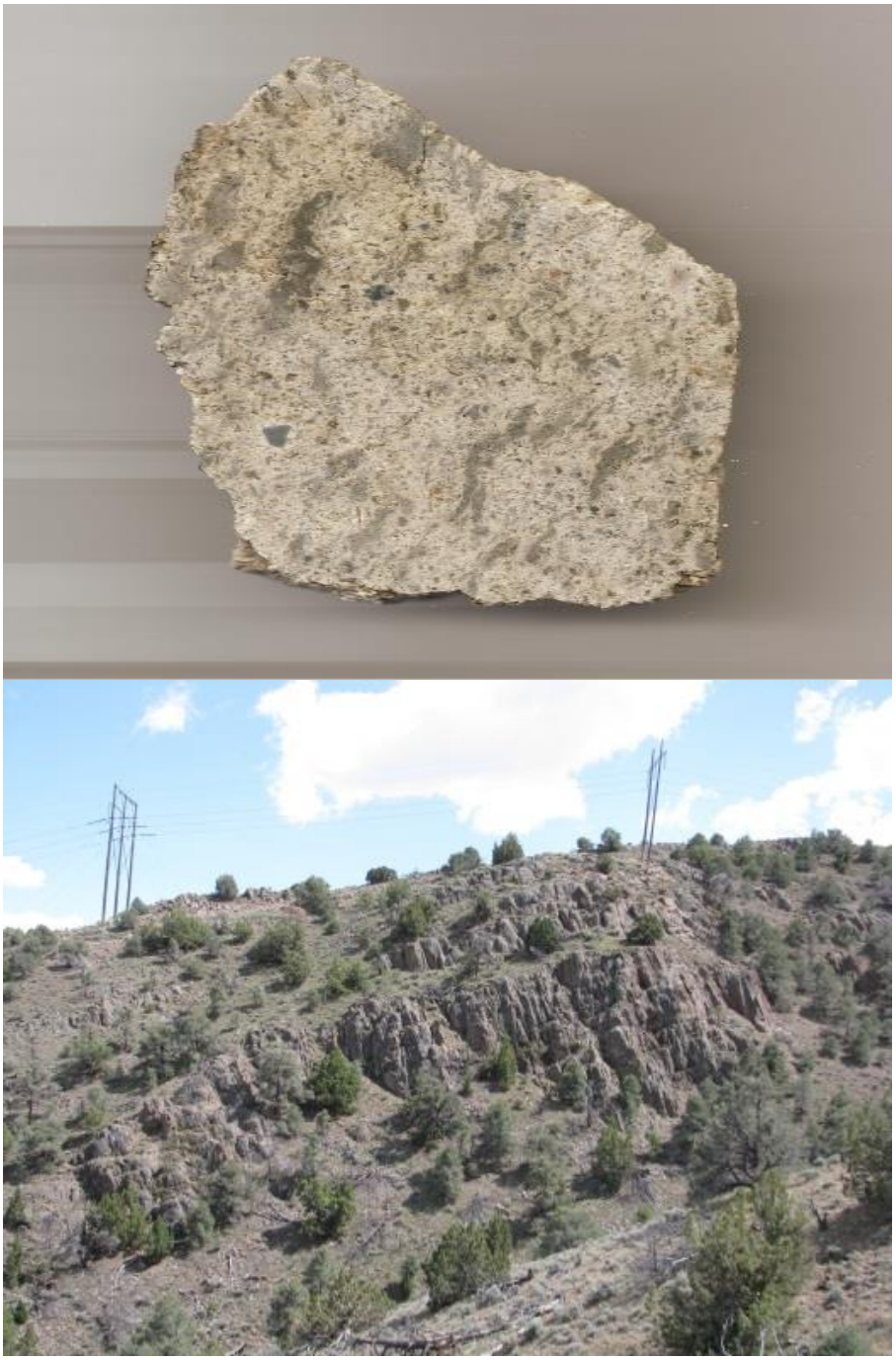

Fig. 4.5 Cont. E) Propylitic alteration in tuff from the southern Stillwater Range, fiamme has chloritized and taken on a green coloring **F)** Multi-tiered cliff face composed entirely of intracaldera tuff.

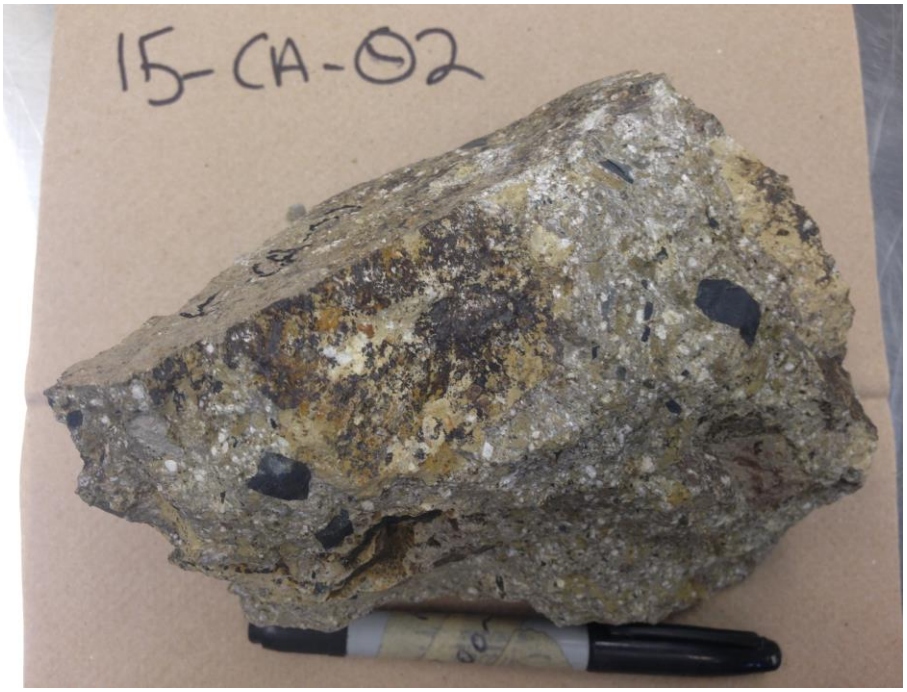

Fig. 4.5 Cont. G) Altered sample of ignimbrite showing black argillite fragments common to the TEC.

5. Methods

5.1 Samples

56 rock samples were collected and prepared for detailed petrographic, geochemical and isotopic studies. Sample locations and rock types are listed in Appendix 1, Table 1. Representative unaltered, non-weathered in-situ samples were collected, covering the full stratigraphic extent of the TEC. Sampling focused on pumice fragments that could be separated from the matrix, but in cases where this was impossible whole rock samples were collected with effort to minimize the number of lithic fragments. Textural evidence at the outcrop scale suggests that the rocks of the southern Stillwater Range exhibit a higher degree of post-depositional hydrothermal alteration and therefore efforts were focused in collecting samples from the less altered Clan Alpine and Louderback Mountains. An additional 20 rock samples were obtained from D. John (USGS) and C. Henry (Nevada Bureau of Mines and Geology) for analysis, including 3 whole rock samples of the TEC from the Desatoya Mountains, 5 samples of outflow tuffs from western Nevada, and 12 samples of exposed Pre-Cenozoic basement units in the region.

Polished thin sections were produced from 55 out of the 56 collected samples at the University of Ottawa Thin Section Laboratory. Thin section blanks of whole rock samples were prepared to include a fragment of pumice in as many thin sections as possible.

5.2 Major and Trace Element Analyses

Sample preparation was done at the Carleton University rock preparation facility. Hand samples were cut into slabs and weathered surfaces removed using a diamond-bladed rock saw. Where possible, pumice fragments were cut from the whole rock matrix. A Bico Chipmunk jaw-crusher was used to crush each sample; the steel plate used for crushing was scrubbed with a wire brush and cleaned with ethanol and compressed air between each sample. The jaw-crusher was pre-contaminated with a small fragment of each sample that was then discarded, ensuring that any material on the steel plates after cleaning would only be the sample being crushed. Whole-rock samples were reduced to pea-sized gravel and examined beneath a binocular microscope to remove lithic fragments and isolate pumice fragments if possible. Then the "cleaned" whole-rock and pumice samples were again crushed to reduced particle size (< 1 mm).

A Rocklabs ring mill with an agate head was then used to reduce each sample to a fine powder. Between each sample the ring mill was cleaned with water, compressed air and ethanol, and then pre-contaminated with about 5g of new sample which was discarded after pulverizing. A subset of samples were powdered using a chrome-steel mill head. Samples 15-CA-33 and 15-CA-36 were duplicated using both mills to ensure contamination was limited with the steel mill, and the comparison is presented in Appendix 1, Tables 5, 6 showing no noticeable elemental contamination.

Whole rock major and trace element concentrations were determined at the Ontario Geological Survey laboratory in Sudbury, Ontario. Major element concentrations were

obtained using fused-disc X-ray fluorescence spectrometry (XRF) and trace element concentrations were measured by closed beaker-digested, solution-mode inductively coupled plasma mass spectrometry (ICP-MS). Replicate analyses of samples and blind standards have determined precisions presented in Appendix 1, Table 7. XRF measures concentrations in weight percent (wt. %) for the following oxides, with detection limits shown in brackets in wt.%; Al_2O_3 , BaO, CaO, Cr_2O_3, Fe_2O_3, K_2O, MgO, MnO, Na_2O, P_2O_5, SiO_2, TiO_2 as well as the loss-on-ignition (LOI, or the weight loss during fusion corresponding to total volatile concentrations, including H_2O, CO_2, S, and trace gases). Trace element concentrations in weight parts-per-million (ppm) were determined by closed-beaker acid digestion ICP-MS for the following elements (detection limits are shown in brackets in ppm); Ba, Be, Bi, Cd, Ce, Co, Cr, Cs , Cu , Dy, Er, Eu, Ga, Gd, Hf, Ho, In , La, Li, Lu, Mo, Nb, Nd, Ni, Pb, Pr , Rb, Sb, Sc, Sm, Sn, Sr, Ta, Tb, Th, Ti, Tl , Tm, U, V, W, Y, Yb, Zn, Zr. Duplicate analyses for quality control are shown in Appendix 1, Table 7.

5.3 Radiogenic Isotope Methods

44 samples were chosen for Sr, Nd and Pb isotopic analyses by thermal ionization mass spectrometry (TIMS) at the Isotope Geochemistry and Geochronology Research Centre (IGGRC), Carleton University. Between 100 and 150 mg of powder were dissolved for each sample in 15 mL closed Savillex beakers using approximately 3 mL of a concentrated HF: HNO_3 mixture (at a ~1:2 ratio). Beakers were placed on a hot plate at 130 °C for 3 days before being opened and allowed to evaporate to near dryness. 1-2 drops of concentrated HNO_3 were added to the precipitate to redissolve the sample before being allowed to dry

down again. The dried residue was then taken up in 6N HCl and placed on a hot plate in closed Savillex beakers at 130 °C for another 2 days. Samples were left to evaporate to complete dryness and taken up in 1N HBr for Pb column chromatography. Elemental separation from the same dissolution was in the order Pb, Sr and Nd, following the procedures detailed in subsequent sections before the separates were loaded and analyzed in a ThermoFinnigan Triton TI.

Because closed-beaker dissolution can sometime lead to incomplete dissolution of some refractory phases (e.g., zircon, titanite), 4 duplicate samples (15-CA-21, 28, 36 and 54) were dissolved in Parr bombs at University of Ottawa to ensure that potential incomplete dissolution of these refractory phases did not affect the measured isotopic compositions of the entire suite. Chemical separation was performed at the IGGRC to ensure matching conditions and influencing blanks. Results obtained for the duplicates from the two dissolution techniques are presented in Appendix 1, Tables 11, 12. Parr bomb Sr, Nd and Pb isotopic compositions are identical to the Teflon beaker isotopic ratios within analytical error and as such data from closed beaker digestion is presented in all plots.

Pb Isotope Analysis

Pb separation requires a 2 pass procedure in which samples dissolved in 3ml of 1.0N HBr were centrifuged and then loaded by pipette into Bio-Rad 10-mL polyethylene Econo columns containing 0.6 mL of cleaned and conditioned AG1-8X anion resin. The 3 ml of HBr and an additional 2.0 ml wash of 1.0N HBr passed through the column and were collected in clean beakers and set aside for Sr and Nd chemistry. 2.0 mL of 1.0N HBr followed by

0.5mL of 2.0N HCl was allowed to pass through the resin and discarded. Pb was then collected with 5.0mL of 6.0N HCl. This fraction was allowed to dry completely before being taken up in 0.5mL of 1.0N HBr to perform a second column pass. Once dissolved, separates were pipetted into columns loaded with 0.2mL of conditioned AG1-8X. Columns were consecutively washed with 2.0 mL of 1.0N HBr and 0.5 mL of 2.0 mL HCl before the cleaned Pb separate was eluted with 3.0 mL of 6N HCl. Once dried, 0.5 mL of 7N HNO_3 was added to the residue to drive off any bromides present. The laboratory protocol has shown to yield Pb concentrations > 95% of original concentrations, with procedural blanks of <150 pg.

Pb separates were diluted in weak HNO_3 and ~0.2 ug was loaded on single rhenium filaments along with 3 μL of Silica gel and 2 μL of H_3PO_4. 5 blocks of 6 ratios for a total of 30 ratios were taken with an integration time of 8.389 seconds. All sample runs were corrected for mass fractionation by monitoring a NIST SRM981 standard which has long-term laboratory average ratios of $^{206}Pb/^{204}Pb$ = 16.895 ± 0.016, $^{207}Pb/^{204}Pb$ = 15.434 ± 0.021, $^{208}Pb/^{204}Pb$ = 36.520 ± 0.071 (n=106, April 2010-October 2016). Appendix 1, Table 13 details the isotopic ratios yielded per sample set as well as the fractionation correction applied to each magazine of samples.

Sr Isotope Analysis

The HBr containing LILE/REE's from Pb columns was dried down, dissolved carefully in 7N HNO_3 and then dried down, and finally taken up in 2.5N HCl before being pipetted into borosilicate glass columns containing ~3mL AG50-X8 cation resin. Sr was collected in 6mL of 2.5N HCl after washing the column with 18mL of the same acid. Rare earth elements were

retained in the resin and then eluted using 6N HCl. A subset of samples required secondary cleaning to remove calcium from the collected cut; this was achieved by dissolving the residue from primary Sr columns in 7N HNO_3 and adding this to conditioned Eichrom Sr-spec resin in polypropylene columns before eluting Sr with water. Sr samples were diluted using weak HNO_3 and ~2.5μg was loaded onto single tantalum filaments along with 3 μL H_3PO_4. 10 blocks of 10 ratios for a total of 100 ratios were taken with an integration time of 8.389 seconds. Isotopic ratios were normalized to $^{86}Sr/^{88}Sr = 0.1194$. Standard runs were conducted on NIST SRM987 ($^{87}Sr/^{86}Sr = 0.710253 \pm 0.000002$, n=91, Jan. 2014-Dec. 2016), and procedural blanks are <750pg. During the period of study NIST SRM987 yielded average values of $^{86}Sr/^{88}Sr = 0.710254 \pm 0.000019$ (n=47, Nov.2015-Dec. 2016). All runs of SRM987 are in agreement with certified standard values (NIST SRM987 $^{87}Sr/^{86}Sr = 0.71034 \pm 0.00026$ (Moore et al., 1982)) and is indistinguishable from "accepted" values from other laboratories (e.g., 0.710248, Weis et al., 2006).

Nd Isotope Analysis

The REE-bearing fraction from Sr columns was dried and taken up in 0.26N HCl and pipetted into Eichrom Ln spec columns containing Teflon powder coated with HDEHP (di(2-ethylhexl) orthophosphoric acid. The columns were washed with 6.5 mL of 0.26 N HCl before Nd was eluted using an additional 5mL of 0.26N HCl. Once dried, ~0.5ug of Nd was loaded on 1 side of a double rhenium filament assembly along with 1 μL H_3PO_4. Isotopic ratios are normalized to $^{146}Nd/^{144}Nd = 0.7219$ to account for instrumental mass fractionation. Initial epsilon^{143}Nd values were calculated at the U-Pb and Ar-Ar ages from

John et al., 2014, with $^{143}Nd/^{144}Nd_{CHUR}$= 0.512638 and $^{147}Sm/^{144}Nd$ = 0.1967 and the decay constant $\lambda=6.54*10^{-12}$. Two Nd standards were analysed: La Jolla (long-term value of $^{143}Nd/^{144}Nd$ = 0.511860 ± 0.000009 (2 sigma, n=6, Aug. 2012-Nov. 2015) and an internal laboratory standard Nd Std (long-term value of $^{143}Nd/^{144}Nd$ = 0.511831 ± 0.000012 (2-sigma, n=104, Jan.2014-Dec. 2015). Analyses of the Nd Std standard during the period of this current study yielded an average ratio of $^{143}Nd/^{144}Nd$ = 0.511831 ± 0.000010 (n=28, Nov.2015-Dec. 2015), and La Jolla yielding ratios of $^{143}Nd/^{144}Nd$ = 0.511860 ± 0.000011 (errors in 2-sigma). Isotope ratios for La Jolla are consistently within error of the accepted ratio of $^{143}Nd/^{144}Nd$=0.511856 ± 0.000009 (Thirwall 1991), and subsequently the reported isotopic ratios were not normalized to the values obtained for the standards. Procedural Nd blanks were <100 pg. Uncertainties listed for each sample are 2 standard deviations of the mean.

BCR-2, as a laboratory solution, was run along with these samples to ensure instrument stability and as a monitor for data quality, during this study period the standard yielded average isotopic ratios of: $^{87}Sr/^{86}Sr$ = 0.705024 ± 0.000017, $^{143}Nd/^{144}Nd$ = 0.512644 ± 0.000012, $^{206}Pb/^{204}Pb$ = 18.777 ± 0.063, $^{207}Pb/^{204}Pb$ = 15.632 ± 0.020 and $^{208}Pb/^{204}Pb$ = 38.803 ± 0.147. All of which are within error of the accepted values (e.g. Weis et al., 2006).

5.4 Electron Microprobe Methods

Phenocrysts from 2 thin-sections were examined using a JEOL 6610LV SEM and JEOL 8230 SuperProbe at the University of Ottawa MicroAnalytical Laboratory. Samples 15-CA-21 and 15-CA-28 were chosen as representative pumice samples with a number of amphiboles present as mineral phases. Beam current was set at 20 nA with an accelerating voltage of 15 kV and beam diameters of 10 microns for hornblende analysis. Integration times were 20 seconds for major elements, 30 seconds for minor elements and 10 seconds for background measurements. Standards used for elemental determinations included: sanidine for K_2O, Al_2O_3 and SiO_2, diopside for CaO and MgO, sphalerite for ZnO, hematite for FeO, tephroite for MnO, vanadinite for V_2O_3, tugtupite for Cl, rutile for TiO_2, chromite for Cr_2O3, fluorite for F and albite for Na_2O_3. Measurements were performed on multiple phenocrysts present in each section, both core and rim measurements were taken from amphibole grains.

6. Results

6.1 Petrography

The TEC is a variably crystal rich tuff, including plagioclase + sanidine + quartz + biotite ± hornblende + Fe-Ti oxides + accessory clinopyroxene, orthopyroxene, zircon, apatite, allanite and monazite. Full thin section descriptions can be found in Appendix 1, Table 2. The total crystal content increases upwards throughout the TEC ranging from roughly 20% near the presumed caldera-floor and increasing to close to 50% in the higher sections of the tuff. Plagioclase contents seem to decrease in abundance in proportion to decreasing total phenocryst abundances, accompanied with a minor increase in the proportion of quartz and sanidine in the phenocryst-poor samples. Mafic minerals are common throughout stratigraphy; biotite and/or hornblende are present in equilibrium in almost every sample and both clinopyroxene and orthopyroxene crystals are present in small numbers which commonly include signs of partial resorption, overgrowths or complete recrystallization as a hydrous phase.

Plagioclase exists as independent, oscillatory-zoned, euhedral-subhedral grains, stubby subhedral grains with complex zoning, and partially resorbed heavily fractured anhedral fragments (Fig. 6.1 A). Grains range in size from 0.2-2.5 mm, and constitute between 25-80% of the phenocryst populations throughout the TEC. Microprobe analysis of plagioclase cores yielded An contents of 17.58-41.90% (Landon-Browne 2016), and the typical plagioclase demonstrated normal chemical zonation. Antiperthitic textures are found in few phenocrysts generally following cleavage planes, as well as recrystallized phases along

intracrystal fractures; no other distinctive overgrowth textures were observed. Commonly, plagioclase crystals show some degree of resorption and in some cases are significantly embayed and infilled with hypocrystaline matrix. Plagioclase crystals also occur as smaller subhedral to anhedral crystals in complex clusters with various intergrowths of quartz, sanidine, biotite, hornblende and oxide phases. These crystals appearing in these clusters are significantly smaller than independent feldspars, on the order of <0.2 mm, and are significantly more “pristine” with no evidence of fracturing or resorption textures.

The proportion of sanidine is almost identical to that of quartz, representing 5-40% of the total number of phenocrysts and often only 5-10% higher than the number of quartz crystals. Sanidine occurs as 2 distinctive size fractions; the first are large 0.5-1 mm euhedral to subhedral crystals which are often heavily fractured with a minor degree of dislocation and infilling (6.1 C), and the second are small, euhedral to subhedral, elongate crystals 0.1-0.2 mm in length that are typically found in clusters either of many small sanidine crystals or intergrown with plagioclase and quartz. Sanidine also exists as thin mantles surrounding calcic plagioclase crystals or as exsolution lamellae along cleavage directions, which are only identifiable under an electron microprobe.

Quartz crystals range in size from 0.05-1 mm and vary in percentage from 5-45% of the total phenocryst population, most often constituting 15-20% of the total number of crystals. Quartz phenocrysts appear as either rounded or subhedral to anhedral crystals as well as rounded and occasionally deformed globules. Quartz occasionally appears in small clustered intergrowths with both feldspars. Most crystals have a significant degree of fracturing and resorption textures are evident along crystal edges. Almost all quartz crystals

have undergone partial embayment, sieve and myrmekitic textures were observed in places.

Biotite grains range from 0.2-2.5 mm in length and appear as elongate lathes and tabular grains. Most grains show some degree of deformation or kinking as they re-aligned with the deformation direction evident in the glassy matrix (Fig. 6.1 B), including a small number of phenocrysts that have been bent around resistive crystals (typically plagioclase). A number of biotite crystals have been partially or completely resorbed into the matrix and, in few cases, the core has been completely removed. The more pristine crystals still demonstrate a degree of oxidation and commonly include an opaque alteration halo along the crystal rims. Overgrowths of Fe-Ti oxides are common, as well as inclusions of zircon, apatite and monazite. Biotite is also found often overgrowing and replacing amphibole crystals.

Amphibole (0.2-2.5 mm) occurs as both a primary phase with a moderate degree of resorption and dehydration textures as well as relict forms which have been completely pseudomomorphed by biotite. Resorption of grains is typically accompanied by biotite and Fe-Ti oxide overgrowths as well as significant infilling of fracture spaces with matrix glass. Primary hornblende is unzoned and has no evident chemical or oxidation rims and shows only a moderate degree of fracturing. Amphibole also appears as an overgrowth phase for relict clinopyroxene and in very few cases has completely replaced pyroxene crystals.

Pyroxene is present in few samples as both primary and xenocrystic crystals. Clinopyroxene is observed as isolated phenocrysts (0.2-1 mm) (Fig. 6.1 D) and is commonly overgrown by amphibole, biotite and Fe-Ti oxides. Euhedral crystals are moderately fractured and show

some degree of infilling, as well as the development of a secondary rim of amphiboles or a thin secondary pyroxene-rim which is unidentifiable under a microscope. Many of these resorbing crystals are missing their cores, having been completely replaced by matrix glass. Small angular fragments of clinopyroxene also appear in a small number of samples, they seem to retain sharp crystal boundaries suggesting they fractured from prismatic/euhedral crystals and are often overgrown by Fe-Ti oxides as well as amphibole and biotite.

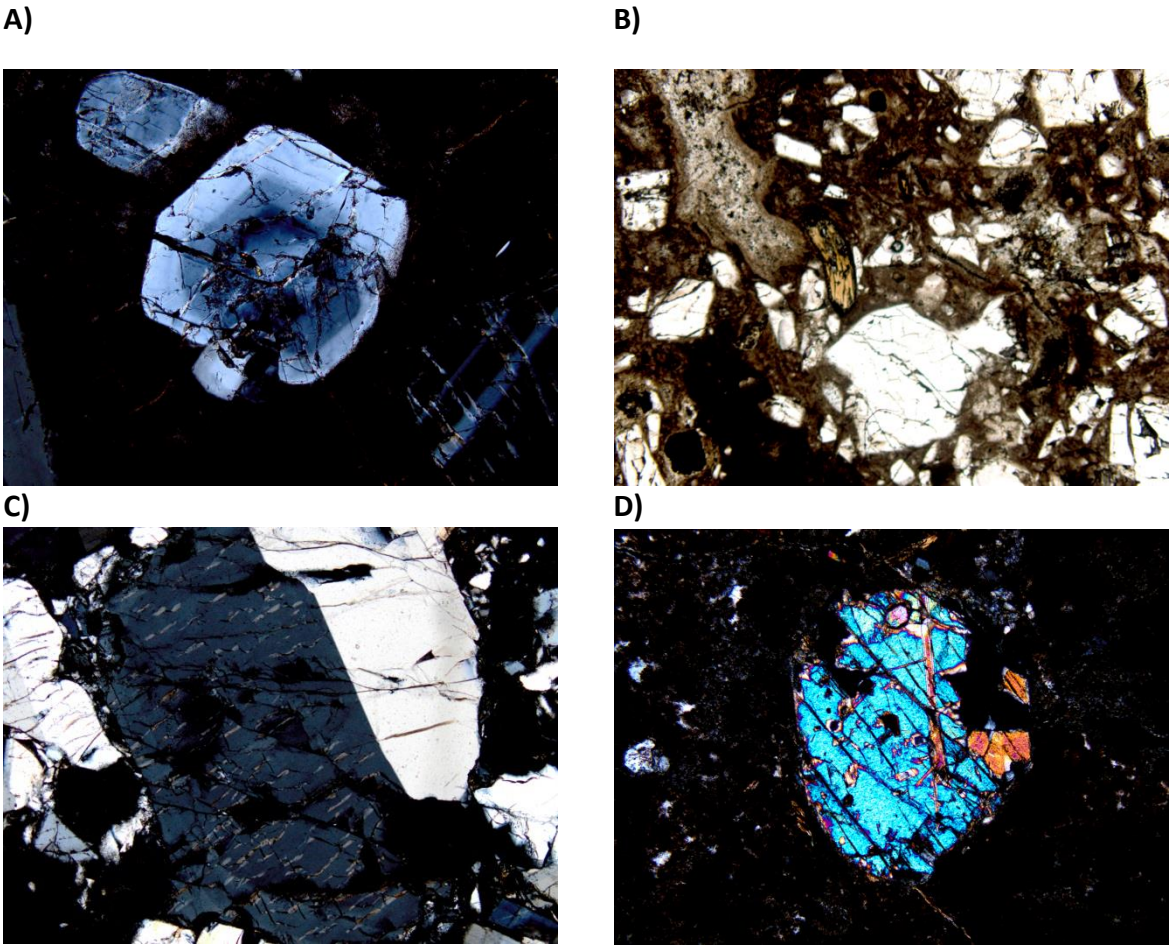

Figure 6.1 A) Oscillatory zoning of euhedral plagioclase crystal with moderate fracturing, a section of crystal has been partially dislocated on the lowermost face. B) Plain-polarized light image showing deformation common to biotite crystals, grains have bent with flow in glassy matrix. C) Perthitic sanidine crystal. D) Relict/xenocrystic clinopyroxene found as accessory phase in 15-CA-17.

6.2 Microprobe Results

Six amphibole phenocrysts were analysed from sections 15-CA-21 and 15-CA-28 using an electron microprobe. Complete analyses are shown in Appendix 1, Table 14. An additional 107 microprobe analyses of plagioclase and sanidine phenocrysts from TEC rocks were performed by Landon-Browne (2016) on samples collected as part of this study. Fig. 6.2 shows a few examples of spot analysis locations.

A) 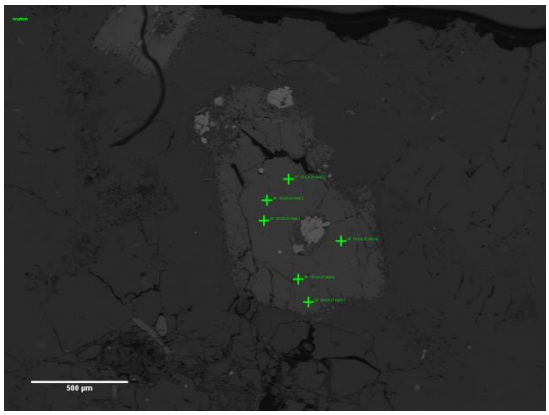 B) 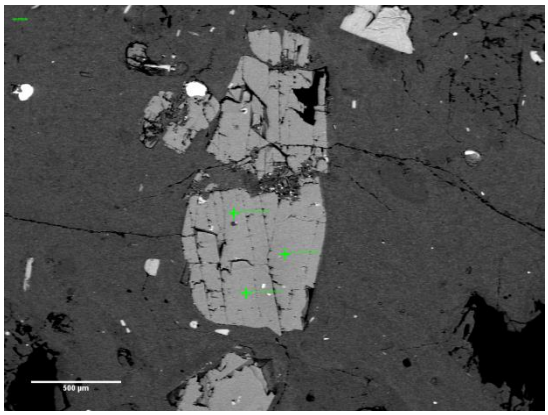

Figure 6.2 Microprobe spot analyses **A)** Hbl2 from sample 15-CA-21. **B)** Hbl3 from sample 15-CA-28.

Feldspars- The majority of plagioclase grains are sodic in composition, with average albite (Ab) contents ranging from Ab_{58} to Ab_{71} (Fig. 6.3). Most grains show normal zonation with more anorthite (An)-rich cores that transition to more orthoclase (Or)-rich rims; average cores have An_{31} and Or_4 which change to an average An_{26} and Or_9 at the rim. Three of the analysed phenocrysts show evidence of sanidine mantles having crystalized around plagioclase grains, with Or_{61} rims surrounding a sodic plagioclase crystal. On average, individual sanidine phenocryst are Or_{60} with An contents between 1 and 2%.

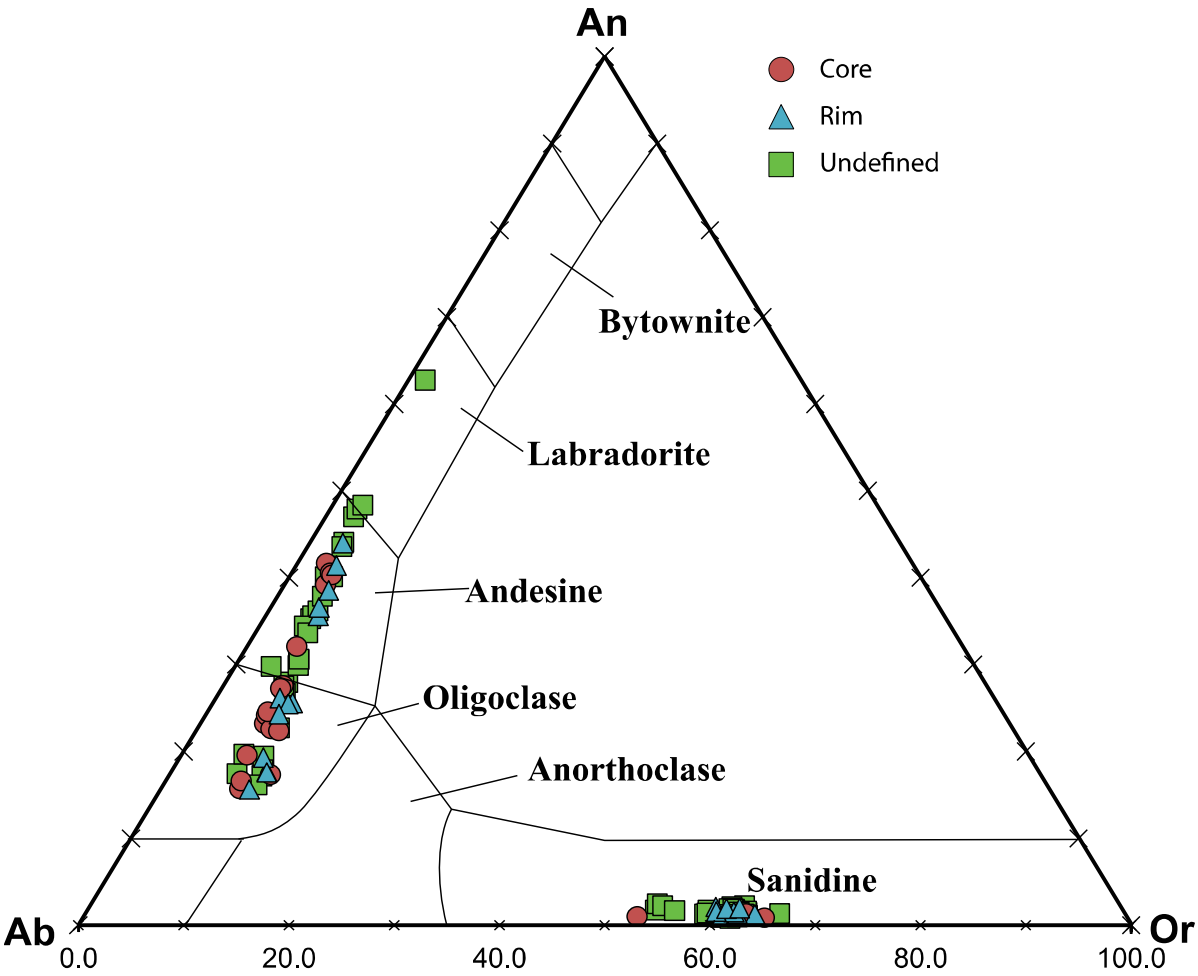

Figure 6.3 Feldspar compositions from microprobe analysis of TEC samples. Data was acquired by Landon-Browne (2016) on a subset of samples from this study.

Amphibole- Phenocrysts in both sections vary in composition; the two most-pristine amphiboles analysed in section 15-CA-21 are classified as hastingsite and the third is classified as ferro-ferri-hornblende. All 3 phenocrysts in section 15-CA-28 are classified as ti-rich magnesio-hastingsite by the IMA amphibole classification scheme of Hawthorne et al. (2012). Using the aluminum in hornblende geobarometer (Ridolfi et al., 2010) the amphiboles in samples 15-CA-21 and 15-CA-28 crystalized at much different depths. The analysed phenocrysts show no evidence of reabsorption or reaction rims and most likely

represent a primary phase satisfying the mandatory criteria (Ridolfi et al., 2010) where $Al/Al_T \leq 0.21$ and $Mg/(Mg+Fe^{2+}) > 0.5$. Three phenocrysts in 15-CA-21 crystalized between 3.4 and 4.4 km depth and 781 to 816 °C, while the 3 phenocrysts analysed in sample 15-CA-28 show crystallization depths between 10.2 and 13.0 km and temperatures between 926 and 963 °C. A summary of these calculations is shown in Appendix 1, Table 15.

6.3 Major Element Geochemistry

Major element compositions are reported in Appendix 1, Table 3 and unless specified, are recalculated to 100% anhydrous compositions for plotting. LOI values are generally low, ranging from 0.80- 3.91 wt. %. The TEC rocks are intermediate to felsic in composition with SiO_2 concentrations ranging from 61.2 to 76.3 wt. % and total alkalis ($Na_2O + K_2O$) ranging from 7.1 to 10.1 wt.%. They fall in the fields of trachydacite to rhyolite on a total alkalis versus silica diagram (Le Maitre et al., 1989, Fig 6.4) exhibiting peraluminous compositions with aluminum saturation index (ASI) = 1.0-1.5 (Fig 6.5) as defined by Peacock (1931). Pumice samples are more variable in composition and commonly have lower concentrations of SiO_2 along with higher concentration of alkalis compared to whole rock compositions.

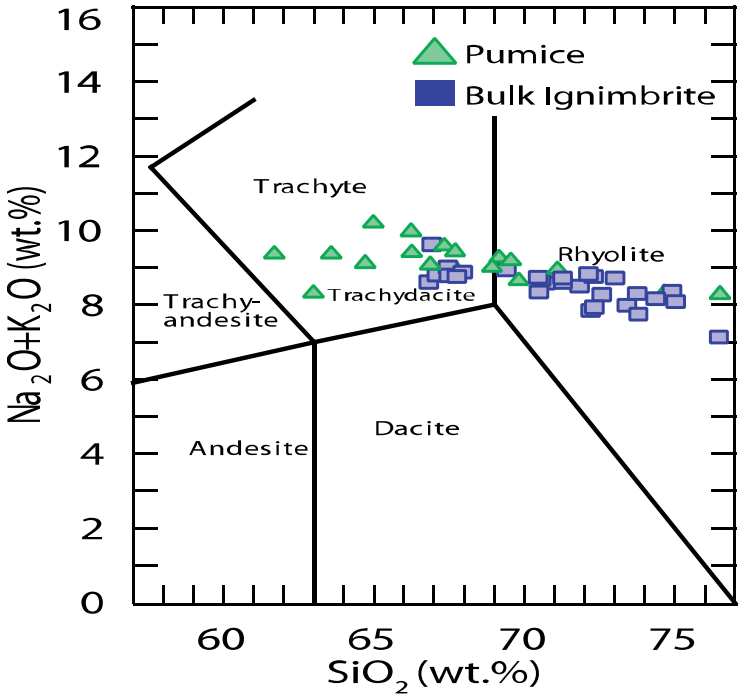

Figure 6.4 Whole rock and pumice samples of the TEC plotted on a total alkali vs. silica (TAS) plot. Figure modified from Le Maitre et al., (1989).

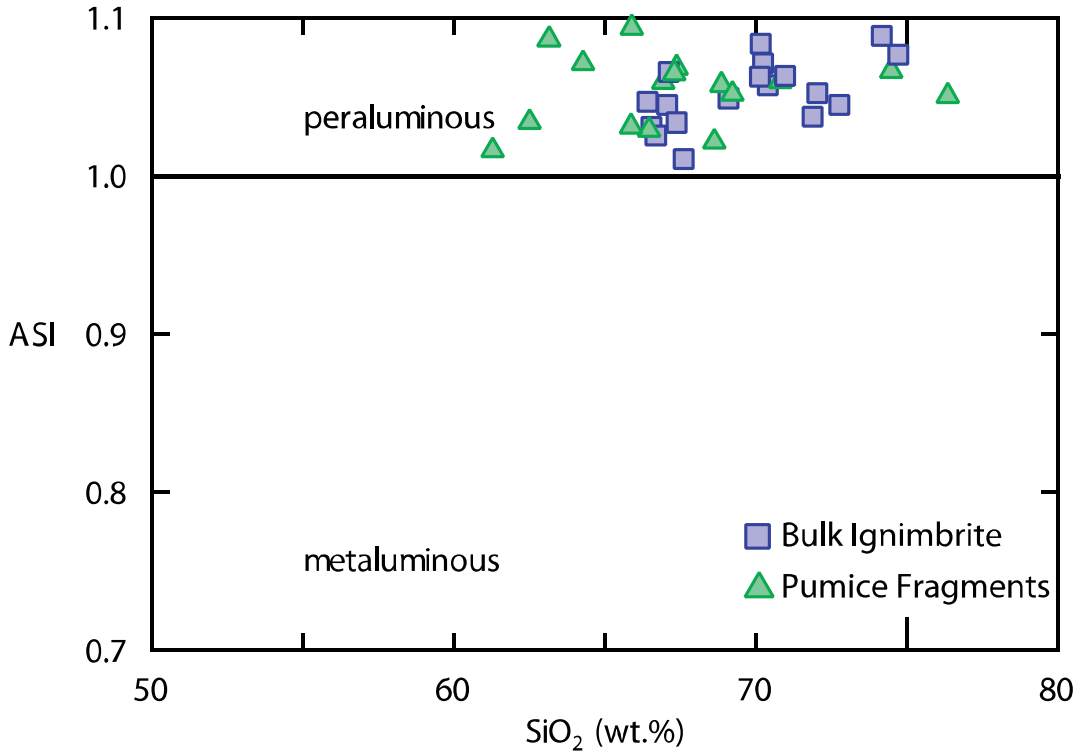

Figure 6.5 Alumina saturation indices of TEC rocks. Modified from Peacock (1931).

All major element oxides except K_2O show strong negative trends with increasing silica content without any observable compositional gaps (Fig. 6.6). Over the range of silica contents Al_2O_3 decreases from 18.19 to 13.35 wt. %, CaO decreases from 3.62 to 0.28 wt. %, Fe_2O_3 decreases from 5.04 to 1.13 wt. %, K_2O increases from 3.39 to 5.80 wt. %, MgO deceases from 1.10 to 0.17 wt. %, MnO decreases from 0.10 to 0.04 wt. %, Na_2O decreases from 5.81 to 1.30 wt. %, P_2O_5 decreases from 0.24 to 0.03 wt. % and TiO_2 decreases from 0.75 to 0.27 wt. %. The rough increase in concentration of K_2O occurs until $SiO_2 \cong 65$ wt.% where it becomes relatively constant at higher silica contents; values of K_2O plotted against LOI show a no variation in K_2O with increasing LOI. Excepting SiO_2 and K_2O, major element oxides are higher and show greater variability in pumice samples compared to bulk ignimbrite.

When plotted in the classification diagrams for granites described by Frost et al. (2001), the rocks of the TEC typically straddle more than one compositional field. In a modified alkali-lime index (MALI) diagram the TEC extends from alkalic to calc-alkalic in composition (Figure 6.7). Pumice samples are more alkalic with greater variability in MALI values when compared to bulk ignimbrite samples. This type of diagram assumes igneous differentiation will increase MALI values with a proportional increase in SiO_2 concentration in tight sub-parallel trends. Trends such as shown by TEC that cross the defined fields require either an atypical fractionating assemblage (predominantly K-feldspar) or the addition of calcium through other means with increasing magma evolution, but Frost et al. (2008) have suggested this best represents mixing of one or more magmas.

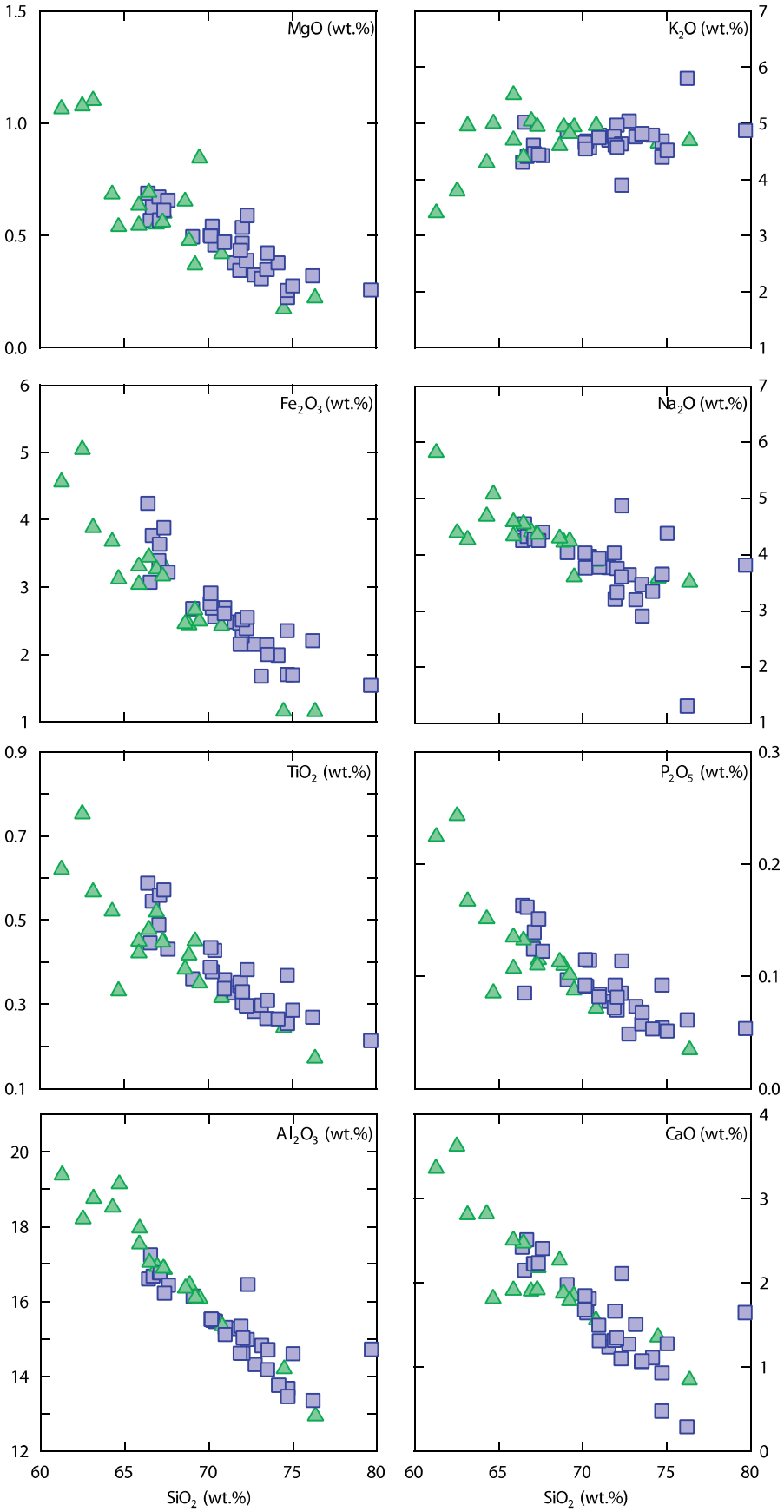

Figure 6.6 Major element variation diagrams of the volcanic rocks of the tuff of Elevenmile Canyon. All major element oxides decrease in concentration with increasing SiO_2 contents in tight trend except for K_2O which increases until $SiO_2 \cong 65$ wt.% then the trend flattens completley. Symbols are the same as Figure 6.4; green triangles are samples of pumice and blue squares are bulk ignimbrite samples.

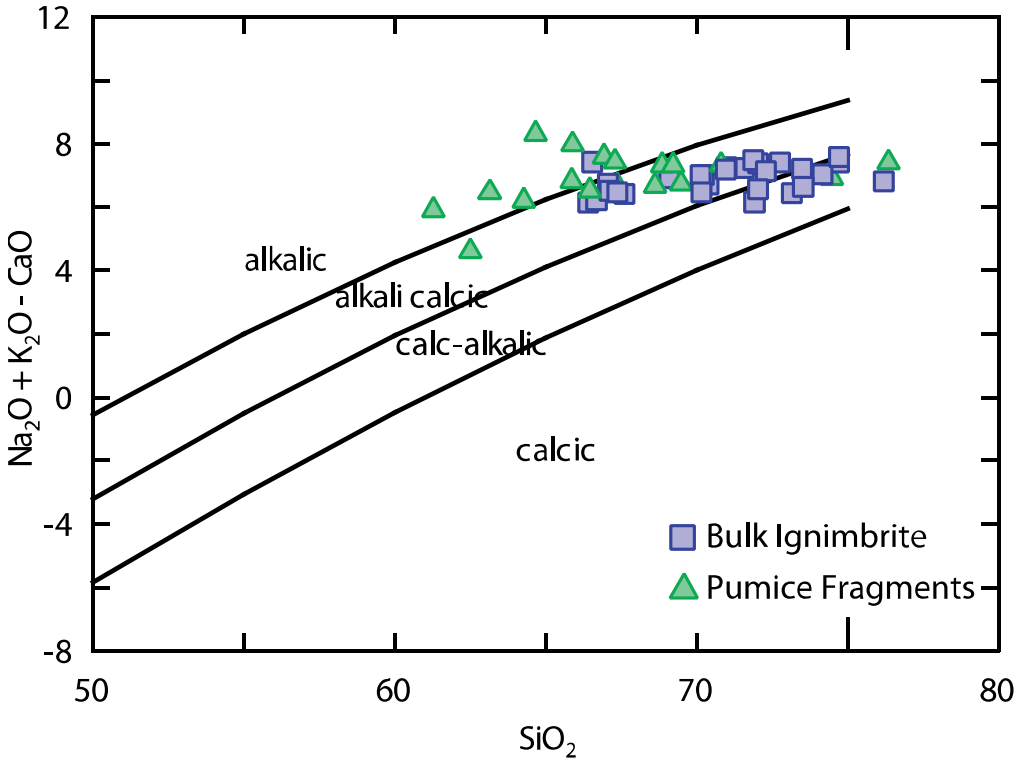

Figure 6.7 Modified alkali-lime index (MALI) plot. TEC rocks show no positive trend and transition from alkali to calc-alkalic in composition. Modified after Frost et al., 2001.

The TEC on a Frost et al. (2008) Fe* [$FeO^{tot}/(FeO^{tot} + MgO)$] classification plot within the ferroan field at low SiO_2 contents and has a flat trend which begins to transition to the magnesian field at higher SiO_2 contents (Fig. 6.8).

Throughout the TEC there are 2 obvious pumice types that can be distinguished: a lighter white-grey-pink, frothy, crystal-rich pumice ("light pumice") with larger phenocrysts, and a darker pink-red-brown, waxy, less crystal-rich pumice ("dark pumice"). The proportion of these 2 magma types appear to be uncorrelated to stratigraphic position, but clear chemical variations do exist (Fig. 6.9).

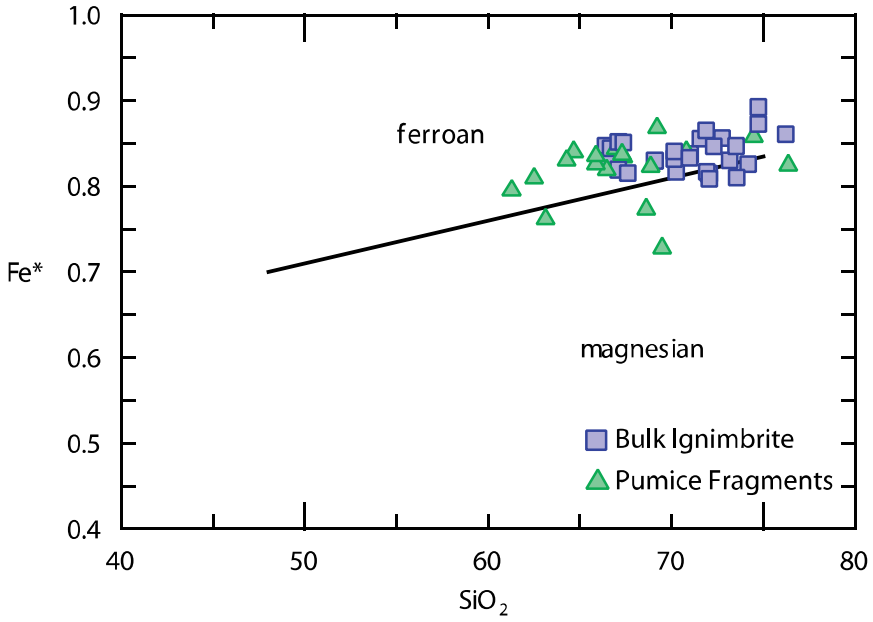

Figure 6.8 Fe* discrimination plot**.** Modified after Frost et al., 2001.

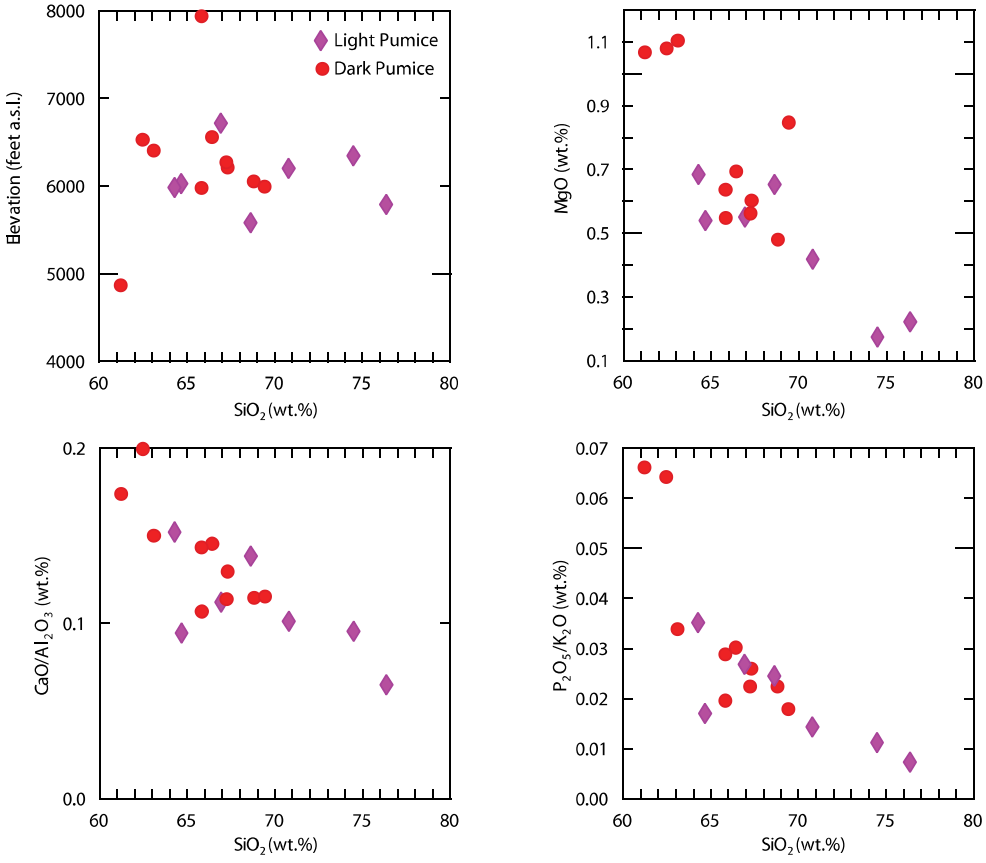

Figure 6.9 Major element distinctions of two pumice types present throughout the TEC. With some overlap, the two groups can be separated on the basis on SiO_2 contents or the proportion of mafic elements.

With a moderate degree of overlap both pumice groups fall on single collinear trends without any compositional gap; the light pumice are more siliceous (SiO_2 = 64.28-76.36 wt.%) with lower concentrations in all major element oxide concentrations (except for K_2O) compared to the dark pumice (SiO_2 = 61.27-69.47). CaO/Al_2O_3 and P_2O_5/K_2O both decrease in roughly proportional trends over the observed range of SiO_2, the dark pumice group has higher values for these ratios compared to light pumice.

6.4 Trace Element Geochemistry

Trace element results are reported in Appendix 1, Table 4. Scandium, V, Zr, Sr, Eu all show decreasing abundances with increasing SiO_2 and behave as compatible elements (Fig. 6.10). Strontium and Eu decrease in very tight trends while Sc, V and Zr also show strong negative trends with increased variability at low silica contents. In general pumice fragments show a larger variability compared to bulk ignimbrite samples and are typically more enriched in compatible trace elements. Incompatible trace elements show a distinct degree of scatter when compared to SiO_2 (Fig. 6.11). Rb and Th (not shown) are the only incompatible elements which show tightly correlated positive trends with increasing silica. Y, La (not shown) show trends similar to Sm and Yb with a scattered cluster of data with no apparent trends. Nb is moderately correlated with little enrichment with increasing silica contents.

On chondrite normalized plots (Fig. 6.12) all rocks of the TEC are enriched in light rare earth elements (LREEs) with nearly flat heavy rare earth element (HREEs) patterns, La/Sm_N and Gd/Yb_N ratios range from 4.05-5.99 and 1.48-2.79. Pumice samples show La/Sm_N ratios ranging from 4.19-5.74 and Tb/Yb_N between 1.30-2.05, and in general have a distinctive negative Eu anomaly. Bulk ignimbrite samples show La/Sm_N ratios ranging 4.06 – 5.09 from and Tb/Yb_N between 1.24-1.54. The majority of pumice samples range in Eu/Eu* values from 0.40 to 0.95 except for a single sample (15-CA-16) with Eu/Eu* > 1 (1.48) and, excepting the one positive anomaly, these values have a moderate negative correlation with increasing SiO_2 (Fig. 6.11). Pumice samples are only marginally more variable in composition compared to bulk ignimbrite, with only a slight depletion in heavy rare earth elements compared to whole rock samples. The La/Sm_N ratios show an apparent but poorly defined concave down trend with increasing silica content, with the highest La/Sm_N ratio at around $\cong$ 68 wt.% SiO_2. The Tb/Yb_N ratios show little correlation with SiO_2. The slope of heavy rare earth elements is much more variable in pumice samples compared to bulk ignimbrite and show a tight trend with a very slight negative trend after $SiO_2 \cong$ 68 wt.%.

Extended primitive mantle normalized trace element plots (Fig. 6.13) show pronounced negative Nb, Ta and Ti anomalies along with a significant enrichment in large ion lithophile elements (LILEs), Th and Pb which is typical of subduction related magmatism (Pearce 1982; Kelemen et al., 2004; Baier et al., 2008). Ba shows a slight negative anomaly and Zr shows variable relative concentrations with both positive and negative anomalies present.

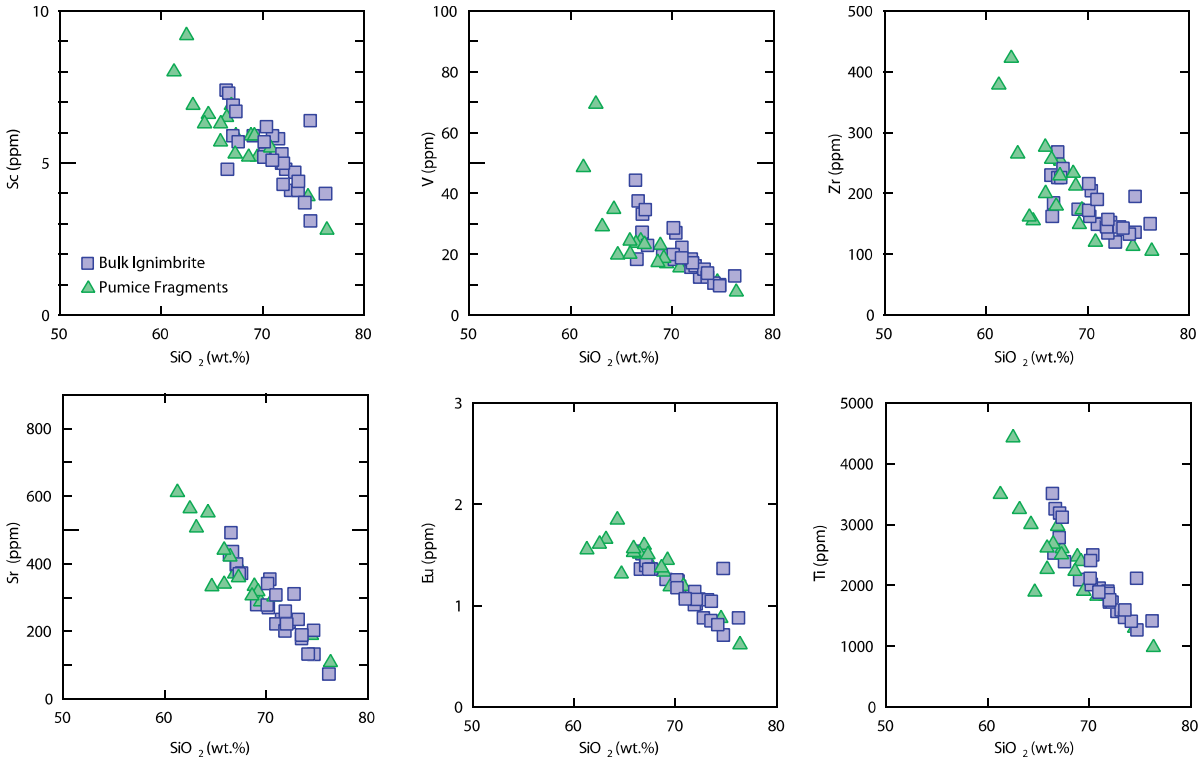

Figure 6.10 Compatible trace element patterns vs SiO_2 contents for pumice fragments and bulk ignimbrite samples of the TEC.

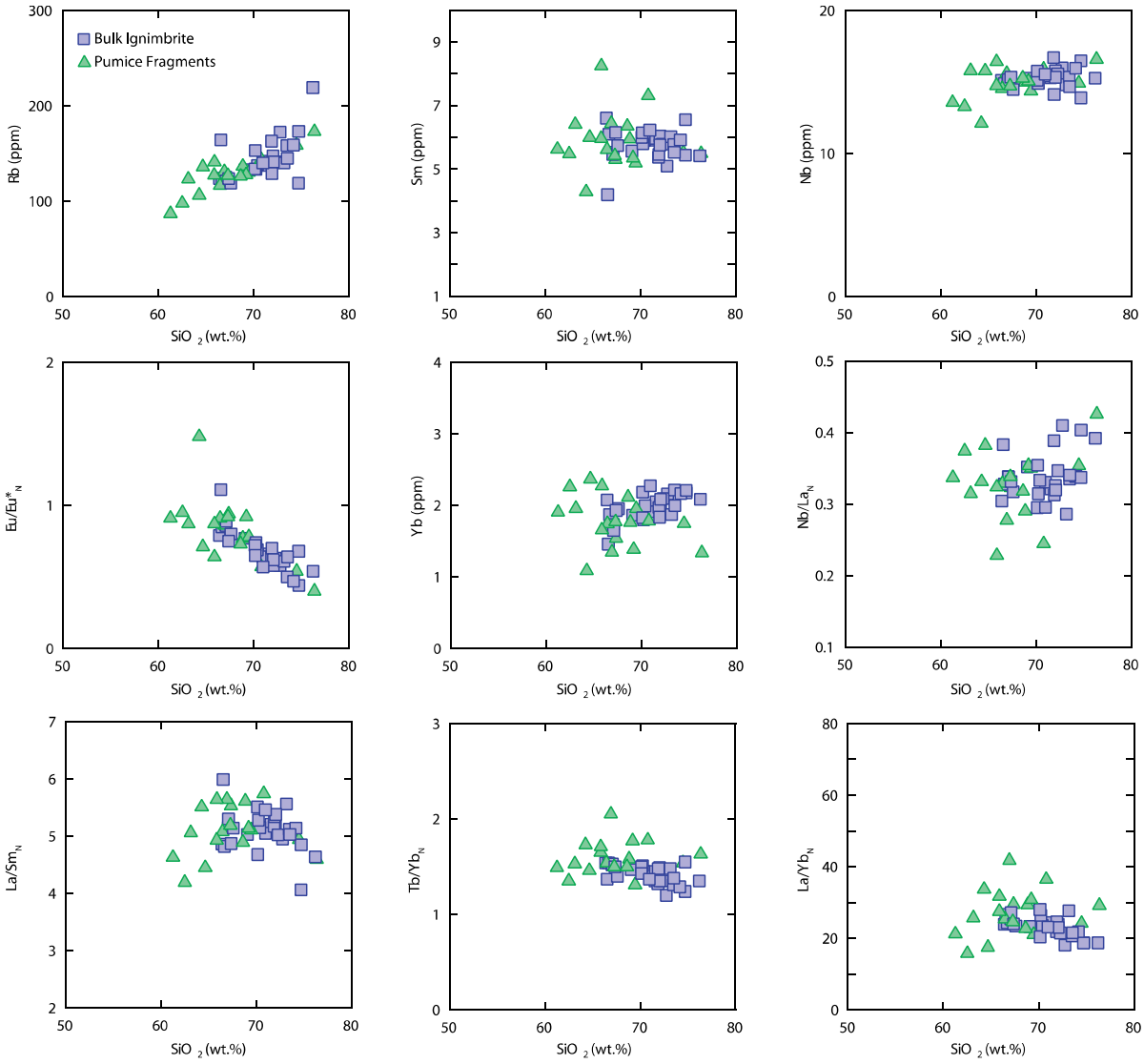

Figure 6.11 Incompatible trace element variations with SiO_2 contents for pumice fragments and bulk ignimbrite samples of the TEC. Normalization was done using chondritic values from Sun and McDonough (1989).

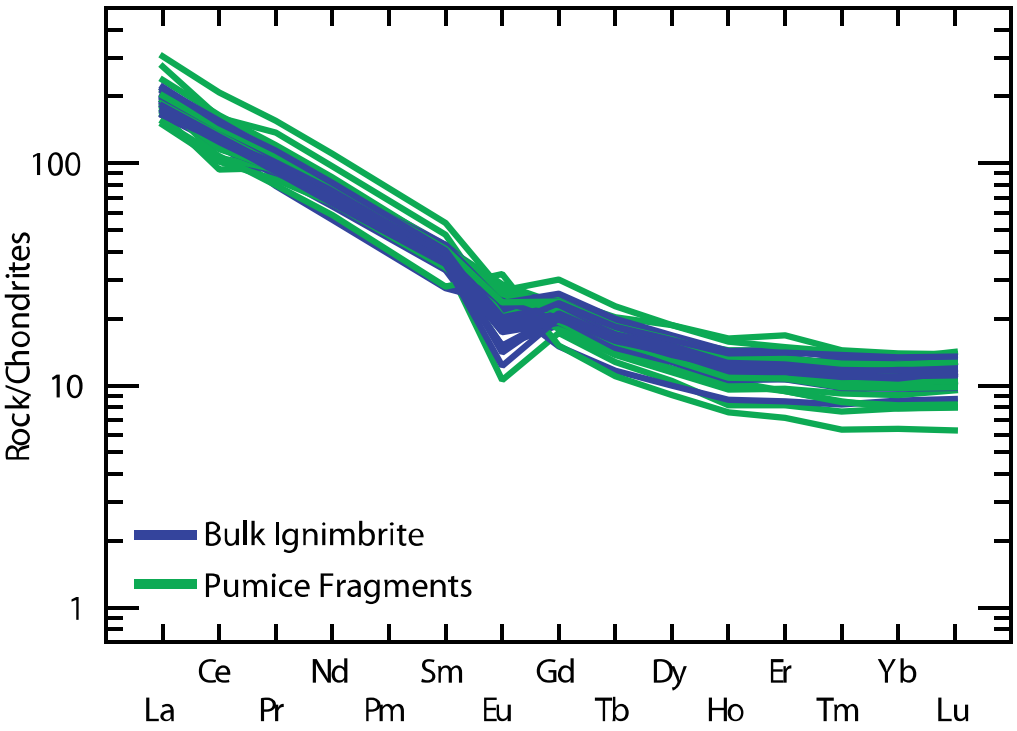

Figure 6.12 Chondrite normalized (Sun and McDonough, 1989) rare earth element patterns for TEC pumice fragments and bulk ignimbrite samples.

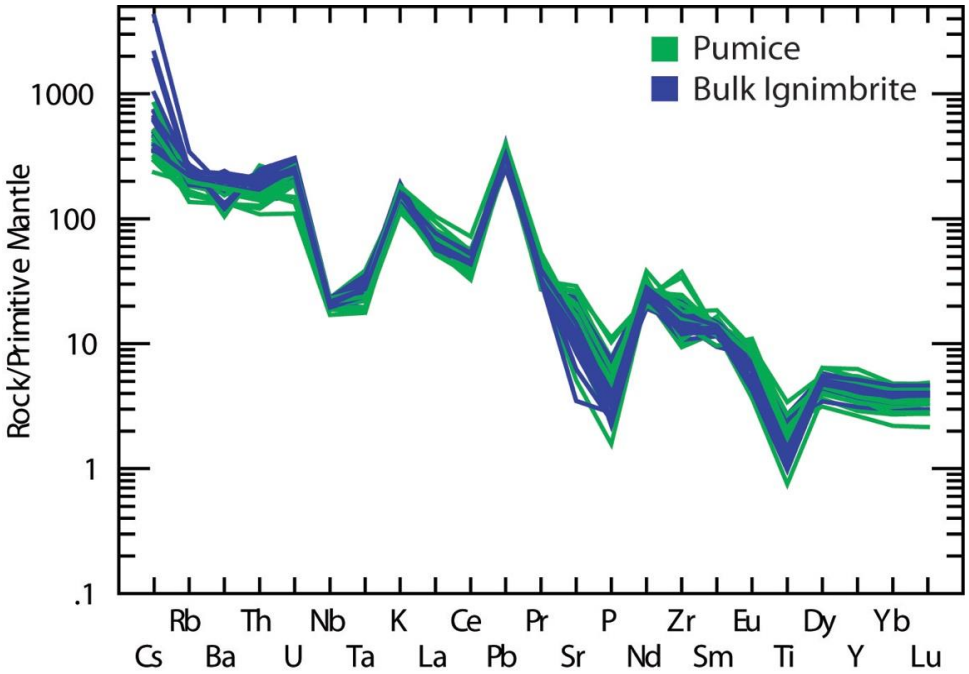

Figure 6.13 Primitive mantle normalized (Sun and McDonough, 1989) incompatible element patterns for pumice fragments and bulk ignimbrite samples of the TEC.

The two pumice types show a greater degree of variability and are distinct from each other in terms of most trace element concentrations (Fig. 6.14). In general, the dark pumice type is enriched in compatible elements and depleted in incompatible elements relative to the light pumice. On chondrite-normalized diagrams the two pumice types are almost indistinguishable, the light pumice being just slightly depleted in HREE and enriched in LREE relative to dark pumice (Fig. 6.15), with a more pronounced negative Eu anomaly (Eu/Eu* = 1.48-0.40) compared to the dark pumice (Eu/Eu* = 0.95-0.64). The degree of the observed Eu anomaly (Eu/Eu*) shows a strong negative correlation plotted against silica or very incompatible trace element concentrations (e.g. Nb) for both pumice types.

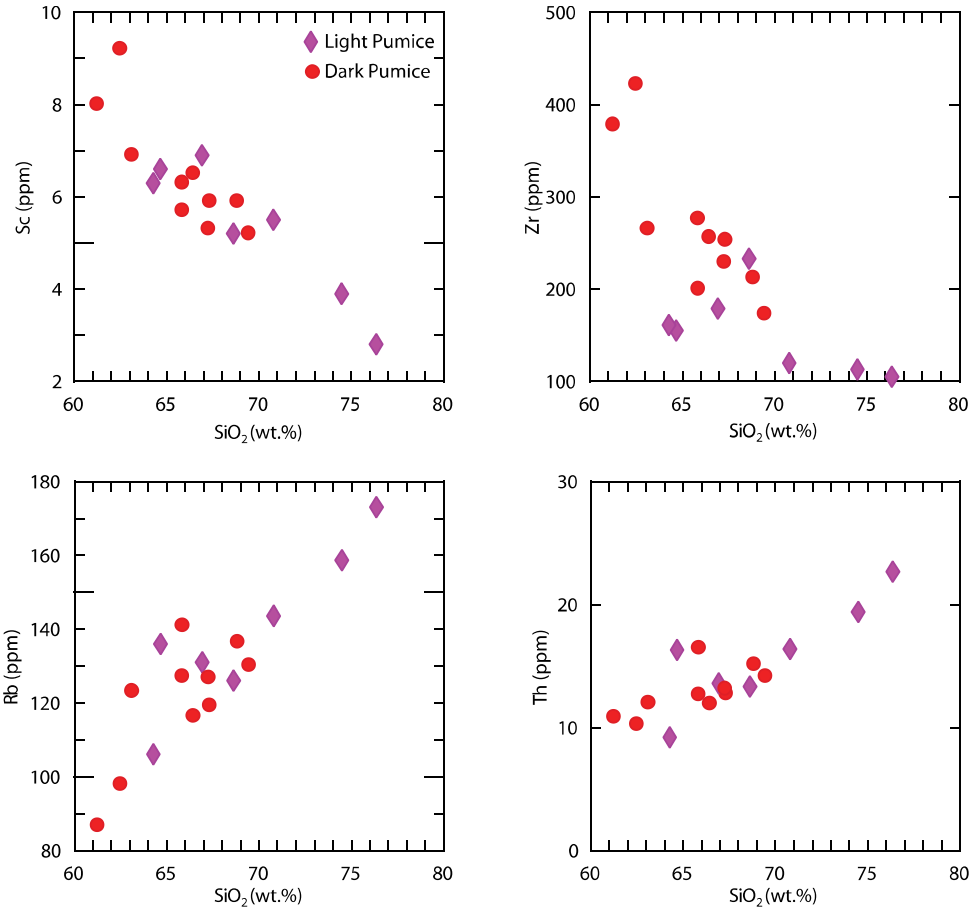

Figure 6.14 Trace element distinctions between two pumice types of the TEC. The dark pumice group are depleted in incompatible elements and enriched in compatible elements relative to the light pumice group.

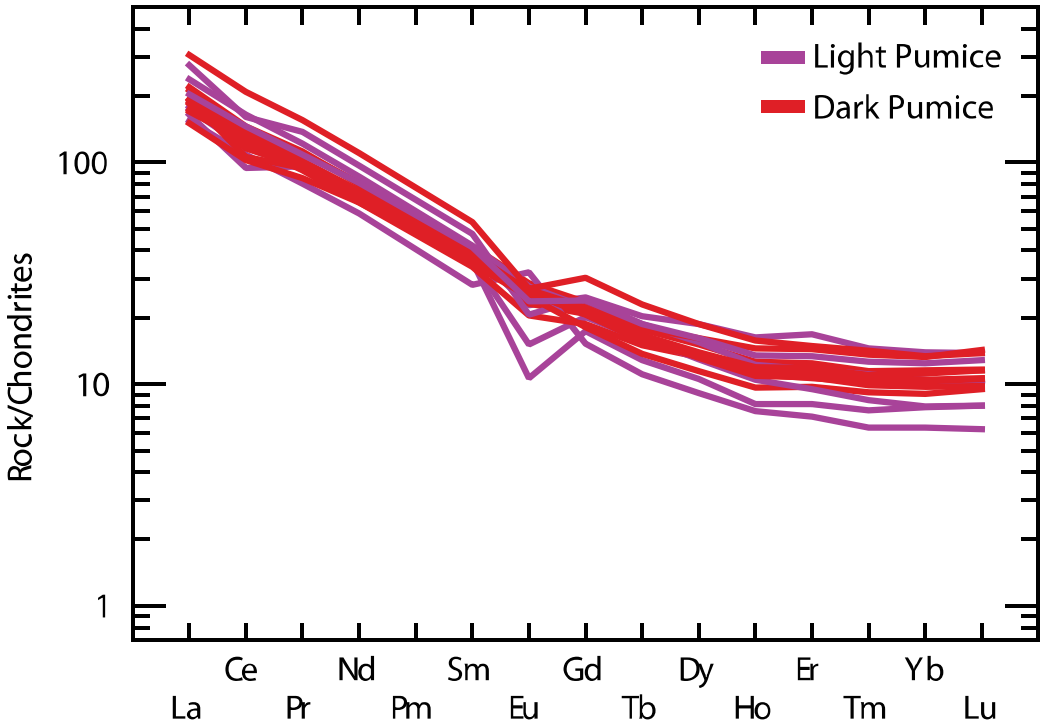

Figure 6.15 Chondrite normalized (Sun and McDonough, 1989) rare earth element patterns for the two pumice groups of the TEC. The easiest distinction can be made by the more pronounced and variable Eu anomaly in the light pumice group, but the two groups can also be separated by relative depletions of HREE and enrichment of LREE in the lighter group.

6.5 Isotope Geochemistry

Within the TEC the age-corrected (25.1 Ma) initial $^{87}Sr/^{86}Sr$ ratios and εNd are very tightly clustered: $^{87}Sr/^{86}Sr$ ratios range between 0.7048 and 0.7053 and εNd between -0.37 to -1.13 (Fig. 6.16; Appendix 1, Table 8). Generally, $^{143}Nd/^{144}Nd_{in}$ ratios show a slight decrease in value with increasing $^{87}Sr/^{86}Sr_{in}$, but this trend follows a very shallow slope. The defined field for TEC rocks fall just below and to the right of Bulk Earth in a $^{87}Sr/^{86}Sr$ vs εNd plot and outside the most radiogenic end of the mantle array, plotting just outside the field for enriched ocean island basalts (Fig. 6.17). Only a few samples, with the lowest Sr concentrations, appear to show some correlation between $^{87}Sr/^{86}Sr_{in}$ ratios and Sr contents. $^{143}Nd/^{144}Nd_{in}$ ratios do not correlate with Nd concentrations (Fig. 6.18). Rocks of the TEC show little co-variation of Sr or Nd isotopic ratios when compared against SiO_2 (Fig. 6.19) or trace element ratios such as La/Sm. When limiting sample selection to just the Clan Alpine Mountains, where consistent stratigraphy can be verified, the TEC demonstrates a very weak trend between $^{87}Sr/^{86}Sr_{in}$ and elevation (Fig. 6.19), where Sr isotopic compositions become slightly less radiogenic at higher elevations. The same suite shows a moderate trend of increasing $^{87}Sr/^{86}Sr_{in}$ with increasing SiO_2 and proxies for melt evolutions (i.e. increasing Th content or decreasing Zr). Initial $^{143}Nd/^{144}Nd$ shows no correlation with SiO_2, incompatible element concentrations or elevation in either the Clan Alpine subset or the entire suite of rocks. A Rb-Sr isochron diagram including all the TEC samples yielded an age of 25.4 $\pm$ 2.4 Ma with an MSWD of 27 and an initial $^{87}Sr/^{86}Sr$ of 0.70517 $\pm$ 0.000078 (Fig. 6.20). This calculated age is in agreement with those derived from more precise U-Pb and Ar-Ar techniques (Fig. 4.4, John 2014).

Pb isotope ratios show a larger degree of variation than the other systems; demonstrating steep, tight trends with age-corrected values of $^{206}Pb/^{204}Pb$ = 19.040-19.175, $^{207}Pb/^{204}Pb$ =15.601-15.692, $^{208}Pb/^{204}Pb$ = 38.729-38.932 (Fig. 6.21; Appendix 1, Table 9). Whole rock samples are slightly more radiogenic in terms of Pb isotopes compared to the pumice. Plotting the same subset of Clan Alpine samples as the previous isotopic systems, Pb isotopes ratios increase with increasing SiO_2 contents or show an inverse trend when plotted against a compatible element (e.g. Sr, Fig. 6.22). When plotted against Pb concentration, both $^{206}Pb/^{204}Pb_{in}$ and $^{207}Pb/^{204}Pb_{in}$ appear as clusters with approximately constant isotopic ratios. $^{208}Pb/^{204}Pb_{in}$ is the only ratio that shows a significant variation in isotopic composition but is not correlated with Pb concentrations.

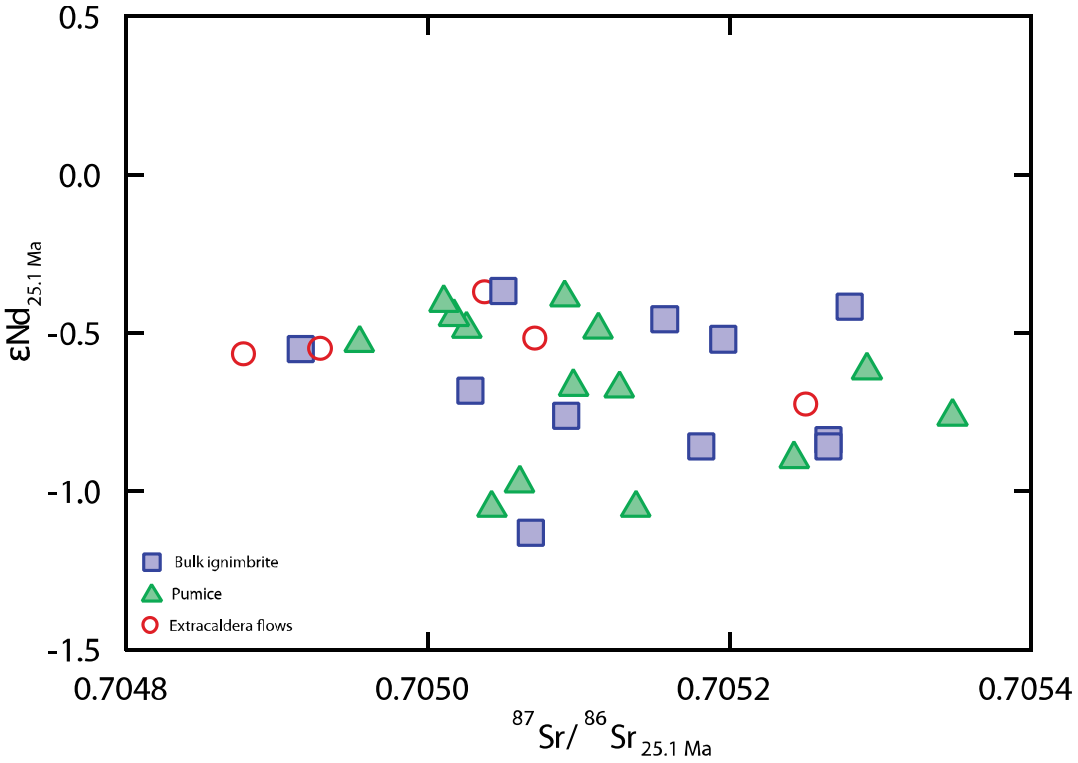

Figure 6.16 Initial $^{87}Sr/^{86}Sr$ plotted against εNd for the rocks of the TEC.

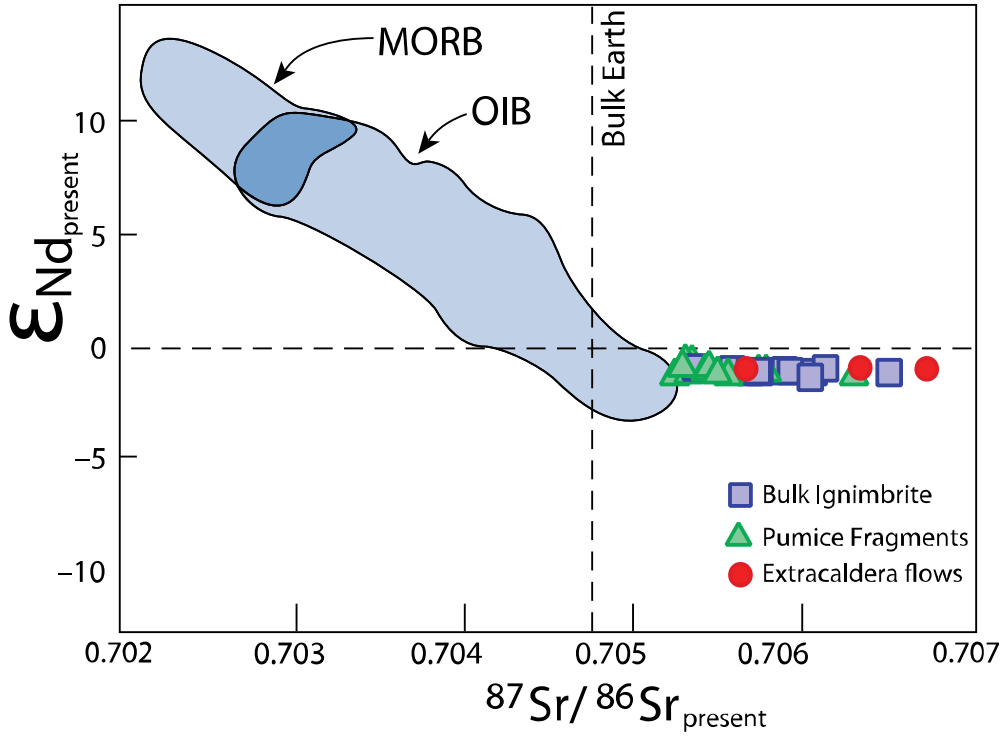

Figure 6.17 Present day $^{87}Sr/^{86}Sr$ plotted against εNd for the rocks of the TEC compared with the MORB-OIB mantle array and bulk earth composition. Modified after Allègre (2008).

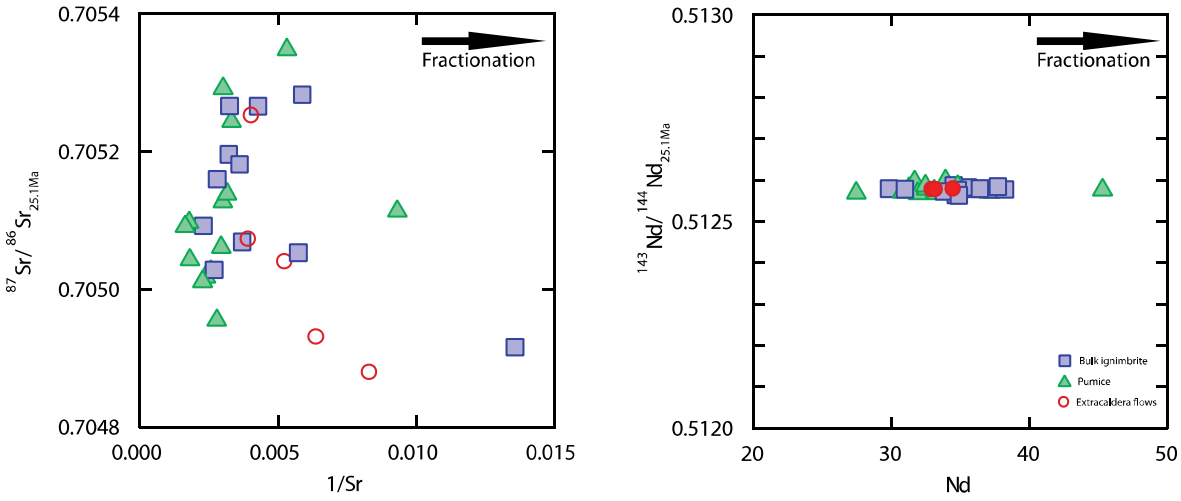

Figure 6.18 Initial isotopic ratios plotted against 1/concentration (concentrations determined by ICPMS). The sample plotting at 1/Sr ≅ 0.014 (15-CA-43) underwent post-cooling alteration and should be considered an outlier. There is no observable variation in $^{143}Nd/^{144}Nd$ when plotted against Nd concentration.

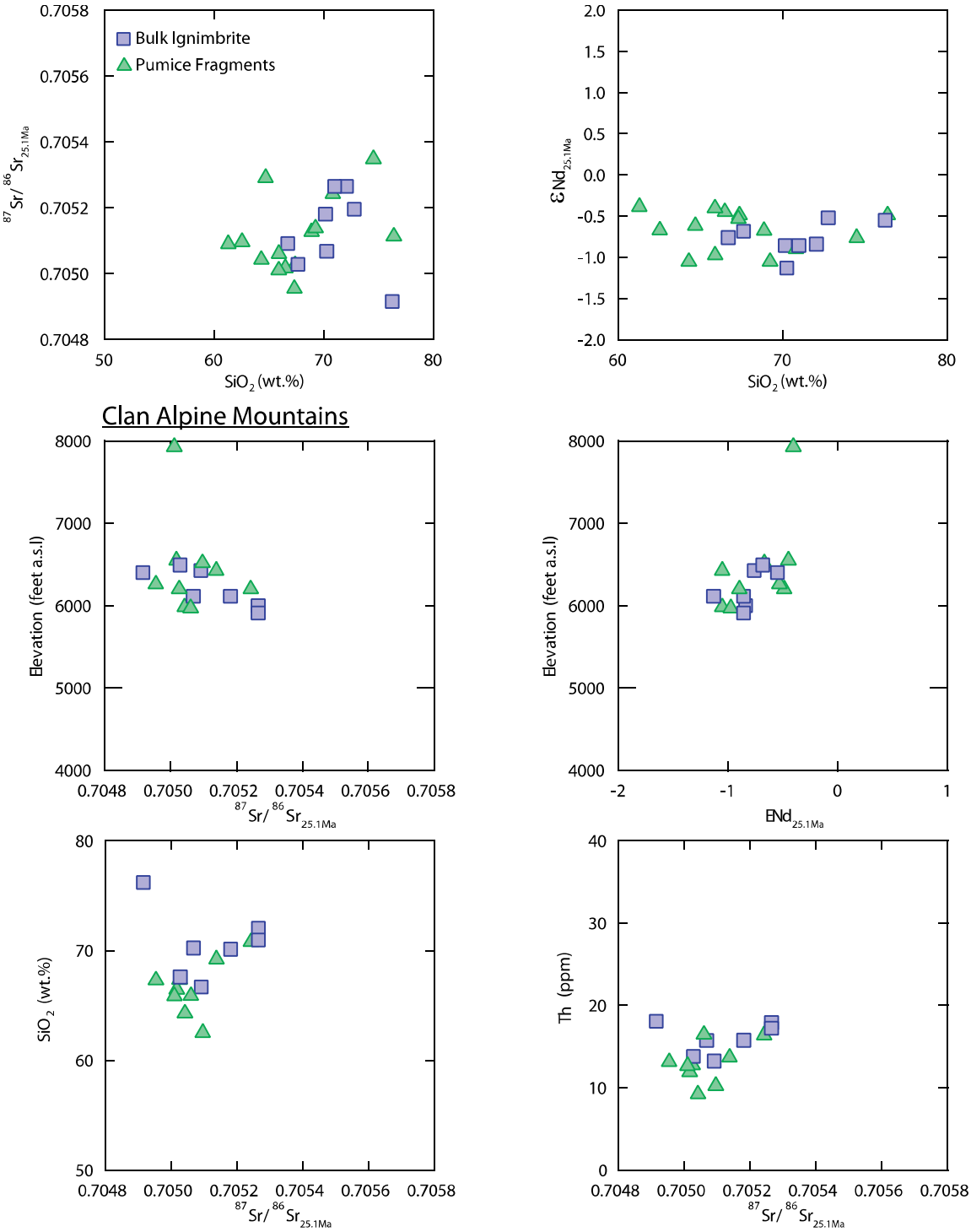

Figure 6.19 Isotopic variation of pumice fragments and bulk ignimbrite samples of the TEC. The top two figures encompass all samples of TEC rocks from 3 mountain ranges and show little variation of $^{87}Sr/^{86}Sr_{25.1\ Ma}$ and $\varepsilon Nd_{25.1Ma}$ with increasing SiO_2. The lower 4 plots only include samples collected in the Clan Alpine Mountains; $^{87}Sr/^{86}Sr_{25.1\ Ma}$ shows a moderate trend which becomes less radiogenic with increasing elevation and more radiogenic with increasing SiO_2 or incompatible element concentrations (e.g. Th). $\varepsilon Nd_{25.1Ma}$ shows no observable trend with elevation, SiO_2 or trace element concentrations.

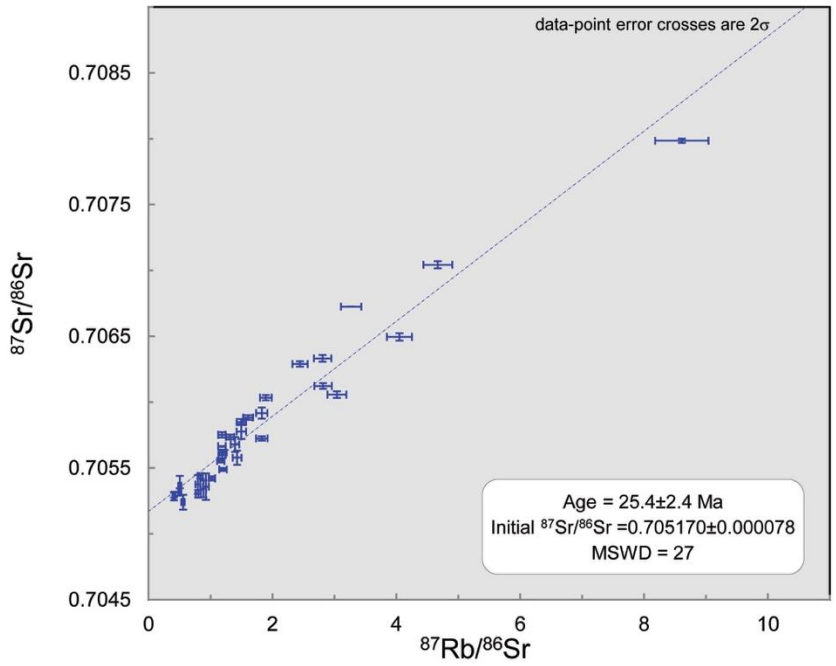

Figure 6.20 Sr-isochron diagram constructed from rocks of the TEC. Parent-daughter ratios were calculated using data from trace determinations using ICP-MS.

Analysis on the Mesozoic rock sequences that make up the regional upper crust yielded extremely variable isotopic ratios. Measured isotopic ratios were age corrected to 25.1 Ma, yielding $^{87}Sr/^{86}Sr$ = 0.7042-0.7082, εNd = -8.13 to +1.95, $^{206}Pb/^{204}Pb$ =18.867-21.214, $^{207}Pb/^{204}Pb$ =15.635-15.759, $^{208}Pb/^{204}Pb$ 38.590-38.996. Fig. 6.24 shows the scatter of Mesozoic sequences relative to the TEC in terms of $^{87}Sr/^{86}Sr$ and εNd. Included in the list of possible assimilated rocks are the black argillite chips found throughout the tuff (15-CA-40) which yield $^{87}Sr/^{86}Sr$ = 0.7082, εNd = -3.52, $^{206}Pb/^{204}Pb$ = 19.125, $^{207}Pb/^{204}Pb$ = 15.670, $^{208}Pb/^{204}Pb$ = 38.919 at 25.1 Ma.

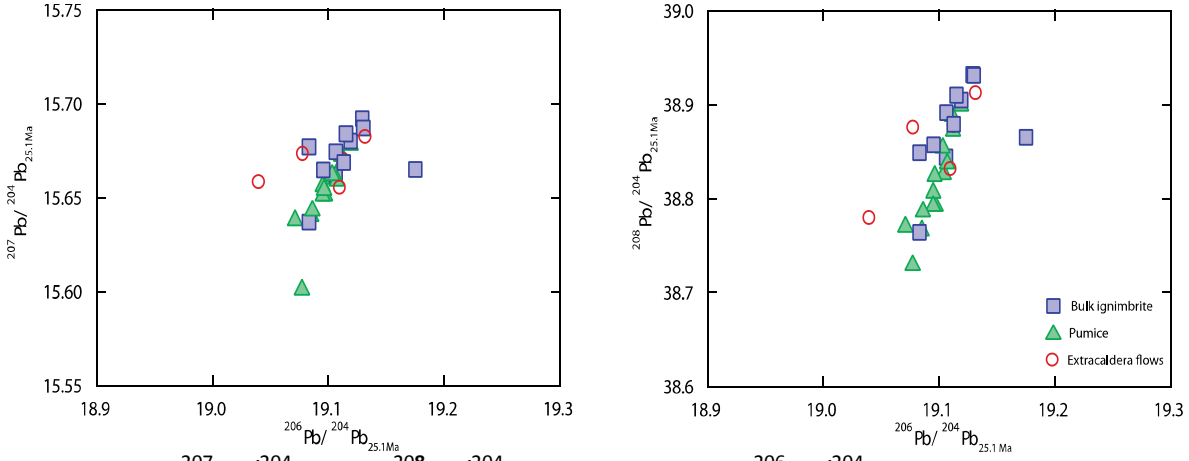

Figure 6.21 $^{207}Pb/^{204}Pb$ and $^{208}Pb/^{204}Pb$ plotted against $^{206}Pb/^{204}Pb$ isotopic ratios for the magmas of the TEC age corrected to 25.1 Ma.

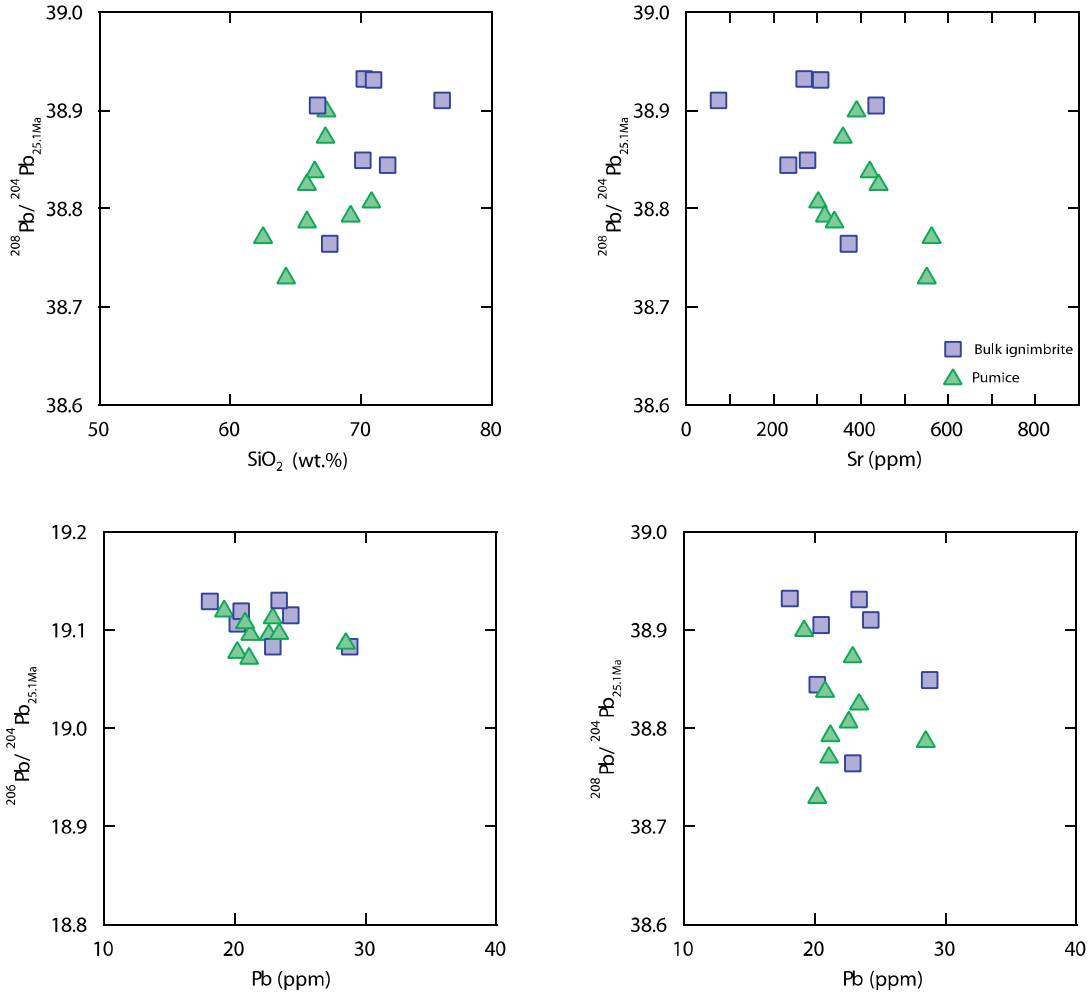

Figure 6.22 Pb isotope ratios of bulk ignimbrite and pumice samples from the TEC within the Clan Alpine Mountains plotted against SiO_2 (top left), Sr concentration (top right), and Pb concentrations (bottom two plots).

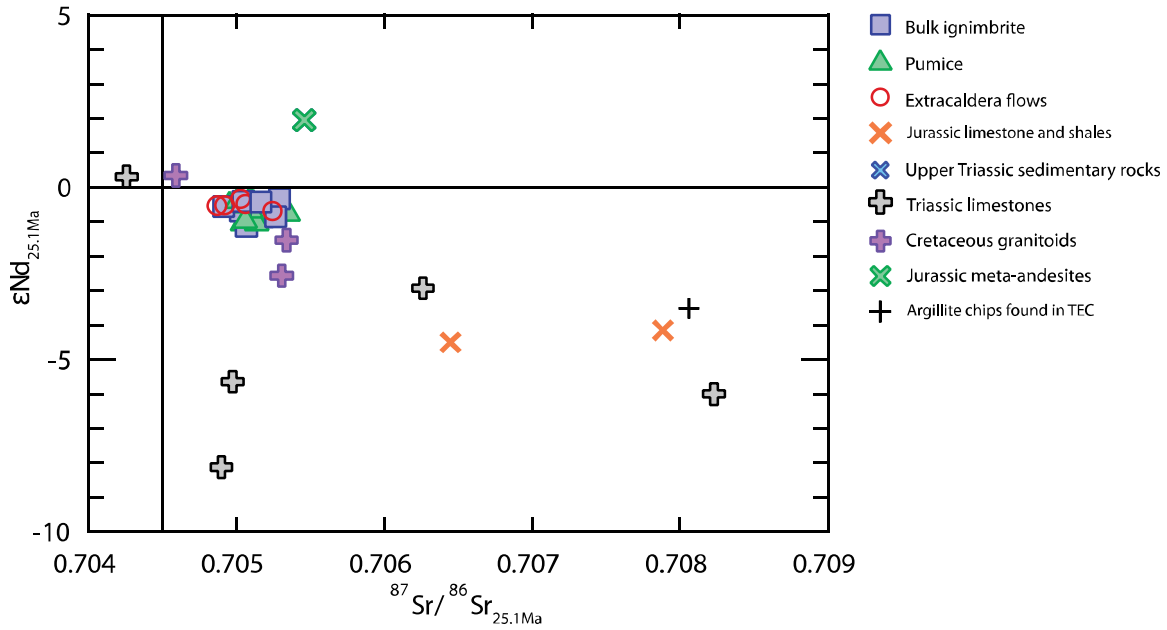

Figure 6.23 Comparison of Sr and Nd isotopic ratios of the TEC to a variety of regional Mesozoic rocks age corrected to 25.1 Ma.

Similar to major and trace elements characteristics, the two pumice groups of the TEC are differentiable in terms of isotopic composition (Fig. 6.25). With a small degree of overlap the light pumice are have higher $^{87}Sr/^{86}Sr$ and lower $^{143}Nd/^{144}Nd$ ratios compared to the dark pumice; the light pumice group has initial $^{87}Sr/^{86}Sr$ ratios from 0.70504-0.70535 and εNd = (-0.49) to (-1.05), the dark pumice show values of $^{87}Sr/^{86}Sr$ = 0.70495-70513 and εNd = (-0.39) to (-0.68). Sr isotopic ratios also show separation of the two groups when plotted against Eu/Eu* values or directly against trace elements which behave as incompatible elements in the TEC system (e.g. Rb, Th); samples with more pronounced Eu anomalies and marginally enriched in incompatible elements tend to have higher $^{87}Sr/^{86}Sr$. Although there is significant overlap in Pb isotope ratios between pumice types, the dark pumice group extends to higher ratios.

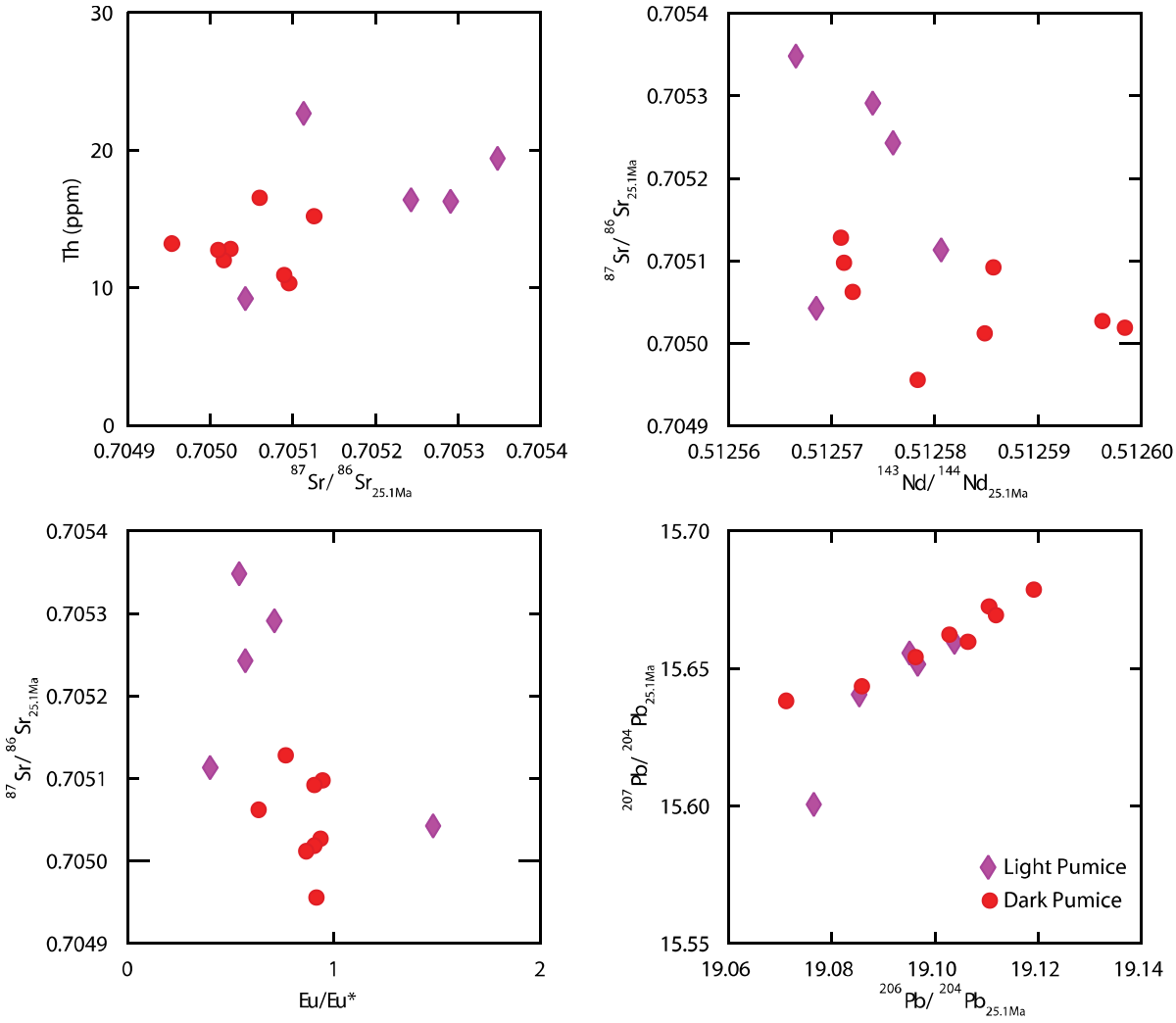

Figure 6.24 Isotopic distinction between pumice groups of the TEC. The light pumice group is slightly enriched in terms of Sr and Nd isotopes compared to the dark pumice group. In terms of Pb isotopes both groups show overlapping values.

6.6 Chemostratigraphic variation in the TEC

A transect of the TEC was conducted up stratigraphy in the Clan Alpine Mountains to investigate potential vertical compositional differences, beginning just above the interpreted caldera floor (exposed ~8 km to the west) and continuing through most of the intracaldera sequence (Fig. 6.25).

The TEC samples exhibit some systematic chemical variations with elevation and thus stratigraphic height (Fig. 6.26): SiO_2, K_2O and TiO_2 concentrations show decreasing values with increasing stratigraphic height, MgO and Al_2O_3 contents are relatively constant with a minor increase in concentration with stratigraphic height. BaO, CaO, Fe_2O_3, MnO, Na_2O, P_2O_5 concentrations show no correlation with stratigraphic position. Eu/Eu* remains relative consistent through the entire stratigraphic sequence, La/Sm ratios decrease in value in the lower half of the sequence before beginning to increase, Gd/Yb ratios are scattered with little correlation to stratigraphic position.

The stratification of the pre-eruptive magmatic system is further supported by trace element variation through the eruptive sequence. U and Yb show negative trends with increasing stratigraphic height; Th and U showing the strongest depletions in the uppermost parts of the transect. Eu, Sc, Sr, Ti, V and Zn are show the opposite behaviour, with positive trends associated to increasing stratigraphic height; this is especially evident for Eu, Sr, Ti and V. Isotopically, the stratigraphic extent of the TEC shows little apparent systematic variation.

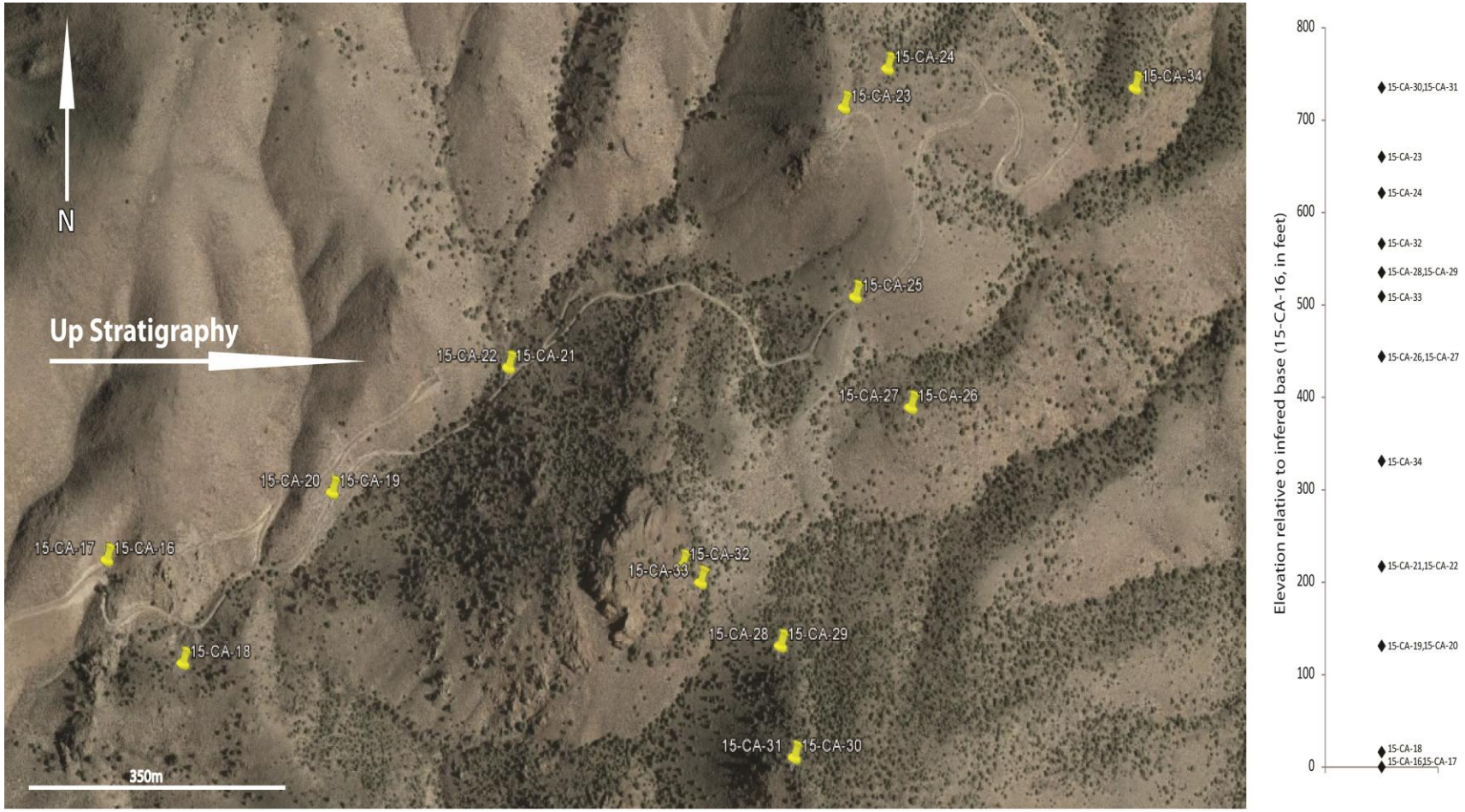

Figure 6.25 A transect of the Clan Alpine Mountains with sample locations shown using yellow pins. Basin and Range faulting has tiled the range to the east such that generally stratigraphic height through the eruptive sequence increases to the east along the range with the exception of 15-CA-30,15-CA-31 which were sampled from the highest accessible peak. On the right, sample heights relative to the lowest collected sample (15-CA-16) are shown in feet.

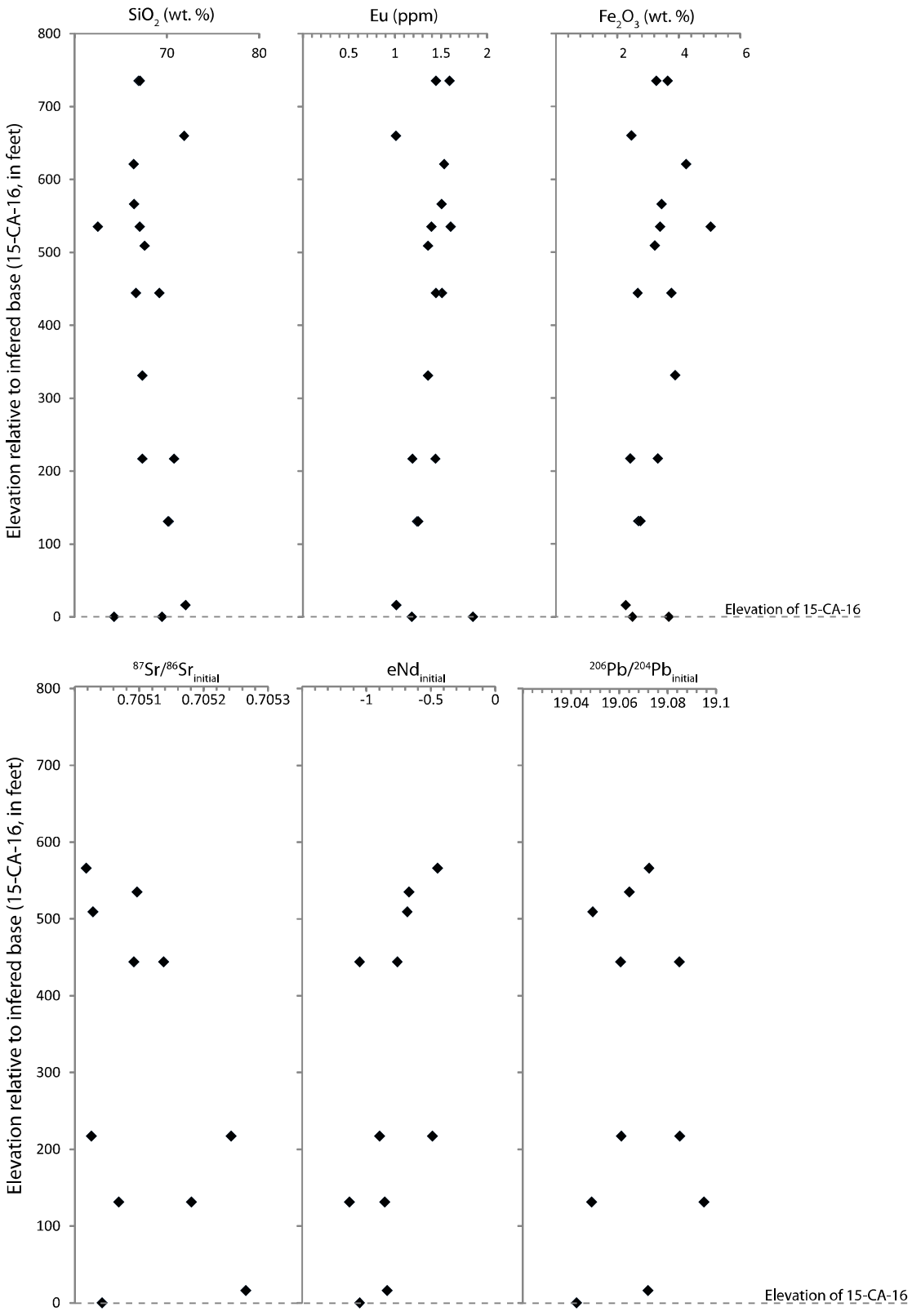

Figure 6.26 Chemostratigraphic and isotopic variation in the TEC from transect across Clan Alpine Mountains. Select major and trace elements show minor variation associated to stratigraphic position, though this appears independent of isotopic composition.

7. Discussion

7.1 Assessment of Element Mobility and Establishing Primary Characteristics

Given the one section of the TEC having undergone significant propylitic alteration, the presence of multiple plutons and cross cutting dikes, and later caldera-scale magmatic systems present, the potential for post-magmatic open system behaviour to have modified major and trace elements as well as isotopic ratios in the TEC is of concern. Steps were taken during sample collection and processing to try to minimize the potential effects of open system modification, such as sampling the freshest looking rocks, removing weathered surfaces and the majority of lithic fragments to acquire the chemical and isotopic composition of the pristine TEC magma.

The first indication that sampling and analysis avoided altered samples include: tight trends between major and trace element concentrations correlating with increasing silica typical of igneous processes; low LOI values (<4%) in all TEC rocks; and petrographic textures that show that almost all chosen samples are unaffected by propylitic alteration. The close agreement of the Sr-isochron (Fig. 6.21) age with the accepted age of eruption, tightly constrained at 25.1 Ma from multiple Ar-Ar and U-Pb zircon ages (Fig. 4.4), strongly suggests that the Rb-Sr isotopic system remained closed and thus the typically mobile elements Rb and Sr have not been measurably affected by post-magmatic processes. Since Rb and Sr can be easily remobilized during alteration, the fact that they seem to have remain relatively unperturbed argues against significant remobilization of other less mobile

elements such as the REE or HFSE. Furthermore, the average Sr contents of >200 ppm are high enough to avoid the effects of open-system behaviour on Sr isotopic ratios as a result of normal weathering processes (Cousens et al., 1993)

Sample 15-CA-43 displays a significantly higher Rb/Sr ratio compared to other TEC rocks (Fig. 4.4), strongly controlling the slope and therefore the age of the isochron. 15-CA-43 also shows has higher K_2O and lower Na_2O contents compared to other TEC rocks, and addition of alkalis is common to propylitic alteration. However, the age-corrected $^{87}Sr/^{86}Sr$ ratio for this sample falls within the range of other TEC samples suggesting that if alteration had occurred, shifting its Rb/Sr to higher values, it most likely occurred concurrently or immediately following deposition of the main tuff sequence and the reset Rb-Sr system remains to give an "age" of 25.1 Ma. Removing this sample from the isochron results in a slightly older calculated age of 28.9 ±2.8 Ma with an initial $^{87}Sr/^{86}Sr$ of 0.705108 ± 0.000076 and an MSWD of 24. This sample also has the lowest Sr concentration of all samples which would be inconsistent with significant addition of Sr through post-magmatic fluids.

The Sm-Nd isotopic system has a higher closure temperature that the Rb-Sr system and Sm and Nd are significantly less mobile than the Rb and Sr. Having established that the $^{87}Sr/^{86}Sr$ ratios of the TEC are relatively unmodified, it is reasonable to expect the Sm-Nd concentrations and $^{143}Nd/^{144}Nd$ are also unaltered. The spread in Sm/Nd ratios in the TEC rocks is too small to yield a Sm-Nd isochron of any age significance, however the initial $^{143}Nd/^{144}Nd$ composition of all the TEC rocks are all nearly identical regardless of Nd concentration (Fig. 6.19). There is a positive trend between initial $^{87}Sr/^{86}Sr$ and 1/Sr below

1/Sr $\leq$ 0.005 indicative of some degree of disequilibrium within the system prior to the closure of the Rb-Sr system. This disequilibrium is not evident in the Nd isotopic system and as discussed in a later section is not present in the $^{87}Sr/^{86}Sr$ ratios of plagioclase crystals suggesting this disequilibrium most likely reflects the minor exchange of Rb and/or Sr post-plagioclase crystallization.

The presented major element and isotopic evidence all suggest the rocks of the TEC have remained as a closed system syn- and post-crystallization; supporting that most chemical characteristics, especially those of the relatively immobile elements such as the REE, are pristine, lending strength to the geochemical models that will be expanded upon in further sections.

7.2 Isotopic Modelling and the Petrogenesis of the TEC

The traditional applications of radiogenic isotopes to continental arc systems, where the continental crust is significantly different isotopically than mantle reservoirs, is obscured within this geographical region. Nevada has been shown to be divided into 2 major isotopic domains; eastern Nevada, overlying Precambrian, crystalline cratonic basement ($^{87}Sr/^{86}Sr$ > 0.706, εNd < -5; Bennett and DePaolo, 1987; Farmer et al., 1989) and western Nevada which overlies a much more heterogeneous and less radiogenic assemblage of Mesozoic oceanic island arcs, inter-arc sedimentary sequences as well as later Sierra Nevada-type granitic intrusions ($^{87}Sr/^{86}Sr$ < 0.706). Cenozoic mafic flows related to Farallon plate rollback are attributed to the partial melting of a metasomatized lithospheric mantle (Timmermans

2015), and within western Nevada demonstrate high radiogenic compositions for mantle-derived melts ($^{87}Sr/^{86}Sr$ up to 0.7061, εNd as low as -4.3; Cousens et al, 2008) similar in composition to the continental crust through which they ascended. While Sr and Nd isotopic contrast is not significant between crustal-derived and mantle-derived magmas, Pb isotopes are more sensitive to interactions between source reservoirs (Cousens et al., 1989) and have demonstrated the ability to distinguish between specific crustal domains (Aitcheson et al., 1995; Siebel et al., 2000). Combining all three systems [Rb-Sr, Sm-Nd, Pb], constraints can be applied to the petrogenesis of the TEC differentiating the fractionation from, or re-melting of, a (previously crystalized) basaltic magma, the partial melting of the continental crust, or a combination of processes. Establishing plausible end-member compositions to represent starting points is vital to constraining any petrogenetic models that can be put forward.

Within the western Great Basin there are few truly basaltic rocks, and this is especially true around the time of the TEC (25.1 Ma). A thick Nevadaplano crust presumably prevented many of these magmas from reaching the surface and provided ample opportunity for mafic magmas to pool within the crust and evolve in composition (Putirka and Busby 2007). Previous work has provided geochemical and isotopic data for 3 mafic to intermediate lavas which erupted in the Southern Stillwater Complex; a basaltic andesite in the Clan Alpine Mountains (11-CN-11, Brian Cousens, personal communication, 2016) and 2 andesitic lavas in the Southern Stillwater Range (04-LT-43 and 04-LT-44a, Timmermans 2015). Only sample 11-CN-11 has been dated (24.02 +/- 0.49 Ma; Timmermans, 2015) and is roughly coeval to

the TEC, the other two flows are believed to be considerably younger (10-15 Ma) based on stratigraphic relations and are possibly the result of extension-related magmatism. Though not contemporaneous, samples 04-LT-43, 04-LT-44a and 11-CN-11 provide the best representation of melts of the mantle within the southern Stillwater Range region. Samples 04-LT-43 and 04-LT-44a both have lower $^{87}Sr/^{86}Sr$ and higher $^{143}Nd/^{144}Nd$ ratios that plot closer to general OIB compositions compared to the TEC (Fig. 7.1), but seemingly along the same mixing line (to a lesser degree). Both 04-LT-43 and 04-LT-44a appear isotopically dissimilar in terms of $^{206}Pb/^{204}Pb$, $^{207}Pb/^{204}Pb$ and $^{208}Pb/^{204}Pb$ (Fig. 7.1). Sample 11-CN-11, which is also the most primitive lava, most closely resembles the TEC in terms of isotopic composition, with overlapping $^{143}Nd/^{144}Nd$ and $^{87}Sr/^{86}Sr$ ratios and more similar Pb-isotope ratios.

The TEC rocks plot along a mixing line defined by Cenozoic basalts of the western, $^{143}Nd/^{144}Nd$ and $^{87}Sr/^{86}Sr$ ratios support a similar source for the TEC which plot closer to the crustal-endmember (Fig. 7.1). Lead isotopes support this generalized mixing of source compositions but show evidence for a more localized contaminant being assimilated into the TEC with TEC rocks plotting on a distinct steeper trend in $^{206}Pb/^{204}Pb$ vs $^{207}Pb/^{204}Pb$ space (Fig. 7.1, inset). For the localized system, sample 11-CN-11 appears to represent the best candidate to serve as an endmember composition reflecting mantle inputs into the TEC system, while variation in each isotopic system precludes the TEC resulting purely from fractional crystallization of a mafic magma like 11-CN-11.

Figure 7.1 $^{87}Sr/^{86}Sr$ vs. $^{143}Nd/^{144}Nd$ ratios for the rocks of the TEC compares against coeval intermediate lavas as well as samples of the regional basement assemblages. The yellow field for western Great Basin mafics (wGM) is from Timmermans (2015), detailing the isotopic compositions of subduction related mafic flows west of the Nevadan $^{87}Sr/^{86}Sr$ = 0.706 Sr-isopleth. The pink field for Western Great Basin Basalts (WGB) encompasses 1000+ samples of basaltic rocks from Cousens et al., (2008) and the GEOROC database (GEOROC, 2007) from the most western regions of the Great Basin adjacent to the Sierra Nevada Range, representing extension related melts of the lithospheric mantle. Inset) $^{206}Pb/^{204}Pb$ vs $^{207}Pb/^{204}Pb$ for the same rocks, symbols and fields are identical. Notice the variation in slope between both WGB basalts and coeval intermediate lavas distinct from the slope shown by TEC rocks. NHRL from Hart (1984).

Although the analysis of local Mesozoic rocks, which presumably constitute the local basement assemblages, shows that they have extremely heterogeneous isotopic ratios (Fig. 6.24), tight trends demonstrated by the TEC are suggestive that either a single crustal reservoir was the predominant crustal-input or that the partial melts from various crustal units were able to homogenize before being assimilated into the mantle-derived magma. Sample 16-DJ-31 was selected to represent the composition of the localized granitic basement on the basis of isotopic constraints, as it represents a near endmember composition (at the terminus of the trend in $^{206}Pb/^{204}Pb$ vs. $^{207}Pb/^{204}Pb$ space as well as $^{87}Sr/^{86}Sr$ ratio), and the fact 16-DJ-31 contains easily fusible hydrous phases.

16-DJ-31 has a lower εNd value than what was being incorporated into the TEC (Fig. 7.2). The small scatter in εNd suggests that the assimilant had similar Nd isotopic ratios to that of the mantle-derived magma, or that one of the components had a significantly higher Nd concentration than what was modelled and fully controls the $^{143}Nd/^{144}Nd$ ratio of the hybrid, or that the Nd of one endmember is hosted in a refractory phase and is not incorporated into the hybrid magma. The latter hypothesis would require a restitic, REE-rich phase, which is unlikely. 16-DJ-31 has almost the exact isotopic composition of $^{87}Sr/^{86}Sr$, $^{206}Pb/^{204}Pb$, $^{207}Pb/^{204}Pb$ and $^{208}Pb/^{204}Pb$ as the enriched end of the trend demonstrated by the TEC, strongly supporting granitoids as the assimilated crustal material.

Mixing models between 16-DJ-31 and 11-CN-11 present extremely variable degrees of mixing required to satisfy isotopic trends (Fig. 7.2a). The models compare binary mixing of two selected endmember compositions with mixing between a 30% batch melt of the granitic endmember with the intermediate lava (shown with solid and dashed lines respectively). The samples of the TEC span the entirety of isotopic compositions between both end-members in terms of $^{87}Sr/^{86}Sr$ and εNd values, and include roughly 20-100% of the crustal component in terms of $^{206}Pb/^{204}Pb$ and $^{207}Pb/^{204}Pb$ (Fig. 7.2a). The slight deviation in TEC data from the proposed Pb isotope mixing line shows the mantle-derived magma had a slightly different $^{206}Pb/^{204}Pb$ ratio compared to the proposed endmember (11-CN-11). The tight trend is steeper and trends towards a composition closer to the NHRL (Figure 7.1, inset) as opposed to the trend shown by the western Great Basin basalts. The offset in terms of $^{87}Sr/^{86}Sr$ vs. εNd data from the modelled lines can be explained by the addition of <20% of the black argillite fragments found within the TEC to one of the more primitive pumice samples (lowest SiO_2); this additional assimilation will not affect the trend shown in Pb-isotope space (Fig. 7.2b).

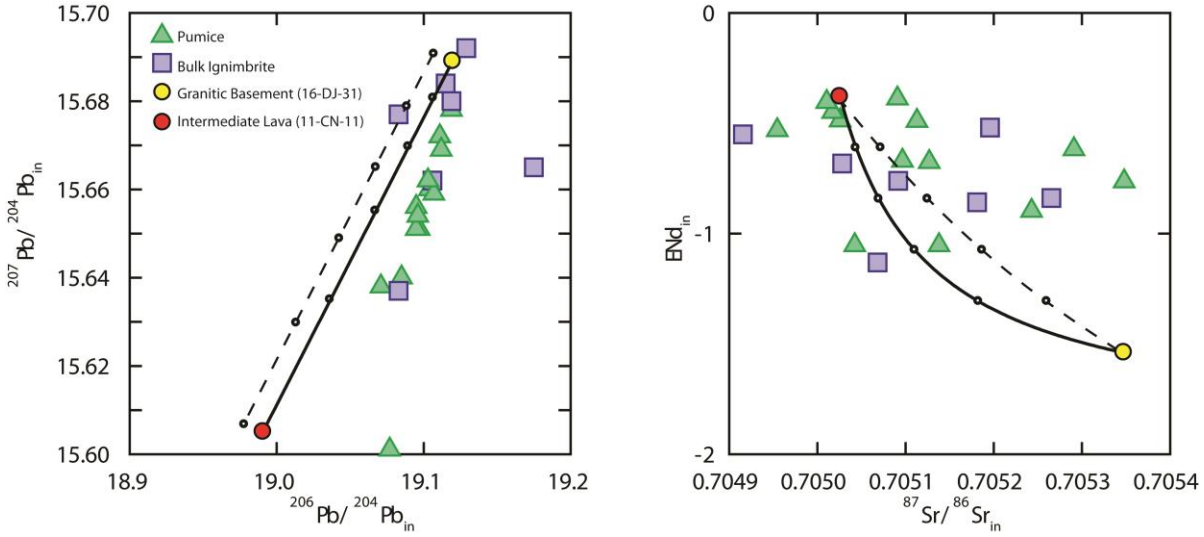

Figure 7.2 a) Left) $^{206}Pb/^{204}Pb$ vs $^{207}Pb/^{204}Pb$ for the rocks of the TEC compared to mixing between a coeval mafic-intermediate lava 11-CN-11 and a Mesozoic granitoid. The solid black mixing line represents purely binary mixing, the dashed line is between a 30% batch melt of the granitoid and the same primitive magma. Dots along each mixing line denote 20% increments of mixing; the dashed line is offset to provide visual emphasis. **Right)** The same mixing curves for $^{87}Sr/^{86}Sr$ vs. εNd.

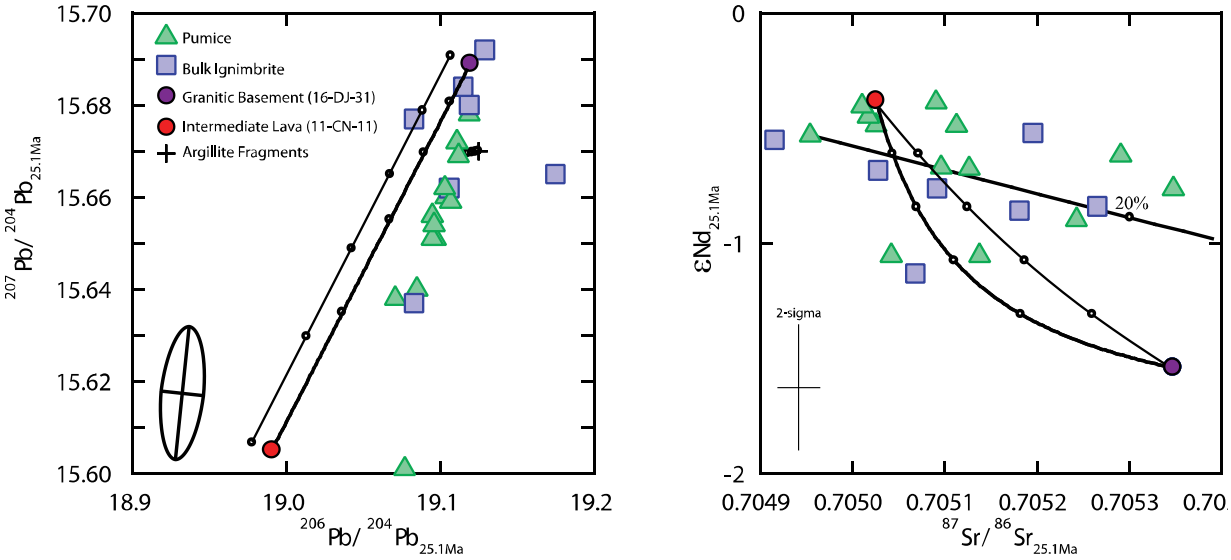

Figure 7.2 b) The same mixing lines as shown in Fig. 7.2(a) with the addition of a mixing line between one of the most primitive pumice samples (lowest SiO_2 contents) with the argillite fragments found throughout the TEC. Withouut affecting Pb isotope trends (left figure) a better fitting line can be projected through the $^{87}Sr/^{86}Sr$ vs. εNd data (right figure). Same symbols are shown in the previous figure.

7.3 Feldspar Isotopic Characteristics and Constraints on Assimilation

Feldspar separates from a number of pumice samples yielded uniform $^{87}Sr/^{86}Sr$ ratios of ~0.7051 (Fig. 7.3; Appendix 1, Table 10) compared to the more variable pumice and bulk ignimbrite samples. The variation observed in bulk pumice could be attributed to the inclusion of other possibly non-cogenetic mineral phases, insufficient removal of lithic fragments or xenocrystic crystals prior to isotopic determinations, or the possibility of slight alteration affecting the pumice glass matrix post-plagioclase crystallization. However, with care having been given to avoid each of these possible contaminants, the isotopic homogeneity of feldspars seems to suggest that they represent a distinct period of crystallization or a "snap shot" of the evolving TEC. Though feldspar crystallization could occur at any point during petrogenesis, this section will compare the observable differences if feldspar crystalized early (in the source) or later (in the shallow magma chamber).

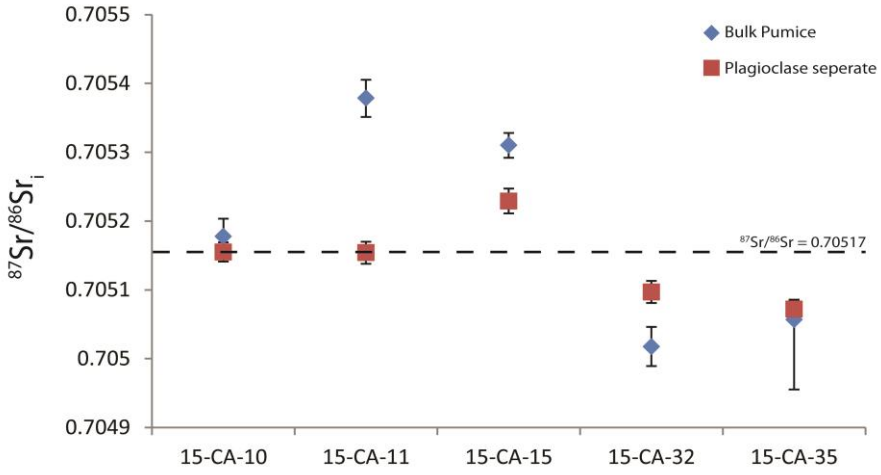

Figure 7.3 Initial $^{87}Sr/^{86}Sr$ ratios (corrected to 25.1 Ma) for each of the 5 feldspar separates compared with the bulk pumice they were separated from. Isotopic ratios of feldspar taken from Landon-Browne, 2016. Dashed line shows the initial isotopic ratio calculated from Rb-Sr isochron of entire TEC suite (Fig 6.18).

The first scenario proposed is one in which feldspar is earlier crystalizing phase and that the bulk of assimilation (i.e. isotopic contamination) occurred after the majority of feldspar crystals formed. Isotopically homogenous feldspar represents one product of the primitive magma crystallizing as heat is lost to crustal anataxis. This homogenous $^{87}Sr/^{86}Sr$ ratio of 0.7051 falls on the mixing lines at around 20% of crustal component, which when translated to Pb isotope space corresponds to the approximate start of the data array shown by the TEC.

Variations in Sr and Pb isotopes past this ~20% mixing point possibly represent the further melting of crustal rocks being assimilated into the hybridized TEC. For example, when magma 11-CN-11 intruded the granitic basement, heat was transferred to melt crustal rocks and plagioclase began to crystalize around 20% hybridization (potentially an early melt fraction from the crust, muscovite melting begins ~760°C [Annen el al., 2006]), then post plagioclase crystallization the biotite solidus (~860°C [Annen el al., 2006], biotite can have high Pb and radiogenic Sr contents, Rb, U, Th and Pb are all compatible elements) was reached within the granite releasing a greater melt fraction responsible for the full spread in TEC data. The less crystal-rich dark pumice of the TEC have lower $^{87}Sr/^{86}Sr$ ratios than the lighter crystal-rich pumice (Fig. 6.24), all below $^{87}Sr/^{86}Sr = 0.7051$, consistent with the lighter pumice representing the liquid that includes a larger crustal component while the darker pumice group reflects more the mantle-derived compositions (or early crystalizing compositions). The overlap in Pb-isotope ratios can be achieved by the small inclusion of

some of the liquid phase represented by the dark pumice along with the crystal-rich light magma during eruption.

A second scenario is also plausible, where the plagioclase represents a late crystalizing phase potentially as a result of the degassing of a shallow magma chamber just prior to eruption. The effects of the TEC system degassing are evident as most hydrous phases within the TEC show evidence of an alteration halo which is common to degassing magmatic systems. Along with this, similar to many other calderas as part of the Ignimbrite Flare-up, the TEC would be considered a cool, wet magmatic system (Best and Christiansen, 1991; Christiansen & McCurry, 2005) and, in general, high water contents within the melt will supress plagioclase crystallization. Once the magma degasses, plagioclase would be free to crystalize and the high CaO and Al_2O_3 concentrations within TEC rocks suggest this plagioclase was not removed from the system prior to eruption. In this model, the isotopic variability of the TEC may represent the evacuation of a stratified magma chamber (Friedrich and Mahood 1987). Typical of many of these systems, a highly evolved silicic liquid caps the shallow chamber which may be represented by the more waxy, less crystal-rich dark pumice of the TEC. As the chamber continued to evacuate, deeper regions were tapped pulling up more crystal rich magmas (the light pumice). The isotopic homogeneity of the plagioclase then represents crystallization in a singular stratified layer within the magma, and the divergence from this homogenous isotopic ratio represents the inclusion of a variable proportion of this more enriched silicic liquid. This model would also account for the linear trending trace element concentrations representing both the fractional

crystallization of phases as well as the variable inclusion of minerals from a partially crystalline magma along with the eruption.

Rather than arguing for the bulk of plagioclase crystallization to have occurred pre- or post-assimilation, it is possible these two events are intimately linked. Plagioclase crystallization would be an exothermic reaction and it's possible that the induction of large scale crystallization as a result of degassing the TEC system may have generated sufficient heat to re-melt surrounding country rocks. These generated liquid may have subsequently been mixed with the plagioclase rich magma during eruptions and could explain some isotopic variation.

7.4 Trace Element Modelling

Along with isotopic similarities between crustal rocks of the region and the influxing mantle-derived magmas, the typical relationship where crustal rocks are enriched in incompatible elements compared to mantle-derived rocks is inverted within the Stillwater Caldera Complex (Fig. 7.4). The intermediate lavas have enriched rare earth element patterns compared to typical mantle-derived rocks, and overlap with the compositions exhibited by TEC samples. Relative to the least enriched of the TEC rocks the intermediate lavas are all more enriched in rare earth elements with a marginally shallower slope for LREE/HREE. Along with this, the local Mesozoic granitoids are more depleted in trace element concentrations relative to TEC samples, with much steeper LREE/HREE slopes.

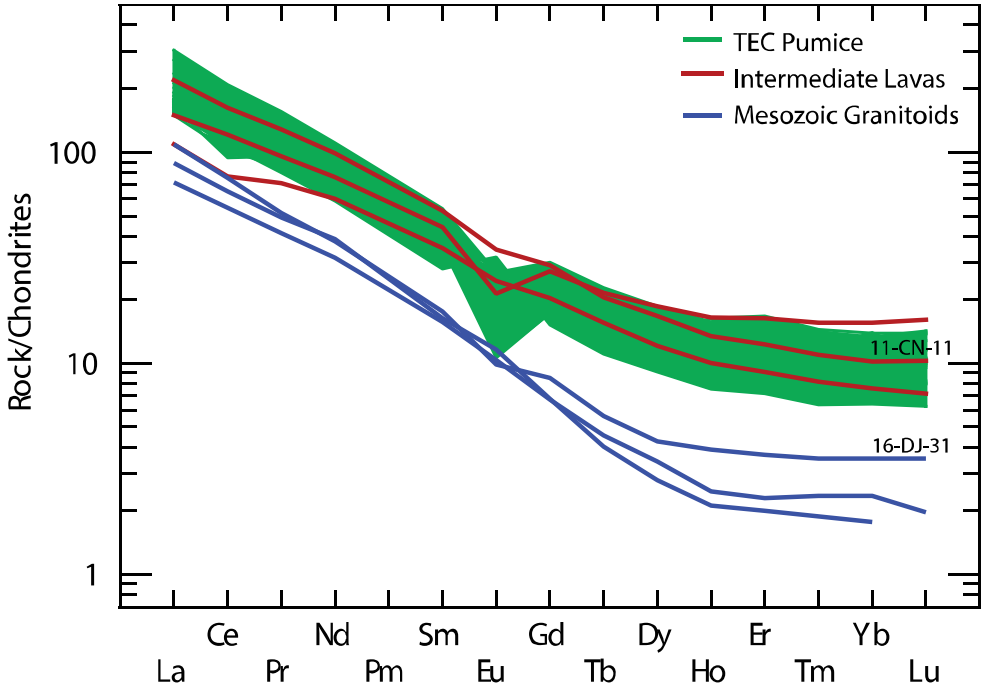

Figure 7.4 Rare earth element patterns for the TEC compared to coeval intermediate lavas and Mesozoic granitoids which presumably constitute basement assemblages. Normalized using values for chondrite from Sun and McDonough (1989).

By modelling a partial batch melt of the representative granitic sample (16-DJ-31) a liquid closely resembling the more primitive TEC samples can be replicated, and subsequent mixing with the andesitic lava would remain within the concentration ranges of the TEC (Fig. 7.5). This process of creating a batch melt enriches the liquid phase in most trace element concentrations, resulting in a small decrease in the degree of mixing required to satisfy isotopic constraints (Fig. 7.2). Having a crustal assemblage with a large amount of residual plagioclase also serves to impart a significant negative Eu anomaly that is evident in some TEC samples without the requirement of a significant amount of plagioclase being fractionated from the hybridized magma. Post-hybridization, some degree of fractional

crystallization serves to explain the few samples more with steeper REE patterns as well as more enriched HREE concentrations. A mantle-derived magma more enriched than the chosen sample being mixed with the TEC can also explain a few of these higher REE concentrations; mixing with a more enriched magma would also lower the amount of mixing required to satisfy the same patterns. Fractional crystallization most likely occurred either during magma ascent or once the magma began pooling in a shallow reservoir; fractionation of some Fe-Ti oxides, apatite as well as some zircon had to occur to account for depletions of compatible trace elements and this was most likely accompanied by fractionation of plagioclase and sanidine.

To fully integrate the TEC into the model of a DCHZ, I propose that the chemical characteristics of the TEC rocks are consistent with the generation of felsic melts and subsequent mixing by the repeated emplacement of basaltic to intermediate dikes and sills into a primarily granitic basement. The rocks adjacent to and between these injections are heated above their solidus and once this melt has been generated from the host granitic rocks, it is free to mix with the still liquid basalt before ascending into a shallow reservoir. This is evidence that a significant amount of chemical variation is influenced by source processes; fractional crystallization and later assimilation may have occurred to a minor degree (i.e. influencing P behaviour as apatite was fractionated), however the major chemical trends seem to be reflective of simple mixing between an andesitic magma and a partial melt of the continental crust.

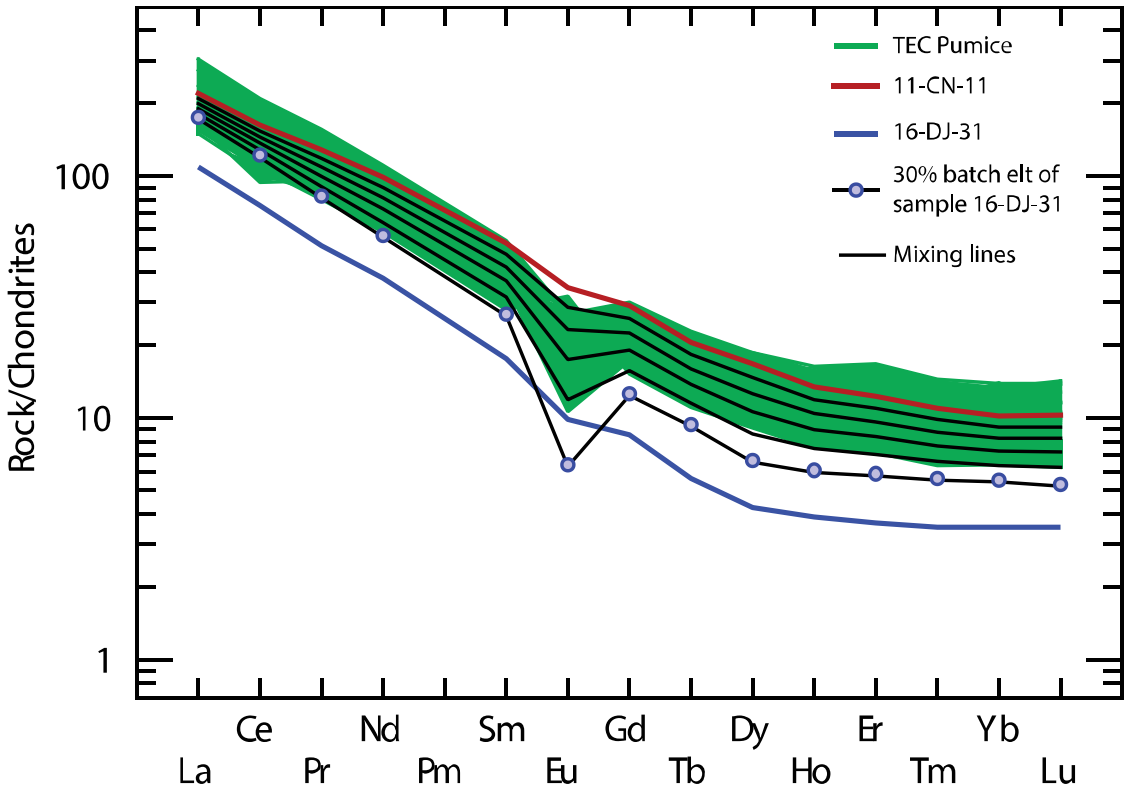

Figure 7.5 Chondrite normalized rare earth patterns of the TEC compared to a batch melt of the representative local basement being mixed with a coeval intermediate lava. The batch melt was produced from a starting assemblage of 30% plagioclase, 28% quartz, 25% potassium feldspar, 15% biotite, 2% apatite and 0.1% zircon from sample 16-DJ-31 and subsequently binary mixed with sample 11-CN-11. Notice the batch melting imparts a strong negative Eu anomaly to the hybridized magma which satisfies the TEC patterns without the subsequent fractionation of a large degree of plagioclase. Mixing lines are divided by 20% intervals of mixing. Sample 16-DJ-31 was received as a previously powdered rock sample described as biotite granite, to determine Kd values it was assigned a modal assemblage of 30% plagioclase, 28% quartz, 25% potassium feldspar, 15% biotite, 2% apatite and 0.1% zircon. Partition coefficients (Kds) used for these calculations can be found in Appendix 1, Table 16. Normalized using values from Sun and McDonough (1989).

7.3 Supporting Clues from Trends in Major Element Chemistry

Recent work using melting experiments (Patiño Douce 1999, and references therein) and in natural settings (Lee et al., 2003; Watts et al., 2016) have added a great deal of understanding to how felsic melts are formed and how to use observed trends in major element concentrations to elucidate the degree of mixing and potential crustal rocks being assimilated.

TEC rocks are less siliceous than experimental melts of common crustal lithologies derived in a laboratory setting, consistent with the TEC not being the product purely of crustal anataxis (Fig. 7.6). Experimental melts produced from common crustal litholgies all have SiO_2 contents greater than 70 wt.% while the TEC magmas range to lower SiO_2 contents (as low as 60 wt.% SiO_2). Producing these lower SiO_2 contents would require either a nearly complete re-melting of a more mafic granitoid which is unlikely, or the hybridization of a partial melt of the continental crust with a low SiO_2 magma. The isotopic signature of a number of local granitoids do support a chemical relation to the TEC rocks (Fig. 7.2), and similar rocks most likely constituted the assimilant involved in TEC petrogenesis.

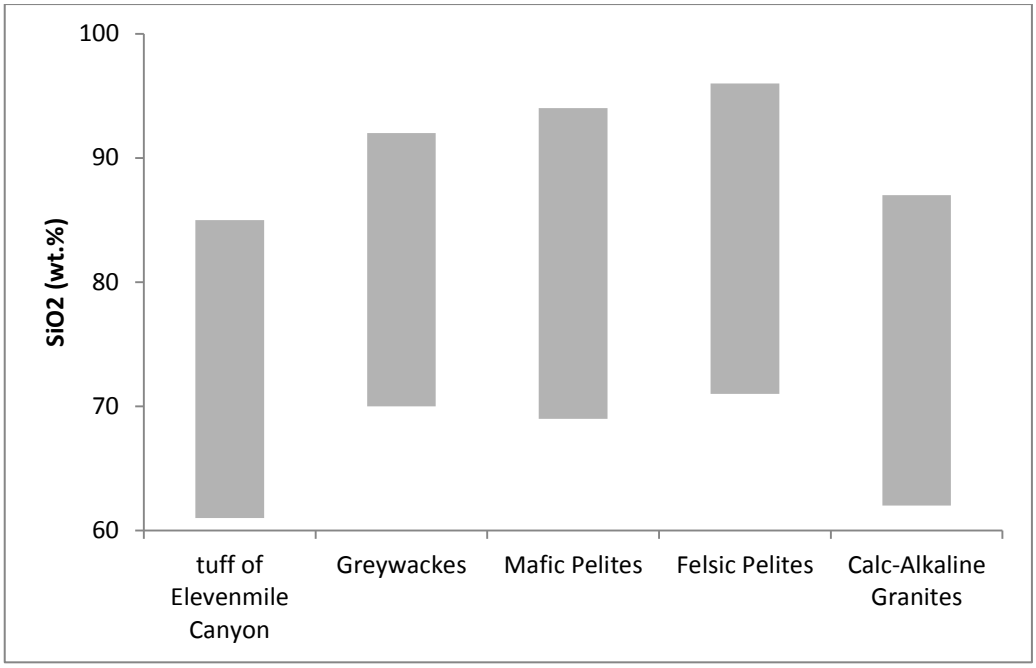

Figure 7.6 SiO_2 contents of the TEC compared to laboratory melts of common crustal protoliths and the range of values observed for Cordilleran calc-alkaline granites. Modified from Patiño Douce (1999).

McCarthy & Patiño Douce (1997) and Patiño Douce (1995, 1999) have illustrated reaction lines between a partially melted calc-alkaline granite and a high aluminum olivine tholeiite magma (HAOT). Similar to AFC reactions, these model the elemental components added by both endmembers as well as components subtracted by crystalizing phases during AFC processes (Fig. 7.7). The modelled reactions are limited by what had been tested experimentally, which was the low pressure hybridization of a melting calk-alkaline granite (melting hornblende + quartz) and an HAOT, but this can be used as a close proxy for the melting of earlier Mesozoic felsic plutons and batholiths that are sprinkled over the western US by younger mafic intrusions.

The TEC supports the previous isotopic and trace element models by demonstrating tightly constrained trends on these plots, similar to the results of Patiño Douce (1995, 1999) (Fig. 7.7). The TEC mirrors modelled trends except for an offset in the initial crustal melt composition which can be explained by a higher proportion of mafic minerals in the crustal endmember of the TEC system compared to what was tested experimentally. The synthetic granite tested by Patiño Douce (1995) had only a fraction of amphibole present in the assemblage, however, when considering the granitic end-members suggested by isotopic models all have considerable amounts of biotite in their mineralogy. The divergence from Patiño Douce models in terms of CaO/Al_2O_3 (Fig. 7.7, subpanel D) is also suggestive of the crystallization of a Ca rich phase (clinopyroxene and hornblende are both present as an accessory phase in the TEC) unaccounted for by the experiments, a differing crystalizing assemblage may also account for some of the offset of TEC data from the trends predicted by models.

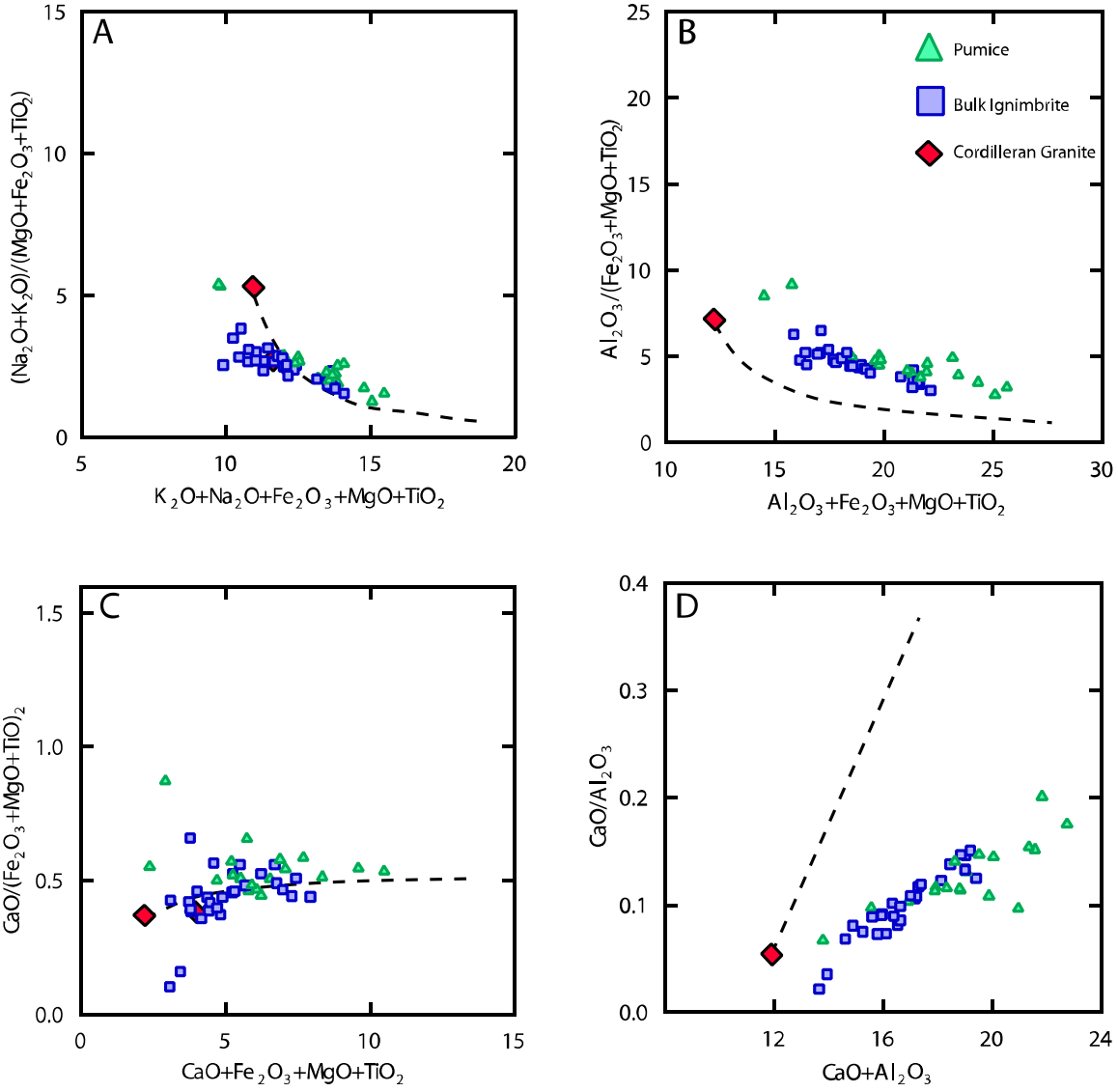

Figure 7.7 Major element trends of the TEC (blue squares and green triangles) compared to the low-pressure hybridization of synthetic calc-alkaline granite (red diamonds) with an HAOT.

Though the TEC is entirely peraluminous it trends towards metaluminous compositions on the plots constructed by Patiño Douce (Fig. 7.8); this behaviour is typical of calc-alkaline felsic suites and reflects the generality of phyllosilicate dehydration in the source for many of these rocks. The TEC exhibits a shallower trend in Fig. 7.8 than what is predicted by the experimental results, consistent with a larger fraction of plagioclase remaining in the source for the TEC. The more shallow trend exhibited by the TEC on Fig. 7.8 compared to the model is a result of the ratio of plagioclase to clinopyroxene in the peritectic assemblage of the TEC system, by increasing clinopyroxene relative to plagioclase in the peritectic assemblage the resultant trend is shallowed on this diagram.

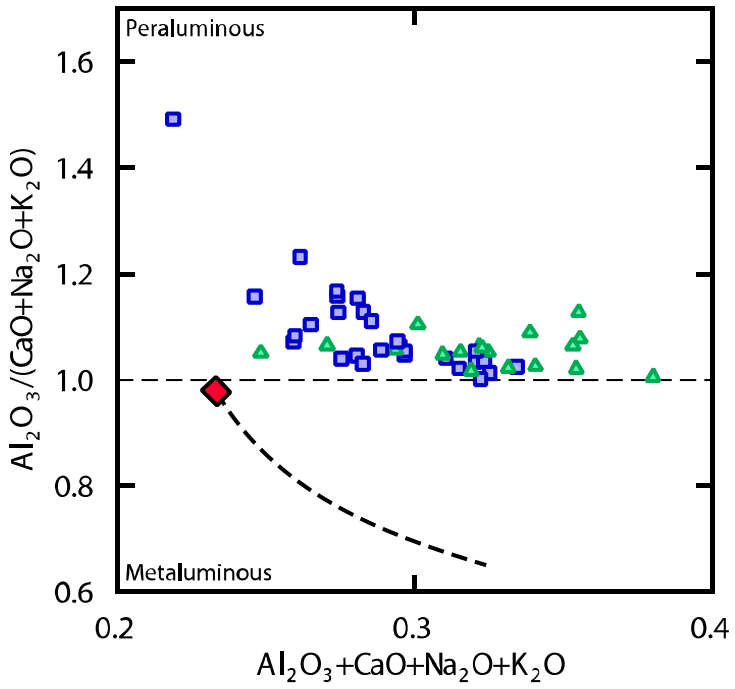

Figure 7.8 Aluminum saturation index of TEC rocks compared to the hybridization of a calc-alkaline granite with an HAOT. Symbols and fields are the same as in Fig. 7.10. Modified after Patiño Douce (1999).

8 Conclusions

8.1 The tuff of Elevenmile Canyon

The tuff of Elevenmile Canyon is an extremely large (2,000+ km^3) 25.1 Ma suite of ashflow tuffs that constitutes the majority of the extrusive volume within the Stillwater Caldera Complex in western Nevada. Its eruption coincided with the subduction-related volcanic front of Mid-Tertiary Ignimbrite Flare-up passing through this region as the Farallon plate rolled-back oceanward beneath North America. Subsequent Basin and Range extension and the related tilting of large fault blocks have exposed nearly the entire intracaldera sequence starting with a recognizable caldera floor, allowing for the sampling of the entire volcanic sequence and the opportunity to examine petrological and geochemical variation throughout.

These volcanic environments are very complex and a variety of petrogenetic processes are acting on evolving magmas to differing degrees. Though geographically associated with 6 other caldera-style deposits and related plutons, the TEC is petrographically and compositionally distinct. Chemically the TEC is more mafic than the other volcanic units of the Stillwater Caldera Complex with SiO_2 contents as low as 61 wt.% and includes biotite as well as pyroxene and amphibole crystals. Major and trace elements for the TEC demonstrate tight trends typical of normal igneous processes such as fractional crystallization or simple mixing between a mantle-derived magma with a liquid generated by the partial fluxing of continental crust.

Models for the petrogenetic development of the TEC are consistent with those of deep crustal hot zones or MASH zones, where a mantle derived primitive magma was able to partially melt a granitic basement and subsequently mix with that crustal melt to varying degrees. Trace element and isotopic modelling suggest the composition of the TEC can be an approximated by 30-40% melt of local granitoid being hybridized with a magma exemplified by a coeval andesite flow. This mixing of partially molten mantle-derived magmas with liquid derived by crustal fluxing is supported with comparisons between TEC data and experimental mixing curves.

On ascent to a shallow magma chamber the TEC was free to degas, evidenced by alteration halos surrounding biotite and amphibole grains, driving crystallization and fractionation of certain mineral phases. This resulted in the crystallization of isotopically homogenous plagioclase crystals from a single stratified section of the chamber which was capped by a highly evolved silicic liquid at the top of the chamber. These two layers are represented by a crystal-rich light pumice and a distinct aphyric darker pumice amongst TEC rocks, poorly defined chemical trends through stratigraphy suggests the eruption of the TEC agitated the boundary between these two layers and each were mixed and erupting simultaneously.

References

Aitcheson, S.J., Harmon, R.S., Moorbath, S., Schneider, A., Soler, P., Soria-Escalante, E., Steele, G., Swainbank, I. and Wörner, G., 1995. Pb isotopes define basement domains of the Altiplano, central Andes. Geology, 23(6), p. 555-558.

Allègre, C.J., 2008. Isotope geology (p. 512). Cambridge: Cambridge University Press.

Annen, C., Blundy, J.D., Sparks, R.S.J., 2006, The Genesis of Calcalkaline Intermediate and Silicic Magmas in Deep Crustal Hot Zones: Journal of Petrology v.47, p. 505-539.

Annen, C., Blundy, J.D., Sparks R.S.J., 2008, The sources of granitic melt in Deep Hot Zones: Transactions of the Royal Society of Edinburgh: Earth Sciences, v. 97(4), p. 297-309.

Armstrong, L.R., Ward, P., 1991, Evolving geographic patterns of Cenozoic magmatism in the North American Cordillera: The temporal and spatial association of magmatism and metamorphic core complexes: Journal of Geophysical Research: Solid Earth, v. 96 (B8), p. 13201-13224.

Atwater, T, 1970, Implications of plate tectonics for the Cenozoic tectonic evolution of western North America: Geological Society of America Bulletin, v. 81(12), p. 3513-3536.

Barth, A.P., Wooden, J.L., 2006, Timing of magmatism following initial convergence at a passive margin, southwestern US Cordillera, and ages of lower crustal magma sources: The Journal of Geology, v. 114(2), p. 231-245.

Bennett, V.C. and DePaolo, D.J., 1987. Proterozoic crustal history of the western United States as determined by neodymium isotopic mapping. GSA Bulletin, 99(5), p. 674-685.

Best, M.G., and Christiansen, E.H., 1991, Limited extension during peak Tertiary volcanism, Great Basin of Nevada and Utah: Journal of Geophysical Research, v. 96, p. 13,509–13,528.

Bouvier, A., Vervoort, J.D. and Patchett, P.J., 2008: The Lu–Hf and Sm–Nd isotopic composition of CHUR: constraints from unequilibrated chondrites and implications for the bulk composition of terrestrial planets. Earth and Planetary Science Letters, 273(1), p. 48-57.

Brown, M., 2013. Granite: From genesis to emplacement. Geological Society of America Bulletin, *125*(7-8), p. 1079-1113.

Cadek, O., Fleitout, L., 2003, Effect of lateral viscosity variation in the top 300 km on the geoid and dynamic topography: Geophysical Journal International, v. 152 (3), p. 566-580.

Camp, V.E., Hanan, B.B., 2008, A plume-triggered delamination origin for the Columbia River Basalt Group: Geosphere, v. 4 (3), p. 480-495.

Camp, V.E., Pierce, K.L. and Morgan, L.A. (2015) Yellowstone plume trigger for Basin and Range extension, and coeval emplacement of the Nevada-Columbia Basin magmatic belt. Geosphere 11, doi: 10.1130/GES01051.1.

Chamberlin, R.M., 1983, Cenozoic domino-style crustal extension in the Lemitar Mountains, New Mexico: A summary. In Guidebook, 34th Field Conference, Socorro Region II (V. 34, p. 111-118). New Mexico Geological Society Socorro, New Mexico.

Chappell, B.W., White, A.J.R., 1974, Two contrasting granite types: Pacific Geology 8, p. 173-174.

Christiansen, R.L., and Yeats, R.S., 1992, Post-Laramide geology of the U.S. Cordilleran region, in Burchfi el, B.C., Lipman, P.W., and Zoback, M.L., eds., The Cordilleran Orogen: Conterminous U.S.: Boulder, Colorado, Geological Society of America, The Geology of North America, v. G-3, p. 261–406.

Christiansen, E.H. and McCurry, M., 2008. Contrasting origins of Cenozoic silicic volcanic rocks from the western Cordillera of the United States. Bulletin of Volcanology, 70(3), p. 251-267.

Clemens, J.D., 2012, Granitic magmatism, from source to emplacement: a personal view: Applied Earth Science, v. 121 (3), p. 107-136.

Clemens, J.D., Helps, P.A., Stevens, G., 2009, Chemical structure in granitic magmas-a signal from the source?: Earth and Environmental Science Transactions of the Royal Society of Edinburgh, v. 100 (1-2), p. 159-172.

Clemens, J.D., Helps, P.A., Stevens, G., 2010, Chemical structure in granitic magmas-a signal from the source?: Geological Society of America Special Paper, 472, p. 159-172.

Clemens, J.D. and Stevens, G., 2012. What controls chemical variation in granitic magmas?: Lithos, 134, p. 317-329.

Cloos, E., 1968, Experimental analysis of Gulf Coast fracture patterns: Aapg Bulletin, v. 52 (3), p. 420-444.

Colgan, J.P., and Henry, C.D., 2009, Rapid middle Miocene collapse of the Sevier orogenic plateau in north-central Nevada: International Geology Review, v. 51, p. 920– 961.

Coney, P.J., 1978, Mesozoic–Cenozoic Cordilleran plate tectonics, in Smith, R.B., and Eaton, G.P., eds., Cenozoic Tectonics and Regional Geophysics of the Western Cordillera: Geological Society of America Memoir 152, p. 33–50.

Coney, P.J., Reynolds, S.J., 1977, Cordilleran Benioff zones: Nature, v. 270, p. 403-406.

Cousens, B.L., Spera, F.J., and Tilton, G., 1989. Isotopic patterns in silicic lavas and ignimbrites of the Mogan and Fataga Formations, Gran Canaria, Canary Islands: temporal changes in mantle source composition. Earth and Planetary Science Letters 96, p. 319-335.

Cousens, B.L., Spera, F.J. and Dobson, P.F., 1993. Post-eruptive alteration of silicic ignimbrites and lavas, Gran Canaria, Canary Islands: Strontium, neodymium, lead, and oxygen isotopic evidence. Geochimica et Cosmochimica Acta, 57(3), p. 631-640.

Cousens, B., Prytulak, J., Henry, C., Alcazar, A. and Brownrigg, T., 2008. Geology, geochronology, and geochemistry of the Miocene–Pliocene Ancestral Cascades arc, northern Sierra Nevada, California and Nevada: The roles of the upper mantle, subducting slab, and the Sierra Nevada lithosphere. Geosphere, 4(5), p. 829-853.

Cross, T.A., Pilger, R.H., 1982, Controls of subduction geometry, location of magmatic arcs, and tectonics of arc and back-arc regions: Geological Society of America Bulletin, v. 93 (6), p. 545-562.

Davidson, J., 1985, Mechanisms of contamination in Lesser Antilles island arc magmas from radiogenic and oxygen isotope relationships: Earth Planet. Sci. Lett., v. 72, p. 163-174.

DeCelles, P.G., 2004, Late Jurassic to Eocene evolution of the Cordilleran thrust belt and foreland basin system, western USA: American Journal of Science, v. 304, p. 105–168.

DeCelles, P.G., Coogan, J.C., 2006, Regional structure and kinematic history of the Sevier fold-and-thrust belt, central Utah: Geological Society of America Bulletin, v. 118 (7-8), p. 841-864.

DePaolo, D.J., 1981. Trace element and isotopic effects of combined wallrock assimilation and fractional crystallization. Earth and planetary science letters, 53(2), p. 189-202.

de Silva, S., 2008, Arc magmatism, calderas, and supervolcanoes: Geology, v. 36, p. 671–672.

Dickin, A.P., 2005. Radiogenic isotope geology. Cambridge University Press.

Dickinson, W.R., 2006, Geotectonic evolution of the Great Basin: Geosphere, v. 2, p. 353–368.

Dickinson, W.R., and Snyder, W.S., 1978, Plate tectonics of the Laramide orogeny, in Matthews, V., III, ed., Laramide Folding Associated with Basement Block Faulting in the Western United States: Geological Society of America Memoir 151, p. 355–366.

Engebretson, D.C., Cox, A., Gordon, R.G, 1985, Relative motions between oceanic and continental plates in the Pacific basin: Geological Society of America Special Papers, 206, p. 1-60.

Ersoy, Y. and Helvacı, C., 2010. FC–AFC–FCA and mixing modeler: a Microsoft® Excel© spreadsheet program for modeling geochemical differentiation of magma by crystal fractionation, crustal assimilation and mixing: Computers & Geosciences, v. 36(3), p. 383-390.

Farmer, G.L., Bailley, T., and Elkins-Tanton, L.T., 2008, Mantle source volumes and the origin of the mid Tertiary ignimbrite flare-up in the southern Rocky Mountains, western U.S.: Lithos, v. 102, p. 279–294.

Farmer, G.L. and DePaolo, D.J., 1983: Origin of Mesozoic and Tertiary granite in the western United States and implications for Pre-Mesozoic crustal structure: 1. Nd and Sr isotopic studies in the geocline of the Northern Great Basin. Journal of Geophysical Research: Solid Earth, 88(B4), p. 3379-3401.

Fridrich, C.J. and Mahood, G.A., 1987, Compositional layers in the zoned magma chamber of the Grizzly Peak Tuff: Geology, v. 15(4), p. 299-303.

Frost, B.R., Barnes, C.G., Collins, W.J., Arculus, R.J., Ellis, D.J. and Frost, C.D., 2001. A geochemical classification for granitic rocks. Journal of petrology, 42(11), p. 2033-2048.

Frost, B.R. and Frost, C.D., 2008. A geochemical classification for feldspathic igneous rocks. Journal of Petrology, 49(11), p. 1955-1969.

Gans, P.B., 1987, An open-system, two-layer crustal stretching model for the Eastern Great Basin: Tectonics, v. 6 (1), p. 1-12.

Geist, D., Richards, M., 1993, Origin of the Columbia Plateau and Snake River Plain: deflection of the Yellowstone plume: Geology, v. 21, p. 789-791.

GEOROC, 2007, Geochemistry of Rocks of the Oceans and Continents: Mainz, Max-Planck-Institute für Chemie: http://georoc.mpch-mainz.gwdg.de/georoc/.

Gill, R., 2010. Igneous rocks and processes: a practical guide. John Wiley & Sons.

Gilluly, J., Gates, O., Plouff, D., Ketner, K.B., 1965, Tectonic and igneous geology of the northern Shoshone Range, Nevada, with sections on gravity in Crescent Valley and economic geology. No. 465. United States Government Printing Office.

Glazner, A.F., 2007, Thermal limitations of incorporation of wall rock into magma: Geology v.35, p. 319-322

Hart, S.R., 1984: A large-scale isotope anomaly in the Southern Hemisphere mantle. Nature, 309(5971), p. 753-757.

Henry, C.D., John, D.A., 2013, Magmatism, ash-flow tuff and calderas of the ignimbrite flareup in the western Nevada volcanic field, Great Basin, USA: Geosphere v.9; no.3; p. 951-1008.

Henry, C.D., McIntosh, W.C., McDowell, F.W., Lipman, P.W., Chapin, C.E., and Richardson, M.T., 2010, Distribution, timing, and controls of the mid-Cenozoic ignimbrite flare up in western North America: Geological Society of America Abstracts with Programs, v. 42, no. 5, p. 144.

Hawthorne, F.C., Oberti, R., Harlow, G.E., Maresch, W.V., Martin, R.F., Schumacher, J.C. and Welch, M.D., 2012. Nomenclature of the amphibole supergroup. *American Mineralogist*, *97*(11-12), p. 2031-2048

Hildreth, W., 1981, Gradients in silicic magma chambers: Implications for lithospheric magmatism: Journal of Geophysical Research, v. 86, p. 10,153–10,192.

Hildreth, W., and Moorbath, S., 1988, Crustal contributions to arc magmatism in the Andes of central Chile: Contributions to Mineralogy and Petrology, v. 98, p. 455– 489.

Hodges, K.V., Walker, J.D., 1992, Extension in the Cretaceous Sevier orogen, North American Cordillera: Geological Society of America Bulletin, v. 104 (5), p. 560-569.

Humphreys, E.D., 1995, Post-Laramide removal of the Farallon slab, western United States: Geology, v. 23, p. 987–990.

Humphreys, E., 2009, Relation of flat subduction to magmatism and deformation in the western United States: Geological Society of America Memoirs, v. 204, p. 85-98.

van Hunen, J., Van Den BERG, A.P., Vlaar, N.J., 2002, On the role of subducting oceanic plateaus in the development of shallow flat subduction: Tectonophysics, v. 352 (3), p. 317-333.

Hutton, J., 1794, II. Observations on Granite: Transaction of the Royal Society of Edinburg, v. 3 (02), p. 77-85.

Jarrard, R.D., 1986, Relations among subduction parameters: Reviews of Geophysics, v. 24(2), p. 217-284.

John, D. A., 1992, Geologic map of the Table Mountain quadrangle, Churchill County, Nevada: U.S. Geological Survey Miscellaneous Field Studies Map MF-2194, scale 1:24 000

John, D. A., 1994. Stillwater caldera complex and road log from Austin to Fallon, Nevada: U.S. Geological Survey Open-File Report 94 –193, p. 20–38.

John, D.A., Henry C.D., Colgan, J.P., Watts, K.E., 2014, $^{40}Ar/^{39}Ar$ and U-Pb Ages of Silicic Ignimbrites, Calderas, and Granitic Plutons, Southern Stillwater Range and Clan Alpine Mountains, Nevada: Linkages between Volcanic and Plutonic Rocks. Abstract 343-11 presented at GSA Annual Meeting in Vancouver, British Columbia.

John, D.A., 1995, Tilted middle Tertiary ash-flow calderas and subjacent granitic plutons, southern Stillwater Range, Nevada: Cross-sections of an Oligocene igneous center: Geological Society of America Bulletin, v. 107, p. 180–200.

Johnson, C.M., 1991, Large-scale crust formation and lithosphere modification beneath Middle to Late Cenozoic calderas and volcanic fields, western North America: Journal of Geophysical Research: Solid Earth, v. 96 (B8), p. 13485-13507.

Lowry, A.R., Ribe, N.M. and Smith, R.B., 2000. Dynamic elevation of the Cordillera, western United States. Journal of Geophysical Research: Solid Earth, 105(B10), p. 23371-23390.

Jones, C.H., Farmer, G.L., Unruh, J., 2004, Tectonics of Pliocene removal of lithosphere of the Sierra Nevada, California: Geol. Soc. Am. Bull., 116, p. 1408-1422.

Landon-Browne, A., 2016, Chemical Disequilibrium between Plagioclase Crystals and Host Magma (Pumice) Samples from the Elevenmile Canyon Caldera, Stillwater and Clan Alpine Mountains, Western Nevada (Bachelor of Science thesis). Carleton University, Ottawa, Ontario.

Leake, B.E., 1978. Nomenclature of amphiboles. The Canadian Mineralogist, 16(4), p. 501-520.

Le Maitre, R.W.B., Dudek, P., Keller, A., Lameyre, J., Le Bas, J., Sabine, M.J., Schmid, P.A., Sorensen, R., Streckeisen, H., Woolley, A. and Zanettin, A.R., 1989. A classification of igneous rocks and glossary of terms: Recommendations of the International Union of

Geological Sciences, Subcommission on the Systematics of Igneous Rocks (No. 552.3 CLA). International Union of Geological Sciences.

Lepage, L.D., 2003, ILMAT: an excel worksheet for ilmenite--magnetite geothermometry and geobarometry: Comput. Geosci, v. 29 (5), p. 673-678.

Livaccari, R.F., Burke, K., Şengör, A.M.C., 1981, Was the Laramide Orogeny related to subduction of an oceanic plateau?: Nature, v. 289 (5795), p. 276-278.

Mackin, J.H., 1960, Structural significance of Tertiary Volcanic rocks in southwestern Utah: American Journal of Science, v. 258 (2), p. 81-131.

Madsen, J.K., Thorkelson, D.J., Friedman R.M., Marshall, D.D., 2006, Cenozoic to Recent plate configurations in the Pacific Basin: Ridge subduction and slab window magmatism in western North America: Geosphere, v. 2 (1), p. 11-34.

Manley, C.R., Glazner, A.F., Farmer, G.L., 2000, Timing of volcanism in the Sierra Nevada of California: Evidence for Pliocene delamination of the batholithic root?: Geology, 28, p. 811-814.

Mann, P., Rogers, R.D., Gahagan, L., 2007, Overiview of plate tectonic history and its unresolved tectonic problems: Central America geology, resources and hazards, v. 1, p. 201-237.

Mann, P., 2007, Overview of tectonic history of northern Central America: Geological Society of America Special Papers, 428, p. 1-19.

McCarthy, T.C. and Douce, A.E.P., 1997. Experimental evidence for high-temperature felsic melts formed during basaltic intrusion of the deep crust. Geology, 25(5), p. 463-466.

McKee, E.H., 1970, Fish Creek Mountains Tuff and volcanic center, Lander County, Nevada: U.S. Geological Survey Professional Paper 681, 17 p.

McKee, E.H., 1971, Tertiary igneous chronology of the Great Basin of the western United States—Implications for tectonic models: Geological Society of America Bulletin, v. 82, p. 3497–3502.

O'Driscoll, L.J., Humphreys, E.D., Saucier, F., 2009, Subduction adjacent to deep continental roots: Enhanced negative pressure in the mantle wedge, mountain building and continental motion: Earth and Planetary Science Letters, v. 280 (1), p. 61-70.

Patiño Douce, A.E., 1995. Experimental generation of hybrid silicic melts by reaction of high-Al basalt with metamorphic rocks. Journal of Geophysical Research: Solid Earth, 100(B8), p. 15623-15639.

Patiño Douce, A.E., 1999. What do experiments tell us about the relative contributions of crust and mantle to the origin of granitic magmas?. Geological Society, London, Special Publications, 168(1), p. 55-75.

Parsons, T., McCarthy, J., Kohlery, W.M., Ammon, C.J., Benz, H.M., Hole J.A., Criley, E.E., 1996, Crustal structure of the Colorado Plateau, Arizona: Application of new long-offset seismic data analysis techniques: Journal of Geophysical Research: Solid Earth, v. 101 (B5), p. 11173-11194.

Peacock, M.A., 1931. Classification of igneous rock series. The Journal of Geology, 39(1), p. 54-67.

Pearce, J.A., 1996, A user's guide to basalt discrimination diagrams. Trace element geochemistry of volcanic rocks: applications for massive sulphide exploration: Geological Association of Canada, Short Course Notes, v. 12 (79), p. 113.

Perry, F.V., DePaolo, D.J. and Baldridge, W.S., 1993, Neodymium isotopic evidence for decreasing crustal contributions to Cenozoic ignimbrites of the western United States: Implications for the thermal evolution of the Cordilleran crust: Geological Society of America Bulletin, v. 105(7), p. 872-882.

Putirka, K. and Busby, C.J., 2007. The tectonic significance of high-K2O volcanism in the Sierra Nevada, California. Geology, 35(10), p. 923-926.

Raia, F. and Spera, F.J., 1997. Simulations of crustal anatexis: implications for the growth and differentiation of continental crust. Journal of Geophysical Research: Solid Earth, 102(B10), p. 22629-22648.

Proffett, J.M., Jr., 1977, Cenozoic geology of the Yerington district, Nevada, and implications for the nature and origin of Basin and Range faulting: Geological Society of America Bulletin, v. 88, p. 247–266.

Rapp, R.P. and Watson, E.B., 1995. Dehydration melting of metabasalt at 8–32 kbar: implications for continental growth and crust-mantle recycling. Journal of Petrology, 36(4), p. 891-931.

Ridolfi, F., Renzulli, A. and Puerini, M., 2010, Stability and chemical equilibrium of amphibole in calc-alkaline magmas: an overview, new thermobarometric formulations and

application to subduction-related volcanoes: Contributions to Mineralogy and Petrology, v.160 (1), p. 45-66.

Riehle, J.R., McKEE, E.H. and Speed, R.C., 1972: Tertiary volcanic center, west-central Nevada. Geological Society of America Bulletin, 83(5), p. 1383-1396.

Sawyer, D.A., Fleck, R.J., Lanphere, M.A., Warren, R.G., Broxton, D.E., and Hudson, M.R., 1994, Episodic caldera volcanism in the Miocene southwestern Nevada volcanic field: Revised stratigraphic framework, $^{40}Ar/^{39}Ar$ geochronology, and implications for magmatism and extension: Geological Society of America Bulletin, v. 106, p. 1304–1318.

Siebel, W., Schnurr, W.B., Hahne, K., Kraemer, B., Trumbull, R.B., van den Bogaard, P. and Emmermann, R., 2001. Geochemistry and isotope systematics of small-to medium-volume Neogene–Quaternary ignimbrites in the southern central Andes: evidence for derivation from andesitic magma sources. Chemical Geology, 171(3), p. 213-237.

Smith, R.L., 1979, Ash-flow magmatism: Geological Society of America Special Paper 180, p. 5-27.

Snell, K.E., Koch, P.L., Druschke, P., Foreman, B.Z., Eiler, J.M., 2014, High elevation of the 'Nevadaplano' during the Late Cretaceous: Earth and Planetary Science Letters, v. 386, p. 52-63.

Solano, J.M.S., Jackson, M.D., Sparks, R.S.J., Blundy, J.D. and Annen, C., 2012. Melt segregation in deep crustal hot zones: a mechanism for chemical differentiation, crustal assimilation and the formation of evolved magmas. Journal of Petrology, 53(10), p. 1999-2026.

Spera, F.J., Bohrson, W.A., 2001, Energy-constrained open-system magmatic processes I: General model and energy-constrained assimilation and fractional crystallization (EC-AFC) formulation: Journal of Petrology, v. 42 (5), p. 999-1018.

Sun, S.S. and McDonough, W.S., 1989. Chemical and isotopic systematics of oceanic basalts: implications for mantle composition and processes. Geological Society, London, Special Publications, 42(1), p. 313-345.

Thirlwall, M.F., 1991. Long-term reproducibility of multicollector Sr and Nd isotope ratio analysis. Chemical Geology: Isotope Geoscience section, 94(2), p. 85-104.

Timmermans, A.C., 2015, A Geochemical Study of Cenozoic Magmatism Along an East-West Transect from Central Great Basin, Nevada to the Ancestral Cascade Arc, California – A

Compositional Journey Over Space and Time (Doctoral Dissertation). Carleton University, Ottawa, Ontario.

Weis, D., Kieffer, B., Maerschalk, C., Barling, J., de Jong, J., Williams, G.A., Hanano, D., Pretorius, W., Mattielli, N., Scoates, J.S., Goolaerts, A., Friedman, R.M. and Mohoney, J.B.,2006, High-precision isotopic characterization of USGS reference materials by TIMS and MC-ICP-MS:Geochem. Geophys. Geosyst. 7, Q08006, doi: 10.1029/2006GC001283.

Winter, J.D., 2010, An Introduction to igneous and metamorphic petrology: New York: Prentice Hall.

Appendix 1 Supporting Tables

Table I: Sample Locations

Sample Number	Sample Description	Latitude	Longitude	Northing	Easting	Elevation (meters)
Collected Summer 2015		Nad 27		UTM Grid 11S		
15-CA-01	Granodiorite	39.3393	-118.1157	4354815	0403852	1409.7
15-CA-02	Pumice	39.3750	-118.0517	4358709	0409414	1836.7
15-CA-03	Tuff	39.3765	-118.0485	4358869	0409687	1949.5
15-CA-04	Tuff	39.3756	-118.0430	4358771	0410165	1893.1
15-CA-05	Tuff	39.3756	-118.0430	4358771	0410165	1893.1
15-CA-06	Pumice	39.3818	-118.0305	4359443	0411244	1949.2
15-CA-07	Tuff	39.3818	-118.0305	4359443	0411244	1949.2
15-CA-08	Pumice	39.3854	-118.0299	4359839	0411299	1933.7
15-CA-09	Pumice	39.3851	-118.0258	4359806	0411654	1841.9
15-CA-10	Pumice	39.3851	-118.0258	4359806	0411654	1841.9
15-CA-11	Pumice	39.3853	-118.0183	4359816	0412304	1764.8
15-CA-12	Hercules Tuff	39.3834	-118.0115	4359602	0412881	1703.2
15-CA-13	Tuff of Lee Canyon	39.6195	-118.2991	4386122	0388488	1459.1
15-CA-14	Tuff	39.6219	-118.2920	4386387	0389107	1496.3
15-CA-15	Unwelded Tuff	39.6219	-118.2920	4386387	0389107	1496.3
15-CA-16	Pumice	39.4103	-117.9607	4362545	417293	1823.9
15-CA-17	Pumice	39.4103	-117.9607	4362545	417293	1823.9
15-CA-18	Tuff	39.4099	-117.9595	4362499	417397	1828.8
15-CA-19	Tuff	39.4110	-117.9571	4362616	0417602	1863.9
15-CA-20	Tuff	39.4110	-117.9571	4362616	0417602	1863.9
15-CA-21	Pumice	39.4122	-117.9543	4362748	0417844	1890.1
15-CA-22	Pumice	39.4122	-117.9543	4362748	0417844	1890.1
15-CA-23	Tuff	39.4148	-117.9490	4363025	0418396	2025.1
15-CA-24	Tuff	39.4151	-117.9483	4363066	0418366	2013.2
15-CA-25	Vitropherous Rhyolite	39.4129	-117.9488	4362820	0418319	1975.4
15-CA-26	Tuff	39.4118	-117.9479	4362700	0418394	1959.3
15-CA-27	Pumice	39.4118	-117.9479	4362700	0418394	1959.3
15-CA-28	Vitrophyric Pumice	39.4095	-117.9500	4362443	0418212	1987.0
15-CA-29	Tuff	39.4095	-117.9500	4362443	0418212	1987.0
15-CA-30	Pumice	39.4084	-117.9498	4362322	0418230	2048.0
15-CA-31	Tuff	39.4084	-117.9498	4362322	0418230	2048.0
15-CA-32	Pumice	39.4103	-117.9515	4362531	0418079	1996.4
15-CA-33	Basal Vitrophyre	39.4101	-117.9513	4362512	0418105	1979.1
15-CA-34	Welded Tuff	39.4150	-117.9444	4363042	0418704	1924.8
15-CA-35	Pumice	39.4172	-117.9449	4363291	0418659	1908.4
15-CA-36	Pumice	39.3067	-118.0324	4351111	0410991	1481.3
15-CA-37	Altered Tuff	39.3126	-118.0362	4351771	0410669	1568.2
15-CA-38	Altered Tuff	39.3142	-118.0373	4351946	0410572	1563.6

Sample Number	Sample Description	Latitude	Longitude	Northing	Easting	Elevation (meters)
		Nad 27		UTM Grid 11S		
15-CA-39	Altered Tuff	39.3143	-118.0383	4351957	0410492	1572.2
15-CA-40	Argillite Chips	39.3146	-118.0392	4351994	0410410	1586.5
15-CA-41	Tuff	39.3144	-118.0391	4351978	0410417	1575.2
15-CA-42	Altered Tuff	39.3137	-118.0387	4351894	0410456	1593.5
15-CA-43	Tuff	39.8770	-117.8551	4380948	0426558	1951.3
15-CA-44	Tuff	39.5784	-117.8564	4381106	0426448	1966.6
15-CA-45	Tuff	39.5907	-117.9291	4382530	0420220	2429.3
15-CA-46	Pumice	39.5898	-117.9295	4382439	0420180	2417.1
15-CA-47	Tuff	39.5916	-117.9362	4382637	0419609	2350.9
15-CA-48	Tuff	39.5783	-117.9396	4381163	0419303	2311.6
15-CA-49	Tuff of Job Canyon	39.3807	-118.0797	4359368	0407008	1601.4
15-CA-50	Altered Tuff	39.3830	-118.0772	4359629	0407227	1635.6
15-CA-51	Tuff	39.3870	-118.0752	4360071	0407402	1674.9
15-CA-52	Job Canyon??	39.3905	-118.0764	4360458	0407301	1705.7
15-CA-53	Pumice	39.3927	-118.0761	4360699	0407330	1702.0
15-CA-54	Pumice	39.4642	-117.8722	4368442	0424964	1819.7
15-CA-55	Tuff	39.4661	-117.8695	4368654	0425202	1801.7
15-CA-56	Tuff	39.4720	-117.8558	4369295	0426390	1726.7
Intermediate lavas collected By Cousens and Timmermans						
04-LT-43	Andesite Flow	39.4420	-118.3490	4366610	383702	
04-LT-44a	Andesite Flow	39.4075	-118.3423	4362653	384434	
11-CN-11	Basaltic-Andesite Flow	39.5615	-117.8297	4379215	428721	

Samples provided by the USGS		Latitude Nad 27	Longitude Nad 27
H12-66	tuff of Incandescent Canyon, upper, middle of unit	39.8925	-119.6719
H12-67	tuff of Incandescent Canyon, upper, near base	39.8919	-119.6721
H12-68	tuff of Incandescent Canyon, lower, near top	39.8920	-119.6724
H12-69	tuff of Incandescent Canyon, lower, near base	39.8921	-119.6731
H12-181	base of outflow tuff above New Pass Tuff	39.5768	-117.5096

	Samples provided by the USGS	Latitude Nad 27	Longitude
15-DJ-15A	Vitrophyre in tuff of Desatoya Peak (tuff of Hercules Canyon)	39.3881	-117.7961
15-DJ-16	Hydrated vitrophyre in upper tuff of Desatoya Peak (tuff of Hercules Canyon)	39.3882	-117.7900
15-DJ-18	Vitrophyre in upper tuff of Desatoya Peak (tuff of Hercules Canyon)	39.3891	-117.7869
16-DJ-2A	well bedded shale, calcareous shale, and limestone; sample of limestone, mouth of Cox Canyon, Stillwater Range	39.6927	-118.2910
16-DJ-3	unit Trcs; calcareous shale/phyllite with minor limestone, Cox Canyon, Stillwater Range	39.6887	-118.2762
16-DJ-28	dark gray dolomite, east side of Chalk Mountain, unit Jd (Jurassic)	39.3209	-118.1173
16-DJ-29	dark gray fine-grained limestone (Jl), west side Clan Alpine Mountains	39.3321	-118.0795
16-DJ-30	black calcareous shale in Jurassic limestone, west side Clan Alpine Mountains	39.3330	-118.0733
16-DJ-31	fine-grained biotite granite, Alameda Canyon, Stillwater Range, Late Cretaceous	39.7153	-118.2039
16-DJ-33	black phyllite with andalusite porphyroblasts, unit Mzp, Sand Springs terrane; La Plata Canyon	39.4213	-118.2896
16-DJ-34	La Plata Canyon pluton, biotite granodiorite, Late Cretaceous; La Plata Canyon	39.4250	-118.2993
16-DJ-35	dark gray to black limestone, unit Trcl (Triassic); La Plata Canyon	39.4441	-118.3084
16-DJ-36	black argillite, unit Trca (Triassic); La Plata Canyon	39.4480	-118.3099
16-DJ-37	dark green finely porphyritic meta-andesite lava flow with abundant chlorite, unit Jmv (Jurassic(?)); La Plata Canyon	39.4838	-118.3117
16-DJ-38	coarsely porphyritic biotite granite, porph phase of Sand Springs pluton, Late Cretaceous; northern Sand Springs Range	39.1996	-118.3399

Table II: Thin Section Descriptions

Sample Number	15-CA-2	15-CA-3	15-CA-4	15-CA-5	15-CA-6
% Phenocrysts	20%	30%	35%	35%	25%
Plagioclase	60%, large independent euhedral crystals and clusters of medium to large anhedral grains. (300-2500um). Very heavily fractured, zoning is disturbed in every grain. Portions of grains have recrystallized into fine grain alteration products (focused on grain fractures).	55% euhedral grains and fragments (300-1500 um). Heavily fractured with a high degree of recrystallization of crystal cores and along fractures. Many grains show high An content (yellow), Complex zoning is often interrupted-shifted with dislocation along fractures.	60%, small to large euhedral grains and fragments (75-1200um). Large grains show completely recrystallized cores surrounded by clear oscillatory zone plagioclase, grains are moderately to heavily fractured, with little resorption of grain boundaries. Some fractures are infilled by glassy matrix, and minor dislocation of fragments effected some crystals.	45%, large euhedral to subhedral grains (500-2000 um). Very heavily fractured and recrystallized, most grains are beginning to dislocated with unsegregated fragments. Complex zoning is broken up by fragmentation\	60%, heavily fragmented euhedral grains (250-2000 um), both oscillatory and complex zoning. Many grains are missing cores, or have begun to dislocate fragments.
Quartz	20%, present only as grain fragments in clusters and small anhedral grains clustered with plagioclase. All grains are interspersed with fine grain alteration products.	25%, Anhedral/rounded crystals and fragments, almost all with concoidal fractured. Scattered as independent grains (150-450um).	25% small globules and rounded crystals (50-200 um). Moderately fractured with some concoidal grain edges, little to no resorption with no obvious embayment.	35%, large globules/ rounded anhedral fragments. Most with concoidal edges or seemingly pulled grains.	20%, heavily fractured rounded grains (200-600um)
Sanidine	none identifiable	5%, anhedral crystals and fragments found through plagioclase fractures/clusters (50-150um).	5%, small euhedral-subhedral (<100 um) grains found in "veins" or tracts through the section clustered around larger plagioclase crystals. Moderately fractured with little to no resorption	15%, large (up to 750 um), simple twins very heavily fractured with some exsolution laminae along cleavage planes. Little embayment of grain edges with rounding of grains.	5%, small subhedral (<100 um) grains found clustered and intergrown with plagioclase crystals. Moderate fracturing, no signs of resorption
Biotite	20%, euhedral sheets and lathes (200-600um in length). All grains show a degree of resorption, most sheets have frayed grain edges and are heavily embayed along the C-axis. Little to no kinking, but with the degree of resorption it is impossible to tell if they have been partially deformed	15%, sheets (up to 800 um in length). Heavily resorbed, grains show strong deformation and kinking. Minor amounts of trace CPX are present in cores of Bt grains.	10%, lathes (up to 300 um in length) strong degree of resorption, most sheets show missing fragments and frayed edges. Only a little kinking, but biotite grains are highly aligned throughout the section	5%, lathes and sheets (80-500 um in length). Little to no deformation/kinking, some oxidation rims and frayed grain edges. Alteration to a very fine grained high interference mineral (white mica) in places. Some overgrowths of oxides	20%, both independent crystals and clustered anhedral grains intergrown with plagioclase crystals around relict CPx fragments. Some overgrowths of oxide. Independent grains show some deformation, minor kinking.
Amphibole	none identifiable	none identifiable	none identifiable	none identifiable	none identifiable
Pyroxene	none identifiable	Trace, small fragments included in biotite grains.	none identifiable	none identifiable	5%, relict crystals and fragments. (50-500 um) Either partially resorbed into matrix or relict fragments in the core of biotite and feldspar clusters. None show intact crystal structures.
Accessory Phases	Trace monazite as independent rounded grains (150-250 um). No fracturing or resorption. Fe-Ti oxides are scattered, but most have begun to resorb into the matrix (brownish-fuzzy transition), some oxides are present as overgrowth on Bt grains	Scattered Fe-Ti oxides as independent rounded crystals, not all that prevalent	Very few oxides, present as globules (50-200 um) scattered throughout matrix	Scattered oxides, both independent rounded and subhedral crystals and overgrowing feldspars and biotite grains	Scattered oxides, both independent rounded and subhedral crystals and overgrowing biotite. Trace monazite included as rounded/subhedral grains included in biotite
Textures	No obvious deformation of matrix or realignment of grains	Minor kinking of biotite grains, but no obvious deformation direction or pulling of glass globules	Grains throughout the section are heavily aligned, probably compaction. Biotite shows a minor degree of kinking	Some degree of flow/compaction evident in the glassy sections of matrix	Minor kinking of biotite grains, but no obvious deformation direction or pulling of glass globules
Alteration	Matrix is heavily chloritized, most grains are rimmed in fine grain alteration minerals and oxides are being completely resorbed into matrix.	Matrix is heavily chloritized, lithic fragments show a mantle of quenched glass and have "cooked" outer rims	None visible, matrix is especially hypocrystalline(?) - no visible crystals	None identifiable	Biotite shows little signs of oxidation, but matrix looks unaltered

Sample Name	15-CA-7	15-CA-8	15-CA-9	15-CA-10	15-CA-11
% Phenocrysts	40%	40%	25%	35%	20%
Plagioclase	35%, medium sized (200-800 um) euhedral and rounded crystals and fragments. Most show resorption of edges and plucking of fragments along fractures. Many larger crystals show complex recrystallized cores and inclusions of Fe-Ti oxides in the rims outside of the recrystallized portions. Also occur as subhedral grains in clusters intergrown with biotite and oxide phases	30%, medium sized independent crystals (300-600 um). Weakly to moderately fractured, but heavily resorbed; most grains are not in equilibrium with the matrix and are severely dissolved/infilled along fractures and embayment. Also appears in complex intergrowths of Qtz, Sanidine and small anhedral plagioclase (<150 um) in clusters, these small crystals show no evidence of fracturing or resorption	55%, Large independent euhedral crystal fragments (500-1500 um) with both oscillatory and complex zoning. The oscillatory zoned crystals show a great degree of fracturing, most only remain as a fragment of a larger grain. Plagioclase also appears in small clusters, 150-250 um sized anhedral fragments, possibly the recrystallization of earlier larger grains (the small clusters seem to be spatially related to the fractured larger grains)	50%, very large (up to 5000 um) highly fractured crystals. Most have broken to the degree that interior crystal structure is entirely dislocated, complex zoning is interrupted/dislocated through fragments. Most grains show evidence of a recrystallized (complex crystal structure) core, and some grains evidence of mantling by a thin unidentifiable feldspar (probably an orthoclase rich rim).	25%, medium sized euhedral (at times cubic) phenocrysts (200-500 um) and rounded fragments. Heavily fractured, large phenocrysts show significant dislocation of fragments. Cores are commonly missing or recrystallized, complex zoning more common than oscillatory (very rare). Crystals that show oscillatory zoning are often a small fragment of a larger missing phenocryst (incomplete zoning ~1/4 of a grain for example)
Quartz	25%, medium to large (100-750 um) rounded globules and grain fragments. Most show concoidal fractures and moderate to heavy embayment (or crystals grew in glob like shapes). All are moderately fractured, with little to no dislocation of fragments	30%, anhedral and rounded (<100 um) crystals occurring in clusters with plagioclase and sanidine. Show no fracturing or resorption, resemble a very late stage phase	10%, very small rounded grains (<100 um) mostly concentrated around clusters of plag and sanidine. Little to no resorption only a minor degree of fracturing	15%, medium sized anhedral-rounded crystal fragments. Typically moderately fractured, most are remains of larger phenocrysts. Moderate degree of embayment/infilling occurs in select crystals	45%, large semi rounded euhedral crystals (400-800 um). Most are missing a good portion of the crystal or resemble a large phenocryst that has been significantly fragmented into pieces. Most independent crystals as well as the smaller fragments are moderately fractured with either infilling of void space with matrix or glass.
Sanidine	20%, small to medium sized (100-300 um) euhedral crystals. Commonly terminated, most grains are moderately to heavily fractures (missing an end). Present as independent phases, simple twins, very little to no resorption	40%, appear as both large (500-900 um) euhedral crystals that are heavily fractured, moderately dislocated and infilled by devitrified glass. Simple twins that follow a dislocated zonation through the crystal, and most of these large crystals are missing at least one of their original grain edges. And small, subhedral-anhedral crystals (<150 um) appearing in clusters with Qtz and Plag showing no fracturing or resorption. Simple twins are arrow straight through these small grains.	25%, larger subhedral-rounded phenocrysts. Lightly fractured- little to no resorption. As well as small number of sanidine crystals occurring in plagioclase clusters around larger fragmented plagioclases.	30%, very large highly fractured crystals (up to 3000 um). Fragments are dislocated and zoning is complicated by the movement of smaller fragments, recrystallization or "grinding-up" of crystals occurred along fracture paths (infilled by smaller phenocrysts and/or fragments). Contains inclusions of complex zoned plagioclase	25%, larger euhedral phenocrysts/fragments (200-1200 um). Moderately fractured with no resorption obvious. Inclusions of complex zoned plagioclase occur.
Biotite	10%, sheets and lathes (up to 500 um in length). Little to no deformation or kinking, no obvious alignment in the matrix, moderate degree of resorption into matrix (or plucking of fragments and subsequent infilling of void space with ash). Overgrowths of oxides are common	Trace, not in equilibrium with matrix, most sheets (up to 500 um) show evidence of fraying or resorption of crystal edges. Both a light yellow-brown pleochroic color, and a darker red-brown "oxidized" grain. No obvious kinking or deformation, no discernable alignment of biotite grains throughout section	10%, larger independent sheets and lathes (up to 1000 um). Typically heavily fractured missing crystal segments, minor oxidation/black rimming of crystals. Inclusions of apatite fairly common with trace zircon. Also appear in clusters of small to medium anhedral crystals around what could have been a relict Cpx crystal. Overgrowths of oxides occur	5%, euhedral to subhedral sheets and lathes (up to 400um in length). Most show fraying of crystals ends, with significant resorption textures in some fractured crystals. Most crystals are kinked (up to 45 degrees), no obvious inclusions.	5%, varying sized lathes and sheets (50-800 um), most are moderately fractured/frayed with infilling by matrix glass. Inclusions of apatite and zircon occur as well as overgrowths of oxide phases. Occur at times in the crystal-shape of Hbl crystals as a complete pseudomorph. Only slight kinking/deformation which is more obvious in the elongate lathes as opposed to sheets
Amphibole	Trace, as only grain fragments , little resorption but severe fracturing. Many retain some degree of diamond-shaped cross-section, commonly only half or a quarter of grain remains	none identifiable	none identifiable	none identifiable	Completely pseudomorphed by biotite grains or resorbed by matrix - retained diamond-shaped cross section
Pyroxene	none identifiable	none identifiable	none identifiable	none identifiable	none identifiable
Accessory Phases	Scattered oxides both as independent phases and overgrowing biotite grains, also found in clusters of biotite and plagioclase crystals. Most are rounded/globules (up to 200 um)	Zircon exists as moderate-heavily fractured independent crystals (<100 um). Euhedral prism shape is intact typically missing one end of the crystal. Very few small rounded oxides (<80 um) found scattered throughout matrix.	Very few scattered Fe-Ti oxides (50-300 um). Most commonly spatially associated with plagioclase crystals (either as inclusions or overgrowths).	Few oxides as rounded grains/globules (up to 250 um). Only present as independent crystals, not overgrowing any other phases. Commonly rimmed by a brown discoloration of matrix glass. Trace zircon in matrix as euhedral fragments	Significant amount of zircon grains scattered through matrix and included in biotite crystals. Euhedral, terminated prisms (~50 um). Rounded oxides (50-250 um) present scattered throughout matrix and often overgrowing Bt grains.
Textures	Ashy matrix shows little deformation around feldspar phenocrysts (probably due to compaction), biotite crystals show no obvious alignment or kinking	Matrix has begun to devitrify, clusters of qtz plag and sanidine have crystalized along veins/pulled glass(?). The matrix shows some degree of compaction, consistent with the direction of these crystalline pockets.	Matrix shows no evidence of compaction or deformation. Biotite crystals are weakly deformed seemingly due to contact with more resistant crystals	Biotite grains are deformed but matrix shows little to no evidence of deformation or flow	Matrix glass shows some evidence of a deformation direction (i.e. compaction), crystals are weakly-moderately aligned in this direction (especially Bt crystals)
Alteration	None identifiable	None identifiable	None identifiable	Oxides are rimmed by a brown discoloration of the matrix (Fe-leaching?)	None identifiable

Sample Name	15-CA-12	15-CA-13	15-CA-14	15-CA-15	15-CA-16
% Phenocrysts	45%	40%	30%	50%	25%
Plagioclase	50%, small to large sized euhedral crystals and fragments (50-1000 um). Complex zonation that is commonly dislocated, most grains are highly fractured with missing crystal segments. Cores are commonly missing or complexly recrystallized. Few fragments show oscillatory zoning, but most of these are incomplete fragments of much larger missing crystals	45%, medium sized (200-1000 um) euhedral and subhedral crystals and partial fragments. Commonly complex zoned with interruptions by crystal fracturing. Some grains are heavily embayed and infilled with matrix. Cores occasionally look recrystallized and in a small number of crystals the cores are missing. Intergrowths with Hbl occur	40%, medium to large euhedral fragments and few complete grains (250-800 um). Very heavily fractured, most crystals are only fragments of larger phenocrysts. Complex zoning, with few number of cores being oscillatory zoned. Little to no resorption or recrystallization, but fractured are often infilled with matrix. Often show exsolution textures along cleavage	60%, small to medium euhedral grains and euhedral-rounded fragments (75-800 um). Many of the larger phenocrysts are oscillatory zoned but only represent 1/4-1/2 of a larger missing crystal. Smaller phenocrysts are typically complex zoned with polysynthetic twins. All plagioclase are moderate to highly fractured but little evidence of resorption.	65%, Euhedral independent grains and clustered anhedral crystals, (100-2500um). Almost all are complex zoned with only a very small number showing oscillatory zoning. Moderate to highly fractured with little to no crystal dislocation. Seemingly An rich (yellow). Crystal fractures have been infilled with holocrystalline matrix.
Quartz	15%, anhedral to rounded crystals and fragments (200-800 um) moderately fractured along a single direction with infilling by glass. Little to no resorption or embayment. Many of the fragments have a triangular crystal shape - related to the grain they were fragmented from (?)	10%, small (<150 um) concoidal fragments and rounded crystals. Only slightly fractured, no obvious recrystallizing, minor infilling with glass and no visible resorption/embayment	15%, small anhedral/rounded fragments (50-200 um). Very heavily fractured, most have concoidal grain boundaries. Little to no resorption or embayment visible.	10%, medium sized (150-750 um) rounded grains and angular crystal fragments. Most have concoidal grain edges and look to be fractured pieces. Moderate to highly fractured, most crystals are dissected by fractures but little dislocation occurred. No obvious resorption textures	25%, small (<250 um) anhedral/globular crystals with rounded grain boundaries. Most grains show concoidal fractures along grain edges, very little embayment
Sanidine	25%, medium sized euhedral crystals (200-500 um). Moderately fractured with uneven grain surfaces, simple twins, little to no dislocation or embayment of grains. Also appears a small (<150 um) independent crystals.	25%, rounded subhedral to anhedral grains (200-600 um). Exsolution laminae along cleavage, weakly to moderately fractured most grains are missing segments from the grain edges. Often the simple twins are interrupted by the fracturing of grains	35%, medium sized (200-600um) subhedral-anhedral grains and rounded fragments. About half the phenocrysts are unzoned, the other half show simple Carlsbad twinning. Highly fractured, most grains show unever crystal edges. Exsolution has occurred along cleavage direction.	25%, smaller subhedral grains and crystal fragments (200-400 um). Most are heavily fractured, little to no embayment/resorption textures. Few grains show exsolution along cleavage plane	5%, (150-300um), subhedral/rounded grains. Very little fracturing, simple twins are consistent.
Biotite	5%, highly frayed lathes and sheets (200-500 um). Complex dissolution and fracturing, with significant infilling by ashy matrix. Few inclusions of apatite, little to no overgrowths of oxides.	10%, medium sized lathes (up to 600um in length), one end of crystals are commonly resorbing into the matrix. Inclusions of apatite, with a rim of fine grained minerals and tiny oxide phases.	10%, lathes (up to 400 um in length). Most are highly fractured with uneven endgrains (broken not frayed). Many grains have no internal structure and have altered to a darker red-brown color. Overgrowths of oxides due occur, but are relatively rare compared to other sections. Little to no deformation or kinking.	5%, euhedral lathes (up to 750 um). Little to no resorption or fracturing. Inclusions of apatite and zircon. Smaller lathes show evidence of bending, but majority are undeformed. No oxide overgrowths	5%, Sheets and books (up to 1200um in length). Most show patchy compositional differences (reddish patches) with frayed crystal edges. Some show black alteration along rims.
Amphibole	5%, euhedral/rounded crystals (50-2000 um). Most retain diamond cross section, but are significantly fractured and reacted. Larger phenocrysts are missing cores, with overgrowths of biotite in cores and rims of grains. Smaller crystals have little to no overgrowths, are weakly-moderately fractured and remain euhedral crystals that look to be in equilibrium.	10%, small to large euhedral crystals (200-1000 um) with good diamond cross sections. Highly fractured with significant recrystallization and infilling by matrix glass, most are missing cores. Some overgrowths with oxide phases	Trace, euhedral diamond shaped grains (300-500 um). Moderately fractured, inclusions of apatite and biotite with biotite and oxide overgrowths as well.	none identifiable	Trace as partially resorbed crystals. Missing core, and recrystallized margins. Crystal looks unzoned.
Pyroxene	none identifiable	Trace Cpx as small fragments (<150 um)	none identifiable	none identifiable	Trace orthopyroxene as unaltered, euhedral, grains with no resorption evident. (~500-1000um).
Accessory Phases	Oxides are present as independent rounded crystals and clusters (50-300 um) scattered around matrix. Comparably a few number compared to other sections	Large number of oxides (50-500 um) commonly overgrowing amphiboles but also present as rounded independent crystals throughout matrix. Some number are included by a brown halo in the matrix	Scattered oxides as overgrowths and independent rounded crystals and globules (up to 300um).	Zircon and apatite crystals are found as inclusions in biotite grains, and zircon is also present as independent small euhedral prisms (<100 um) scattered in few numbers through the matrix. Very few numbers of oxides, little evidence of them overgrowing the mafic phases.	Trace independent zircons, lots of independent Fe-Ti oxides present as euhedral crystals up to 750um in length
Textures	Matrix shows little evidence of a consistent deformation direction, but matrix is deformed around larger phenocrysts. Biotite grains show no evidence of realignment or kinking	Spherulites present in glassy pockets. The matrix shows deformation with most crystals aligned along this direction. Biotite grains are aligned, but don't show any kinking/bending	Matrix has devitrified, little to no alignment of crystals, no deformation/kinking of biotite	Matrix is crystalline-composed of tiny qtz, plag and sanidine crystals. Biotite shows some deformation in thin lathes but overall little obvious bending. Matrix is not compacted	Some deformation of glass (i.e. compression/pulling). Realignment and kinking of some biotite grains
Alteration	None identifiable	None identifiable	None identifiable	None identifiable	Matrix looks hydrated/hypohyaline ash

Sample Name	15-CA-17	15-CA-18	15-CA-19	15-CA-20	15-CA-21
% Phenocrysts	20%	30%	25%	30%	30%
Plagioclase	65%, as both large highly fractured phenocrysts and intergrown anhedral clusters. Most look to have complex zoning. Large phenocryst are significantly resorbed, commonly missing cores and with large pits and embayment along grain edges. Up to 3000um in length	60%,complex zones subhedral clusters and euhedral independent crystals (200-1500um). Moderately fractured, no embayment or sieve textures, Contains inclusions of biotite and zircon. Some crystals are oscillatory zoned (larger phenocrysts), typically missing a core are sometimes overgrown by a second plagioclase showing polysynthetic twinning.	45%, euhedral grains and sharp crystal fragments (200-750 um). Highly fractured, dislocated grains. Little resorption, but most are missing a significant fraction of the crystal. Most grains have polysynthetic twins, but very few show oscillatory zoning.	55%, large euhedral crystals (up to 1500 um) and medium sized euhedral-subhedral clusters (200-500 um). Larger grains are typically oscillatory zoned but highly fractured, many show significant dislocation of grain fragments. Generally missing cores or a large portion of the grain's interior; a very fine grained mantle of another feldspar coats a few large grains. The smaller clusters are typically complex zoned with polysynthetic twins, appear to have grown from globules/pockets. Little evidence of resorption of these smaller grains, they are also significantly less fractured than larger phenocryst	60%, concentrated in clusters of smaller complex zoned crystals with the occasional large independent euhedral grain. Larger grains are highly fractured and some show antiperthitic textures.
Quartz	15%, 200-700um in size, anhedral crystals and fragmented sections, show undulous extinction with typically concoidal grain edges and minor embayment textures	10%, medium sized (150-750 um) angular crystal fragments. Most have concoidal grain edges and look to be fractured pieces. Moderate to highly fractured, most crystals are dissected by fractures but little dislocation occurred.	10%, small (100-300 um) rounded grains and fragments. Highly fractured and dislocated, most are just fragments of larger grains. Concoidal/uneven grain edges, but no dissolution textures.	15%, small to large sized (200-1000 um) rounded and angular crystal fragments. Moderately fractured, these fractures seem to be concentrated in one direction. Little to no embayment/resorption, these quartz crystals do not look like they crystalized in globules as in other sections.	15% Large to medium sized globular/euhedral crystals (up to 1500um). Moderately fractured with few fluid inclusions as well as small sanidine crystals. Many show grain deformation with irregular/blocky extinction patterns
Sanidine	5%, presumed to be small fractured grains <100um due to lack of complex twining with feldspar cleavage .	25%, euhedral grains and crystal fragments. Some appear in small clusters but more are medium sized independent grains (200-500um) Twinning is often disrupted by crystal fractures. No obvious resorption. One grain was found overgrowing the relicts of a pyroxene crystal, which was almost completely dissolved.	35%, euhedral-rounded grains and fragments (150-600 um). Moderate to highly fractured, larger phenocrysts are missing a large number of segments. Small fractures are filled with a mix of very fine crystals (high relief). Minor exsolution along cleavage.	25%, euhedral-rounded/fragmented crystals (50- 200um). Independent crystals and fragments found scattered through matrix, seem to be a late crystalizing phase (less fractured than Qtz, plag), no signs of resorption	10%, up to 500um. Included in larger globule quartz crystals. Look to have grown as subhedral-anhedral grains.
Biotite	15%, largely undeformed sheets and books (up to 3000um). Minor kinking in a few. Most crystals look pristine with reddish patches. Inclusions of apatite are common	5%, sheets and lathes (200-1000um). 2 different crystals a dark red-brown crystal, that shows significant resorption, infilling of matrix and a rim of fine grained alteration products. Light-brown beige biotite shows little dissolution or fracturing, most grains are fully intact with only minor fraying on grain ends. Inclusions of apatite occur , with very few oxide overgrowths. Only minor degree of bending/kinking	5%, euhedral sheets and lathes (50-600 um). Most are not fractured but show significant resorption. Alteration rims of black fine grained material along most grain edges. Some kinking of the thinner lathes (realigned along with compaction direction). Inclusions of apatite, and alanite	5%, mostly as sheets (200-600 um). Lathes show significant kinking (up to ~35 degrees). Most grains have frayed endgrains with a fine grained black alteration rim. Inclusions of zircon common, apatite less so. Overgrowths of scattered small oxides cover most biotite grains	10%, appear as sheets and needles up to 500um in length. Most grains are euhedral but show evidence of in equillbrium with matrix (i.e. partial to almost complete resorption or patchy grain boundaries
Amphibole	Present only in trace amounts overgrowing cpx	Trace, small euhedral crystals and fragments (diamond and triangle shaped, 75-250 um). Overgrown by oxides	Trace, single grain not in equilibrium. Higher dissolved/resorbed.	Trace hbl, relict fragments (100-200 um). Rimed with thin rim of a fine grained brown mineral (probably mica/biotite), just small rounded and angular fragments remain. Often overgrown by oxide phases	5%, up to 500 um, euhedral and terminated prismatic crystals. Moderately fractured, with inclusions of Fe-Ti oxides and minor rim of biotite in place
Pyroxene	5%,CPX as independent euhedral crystals and in clusters with overgrowing biotite. (up to 1500um in length)	Trace, single relict crystal. Highly resorbed and fractured. No obvious overgrowths	none identifiable	none identifiable	none identifiable
Accessory Phases	Large oxides (up to 1500um), apatite inclusions in biotite grains and the rare independent zircon crystal	Trace alanite and trace zircon both as independent phases through the matrix and included in biotite crystals. Small number of fe-ti oxides as cubic crystals and rounded globules (25-150um) found mostly as independent crystals but few occur overgrowing biotite grains	Trace zircon as independent crystals, trace alanite and apatite included in biotite crystals	Trace zircon as independent crystals and inclusions in biotite grains, trace apatite in biotite crystals and scattered oxides (50-100 um) common as overgrowths of biotite and amphibole also present as rounded globules throughout matrix	Fe-Ti oxides present and show subhedral crystal shapes (50-300um). Some opaque minerals have distinctive cubic crystal habit.
Textures	Ashy matrix shows little deformation, only very slight kinking of biotite	Matrix shows evidence of deformation, ash looks pulled and compacted around phenocrysts. Biotite doesn't show major deformation, grains are not aligned.	Glassy matrix shows evidence of deformation (i.e. compaction) mineral grains are realigned along this plane, biotite shows some kinking. Lots of examples of matrix being deformed around a phenocryst.	Matrix shows signs of deformation (compaction), matrix glass is deformed around phenocrysts with a weak to moderate alignment of crystal phases. Biotite shows some kinking	Little to no deformation, matrix looks static. No pulling apart of grains other than "in place" fracturing
Alteration	Matrix looks only slightly hydrated	Matrix looks ashy, not necessarily hydrated	None identifiable	None identifiable	Matrix looks a little fuzzy, but no grains show secondary rimming or major resorption textures

Sample Name	15-CA-22	15-CA-23	15-CA-24	15-CA-25	15-CA-26
% Phenocrysts	35%	40%		40%	45%
Plagioclase	80%, both concentrated in complex clusters of smaller grains (<1000 um) and as very large, heavily fractured grains (2000-3000 um). Few grains show antiperthitic intergrowth along cleavage fractures. Many crystals show high An content (yellow).	60%, euhedral crystals, moderate to heavily fractured, little to no resorption	50%, euhedral crystals. Minor to moderate fracturing.	45%	60%
Quartz	10% Medium sized 200-600um sized globular/anhedral grains. Very rounded, moderate to heavily fractured but fragments remain in place. No obvious inclusions	15%, subhedral to rounded grains. Minor to moderate embayment	15%, rounded crystals and globules. Most show fractured grain edges and moderate degree of resorption	20%	10%
Sanidine	Only present as little antiperthitic laminae filling cleavage fractures in few plagioclase grains	20%, euhedral to subhedral grains. Moderately fractured	25%, euhedral crystals minor to moderate fracturing	25%	20%
Biotite	10%, lathes up to 800um. Little to fracturing or kinking, but few crystals are completely replaced by brown/black "fuzz" (oxidation?)	5%, lathes and sheets. Moderate kinking	10%, no evidence of kinking. Lathes and sheets.	10%	10%
Amphibole	There are apparent amphibole lathes present completely pseudomorphed/resorbed into glass. Only appear as a black/brown fuzz in the shape of a hornblende crystal	Trace	none identifiable	Trace	none identifiable
Pyroxene	none identifiable	none identifiable	none identifiable	Trace Cpx	none identifiable
Accessory Phases	Few Fe-Ti oxides present as independent crystals with few overgrowing biotite crystals. Few apatite and zircon crystals included in biotite, as well as visible radiation damage surrounding small high relief mineral (zircon/monazite)	none	none		
Textures	Small degree of deformation in biotite grains, no obviously deformation of matrix.	Matrix seems undeformed, biotite crystals show kinking	Matrix shows no evidence of deformation, biotite crystals are undeformed		
Alteration	Matrix looks glassy/ashy with no discernible crystals (sign of hydration?)	None identifiable	None identifiable		

Sample Name	15-CA-27	15-CA-28	15-CA-29	15-CA-30	15-CA-31
% Phenocrysts	30%	25%	45%	45%	45%
Plagioclase	70%, extremely large (2000-3000um) euhedral/rounded grains that are extremely heavily fractured and dislocated. Some exsolution laminae present	50%, medium sized grains (200-500um). Euhedral but subsequently rounded, heavily embayed to the point some grains look mymikitic. Most are complex zoned with high An contents (yellow). Heavily fractured	55%	65%, mostly concentrated as anhedral medium to small sized crystals (50-250um) in feldspar rich clusters/veins. These small crystals show little to no fracturing, but most have uneven grain edges (potentially fractured from larger crystal). Less common are large independent euhedral plag, showing both complex and oscillatory zoning. Larger crystals are also only moderately fractured with little to no embayment/resorption textures.	55%
Quartz	10%, rounded/subhedral grains (100-300um). Found in clusters with feldspars.	5%, very small globules (<100um). Heavily fractured and resorbed, could easily be misidentified plagioclase	10%	10%, small rounded/globule crystals (100-300um). Moderately fractured, with little to no resorption	10%
Sanidine	10% Found as tiny euhedral crystals (50-150um) in clusters with plagioclase feldspar. No evidence of fracturing or resorption	none identifiable	20%	15%, very large (up to 2.5 mm) independent euhedral grains as well as scattered as very small crystallising feldspar-rich veins through the section. Large grains show some evidence of mechanical stress (i.e. deformation of simple twins) as well as cleavage fractures infilled with perthitic plagioclase in places.	20%
Biotite	10%, euhedral lathes(up to 500um in length) many show significant resorption, Little to no fracturing or deformation	15%, Most common as fragments of grains (100-200um in size) with both rounded and euhedral grain edges. Found intergrown with amphibole crystals	10%	10%, euhedral/subhedral sheets and euhedral lathes up to 300um in length. Most are bent significantly and show a degree resorption into the matrix. Inclusions of apatite and monazite are common	5%
Amphibole	Trace, almost entirely recrystallized/resorbed into matrix	25%, both fragments of euhedral crystal and rounded grains (50-600um in length). Intergrown with Bt in places and occasionally overgrown by oxides. Found spatially close to relict cpx crystals. Moderate to heavily fractured but no resorption.	Trace	None identifiable	10%
Pyroxene	none identifiable	5%, only present as relict fragments typically overgrown with Hbl and oxides or very heavily fractured partial grain fragments.	none identifiable	Trace CPx as 90% resorbed/recrystallized phase	none identifiable
Accessory Phases	Scattered Fe-Ti oxides as independent rounded crystals. Monazite and trace zircon as inclusions in biotite	Abundant Fe-Ti oxides are rounded crystals appearing as independent phases throughout the matrix but occasionally overgrowing Hbl and relict pyroxene crystals	5% Fe-Ti oxides	Abundant Fe-Ti oxides are rounded/cubic crystals mostly appearing as independent phases throughout the matrix but occasionally overgrowing Bt and relict pyroxene crystals	
Textures	No obvious deformation of matrix, biotite show little to no bending	No obvious deformation of matrix, biotite show some kinking		Biotite grains are deformed but matrix shows little to no evidence of deformation or flow	
Alteration	Matrix looks partially devitrified	Matrix is glassy (to the point it looks like a dull brown fuzz)		Biotite crystals are heavily oxidized and matrix has lost all crystallinity (resembles fuzzy glass)	

Sample Name	15-CA-32	15-CA-33	15-CA-34	15-CA-35	15-CA-36
% Phenocrysts	35%	25%	40%	25%	35%
Plagioclase	70%, range from 200-2500um. Most grains are moderately fractured euhedral grains, both oscillatory and complex zoning are about equal proportions of the entire population. In one place plagioclase has completely enclosed a relict CPx crystal that is almost completely resorbed. Some grains show extreme embayment, almost look partially remelted or globular	60%	50%, sieve textures	70%, appears in complex clusters of medium to small sized euhedral to subhedral grains. Most are heavily fractured and fragmented, complex zonation is broken by fracturing.	55%
Quartz	10%, 100-500um. Heavily fractured rounded/anhedral grains. Look like globules.	10%	10%	15%, highly fragmented subhedral grains or rounded globules. Clustered amongst feldspar gains	15%
Sanidine	None identifiable, could be small fractured grains <100um or present in complex clusters of feldspar crystals.	15%	15%	5%, <100 um euhedral grains clustered with quartz and plagioclase grains. Little fracturing, no resorption. Simple twins	20%
Biotite	15%, euhedral sheets/fragments up to 800um in length. Heavily oxidized with black rims, commonly overgrown by Fe-Ti oxides. Little to moderate kinking, but not necessarily realignment.	15%	15%	10%, euhedral sheets and lathes (up to 500 um in length). Most are deformed and slightly bent, with little oxidation or resorption. Aligned with pulling of glassy matrix.	10%
Amphibole	Trace, 2 identifiable crystals	none identifiable	10%, replacing cpx grains	None identifiable	none identifiable
Pyroxene	5%, clinopyroxene left as small fragments (150-250um) that are almost completely resorbed. In places the remains of CPx grains are poikilitic inside plagioclase crystals. 1 grain of partially resorbed Opx	none identifiable	none identifiable	none identifiable	none identifiable
Accessory Phases	Globular monazite crystals in a cluster with biotite grains, abundant Fe-Ti oxides as overgrowing crystals as well as independent grains (all are rounded)	Trace monazite	Few Fe-Ti oxides present as independent crystals with an additional few overgrowing biotite crystals.		Globular monazite crystals in a cluster with biotite grains, abundant Fe-Ti oxides as overgrowing crystals as well as independent grains (all are rounded)
Textures	No obvious deformation of matrix, biotite show some kinking			Ashy matrix shows some deformation, compaction or pulling with realignment of biotite grains	
Alteration	Groundmass looks glassy /"fuzzy", biotites are heavily oxidized.	unaltered	little to none		Groundmass looks glassy/"fuzzy", biotite is heavily oxidized.

Sample Name	15-CA-37	15-CA-38	15-CA-39	15-CA-41	15-CA-42
% Phenocrysts	25%	25%	40%	35%	35%
Plagioclase	60%	60%, range from 200-2000um, most grains too fractured to see twinning, some embayment but mostly fractured surfaces, euhedral-anhedral grain shapes	70%, range from 150-3000 um. Grains are extremely fractured and in places completely broken and infilled with hydrated glass, most remain euhedral in shape with very minor degrees of resorption on grain edges. Some intergrowth with biotite inside grain boundary	65%, moderate to heavily fractured grains from 50-2000 um in length most are subhedral with the occasional rounded/euhedral grain. Minor embayment/resorption with most grain edges being fractured instead. Some grains contain completely recrystallized plagioclase core.	80%, mostly subhedral-anhedral grains with occasion anhedral grain (typically anorthite rich (yellow)). Lots have grains have fractured with recrystallization along the channels opened by fracturing. Few grains show extreme fracturing, with the crystal structure of plagioclase completely reorganized (twins look very disorganized)
Quartz	10%	15%, 100-600 um, heavily fractured, anhedral grains, no resorption but most surfaces are uneven due to fracturing	5%, <150um in length anhedral grains with minor degrees of fracturing/resorption. Very hard to distinguish from small plagioclase grains	5%, 100-200 um in length. Rounded grains with little evidence of resorption/fracturing	5%, small rounded/anhedral grains. <100um in size. Occur scattered through matrix
Sanidine	15%	10%, 100-200 um, very minor phase, highly fractured with alteration to clay phases visible	5%, moderately-heavily fractured <150um in length. Could be misidentifying plagioclase. Can't see distinctive Carlsbad twins	20%, lathes 50-200 um in length along channels within flow structures. Perfectly euhedral grains, with no fracturing or alteration . Only appear clustered in two groupings in section	None identifiable, could be small fractured grains <100um .
Biotite	15%	15%, kinked lathes, 300-600um in length, most show missing centers (looks resorbed) exposing glassy/ashy matrix	15%, almost completely resorbed lathes, minor kinking, up to 2500um in length. Overgrowing amphiboles in place, most grains were plucked/resorbed and pass clear through thin section	10%, sheets up to 300 um in length. Deformed/kinked most grains have realigned in relation to matrix. Reddish cores present in few grains with typical brown/yellow outer sections. All biotite show black very fine grain edge boundaries, possibly related to interactions with matrix.	10%, 200-400um in length appear as sheets/lathes. Show blackened/altered grain boundaries, and some deformation/kinking.
Amphibole	Trace	Trace, almost entirely pseudomorphed	5%, 200-400 um in length, all partially resorbed with overgrowths of FeTi oxides and biotite, show little evidence of fracturing and remain euhedral in shape.	Trace, one grain that looks like hbl grain shape completely pseudomorphed into fine grain "garbage". Looks like micas/matrix-ish glass.	5%, euhedral-pseudomorphed crystals 300-500um in length. Alteration is to a very fine grain brown phase or completely resorbed with biotite/FeTi overgrowths and plucked cores.
Pyroxene	Trace	**None**	**None**	**None**	None
Accessory Phases	**None**	none	Lots of FeTi oxides overgrowing resorbed amphiboles and present throughout matrix	Some FeTi oxides present, as well as one opaque that is red under ppl	FeTi Oxides present throughout the section showing orange halos/surrounding alteration of the matrix. Trace zircons
Textures		Flow banded pumice, pulled fiamme, euhedral to anhedral grains	Some flow evident in matrix, but primarily just hydrated glass. Parts of section show broken unidentifiable lithics and groupings of small mineral phases	Minor banding, biotite have been re-aligned but other grains don't show mechanical interactions with matrix. Glass looks pulled/compressed in places.	Lots of flow texture in the glass, elongation/realigned amphiboles and biotite with channels and pulled glass around more resistant phases.
Alteration		Heavily Altered/hydrated, alteration to micas observable in some feldspars/biotite, orange-brown alteration halos surround fine grained unidentifiable lithic fragments	hydrated glass and brown-ish halos around lithic fragments. Little micaceous alteration of primary phases, but most phases show overgrowths of secondary minerals	Matrix has transitioned to the "fuzzy grey/brown" that is possibly related to hydration	Fuzzy brown matrix

Sample Name	15-CA-43	15-CA-44	15-CA-45	15-CA-46	15-CA-48
% Phenocrysts	30%	45%	40%	45%	20%
Plagioclase	75%, 200-800um, 2 groups of plagioclase types. 1st group is the larger phenocrysts, subhedral, with minor embayment, but crystal has become very fine grained with little organization. 2nd group is smaller and more euhedral and complete grains with some twinning but significant embayment/ resorption of grain edges.	75%, 50-2500um, Similar to the last thin section, 1 group of smaller unaltered plag that are ~subhedral, with embayment along grain boundaries and the second larger group of plagioclase that are reorganized into medium-fine grain crystals along with a great degree of fracturing.	80%, 200-800um, euhedral-subhedral grains. Most show fracturing/angular grain edges with some plucking and refilling of void space with matrix. A small number of grains show exsolution textures (antiperthitic). No obvious resorption or overgrowth textures	70%, 200-1500um, euhedral to subhedral grains. Some are heavily fractured, others are near pristine. Minor embayment/resorption of the fractured crystals. Some grains show antiperthitic texture. Scattered through matrix with 2 clusters of intergrown small-medium sized grains.	50%, Complex twins, euhedral grains, exsolution rims (?)
Quartz	5%, rounded/anhedral grains 50-200um in length. Most show concoidal grain edges	5% rounded-anhedral grains, moderate to heavily fractured. 50-150um in length. Appear scattered through matrix with 1 concentration in a glass flow-channel.	5%, 50-100um in size. Fully rounded grains, no resorption or fracturing. Scattered throughout matrix.	15%, 50-1000um, either v. heavily embayed or myrmekitic. Intergrown with plagioclase	5%, present as subhedral/ globules
Sanidine	5%, moderately fractured <100um in length. Could be misidentifying plagioclase.	None identifiable, could be small fractured grains <100um .	5%, lathes ~50um in length. Carlsbad twinning visible, concentrated in one section of glass.	5%, 100-200um. Moderate to weakly fractured. No resorption textures	30%, good twinning. Some minor exsolution laminae visible (pethitic)
Biotite	15%, in lathes and sheets. Significant deformation and dissolution of sheets. 200-800um in length, bent around plagioclase and deformed with glass flow. Plenty of Fe-Ti oxides have overgrown all grains.	5%, lathes 200-250um in length, little fracturing or deformation but they do align with glass channels. Some evidence of overgrowing of Hbl by biotite in a few cases. Biotite are overgrown by FeTi oxides	10%, lathes 200-600um in length. Sheets have deformed/resorbed edges, altered to fine-grain black boundary found in other sections. Little to no overgrowth by Fe-Ti oxides, but they are present as proximal phases.	10%, lathes and tabular grains up to 800um in length. Containing inclusions of apatite. Most show resorption of grain boundaries, no typical "black-alteration". Overgrowths of FeTi oxides	15%, larger sheets and lathes, moderate to heavily deformed.
Amphibole	None identifiable	10%, 150-250um, heavily resorbed/fractured. Overgrown with Fe-Ti oxides.	None identifiable	None identifiable	none identifiable
Pyroxene	none identifiable	none identifiable	none identifiable	none identifiable	none identifiable
Accessory Phases	FeTi oxides present. Overgrowing biotite and intergrown with plag, in globules within glass channels and scattered through matrix.	Relict CPX-overgrown by amphiboles which subsequently were resorbed and overgrown by FeTi oxides	Fe-Ti oxides present and show subhedral crystal shapes (50-300um).	Small Fe Ti oxides (50-100um)	FeTi oxides present as small globules
Textures	Glass shows channels, with significant deformation of mica around feldspar grains.	Glass shows directional channels, some movement around phenocrysts. Concentrations of small crystals present in these glass-rich areas. Majority of the matrix looks like static glass	Matrix looks static, inclusions of fine grained grey/white lithic clasts.	Matrix looks static, inclusion of fine grained grey/white lithic clasts (have oxide phases inside them).	Matrix shows little deformation, but biotite grains are kinked
Alteration	Fuzzy brown matrix, many feldspars have altered to unidentifiable fine grained minerals	Fuzzy brown-grey matrix. Most small plagioclase grains show alteration towards this fine-grained "fuzz"	Fuzzy brown matrix, small degree of yellow-brown halos around oxides	Fuzzy grey-brown matrix	None visible

Sample Name	15-CA-49	15-CA-50	15-CA-51	15-CA-52	15-CA-53
% Phenocrysts	25%	35%	15%	25%	30%
Plagioclase	60%	40%	30%	50%	50%
Quartz	15%, heavily fractured, moderately embayed	25%	30%	30%	10%
Sanidine	25%	30%	40%	20%	25%
Biotite	Trace, if present have been resorbed back into matrix. Fine grain alteration products remain	5%	None identifiable	None identifiable	5%, fully altered/replaced
Amphibole	none identifiable	Trace	none identifiable	none identifiable	10%
Pyroxene	none identifiable	none identifiable	none identifiable	none identifiable	none identifiable
Accessory Phases	none identifiable	Minor oxide phases		Trace zircon	Trace monazite
Textures	Little to no deformation, but no biotite to identify kinking				
Alteration	Matrix looks crystalline, not necessarily hydrated(waxy)				

Sample Name	15-CA-54	15-CA-55	15-CA-56
% Phenocrysts	25%	40%	40%
Plagioclase	65%, 2 populations of plagioclase grains. Large independent euhedral crystals (500-2500 um), very fractured and fragmented with every large crystal showing missing portions of the crystal. A secondary mantle of very small Sanidine crystals (<75 um). The second group are small (100-300 um) tightly clustered grains, intergrown with kspar and quartz crystals. Most are only moderately fractured with little embayment	55%	60%
Quartz	15%, small (<100um) rounded and anhedral grains in clusters with plagioclase and sanidine lathes. Most show little fracturing, little to no resorption	10%	10%
Sanidine	10%, present as both independent <150 um grains in clusters with quartz and plag as well as mantle-ing larger plagioclase grains. Most are euhedral-subhedral crystals with simple twins. Little to no fracturing or resorption	20%	20%
Biotite	5%, euhedral sheets (up to 400 um in length) typically with frayed ends. Kinking and deformation is common. Inclusions of apatite/monazite present as well as overgrowths of oxides.	15%	10%
Amphibole	5%, euhedral-relict crystals (250-400 um). Partially resorbed, and heavily fractured it is only fragments of the euhedral crystals that remain. Overgrown by oxides	Trace	Trace
Pyroxene	none identifiable	none identifiable	none identifiable
Accessory Phases	Fe-Ti oxides scattered as independent rounded grains (100-250 um)	none identifiable	none identifiable
Textures	The bulk-ignimbrite section shows welding but the pumice "glob" shows little pulling or realignment of crystal phases	Kinked Biotite	Kinked Biotite
Alteration	None	None	None

Sample Name	H12-66	H12-67	H12-68	H12-69	H12-181
% Phenocrysts	25%	30%	35%	25%	20%
Plagioclase	40%, euhedral-subhedral crystals and clustered intergrowths, 200-1200um. Little to moderate fracturing, crystals shape remains and pieces haven't been pulled off.	40%, euhedral grains, moderately fractured (100-2000um) with small fragments missing from grain edges. Some terminated crystals. No clusters, only independent crystals. Normal zoning,	45%, independent crystals and in clusters intergrown with biotite. Most grains are subhedral with rounded crystal margins, in clusters plagioclase is anhedral. (100-2000um). Normal and oscillatory zoned. Moderate fracturing, some grains have been pulled into fragments separated by glass and matrix.	35%, more smaller crystals (100-800um). Moderately fractured, complex zoning in more typical. Grains only appear as individual crystals, no clusters. Mostly euhedral.	40%, individual crystals with normal and complex zoning. Most 400-800um in length. Euhedral crystals with slightly fractured margins. And fragments of larger grains spread through matrix
Quartz	35%, euhedral-rounded grains. Concoidal edges but little fracturing. 200-500 um in size. Show little to no undulous extinction	45%, Rounded globules and euhedral grains. Most show some degree of resorption and moderate embayment along grain boundaries. No undulous extinction. (200-2500um)	35%, Rounded anhedral/globular grains. Very few have straight crystal edges. Moderately fractured, but few are pulled apart. Significant embayment, but could be a result crystalizing as globules.	45%, mostly globules of qtz with some anhedral grains. Almost all show rounded grain edges with some degree of embayment or deformation. Moderately fractured with little dislocation. (200-1500um)	40%, Larger phenocrysts (up to 2000um). Both euhedral grains with distinct grain edges, and globules with embayed and curved margins. Occasionally contain glass/fluid inclusions
Sanidine	5%, 50-100um. Euhedral grains. Few terminintated crystals. Little to no fracturing. No resorption	5%, 50-200um. Euhedral moderately fractures. No embayment. Simple Carlsbad twins.	10%, <150um in length. Carlsbad twins, barely fractured, no resorption textures.	10%, <150 um. Euhedral crystals with moderate fracturing. Most crystals look broken to degree. Simple twins.	5%, 100-200 um. Simple twins in euhedral grains. Little to moderate fracturing, no dislocation.
Biotite	10%, up to 1000um in length. Little to no deformation. Oxidation rims surround most crystals, minor degree of infilling by matrix. Minor overgrowth of FeTi oxides, and few inclusions of apatite visible	10%, undeformed euhedral sheets, up to 1500um in length. Some look oxidized with black alerted rims, others look pristine. Inclusions of apatite common, 1 grain with inclusion of zircon. Very rarely poikilitic	10%, books and sheets (up to 3000um in length). Little deformation, but a few crystals are seemingly "re-equilibrating" with surrounding glass and are resorbing locally. Most show partially resorption or infilling with glass. Most crystals are "grey" (?)	10%, sheets and books up to 1000um in length. Most show black oxidized rim with minor degrees of resorption of outer margins or fracturing of grain boundaries. No deformation or overgrowths visible, minor inclusions of Apatite	15%, oxidized, only slightly deformed sheets up to 1500um in length. Often with apatite inclusions, minor zircon. Most show black oxidized rim.
Amphibole	None identifiable	None identifiable	None identifiable	None identifiable	None identifiable
Pyroxene	None identifiable	None identifiable	None identifiable	None identifiable	None identifiable
Accessory Phases	FeTi oxides, less common than intracaldera tuff but still ubiquitous. Up to 1000um in length	FeTi oxides present in few numbers. Smaller, up to 500um in length. All independent crystals	Trace zircon inclusions in FeTi oxide, FeTi oxides are present but not common (most are <300um)	Trace zircon as independent crystals. Small number of Fe-Ti oxides (most <200um)	Trace zircon contained in biotite crystals, very few Fe-Ti oxides scattered throughout matrix.
Textures	No obvious welding/pulling or deformation of the matrix. It looks static. No realignment of grains	No obvious welding/pulling or deformation of the matrix. It looks static. No realignment of grains	Glass shows slight deformation, probably related to settling/cooling. Mineral phases are not aligned with this deformation, nor is it constant throughout the section.	Little to no deformation visible. Some glass shows a degree of movement, but it hasn't affected more than local areas.	Glass channels show quenching from contact with holocrystalline matrix, few spherulites present. Little to no deformation of included glass.
Alteration	Oxidation of FeTi oxides and biotite. Little to no embayment of felsic minerals. Matrix looks holocrystalline (less hydrated?)	oxidation of few biotite crystals. Matrix is holocrystalline (less hydrated?)	Biotite crystals are grey and seemingly the same color as the matrix.	Matrix looks less crystalline than previous samples.	Matrix shows slight hydration, hypocrystalline

Table III: Major Element Oxide Abundances

Sample	Rock Type	Oxide (wt. %) by XRF Analysis												
		SiO_2	TiO_2	Al_2O_3	Fe_2O_3	MnO	MgO	CaO	Na_2O	K_2O	P_2O_5	BaO	LOI	Total
LOD		**0.04**	**0.01**	**0.02**	**0.01**	**0.002**	**0.01**	**0.006**	**0.02**	**0.01**	**0.002**	**0.004**	**0.05**	
Pumice Samples														
15-CA-02	Pumice	62.41	0.32	18.47	3.01	0.069	0.52	1.747	4.9	4.82	0.082	0.17	3.21	99.72
15-CA-06	Pumice	60.2	0.54	17.88	3.7	0.066	1.05	2.675	4.07	4.72	0.159	0.29	3.91	99.26
15-CA-08	Pumice	73.15	0.24	13.94	1.13	0.01	0.17	1.331	3.52	4.56	0.051	0.12	1.43	99.64
15-CA-10	Pumice	67.85	0.41	16.2	2.4	0.023	0.47	1.848	4.16	4.86	0.108	0.21	1.45	99.99
15-CA-11	Pumice	75.76	0.17	12.84	1.14	0.013	0.22	0.834	3.48	4.65	0.034	0.08	0.87	100.09
15-CA-16	Pumice	62.98	0.51	18.14	3.6	0.058	0.67	2.761	4.59	4.21	0.148	0.32	2.01	99.99
15-CA-17	Pumice	67.5	0.34	15.61	2.42	0.067	0.82	1.792	3.5	4.79	0.085	0.23	2.82	99.98
15-CA-21	Pumice	69.53	0.31	15.07	2.38	0.063	0.41	1.527	3.81	4.87	0.07	0.18	1.73	99.95
15-CA-22	Pumice	66.36	0.44	16.61	3.27	0.068	0.59	2.145	4.29	4.38	0.113	0.26	1.67	100.19
15-CA-27	Pumice	67.68	0.44	15.74	2.6	0.038	0.36	1.745	4.15	4.71	0.099	0.23	1.06	98.85
15-CA-28	Pumice	61.52	0.74	17.91	4.96	0.105	1.06	3.565	4.32	3.73	0.239	0.26	1.91	100.33
15-CA-30	Pumice	65.75	0.51	16.63	3.21	0.051	0.54	1.866	4.33	4.95	0.133	0.28	1.21	99.45
15-CA-32	Pumice	65.45	0.47	16.78	3.39	0.059	0.68	2.432	4.48	4.33	0.13	0.27	0.95	99.42
15-CA-35	Pumice	66.2	0.44	16.61	3.11	0.039	0.55	1.884	4.29	4.86	0.108	0.28	1.32	99.7
15-CA-36	Pumice	59.29	0.6	18.75	4.41	0.07	1.03	3.25	5.63	3.29	0.217	0.23	2.86	99.63
15-CA-46	Pumice	64.51	0.44	17.17	3.24	0.032	0.62	2.453	4.49	4.6	0.132	0.24	1.45	99.39
15-CA-53	Pumice	66.29	0.37	15.8	2.37	0.064	0.63	2.188	4.15	4.44	0.109	0.2	2.7	99.31
15-CA-54	Pumice	64.13	0.41	17.48	2.96	0.057	0.53	1.858	4.22	5.36	0.104	0.24	2.25	99.6
Whole Rock Samples														
15-CA-03	Tuff	70.03	0.32	14.95	2.43	0.037	0.37	1.212	3.69	4.6	0.076	0.16	2.01	99.88
15-CA-04	Tuff	67.07	0.35	15.67	2.6	0.056	0.48	1.921	3.92	4.72	0.094	0.22	2.25	99.35
15-CA-05	Tuff	69.36	0.35	14.96	2.63	0.057	0.46	1.282	3.69	4.68	0.082	0.17	1.66	99.37
15-CA-07	Tuff	69.08	0.42	15.18	2.51	0.023	0.45	1.777	3.9	4.48	0.112	0.18	1.43	99.57
15-CA-14	Tuff	65.65	0.44	17.01	3.03	0.07	0.56	2.12	4.49	4.95	0.084	0.27	1.41	100.07
15-CA-15	Tuff	71.89	0.28	14.14	2.12	0.042	0.32	1.254	3.6	4.98	0.048	0.14	1.14	99.96
15-CA-18	Tuff	71.21	0.3	14.45	2.25	0.038	0.46	1.319	3.71	4.91	0.069	0.15	1.42	100.29
15-CA-19	Tuff	68.8	0.37	15.18	2.63	0.084	0.53	1.611	3.88	4.59	0.089	0.2	1.9	99.86
15-CA-20	Tuff	68.7	0.38	15.21	2.7	0.064	0.49	1.643	3.95	4.56	0.09	0.2	1.59	99.56
15-CA-23	Tuff	70.94	0.34	14.43	2.43	0.055	0.34	1.3	3.98	4.7	0.071	0.14	0.82	99.53
15-CA-24	Tuff	65.59	0.58	16.4	4.19	0.105	0.68	2.394	4.2	4.25	0.161	0.23	1.11	99.89
15-CA-26	Tuff	66.08	0.54	16.53	3.73	0.056	0.62	2.489	4.29	4.37	0.16	0.25	1.16	100.27
15-CA-29	Tuff	65.88	0.48	16.47	3.33	0.058	0.66	2.19	4.27	4.53	0.122	0.25	1.47	99.71
15-CA-31	Tuff	66.06	0.55	16.51	3.58	0.049	0.56	2.189	4.21	4.39	0.137	0.24	1.51	99.97
15-CA-34	Tuff	65.99	0.56	15.89	3.8	0.053	0.6	2.19	4.17	4.35	0.148	0.22	1.38	99.35
15-CA-41	Tuff	69.53	0.34	14.83	2.08	0.047	0.42	1.607	3.1	4.46	0.089	0.19	2.73	99.42
15-CA-43	Tuff	73.68	0.26	12.91	2.13	0.045	0.31	0.279	1.26	5.61	0.059	0.13	2.18	98.87
15-CA-44	Tuff	71.79	0.26	13.85	2.09	0.049	0.34	1.037	3.39	4.69	0.056	0.13	1.9	99.58
15-CA-45	Tuff	67.82	0.42	15.01	2.81	0.034	0.48	1.787	3.64	4.39	0.111	0.17	1.86	98.54
15-CA-47	Tuff	73.44	0.25	13.44	1.67	0.027	0.22	0.914	3.59	4.6	0.053	0.09	0.99	99.29
15-CA-48	Tuff	72.65	0.26	13.48	1.95	0.055	0.37	1.087	3.28	4.69	0.052	0.1	1.67	99.64
15-CA-51	Tuff	73.04	0.36	13.16	2.3	0.045	0.25	0.465	3.57	4.3	0.09	0.18	1.71	99.48
15-CA-55	Tuff	69.46	0.33	14.8	2.55	0.07	0.46	1.462	3.85	4.64	0.08	0.16	1.56	99.45
15-CA-56	Tuff	71.34	0.3	14.27	1.94	0.023	0.41	1.039	2.82	4.67	0.066	0.15	2.31	99.34
15-CA-37	Tuff	70.72	0.29	14.66	2.33	0.077	0.38	1.074	3.53	4.53	0.083	0.17	1.74	99.58
15-CA-39	Tuff	71.18	0.29	14.42	1.63	0.03	0.3	1.465	3.11	4.63	0.071	0.17	2.34	99.64
15-CA-42	Tuff	69.92	0.32	14.59	2.44	0.058	0.52	1.306	3.23	4.44	0.079	0.17	2.18	99.25
15-CA-33		65.9	0.42	16.02	3.14	0.087	0.64	2.348	4.29	4.31	0.119	0.22	2.25	99.74
15-CA-01		70.97	0.36	13.96	2.89	0.071	0.8	1.892	3.84	3.87	0.104	0.06	0.8	99.6
15-CA-25		67.09	0.38	16.42	2.69	0.037	0.52	1.913	4.35	4.72	0.097	0.2	1.3	99.72
15-CA-40		64.99	0.64	19.75	1.94	0.086	0.56	1.245	2.26	4.41	0.121	0.2	3.66	99.87
15-CA-49		74.75	0.19	13.56	1.59	0.077	0.32	0.343	4.14	2.81	0.033	0.06	2.18	100.05

Table IV: Trace Element Abundances

Sample	Rock Type	Element (ppm) by ICP-MS														
		Ba	Be	Bi	Cd	Ce	Co	Cr	Cs	Cu	Dy	Er	Eu	Ga	Gd	Hf
LOD		0.8	0.004	0.47	0.013	0.12	0.13	3	0.013	1.4	0.009	0.007	0.0031	0.04	0.009	0.14
Pumice Samples																
15-CA-02	Pumice	1497	3.33	<0.47	0.15	71.5	1.25	3	3.70	3.2	4.74	2.78	1.31	21.0	5.06	4.43
15-CA-06	Pumice	>1740	2.46	<0.47	0.16	87.1	3.31	4	1.86	3.5	3.83	2.05	1.66	22.6	4.81	6.25
15-CA-08	Pumice	1073	2.7	<0.47	0.03	71.8	0.98	3	3.20	2.9	3.43	1.86	0.87	17.4	4.11	3.71
15-CA-10	Pumice	>1740	2.4	<0.47	0.08	88.9	2.97	4	2.44	2.9	3.47	1.77	1.33	20.2	4.25	5.40
15-CA-11	Pumice	729	3.52	<0.47	0.04	57.7	0.96	3	3.92	5.0	2.67	1.35	0.62	17.5	3.56	3.77
15-CA-16	Pumice	>1740	2.14	<0.47	0.10	66.2	3.16	4	2.30	4.6	2.31	1.18	1.85	21.8	3.12	4.02
15-CA-17	Pumice	>1740	2.67	<0.47	0.14	74.2	2.26	3	3.23	5.9	3.38	1.93	1.19	18.8	3.84	4.72
15-CA-21	Pumice	1628	2.27	<0.47	0.09	98.2	1.88	3	3.40	2.9	3.92	1.93	1.19	19.5	5.00	3.67
15-CA-22	Pumice	>1740	2.38	<0.47	0.12	64.9	2.76	3	3.50	3.2	2.91	1.61	1.44	21.1	3.71	6.10
15-CA-27	Pumice	>1740	2.13	<0.47	0.06	72.9	1.83	3	2.34	5.3	3.03	1.56	1.45	20.0	3.99	4.07
15-CA-28	Pumice	>1740	2.25	<0.47	0.24	62.7	7.21	181	2.29	6.5	4.11	2.38	1.61	21.7	4.63	8.72
15-CA-30	Pumice	>1740	2.11	<0.47	0.05	100.6	2.92	3	3.23	2.0	3.28	1.57	1.60	21.1	4.55	4.69
15-CA-32	Pumice	>1740	1.96	<0.47	0.10	78.5	3.03	3	2.93	3.0	3.41	1.87	1.51	20.6	4.24	6.17
15-CA-35	Pumice	>1740	2.18	<0.47	0.05	70.9	2.86	3	2.32	2.6	3.38	1.86	1.50	20.1	4.27	5.78
15-CA-36	Pumice	>1740	2.02	<0.47	0.15	76.0	6.44	4	3.32	5.9	3.53	1.96	1.55	19.5	4.54	8.14
15-CA-46	Pumice	>1740	2.12	<0.47	0.09	84.3	3.38	69	6.58	4.0	3.33	1.77	1.52	21.4	4.41	6.64
15-CA-53	Pumice	>1740	2.43	<0.47	0.19	88.8	2.54	5	3.99	6.4	4.10	2.21	1.37	18.3	4.89	5.79
15-CA-54	Pumice	>1740	2.26	<0.47	0.11	127.9	2.34	3	2.53	3.5	4.74	2.47	1.56	21.4	6.18	5.40
Whole Rock Samples																
15-CA-03	Tuff	1476	2.51	<0.47	0.10	84.0	1.01	5	2.86	4.0	3.59	2.10	1.13	18.8	4.20	4.29
15-CA-04	Tuff	>1740	2.53	<0.47	0.18	81.3	1.73	3	2.87	2.6	3.40	1.90	1.26	20.0	4.10	4.75
15-CA-05	Tuff	1562	2.51	<0.47	0.12	88.1	2.33	80	3.14	4.9	3.70	2.00	1.12	19.2	4.35	4.38
15-CA-07	Tuff	>1740	2.52	<0.47	0.06	85.6	3.1	85	2.71	2.7	3.74	2.05	1.19	19.9	4.40	5.34
15-CA-14	Tuff	>1740	2.5	<0.47	0.10	74.7	2.72	3	2.74	2.4	2.55	1.41	1.36	20.1	3.09	4.16
15-CA-15	Tuff	1221	2.38	<0.47	0.08	75.9	1.56	3	4.02	1.6	3.56	2.00	0.88	17.9	3.86	3.86
15-CA-18	Tuff	1322	2.55	<0.47	0.08	81.5	1.64	3	3.61	2.3	3.81	2.04	1.02	17.5	4.44	4.20
15-CA-19	Tuff	>1740	2.49	<0.47	0.13	79.4	2.3	3	3.87	2.8	3.43	1.86	1.24	19.1	4.16	4.59
15-CA-20	Tuff	>1740	2.38	<0.47	0.13	83.8	2.26	4	3.85	2.5	3.52	1.89	1.25	19.8	4.20	4.69
15-CA-23	Tuff	1260	2.94	<0.47	0.07	72.0	1.56	3	5.00	1.6	3.44	1.99	1.01	19.6	3.94	4.41
15-CA-24	Tuff	>1740	2.38	<0.47	0.22	91.5	4.92	72	3.84	3.5	4.03	2.23	1.54	21.1	4.92	5.60
15-CA-26	Tuff	>1740	2.27	<0.47	0.08	83.0	4.28	3	2.78	3.2	3.66	1.94	1.51	20.9	4.50	4.64
15-CA-29	Tuff	>1740	2.25	<0.47	0.11	73.3	3.05	6	2.82	2.7	3.35	1.86	1.40	20.4	4.15	6.40
15-CA-31	Tuff	>1740	2.05	<0.47	0.07	81.1	3.52	3	2.75	2.7	3.23	1.77	1.45	20.4	4.15	5.64
15-CA-34	Tuff	>1740	2.23	<0.47	0.09	83.4	3.81	69	2.71	2.8	3.72	2.00	1.36	20.1	4.54	5.75
15-CA-41	Tuff	1668	2.37	<0.47	0.14	83.2	1.2	5	5.61	4.0	3.48	2.00	1.14	17.9	4.18	4.20
15-CA-43	Tuff	1228	2.7	<0.47	0.07	78.3	1.59	107	33.20	1.8	3.73	2.20	0.88	16.9	4.24	4.42
15-CA-44	Tuff	1171	2.92	<0.47	0.07	85.1	1.38	3	16.89	2.4	3.83	2.14	0.85	17.5	4.43	4.35
15-CA-45	Tuff	1617	2.57	<0.47	0.10	82.9	2.7	4	8.00	2.5	3.87	2.17	1.18	20.1	4.69	5.60
15-CA-47	Tuff	839	2.95	<0.47	0.05	76.6	1.1	114	5.20	1.7	3.56	2.13	0.71	17.8	4.15	4.33
15-CA-48	Tuff	930	2.9	<0.47	0.13	88.7	1.18	3	3.06	2.2	3.63	2.04	0.81	18.0	4.35	4.29
15-CA-51	Tuff	1692	2.32	<0.47	0.11	77.8	0.96	4	4.71	4.7	4.28	2.39	1.37	15.3	5.36	5.15
15-CA-55	Tuff	1451	2.59	<0.47	0.14	92.7	2.35	75	2.82	2.5	4.07	2.33	1.07	18.5	4.83	5.16
15-CA-56	Tuff	1389	2.27	<0.47	0.06	80.8	1.67	3	14.78	2.0	3.48	2.03	1.04	17.6	4.08	4.20
15-CA-37	Altered Tuff	1495	2.68	<0.47	0.11	86.4	2.08	4	4.73	3.7	3.73	2.11	1.07	18.9	4.21	4.44
15-CA-39	Altered Tuff	1634	2.55	<0.47	0.06	95.1	0.51	4	5.78	3.5	3.46	1.90	1.06	17.8	4.31	4.32
15-CA-42	Altered Tuff	1507	2.47	<0.47	0.10	87.7	1.64	4	5.61	2.5	3.69	2.12	1.06	18.4	4.36	4.55
15-CA-33	Basal Vitrophyre	>1740	2.3	<0.47	0.13	85.6	2.62	4	4.85	3.4	3.58	2.01	1.36	20.1	4.30	6.03
Associated Rock Units																
15-CA-01	Granodiorite	523	3.33	<0.47	0.07	63.6	3.89	7	3.03	5.1	2.97	1.72	0.66	18.8	3.21	2.76
15-CA-25	Vitropherous Rhyolite	>1740	2.43	<0.47	0.13	82.7	2.68	5	6.02	2.3	3.62	2.01	1.34	20.4	4.42	4.79
15-CA-40	Argillite Chips	>1740	5.63	<0.47	0.18	64.8	2.74	91	9.07	9.1	4.36	2.74	1.32	17.7	4.44	4.25
15-CA-49	Tuff of Job Canyon	532	2.8	<0.47	0.11	81.6	1.03	3	8.25	1.4	3.84	2.30	0.62	17.0	4.02	3.86

Table IV: Trace Element Abundances Cont.

Sample	Rock Type	Element (ppm) by ICP-MS														
		Ho	In	La	Li	Lu	Mo	Nb	Nd	Ni	Pb	Pr	Rb	Sb	Sc	Sm
LOD		0.0025	0.0018	0.1	0.4	0.002	0.008	0.028	0.06	0.7	0.18	0.014	0.11	0.04	1.1	0.026
Pumice Samples																
15-CA-02	Pumice	0.92	0.04	41.3	27.3	0.35	0.48	15.8	33.1	1.3	19.3	9.00	136	1.02	6.6	6.00
15-CA-06	Pumice	0.71	0.05	50.2	25.1	0.30	1.33	15.8	37.7	1.4	22.5	10.51	123	0.70	6.9	6.40
15-CA-08	Pumice	0.62	0.02	42.2	27.5	0.25	0.68	14.9	33.3	1.1	21.2	9.30	159	0.37	3.9	5.52
15-CA-10	Pumice	0.63	0.04	51.7	20.8	0.26	0.89	15.0	37.0	1.6	21.0	10.61	136	1.16	5.9	5.94
15-CA-11	Pumice	0.46	0.03	39.0	25.6	0.20	1.12	16.6	31.3	1.3	20.8	9.08	173	0.55	2.8	5.48
15-CA-16	Pumice	0.43	0.04	36.6	23.2	0.16	1.25	12.1	27.5	1.6	20.2	7.60	106	0.41	6.3	4.28
15-CA-17	Pumice	0.63	0.04	41.0	39.1	0.29	0.61	14.4	30.9	1.3	21.5	8.74	130	0.70	5.2	5.18
15-CA-21	Pumice	0.69	0.03	65.0	32.6	0.25	1.11	15.9	45.3	1.4	22.6	13.08	144	0.35	5.5	7.30
15-CA-22	Pumice	0.54	0.04	45.4	29.3	0.24	1.01	14.7	31.7	1.3	19.2	8.93	119	0.39	5.9	5.30
15-CA-27	Pumice	0.58	0.04	42.6	26.9	0.21	1.25	15.1	31.9	1.2	21.2	8.85	128	0.53	5.9	5.35
15-CA-28	Pumice	0.82	0.05	35.5	19.8	0.36	2.14	13.3	30.8	3.2	21.1	8.06	98	0.56	9.2	5.47
15-CA-30	Pumice	0.59	0.05	56.2	18.2	0.20	1.38	15.6	40.4	1.0	20.4	11.50	131	0.34	6.9	6.43
15-CA-32	Pumice	0.64	0.04	44.2	20.7	0.27	1.27	14.5	33.9	1.4	20.8	9.35	116	0.56	6.5	5.61
15-CA-35	Pumice	0.65	0.04	43.5	25.9	0.27	1.11	14.7	32.5	0.9	22.9	9.07	127	0.39	5.3	5.42
15-CA-36	Pumice	0.67	0.05	40.3	14.6	0.29	0.87	13.6	32.5	1.6	22.1	8.82	87	0.52	8	5.62
15-CA-46	Pumice	0.61	0.05	45.5	17.6	0.25	1.62	14.7	34.8	1.5	23.4	9.67	127	1.96	5.7	5.96
15-CA-53	Pumice	0.76	0.03	48.0	28.7	0.33	1.32	15.3	37.9	2.0	22.0	10.33	126	0.87	5.2	6.34
15-CA-54b	Pumice	0.89	0.05	72.0	21.0	0.35	0.84	16.4	51.6	1.2	28.5	14.80	141	0.70	6.3	8.24
Whole Rock Samples																
15-CA-03	Tuff	0.70	0.04	47.7	24.6	0.31	1.74	15.3	35.6	1.5	22.5	10.03	138	1.76	5.8	5.91
15-CA-04	Tuff	0.66	0.03	43.4	23.3	0.28	1.63	15.3	32.6	1.0	22.2	9.17	133	0.95	5.9	5.57
15-CA-05	Tuff	0.68	0.04	46.7	24.3	0.29	1.45	15.4	34.6	2.4	22.8	9.93	142	1.00	5.9	5.96
15-CA-07	Tuff	0.70	0.04	47.0	23.6	0.30	1.27	15.6	35.1	1.8	20.7	9.85	138	1.00	6.2	5.89
15-CA-14	Tuff	0.49	0.04	38.9	36.8	0.22	0.37	14.9	26.0	1.2	20.8	7.53	164	0.82	4.8	4.19
15-CA-15	Tuff	0.68	0.03	39.0	35.4	0.32	0.70	16.0	29.8	0.7	22.7	8.39	173	1.53	4.1	5.09
15-CA-18	Tuff	0.70	0.04	48.4	30.1	0.31	0.72	15.8	36.2	0.8	20.2	10.20	147	0.56	4.3	6.04
15-CA-19	Tuff	0.64	0.04	47.4	29.0	0.27	0.88	14.9	34.7	1.8	18.1	9.79	133	0.48	5.3	5.80
15-CA-20	Tuff	0.65	0.04	51.2	27.4	0.29	0.96	15.1	37.3	1.4	28.8	10.55	134	0.38	5.2	6.00
15-CA-23	Tuff	0.67	0.05	43.0	30.9	0.30	1.26	16.7	31.7	0.7	22.0	8.93	163	0.98	5	5.37
15-CA-24	Tuff	0.76	0.06	49.7	21.4	0.31	2.00	15.1	38.7	2.4	22.3	10.65	124	0.97	7.4	6.60
15-CA-26	Tuff	0.70	0.04	45.5	21.4	0.29	1.61	14.9	35.5	1.4	20.5	9.75	120	0.72	7.3	6.10
15-CA-29	Tuff	0.64	0.04	44.1	20.1	0.27	1.11	14.9	33.1	2.4	20.9	9.38	125	0.65	5.9	5.52
15-CA-31	Tuff	0.60	0.05	44.9	22.4	0.25	1.06	15.2	33.7	1.1	19.5	9.41	121	0.57	6.9	5.46
15-CA-34	Tuff	0.69	0.05	46.3	23.1	0.29	1.57	15.3	36.4	1.9	20.5	9.96	124	0.67	6.7	6.15
15-CA-41	Tuff	0.65	0.06	45.2	36.9	0.29	2.44	14.1	33.5	1.3	25.2	9.48	129	1.09	5.3	5.46
15-CA-43	Tuff	0.73	0.04	39.0	79.3	0.33	1.37	15.3	31.0	1.4	24.3	8.75	219	13.15	4	5.42
15-CA-44	Tuff	0.74	0.04	45.8	63.4	0.33	0.75	15.3	34.5	1.0	24.3	9.66	158	3.19	4.1	5.77
15-CA-45	Tuff	0.75	0.05	44.5	19.8	0.33	0.85	15.8	34.4	1.0	23.1	9.76	153	2.18	5.7	6.14
15-CA-47	Tuff	0.69	0.04	40.8	32.7	0.33	1.78	16.5	31.2	1.6	24.2	8.91	173	4.56	3.1	5.44
15-CA-48	Tuff	0.72	0.03	47.1	34.4	0.31	0.89	16.0	34.6	1.0	23.3	10.11	159	1.22	3.7	5.92
15-CA-51	Tuff	0.81	0.05	41.2	20.4	0.33	0.88	13.9	36.3	1.4	19.6	9.54	119	1.00	6.4	6.56
15-CA-55	Tuff	0.79	0.04	52.6	26.2	0.34	1.22	15.5	38.2	1.6	23.4	10.85	140	0.80	5.1	6.22
15-CA-56	Tuff	0.69	0.04	43.1	112.9	0.30	0.71	14.7	32.7	0.8	22.4	9.24	145	6.61	4.4	5.53
15-CA-37	Altered Tuff	0.70	0.04	44.9	24.1	0.33	1.79	15.6	34.3	1.6	23.8	9.77	141	0.75	4.8	5.78
15-CA-39	Altered Tuff	0.64	0.04	51.8	29.5	0.28	0.66	14.8	36.7	0.7	18.5	10.62	140	0.84	4.7	6.01
15-CA-42	Altered Tuff	0.72	0.04	48.0	37.2	0.31	1.03	15.3	35.1	1.0	22.7	9.91	141	0.91	5	5.76
15-CA-33	Basal Vitrophyre	0.68	0.05	45.7	25.4	0.30	2.76	14.5	34.5	1.4	22.9	9.56	119	0.71	5.7	5.74
Associated Rock Units																
15-CA-01	Granodiorite	0.57	0.03	33.0	14.4	0.29	1.40	16.0	24.6	2.3	19.6	7.06	162	0.21	4.6	4.33
15-CA-25	Vitropherous Rhyolite	0.69	0.04	45.7	25.2	0.28	2.33	15.0	35.4	0.9	22.9	9.76	127	0.94	5.7	5.89
15-CA-40	Argillite Chips	0.90	0.05	33.4	>207	0.43	1.14	12.1	28.7	4.2	32.9	7.62	141	1.57	15.8	5.39
15-CA-49	Tuff of Job Canyon	0.76	0.03	41.6	27.9	0.37	0.78	15.4	31.4	<0.7	36.5	9.12	158	1.54	2.9	5.35

Table IV: Trace Element Abundances Cont.

Sample	Rock Type	Element (ppm) by ICP-MS														
		Sn	Sr	Ta	Tb	Th	Ti	Tl	Tm	U	V	W	Y	Yb	Zn	Zr
LOD		0.16	0.6	0.007	0.0023	0.018	7	0.002	0.0019	0.011	0.8	0.05	0.05	0.009	1.8	6
Pumice Samples																
15-CA-02	Pumice	2.27	332	1.11	0.76	16.3	1891	0.82	0.37	4.23	19.8	1.01	28.6	2.37	72	155
15-CA-06	Pumice	1.88	506	0.94	0.66	12.0	3248	0.62	0.29	4.03	29.1	1.47	20.9	1.96	86	265
15-CA-08	Pumice	1.51	188	1.29	0.59	19.4	1296	0.68	0.26	4.52	10.9	1.11	17.8	1.75	31	113
15-CA-10	Pumice	1.97	333	1.05	0.61	15.1	2468	0.66	0.26	5.23	23.0	0.80	17.8	1.76	70	212
15-CA-11	Pumice	3.16	107	1.57	0.48	22.7	978	0.79	0.19	4.52	7.6	0.63	13.2	1.34	52	105
15-CA-16	Pumice	1.47	551	0.72	0.41	9.2	3002	0.59	0.16	2.32	34.8	0.63	12.0	1.09	62	161
15-CA-17	Pumice	1.83	287	1.00	0.56	14.1	1906	0.67	0.28	4.32	17.0	0.79	18.1	1.95	62	173
15-CA-21	Pumice	2.32	302	1.09	0.70	16.4	1822	0.77	0.28	4.16	15.6	0.72	19.0	1.78	54	120
15-CA-22	Pumice	1.87	390	0.90	0.51	12.7	2604	0.64	0.24	4.19	24.3	0.79	15.3	1.54	73	253
15-CA-27	Pumice	1.75	317	0.98	0.54	13.7	2392	0.56	0.22	2.83	18.7	0.57	17.2	1.38	59	149
15-CA-28	Pumice	1.84	562	0.76	0.67	10.2	4427	0.54	0.35	3.95	69.4	0.83	25.0	2.26	103	422
15-CA-30	Pumice	1.84	370	0.94	0.61	13.6	2971	0.62	0.22	3.14	24.5	0.82	16.3	1.35	63	179
15-CA-32	Pumice	1.82	420	0.89	0.59	11.9	2679	0.62	0.26	4.03	23.6	0.81	18.2	1.74	75	256
15-CA-35	Pumice	1.83	358	0.94	0.59	13.1	2502	0.68	0.27	3.95	23.3	0.64	18.7	1.77	69	229
15-CA-36	Pumice	1.65	611	0.81	0.62	10.8	3496	0.49	0.28	4.17	48.6	1.27	18.9	1.90	86	378
15-CA-46	Pumice	1.97	440	0.94	0.60	12.7	2615	0.70	0.25	4.55	24.4	1.02	17.1	1.66	71	276
15-CA-53	Pumice	1.68	305	0.97	0.70	13.3	2229	0.72	0.32	4.77	17.3	1.52	22.5	2.12	54	233
15-CA-54b	Pumice	2.15	339	1.10	0.85	16.5	2264	0.82	0.36	5.59	20.1	0.85	24.5	2.27	72	200
Whole Rock Samples																
15-CA-03	Tuff	1.98	235	1.13	0.61	16.2	1860	0.78	0.30	5.12	18.2	1.29	19.4	2.05	62	150
15-CA-04	Tuff	1.52	278	1.02	0.60	13.8	2096	0.67	0.28	4.49	19.6	1.03	19.2	1.86	59	174
15-CA-05	Tuff	1.73	222	1.12	0.61	16.3	1956	0.72	0.29	5.05	22.3	1.14	20.0	1.91	57	149
15-CA-07	Tuff	2.17	354	1.12	0.64	15.8	2503	0.63	0.30	5.14	27.1	1.45	21.1	1.99	62	204
15-CA-14	Tuff	2.40	492	0.80	0.44	12.0	2532	0.61	0.21	3.14	18.4	0.59	14.2	1.46	67	162
15-CA-15	Tuff	1.34	311	1.29	0.57	18.5	1571	0.64	0.31	4.80	12.5	0.98	19.6	2.16	57	120
15-CA-18	Tuff	2.34	233	1.20	0.66	17.9	1728	0.80	0.30	5.80	16.9	0.92	19.4	2.03	57	135
15-CA-19	Tuff	1.96	270	1.06	0.60	15.7	2015	0.69	0.27	4.31	18.3	0.84	18.1	1.80	60	162
15-CA-20	Tuff	2.11	277	1.05	0.60	15.8	2116	0.71	0.29	4.29	19.9	0.70	18.5	1.83	63	172
15-CA-23	Tuff	2.62	201	1.35	0.57	20.0	1907	0.57	0.29	5.19	15.7	1.10	19.5	1.97	63	146
15-CA-24	Tuff	2.21	428	0.97	0.71	13.9	3514	0.88	0.31	4.21	44.4	1.46	21.5	2.08	81	230
15-CA-26	Tuff	2.02	435	0.93	0.63	13.2	3259	0.63	0.28	4.09	37.6	0.89	20.8	1.87	82	184
15-CA-29	Tuff	2.11	395	0.96	0.58	13.6	2788	0.65	0.27	4.33	27.3	0.82	18.6	1.74	73	268
15-CA-31	Tuff	1.95	399	0.99	0.55	13.4	3190	0.56	0.25	4.18	33.2	0.76	16.8	1.65	71	226
15-CA-34	Tuff	2.00	370	1.00	0.64	14.2	3123	0.60	0.29	4.49	34.7	0.86	20.1	1.93	76	226
15-CA-41	Tuff	2.57	259	1.02	0.60	15.5	1868	0.70	0.28	4.88	18.4	1.27	19.2	1.84	56	145
15-CA-43	Tuff	2.38	74	1.22	0.62	18.1	1415	1.38	0.32	5.86	12.9	2.89	20.4	2.09	52	150
15-CA-44	Tuff	2.58	179	1.25	0.64	19.4	1471	0.87	0.33	6.20	12.5	1.03	21.6	2.21	53	141
15-CA-45	Tuff	2.43	341	1.17	0.69	17.6	2406	0.89	0.32	6.02	28.7	1.34	21.7	2.18	68	216
15-CA-47	Tuff	2.87	132	1.44	0.59	21.2	1268	0.85	0.31	6.44	10.0	2.55	19.9	2.17	52	136
15-CA-48	Tuff	2.51	132	1.33	0.61	20.2	1408	0.80	0.31	5.76	10.5	0.98	20.0	2.16	59	133
15-CA-51	Tuff	2.12	202	0.98	0.75	14.2	2119	0.61	0.34	4.65	9.7	1.35	22.8	2.21	49	195
15-CA-55	Tuff	2.16	308	1.13	0.69	17.2	1890	0.76	0.35	5.38	18.8	0.89	23.4	2.27	62	190
15-CA-56	Tuff	2.05	189	1.12	0.61	16.3	1595	0.69	0.29	4.93	13.8	2.92	19.1	2.00	51	143
15-CA-37	Altered Tuff	2.17	227	1.16	0.62	17.0	1725	0.75	0.31	5.24	16.2	1.37	19.2	2.09	60	152
15-CA-39	Altered Tuff	2.22	235	1.12	0.61	17.9	1598	0.73	0.28	5.23	15.1	1.14	18.4	1.87	41	145
15-CA-42	Altered Tuff	2.19	222	1.16	0.62	17.2	1759	0.79	0.31	5.48	17.2	1.24	20.5	2.09	56	157
15-CA-33	Basal Vitrophyre	2.08	372	0.99	0.60	13.8	2391	0.72	0.29	4.94	22.9	1.32	19.3	1.95	71	241
Associated Rock Units																
15-CA-01		2.12	268	1.45	0.49	20.8	2136	0.78	0.26	4.73	42.0	1.70	17.8	1.87	46	83
15-CA-25		2.01	373	1.02	0.62	14.4	2613	0.78	0.29	4.89	25.3	1.41	19.9	1.89	76	180
15-CA-40		4.83	330	0.90	0.69	13.7	3832	1.25	0.39	3.88	106.2	2.30	27.1	2.72	102	142
15-CA-49		3.19	118	1.41	0.61	22.6	998	0.89	0.35	5.72	6.4	0.65	22.8	2.47	54	108

Table V: Major Element Variation using chrome mill

	Element (wt. %) by Fused Disk XRF												
Sample	SiO2	TiO2	Al2O3	Fe2O3	MnO	MgO	CaO	Na2O	K2O	P2O5	BaO	LOI	Total
15-CA-33	65.9	0.42	16.02	3.14	0.087	0.64	2.348	4.29	4.31	0.119	0.22	2.25	99.74
15-CA-33 chrome	66.01	0.4	16.02	3.16	0.087	0.62	2.326	4.3	4.36	0.12	0.22	2.28	99.91
Variation (%)	-0.17	4.76	0.00	-0.64	0.00	3.13	0.94	-0.23	-1.16	-0.84	0.00	-1.33	-0.17
15-CA-36	59.29	0.6	18.75	4.41	0.07	1.03	3.25	5.63	3.29	0.217	0.23	2.86	99.63
15-CA-36 chrome	58.87	0.62	18.64	4.44	0.069	1.01	3.331	5.61	3.25	0.216	0.23	3.17	99.45
Variation (%)	0.71	-3.33	0.59	-0.68	1.43	1.94	-2.49	0.36	1.22	0.46	0.00	-10.84	0.18

Table VI: Select Trace Element Variation using chrome mill

	Element (ppm) by ICP-MS													
Sample	Cr	Cu	Eu	Lu	Nd	Pb	Rb	Sm	Sr	Th	U	Yb	Nb	Ta
15-CA-33	4	3.4	1.3615	0.3022	34.5	22.9	118.89	5.735	371.7	13.826	19.33	1.953	14.474	0.994
15-CA-33 chrome	76	3.7	1.3697	0.3061	33.56	22.8	120.97	5.774	371.2	13.759	20	1.979	14.593	0.956
Variation (%)	94.74	8.11	0.60	1.27	-2.80	-0.44	1.72	0.68	-0.13	-0.49	1.81	1.31	-0.82	3.82
15-CA-36	4	5.9	1.5528	0.2923	32.45	22.1	86.76	5.616	610.5	10.846	4.165	1.903	13.561	0.805
15-CA-36 chrome	76	7.9	1.5601	0.3065	32.13	21.7	85.36	5.542	612.3	10.664	4.139	1.862	13.246	0.803
Variation (%)	94.74	25.32	0.47	4.63	-1.00	-1.84	-1.64	-1.34	0.29	-1.71	-0.63	-2.20	2.32	0.25

Table VII: Precision of OGS Analysis

	Element (wt. %) by Fused Disk XRF											
	SiO2	TiO2	Al2O3	Fe2O3	MnO	MgO	CaO	Na2O	K2O	P2O5	BaO	LOI
First Run												
15-CA-10	67.85	0.41	16.2	2.4	0.023	0.47	1.848	4.16	4.86	0.108	0.21	1.45
15-CA-20	68.7	0.38	15.21	2.7	0.064	0.49	1.643	3.95	4.56	0.09	0.2	1.59
15-CA-30	65.75	0.51	16.63	3.21	0.051	0.54	1.866	4.33	4.95	0.133	0.28	1.21
15-CA-40	64.99	0.64	19.75	1.94	0.086	0.56	1.245	2.26	4.41	0.121	0.2	3.66
15-CA-49	74.75	0.19	13.56	1.59	0.077	0.32	0.343	4.14	2.81	0.033	0.06	2.18
Duplicate Run												
15-CA-10	67.59	0.43	16.16	2.37	0.024	0.47	1.836	4.13	4.8	0.108	0.21	1.45
15-CA-20	68.53	0.38	15.16	2.69	0.062	0.49	1.634	3.95	4.6	0.089	0.2	1.54
15-CA-30	66.06	0.5	16.72	3.24	0.051	0.55	1.866	4.37	5.06	0.134	0.27	1.21
15-CA-40	64.93	0.64	19.68	1.95	0.086	0.55	1.235	2.21	4.4	0.12	0.2	3.66
15-CA-49	74.76	0.19	13.52	1.58	0.079	0.32	0.345	4.15	2.81	0.032	0.06	2.17
Variation between analyses (%)												
15-CA-10	0.38	-4.88	0.25	1.25	-4.35	0.00	0.65	0.72	1.23	0.00	0.00	0.00
15-CA-20	0.25	0.00	0.33	0.37	3.13	0.00	0.55	0.00	-0.88	1.11	0.00	3.14
15-CA-30	-0.47	1.96	-0.54	-0.93	0.00	-1.85	0.00	-0.92	-2.22	-0.75	3.57	0.00
15-CA-40	0.09	0.00	0.35	-0.52	0.00	1.79	0.80	2.21	0.23	0.83	0.00	0.00
15-CA-49	-0.01	0.00	0.29	0.63	-2.60	0.00	-0.58	-0.24	0.00	3.03	0.00	0.46
Average Variation (%)	**0.05**	**0.58**	**0.14**	**0.16**	**0.76**	**0.01**	**0.28**	**0.35**	**0.33**	**0.84**	**0.71**	**0.72**

Table VII: Precision of OGS Analysis Cont.

	Element (ppm) by ICP-MS													
	Ba	Be	Bi	Cd	Ce	Co	Cr	Cs	Cu	Dy	Er	Eu	Ga	Gd
First Run														
15-CA-11	729.3	3.52	<0.47	0.035	57.7	0.96	3	3.919	5	2.673	1.348	0.6158	17.54	3.557
15-CA-20	>1740	2.38	<0.47	0.133	83.8	2.26	4	3.853	2.5	3.515	1.885	1.2536	19.78	4.201
15-CA-30	>1740	2.11	<0.47	0.046	100.57	2.92	3	3.228	2	3.281	1.566	1.5953	21.1	4.554
15-CA-39	1634.3	2.55	<0.47	0.059	95.14	0.51	4	5.784	3.5	3.456	1.903	1.0591	17.83	4.313
15-CA-49	531.9	2.8	<0.47	0.113	81.59	1.03	3	8.254	1.4	3.837	2.302	0.6233	16.97	4.018
Duplicate Runs														
15-CA-11	735.4	3.33	0.15	0.043	58.2	1.01	4	4.018	4.5	2.619	1.315	0.6135	17.32	3.526
15-CA-20	1807.8	2.5	0.12	0.115	82.64	2.23	4	3.788	2.3	3.574	1.939	1.2586	19.59	4.421
15-CA-30	2540.5	2.08	0.07	0.055	96.78	2.89	3	3.195	2.1	3.266	1.545	1.6562	20.65	4.568
15-CA-39	1621.6	2.42	0.23	0.055	91.42	0.45	4	5.788	3.6	3.458	1.875	1.0573	17.67	4.266
15-CA-49	524.5	3.11	0.29	0.094	79.96	1.12	3	8.278	1.3	3.715	2.269	0.5751	17.01	3.893
Variation (%)														
15-CA-11	0.83	-5.71		18.60	0.86	4.95	25.00	2.46	-11.11	-2.06	-2.51	-0.37	-1.27	-0.88
15-CA-20		4.80		-15.65	-1.40	-1.35	0.00	-1.72	-8.70	1.65	2.78	0.40	-0.97	4.98
15-CA-30		-1.44		16.36	-3.92	-1.04	0.00	-1.03	4.76	-0.46	-1.36	3.68	-2.18	0.31
15-CA-39	-0.78	-5.37		-7.27	-4.07	-13.33	0.00	0.07	2.78	0.06	-1.49	-0.17	-0.91	-1.10
15-CA-49	-1.41	9.97		-20.21	-2.04	8.04	0.00	0.29	-7.69	-3.28	-1.45	-8.38	0.24	-3.21
Average Variation (%)	**0.45**	**0.45**		**1.63**	**2.11**	**0.55**	**5.00**	**0.01**	**3.99**	**0.82**	**0.81**	**0.97**	**1.02**	**0.02**

Table VII: Precision of OGS Analysis Cont.

	Element (ppm) by ICP-MS													
	Ho	In	La	Li	Lu	Mo	Nb	Nd	Ni	Pb	Pr	Rb	Sb	Sc
First Run														
15-CA-11	0.4608	0.029	38.95	25.6	0.2035	1.12	16.577	31.29	1.3	20.8	9.08	173.03	0.55	2.8
15-CA-20	0.6497	0.0405	51.24	27.4	0.2873	0.96	15.112	37.25	1.4	28.8	10.554	133.87	0.38	5.2
15-CA-30	0.594	0.0481	56.22	18.2	0.2028	1.38	15.596	40.43	1	20.4	11.498	131.02	0.34	6.9
15-CA-39	0.6414	0.0418	51.81	29.5	0.2836	0.66	14.805	36.69	0.7	18.5	10.615	140.22	0.84	4.7
15-CA-49	0.7648	0.0347	41.58	27.9	0.3723	0.78	15.402	31.35	<0.7	36.5	9.116	157.57	1.54	2.9
Duplicate Runs														
15-CA-11	0.4702	0.0263	39.32	25.6	0.2105	1.05	17.064	31.83	1.5	21.1	9.12	173.15	0.55	2.8
15-CA-20	0.6648	0.04	50.88	27.5	0.2835	0.92	15.036	37.14	1.3	29.3	10.342	136.29	0.36	5.2
15-CA-30	0.5861	0.0453	54.15	18.2	0.1973	1.2	15.436	39.81	1	20.3	11.077	130.25	0.35	6.8
15-CA-39	0.6522	0.0403	49.93	29.5	0.284	0.65	14.867	35.91	0.9	18.5	10.331	139.15	0.87	4.7
15-CA-49	0.7229	0.0337	40.48	29.3	0.3624	0.8	15.798	30.52	0.6	35.5	8.913	160.61	1.55	2.9
Variation (%)														
15-CA-11	2.00	-10.27	0.94	0.00	3.33	-6.67	2.85	1.70	13.33	1.42	0.44	0.07	0.00	0.00
15-CA-20	2.27	-1.25	-0.71	0.36	-1.34	-4.35	-0.51	-0.30	-7.69	1.71	-2.05	1.78	-5.56	0.00
15-CA-30	-1.35	-6.18	-3.82	0.00	-2.79	-15.00	-1.04	-1.56	0.00	-0.49	-3.80	-0.59	2.86	-1.47
15-CA-39	1.66	-3.72	-3.77	0.00	0.14	-1.54	0.42	-2.17	22.22	0.00	-2.75	-0.77	3.45	0.00
15-CA-49	-5.80	-2.97	-2.72	4.78	-2.73	2.50	2.51	-2.72		-2.82	-2.28	1.89	0.65	0.00
Average Variation (%)	**0.24**	**4.88**	**2.01**	**1.03**	**0.68**	**5.01**	**0.85**	**1.01**	**6.97**	**0.04**	**2.09**	**0.48**	**0.28**	**0.29**

Table VII: Precision of OGS Analysis Cont.

	Element (ppm) by ICP-MS													
	Sn	Sr	Ta	Tb	Th	Ti	Tl	Tm	U	V	W	Y	Yb	Zn
First Run														
15-CA-11	3.16	107.2	1.571	0.4796	22.673	978	0.787	0.1945	4.524	7.6	0.63	13.15	1.337	52
15-CA-20	2.11	277.3	1.05	0.6028	15.78	2116	0.712	0.2856	4.294	19.9	0.7	18.54	1.829	63
15-CA-30	1.84	369.5	0.944	0.6088	13.607	2971	0.616	0.2165	3.139	24.5	0.82	16.34	1.347	63
15-CA-39	2.22	234.8	1.117	0.6095	17.885	1598	0.734	0.2785	5.232	15.1	1.14	18.41	1.872	41
15-CA-49	3.19	118.3	1.409	0.6116	22.606	998	0.891	0.3485	5.721	6.4	0.65	22.8	2.473	54
Duplicate Runs														
15-CA-11	3.27	107	1.58	0.489	23.016	998	0.779	0.1964	4.568	7.8	0.61	13.29	1.348	52
15-CA-20	2.08	279.5	1.047	0.603	16.002	2165	0.713	0.28	4.389	20.5	0.72	19.01	1.853	64
15-CA-30	1.77	365.7	0.937	0.5845	13.316	2952	0.605	0.2117	3.076	23.4	0.69	16.12	1.361	64
15-CA-39	2.19	232.8	1.153	0.6064	17.62	1603	0.752	0.2849	5.28	15.2	1.16	17.9	1.847	46
15-CA-49	3.12	116.9	1.362	0.5874	22.114	1016	0.853	0.3457	5.552	6.4	0.64	22.17	2.383	51
Variation (%)														
15-CA-11	3.36	-0.19	0.57	1.92	1.49	2.00	-1.03	0.97	0.96	2.56	-3.28	1.05	0.82	0.00
15-CA-20	-1.44	0.79	-0.29	0.03	1.39	2.26	0.14	-2.00	2.16	2.93	2.78	2.47	1.30	1.56
15-CA-30	-3.95	-1.04	-0.75	-4.16	-2.19	-0.64	-1.82	-2.27	-2.05	-4.70	-18.84	-1.36	1.03	1.56
15-CA-39	-1.37	-0.86	3.12	-0.51	-1.50	0.31	2.39	2.25	0.91	0.66	1.72	-2.85	-1.35	10.87
15-CA-49	-2.24	-1.20	-3.45	-4.12	-2.22	1.77	-4.45	-0.81	-3.04	0.00	-1.56	-2.84	-3.78	-5.88
Average Variation (%)	**1.13**	**0.50**	**0.16**	**1.37**	**0.61**	**1.14**	**0.95**	**0.37**	**0.21**	**0.29**	**3.84**	**0.71**	**0.40**	**1.62**

Table VIII: Sr and Nd Isotopic Results

	Sample ID	$^{87}Rb/^{86}Sr$	$^{87}Sr/^{86}Sr$ measured	$^{87}Sr/^{86}Sr$ initial	2σ	$^{147}Sm/^{144}Nd$	$^{143}Nd/^{144}Nd$ measured	$^{143}Nd/^{144}Nd$ initial	2σ	$\varepsilon Nd_{initial}$
Pumice Samples	15-CA-02	1.18442	0.70575	0.70533	2	0.10947	0.512592	0.512574	10	-0.62
	15-CA-08	2.44512	0.70629	0.70542	2	0.10024	0.512583	0.512567	14	-0.76
	15-CA-10	1.18528	0.70560	0.70518	3	0.09707	0.512587	0.512571	12	-0.68
	15-CA-11	4.66994	0.70704	0.70538	3	0.10596	0.512598	0.512581	12	-0.49
	15-CA-16	0.55743	0.70524	0.70504	6	0.09423	0.512584	0.512569	8	-0.73
	15-CA-21	1.49808	0.70578	0.70524	6	0.09747	0.512592	0.512576	12	-0.58
	15-CA-22	0.88445	0.70534	0.70503	6	0.10119	0.512613	0.512596	13	-0.18
	15-CA-27	1.16434	0.70555	0.70514	1	0.10125	0.512584	0.512567	9	-0.75
	15-CA-28	0.50383	0.70532	0.70514	3	0.10744	0.512589	0.512571	10	-0.67
	15-CA-32	0.80138	0.70530	0.70502	3	0.10006	0.512615	0.512599	12	-0.14
	15-CA-35	1.02313	0.70542	0.70506	2	0.10071	0.512595	0.512578	8	-0.53
	15-CA-36	0.41110	0.70528	0.70514	3	0.10463	0.512603	0.512586	12	-0.39
	15-CA-43	8.61015	0.70799	0.70492	2	0.10573	0.512595	0.512578	4	-0.55
	15-CA-46	0.83538	0.70544	0.70514	2	0.10349	0.512602	0.512585	8	-0.40
	15-CA-54	1.20137	0.70549	0.70506	1	0.09658	0.512588	0.512572	12	-0.65
Bulk Ignimbrite Samples	15-CA-15	1.60764	0.70588	0.70531	2	0.10313	0.512596	0.512579	13	-0.52
	15-CA-18	1.82772	0.70592	0.70527	4	0.10093	0.512595	0.512578	12	-0.53
	15-CA-19	1.42968	0.70558	0.70507	5	0.10107	0.512599	0.512582	8	-0.45
	15-CA-20	1.39656	0.70568	0.70518	6	0.09740	0.512594	0.512578	6	-0.54
	15-CA-26	0.79483	0.70538	0.70509	7	0.10368	0.512599	0.512582	7	-0.46
	15-CA-33	0.92526	0.70536	0.70503	10	0.10050	0.512603	0.512587	12	-0.37
	15-CA-55	1.31665	0.70574	0.70527	2	0.09841	0.512594	0.512578	14	-0.54
tuff of Elevenmile Canyon outflow and associated Desatoya tuff	H12-66	1.82948	0.70572	0.70507	2	0.09799	0.512595	0.512579	9	-0.52
	H12-67	3.04132	0.70606	0.70497	3	0.09902	0.512593	0.512577	10	-0.57
	H12-68	2.81685	0.70612	0.70512	2	0.09622	0.512601	0.512585	7	-0.40
	H12-69	4.05032	0.70650	0.70505	3	0.10017	0.512591	0.512575	14	-0.61
	H12-181	1.89336	0.70603	0.70536	2	0.09354	0.512581	0.512566	11	-0.78
	15-DJ-15A	1.18344	0.70566	0.70524	0	0.10259	0.512596	0.512579	10	-0.52
	15-DJ-16	3.26977	0.70673	0.70556	0	0.09651	0.512596	0.512580	10	-0.50
	15-DJ-18	2.80943	0.70633	0.70533	3	0.10164	0.512599	0.512582	5	-0.46
Local Basement	16-DJ-2A	0.02974	0.70832	0.70823	1	0.13203	0.512244	0.512067	14	-6.00
	16-DJ-3	3.60186	0.71541	0.70491	2	0.12539	0.512126	0.511958	6	-8.13
	16-DJ-28	0.01770	0.70742	0.70738	2	0.07557	0.511462	0.511393	108	-20.78
	16-DJ-29	0.35075	0.70858	0.70789	2	0.10218	0.512339	0.512245	8	-4.15
	16-DJ-30	0.86393	0.70817	0.70645	2	0.13529	0.512351	0.512227	11	-4.50
	16-DJ-31	0.62072	0.70579	0.70535	1	0.09222	0.512525	0.512495	10	-1.54
	16-DJ-33	1.36492	0.70843	0.70426	2	0.11423	0.512537	0.512376	10	0.29
	16-DJ-34	0.38555	0.70558	0.70531	1	0.08350	0.512469	0.512442	8	-2.57
	16-DJ-35	0.72259	0.70709	0.70499	2	0.10560	0.512223	0.512081	8	-5.71
	16-DJ-36	0.28354	0.70709	0.70627	2	0.13056	0.512399	0.512224	4	-2.93
	16-DJ-37	0.15768	0.70577	0.70546	2	0.12777	0.512675	0.512558	4	1.95
	16-DJ-38	0.50899	0.70495	0.70459	1	0.09871	0.512624	0.512592	12	0.35
	15-CA-01	1.74769	0.70560	0.70498	1	0.10637	0.512612	0.512595	8	-0.22
	15-CA-40	1.23807	0.70868	0.70824	2	0.11364	0.512444	0.512425	14	-3.52

Table IX: Pb Isotope Results

	Sample ID	U (ppm)	Th (ppm)	Pb (ppm)	$^{208}Pb/^{204}Pb$ measured	$^{207}Pb/^{204}Pb$ measured	$^{206}Pb/^{204}Pb$ measured
Pumice Samples	15-CA-02	4.228	16.291	19.3	38.807	15.635	19.133
	15-CA-08	4.52	19.402	21.2	38.872	15.654	19.150
	15-CA-10	5.23	15.128	21	38.918	15.667	19.166
	15-CA-11	4.524	22.673	20.8	38.853	15.646	19.144
	15-CA-16	2.317	9.225	20.2	38.750	15.596	19.101
	15-CA-21	4.158	16.374	22.6	38.849	15.652	19.137
	15-CA-22	4.193	12.732	19.2	38.937	15.675	19.170
	15-CA-27	2.827	13.695	21.2	38.829	15.647	19.124
	15-CA-28	3.947	10.234	21.1	38.781	15.632	19.111
	15-CA-32	4.034	11.904	20.8	38.867	15.656	19.151
	15-CA-35	3.946	13.132	22.9	38.890	15.663	19.148
	15-CA-36	4.165	10.846	22.1	38.865	15.656	19.143
	15-CA-43	5.86	18.078	24.3	38.979	15.688	19.176
	15-CA-46	4.552	12.674	23.4	38.839	15.648	19.138
	15-CA-54	5.591	16.467	28.5	38.817	15.640	19.131
Bulk Ignimbrite Samples	15-CA-15	4.797	18.462	22.7	38.903	15.659	19.221
	15-CA-18	5.796	17.902	20.2	38.900	15.660	19.174
	15-CA-19	4.309	15.736	18.1	38.987	15.689	19.185
	15-CA-20	4.294	15.78	28.8	38.877	15.673	19.116
	15-CA-26	4.088	13.245	20.5	38.942	15.677	19.165
	15-CA-33	4.935	13.826	22.9	38.797	15.634	19.133
	15-CA-55	5.378	17.229	23.4	38.975	15.684	19.184
tuff of Elevenmile Canyon outflow and associated Desatoya tuff	H12-66	4.35	16.900	21	38.986	15.686	19.185
	H12-67	4.93	20	25	38.838	15.640	19.145
	H12-68	5.06	19.6	17	38.815	15.644	19.100
	H12-69	5.36	22.1	24	38.895	15.655	19.155
	H12-181	5.99	15.6	23	38.872	15.659	19.129
	15-DJ-15A	5.98	15.5	25	38.848	15.650	19.142
	15-DJ-16	8.01	21.5	28	38.895	15.660	19.164
	15-DJ-18	7.33	20	28	38.877	15.654	19.164
Local Basement	16-DJ-2A	1.33	1.2	2.5	38.875	15.684	19.721
	16-DJ-3	2.62	9.8	17	39.051	15.673	18.907
	16-DJ-28	2.76	0.1	2.5	38.832	15.773	21.502
	16-DJ-29	1.22	1.5	2.5	38.647	15.659	19.521
	16-DJ-30	6.09	4.7	12	38.855	15.698	19.942
	16-DJ-31	3.49	11.3	23	38.963	15.692	19.159
	16-DJ-33	3.37	13.2	17	38.947	15.660	19.096
	16-DJ-34	3.26	5	21	38.982	15.713	19.103
	16-DJ-35	4.39	4.8	17	38.940	15.699	19.677
	16-DJ-36	6.13	6.4	25	38.885	15.678	19.165
	16-DJ-37	1.66	5.4	2.5	38.933	15.644	19.273
	16-DJ-38	3.28	7.6	20	38.818	15.684	19.052
	15-CA-01	4.72	20.78	19.6	38.994	15.685	19.183
	15-CA-40	3.88	13.738	32.9	38.924	15.663	19.147

Table IX: Pb Isotope Results Cont.

	Sample ID	$^{208}Pb/^{204}Pb_i$	2σ	$^{207}Pb/^{204}Pb_i$	2σ	$^{206}Pb/^{204}Pb_i$	2σ
Pumice Samples	15-CA-02	38.737	0.007	15.632	0.002	19.078	0.002
	15-CA-08	38.796	0.014	15.651	0.004	19.097	0.004
	15-CA-10	38.858	0.011	15.664	0.003	19.103	0.003
	15-CA-11	38.763	0.012	15.643	0.004	19.089	0.003
	15-CA-16	38.585	0.002	15.557	0.001	19.042	0.001
	15-CA-21	38.662	0.007	15.612	0.002	19.061	0.002
	15-CA-22	38.755	0.015	15.635	0.004	19.085	0.004
	15-CA-27	38.649	0.004	15.608	0.001	19.061	0.001
	15-CA-28	38.741	0.009	15.630	0.002	19.064	0.002
	15-CA-32	38.693	0.016	15.616	0.005	19.072	0.004
	15-CA-35	38.843	0.004	15.661	0.001	19.105	0.002
	15-CA-36	38.824	0.018	15.654	0.005	19.096	0.004
	15-CA-43	38.918	0.006	15.685	0.002	19.115	0.002
	15-CA-46	38.794	0.018	15.645	0.006	19.089	0.005
	15-CA-54	38.642	0.006	15.600	0.002	19.052	0.002
Bulk Ignimbrite Samples	15-CA-15	38.836	0.008	15.656	0.002	19.168	0.002
	15-CA-18	38.700	0.006	15.619	0.001	19.072	0.001
	15-CA-19	38.788	0.030	15.648	0.010	19.095	0.010
	15-CA-20	38.705	0.014	15.633	0.004	19.049	0.003
	15-CA-26	38.761	0.016	15.636	0.003	19.085	0.003
	15-CA-33	38.620	0.003	15.594	0.001	19.049	0.001
	15-CA-55	38.786	0.012	15.643	0.004	19.096	0.003
tuff of Elevenmile Caynon outflow and associated Desatoya tuff	H12-66	38.920	0.006	15.683	0.002	19.133	0.002
	H12-67	38.772	0.004	15.637	0.001	19.096	0.001
	H12-68	38.720	0.014	15.640	0.004	19.025	0.003
	H12-69	38.819	0.016	15.652	0.004	19.099	0.004
	H12-181	38.816	0.003	15.656	0.001	19.064	0.001
	15-DJ-15A	38.797	0.006	15.647	0.001	19.082	0.001
	15-DJ-16	38.832	0.016	15.656	0.004	19.092	0.004
	15-DJ-18	38.818	0.011	15.651	0.003	19.098	0.003
Local Basement	16-DJ-2A	38.546	0.005	15.628	0.002	18.603	0.002
	16-DJ-3	38.659	0.006	15.657	0.002	18.586	0.002
	16-DJ-28	38.813	0.006	15.694	0.002	19.887	0.002
	16-DJ-29	38.369	0.007	15.625	0.002	18.828	0.002
	16-DJ-30	38.672	0.003	15.662	0.001	19.216	0.001
	16-DJ-31	38.882	0.003	15.688	0.001	19.083	0.001
	16-DJ-33	38.393	0.006	15.638	0.002	18.662	0.002
	16-DJ-34	38.943	0.006	15.709	0.002	19.025	0.002
	16-DJ-35	38.747	0.009	15.672	0.002	19.134	0.002
	16-DJ-36	38.711	0.003	15.652	0.001	18.654	0.001
	16-DJ-37	37.930	0.010	15.598	0.003	18.331	0.004
	16-DJ-38	38.755	0.008	15.680	0.020	18.970	0.002
	15-CA-01	38.906	0.003	15.682	0.001	19.122	0.001
	15-CA-40	38.890	0.014	15.661	0.005	19.117	0.004

Initial ratios calculated to 25.1 Ma

Table X: $^{87}Sr/^{86}Sr$ values for plagioclase separates

	Sample Number	15-CA-10	15-CA-11	15-CA-15	15-CA-32	15-CA-35
Plagioclase Phenocrysts	$^{87}Rb/^{86}Sr$	1.18529	4.66994	1.60765		1.02314
	$87Sr/86Sr_{measured}$	0.70570	0.70705	0.70594		0.70550
	$^{87}Sr/^{86}Sr_{initial}$	0.70527	0.70538	0.70537		0.70513
	2σ	2	3	7		3
Host Pumice	$^{87}Rb/^{86}Sr$	1.18528	4.66994	1.60764	0.80138	1.02313
	$87Sr/86Sr_{measured}$	0.70560	0.70704	0.70588	0.70530	0.70542
	$^{87}Sr/^{86}Sr_{initial}$	0.70518	0.70538	0.70531	0.70502	0.70506
	2σ	3	3	2	3	2
Variation ($^{87}Sr/^{86}Sr_{initialseperate}$ - $^{87}Sr/^{86}Sr_{initialpumice}$)		0.00010	0.00001	0.00006		0.00007

Initial ratios calculated to 25.1 Ma

Table XI: Sr and Nd isotopic results comparing dissolution by Parr bombs and closed beaker Savilex

	Sample	$^{87}Rb/^{86}Sr$	$^{87}Sr/^{86}Sr$ measured	$^{87}Sr/^{86}Sr_i$	2σ	$^{147}Sm/^{144}Nd$	$^{143}Nd/^{144}Nd$ measured	$^{143}Nd/^{144}Nd_i$	2σ	εNd_i
Dissolved by Closed Beaker	15-CA-21	1.49808	0.70578	0.70524	6	0.09747	0.512592	0.512576	12	-0.58
	15-CA-28	0.50383	0.70532	0.70514	3	0.10744	0.512589	0.512571	10	-0.67
	15-CA-36	0.41110	0.70528	0.70514	3	0.10463	0.512603	0.512586	12	-0.39
	15-CA-54	1.20137	0.70549	0.70506	1	0.09658	0.512588	0.512572	12	-0.65
Dissolved by Parr Bombs	15-CA-21	1.49809	0.70585	0.70531	2	0.09747	0.512591	0.512575	10	-0.60
	15-CA-28	0.50383	0.70537	0.70519	7	0.10744	0.512591	0.512573	5	-0.63
	15-CA-36	0.41110	0.70530	0.70515	2	0.10463	0.512599	0.512582	11	-0.47
	15-CA-54	1.20138	0.70562	0.70519	2	0.09658	0.512592	0.512576	8	-0.58

Initial ratios calculated to 25.1 Ma

Table XII: Pb isotopic results comparing dissolution by Parr bombs and closed beaker Savilex

	Sample ID	$^{208}Pb/^{204}Pb$ measured	$^{208}Pb/^{204}Pb_i$	2σ	$^{207}Pb/^{204}Pb$ measured	$^{207}Pb/^{204}Pb_i$	2σ	$^{206}Pb/^{204}Pb$ measured	$^{206}Pb/^{204}Pb_i$	2σ
Dissolved by Closed Beaker	15-CA-21	38.849	38.662	0.007	15.652	15.612	0.002	19.137	19.061	0.002
	15-CA-28	38.781	38.741	0.009	15.632	15.630	0.002	19.111	19.064	0.002
	15-CA-36	38.865	38.824	0.018	15.656	15.654	0.005	19.143	19.096	0.004
	15-CA-54	38.817	38.642	0.006	15.640	15.600	0.002	19.131	19.052	0.002
Dissolved by Parr Bombs	15-CA-21	38.776	38.716	0.013	15.639	15.637	0.004	19.071	19.025	0.003
	15-CA-28	38.872	38.832	0.003	15.661	15.659	0.001	19.132	19.085	0.001
	15-CA-36	38.812	38.771	0.009	15.643	15.641	0.003	19.123	19.076	0.003
	15-CA-54	38.853	38.805	0.006	15.650	15.647	0.002	19.139	19.090	0.002

Initial ratios calculated to 25.1 Ma using concentrations from Table IX

Table XIII: Pb isotope fractionation correction

	$^{206}Pb/^{204}Pb$	$^{207}Pb/^{204}Pb$	$^{208}Pb/^{204}Pb$
NIST SRM981 Values of Todt et al. (1984)	**16.9356**	**15.4891**	**36.7006**
NIST SRM981 Values Measured			
Barrel 1 – Nov. 6, 2015	16.9052	15.4462	36.5646
Barrel 2 – Apr. 22, 2016	16.9024	15.4435	36.5529
Barrel 3 – Apr. 25, 2016	16.8960	15.4345	36.5247
Barrel 4 - Aug. 12, 2016	16.9094	15.4527	36.5874
Fractionation Correction Applied			
Barrel 1	0.00180	0.00277	0.00372
Barrel 2	0.00196	0.00295	0.00404
Barrel 3	0.00234	0.00353	0.00481
Barrel 4	0.00155	0.00235	0.00309

Barrel Constituents

Barrel 1	**Barrel 2**	**Barrel 3**	**Barrel 4**
15-CA-16	15-CA-02	H12-67	16-DJ-2A*
15-CA-18	15-CA-08	H12-68	16-DJ-3
15-CA-19	15-CA-10	H12-69	16-DJ-28*
15-CA-20	15-CA-11	H12-181	16-DJ-29*
15-CA-21	15-CA-15	15-DJ-15A	16-DJ-30
15-CA-22	15-CA-28	15-DJ-16	16-DJ-31
15-CA-26	15-CA-35	15-DJ-18	16-DJ-33
15-CA-27	15-CA-36	15-CA-21 (Parr Bomb)	16-DJ-34
15-CA-32	15-CA-40	15-CA-28 (Parr Bomb)	16-DJ-35
15-CA-33	15-CA-46	15-CA-36 (Parr Bomb)	16-DJ-36
15-CA-54		15-CA-54 (Parr Bomb)	16-DJ-37*
15-CA-55			16-DJ-38
			15-CA-01
			15-CA-43
			H12-66

Table XIV: Electron Microprobe Results - Amphiboles

Sample-Amphibole	Spot	K2O	CaO	F	Al2O3	ZnO	FeO	MnO	V2O3	Cl	TiO2	Cr2O3	Na2O	MgO	SiO2	Total
15-CA-21 Hbl1	1	0.83	10.32	0.38	7.07	0.06	20.91	0.87	0.04	0.15	1.88	0.01	1.79	9.37	44.35	98.02
15-CA-21 Hbl1	2	0.79	10.23	0.47	7.01	0.04	20.72	0.91	0.05	0.15	1.76	-	1.77	9.29	44.20	97.39
15-CA-21 Hbl1	3	0.82	10.22	0.63	6.81	0.07	21.06	0.91	0.07	0.15	1.80	0.00	1.82	9.58	44.66	98.61
15-CA-21 Hbl1	4	0.82	10.28	0.27	7.05	0.08	21.07	0.96	-	0.16	1.77	0.01	1.78	9.21	44.40	97.85
15-CA-21 Hbl1	5	0.82	10.28	0.33	6.85	-	20.94	0.90	0.05	0.15	1.77	-	1.69	9.24	44.61	97.63
15-CA-21 Hbl2	1	0.74	10.12	0.16	6.51	-	20.84	0.92	0.01	0.16	1.49	-	1.69	9.68	45.16	97.48
15-CA-21 Hbl2	2	0.69	9.99	0.50	6.16	0.03	20.80	0.95	0.03	0.16	1.50	0.01	1.70	9.84	45.17	97.53
15-CA-21 Hbl2	3	0.74	10.05	0.38	6.11	0.05	20.65	0.87	-	0.13	1.39	0.01	1.63	9.85	45.43	97.30
15-CA-21 Hbl2	4	0.66	10.04	0.51	6.17	0.06	20.86	0.97	0.01	0.16	1.57	0.02	1.67	9.80	45.16	97.66
15-CA-21 Hbl2	5	0.70	10.03	0.76	6.23	0.07	21.33	0.93	-	0.15	1.47	0.01	1.67	9.73	44.96	98.04
15-CA-21 Hbl2	6	0.67	9.98	0.45	6.20	0.06	20.68	0.96	0.02	0.13	1.56	0.00	1.66	9.90	45.41	97.69
15-CA-21 Hbl3	1	0.69	9.98	0.76	6.19	0.03	21.11	0.96	-	0.16	1.49	-	1.74	9.70	45.14	97.96
15-CA-21 Hbl3	2	0.70	10.05	0.70	6.21	0.04	21.19	0.97	0.05	0.16	1.55	-	1.67	9.55	45.12	97.95
15-CA-21 Hbl3	3	0.70	10.03	0.50	6.14	0.06	21.35	1.04	-	0.15	1.56	0.00	1.63	9.60	45.11	97.89
15-CA-28 Hbl1	1	0.30	1.03	1.03	2.31	-	0.12	0.01	0.00	0.07	0.02	0.00	0.16	0.02	5.61	10.70
15-CA-28 Hbl1	2	1.04	10.84	0.26	10.68	0.01	14.49	0.33	0.03	0.06	3.32	0.01	2.23	12.09	41.80	97.19
15-CA-28 Hbl1	3	1.01	10.83	0.31	10.57	-	14.51	0.44	0.04	0.04	3.30	-	2.26	11.98	41.55	96.84
15-CA-28 Hbl1	4	0.00	0.01	0.66	-	-	0.06	-	0.02	0.06	-	0.01	-	0.00	0.01	0.84
15-CA-28 Hbl1	5	1.04	10.86	0.30	10.79	0.05	13.86	0.38	0.03	0.05	3.38	0.02	2.27	12.25	41.83	97.10
15-CA-28 Hbl1	6	1.03	10.85	0.25	10.68	-	14.18	0.33	0.06	0.05	3.41	-	2.25	12.23	41.96	97.28
15-CA-21 Hbl8	7	1.01	10.97	0.20	10.99	0.05	13.77	0.28	0.07	0.04	3.39	0.00	2.31	12.51	42.09	97.68
15-CA-28 Hbl1	8	1.02	10.87	0.10	10.71	0.00	14.43	0.33	0.05	0.05	3.46	0.00	2.29	12.00	41.74	97.06
15-CA-28 Hbl2	1	1.03	10.95	0.17	11.03	0.06	13.99	0.30	0.07	0.04	3.23	0.01	2.28	12.41	41.69	97.27
15-CA-28 Hbl2	2	1.06	10.84	0.24	10.46	-	14.57	0.38	0.05	0.05	3.32	0.02	2.32	12.01	41.98	97.30
15-CA-28 Hbl2	3	0.96	10.99	0.21	11.00	0.02	13.95	0.32	0.09	0.03	3.28	0.01	2.41	12.64	41.79	97.69
15-CA-28 Hbl2	4	0.88	11.05	0.44	11.33	-	13.49	0.26	0.11	0.03	3.34	-	2.44	12.76	41.32	97.45
15-CA-28 Hbl2	5	0.85	11.08	0.19	11.63	-	13.11	0.22	0.07	0.03	3.46	-	2.41	13.24	41.59	97.88
15-CA-28 Hbl3	1	0.92	11.08	0.26	11.02	0.04	13.26	0.29	0.12	0.03	3.53	0.01	2.27	12.71	41.62	97.15
15-CA-28 Hbl3	2	1.01	10.93	0.14	10.95	-	13.86	0.35	0.04	0.05	3.50	0.02	2.38	12.41	41.82	97.45
15-CA-28 Hbl3	3	1.08	11.07	0.31	11.07	-	13.32	0.28	0.01	0.03	3.81	-	2.31	12.65	41.59	97.54

Units are in wt. %

Table XV: Aluminum in hornblende barometry

Sample	15-CA-21													
Phenocryst #	Hbl1	Hbl1	Hbl1	Hbl1	Hbl1	Hbl2	Hbl2	Hbl2	Hbl2	Hbl2	Hbl2	Hbl3	Hbl3	Hbl3
Spot	1 / 5	2 / 5	3 / 5	4 / 5	5 / 5	1 / 6	2 / 6	3 / 6	4 /6	5/ 6	6 /6	1 / 3	2 / 3	3 /3
SiO2 (wt. %)	44.35	44.20	44.66	44.40	44.61	45.16	45.17	45.43	45.16	44.96	45.41	45.14	45.12	45.11
TiO2 (wt. %)	1.88	1.76	1.80	1.77	1.77	1.49	1.50	1.39	1.57	1.47	1.56	1.49	1.55	1.56
Al2O3 (wt. %)	7.07	7.01	6.81	7.05	6.85	6.51	6.16	6.11	6.17	6.23	6.20	6.19	6.21	6.14
Cr2O3 (wt. %)	0.01	-	0.00	0.01	-	-	0.01	0.01	0.02	0.01	0.00	-	-	0.00
FeO (wt. %)	20.91	20.72	21.06	21.07	20.94	20.84	20.80	20.65	20.86	21.33	20.68	21.11	21.19	21.35
MnO (wt. %)	0.87	0.91	0.91	0.96	0.90	0.92	0.95	0.87	0.97	0.93	0.96	0.96	0.97	1.04
MgO (wt.%)	9.37	9.29	9.58	9.21	9.24	9.68	9.84	9.85	9.80	9.73	9.90	9.70	9.55	9.60
CaO (wt. %)	10.32	10.23	10.22	10.28	10.28	10.12	9.99	10.05	10.04	10.03	9.98	9.98	10.05	10.03
Na2O (wt. %)	1.79	1.77	1.82	1.78	1.69	1.69	1.70	1.63	1.67	1.67	1.66	1.74	1.67	1.63
K2O (wt. %)	0.83	0.79	0.82	0.82	0.82	0.74	0.69	0.74	0.66	0.70	0.67	0.69	0.70	0.70
F (wt. %)	0.38	0.47	0.63	0.27	0.33	0.16	0.50	0.38	0.51	0.76	0.45	0.76	0.70	0.50
Cl (wt. %)	0.15	0.15	0.15	0.16	0.15	0.16	0.16	0.13	0.16	0.15	0.13	0.16	0.16	0.15
Check composition and Classification														
H2Oamp (wt. %)	1.63	1.58	1.53	1.68	1.65	1.73	1.57	1.63	1.57	1.46	1.61	1.45	1.48	1.57
Fe2O3 (wt. %)	8.31	8.26	9.12	8.41	8.11	9.40	10.00	9.41	10.00	10.69	10.03	10.09	9.75	10.41
FeO (wt. %)	13.43	13.28	12.85	13.50	13.64	12.38	11.80	12.18	11.86	11.71	11.66	12.03	12.42	11.98
O=F,Cl (wt. %)	-0.19	-0.23	-0.30	-0.15	-0.17	-0.10	-0.25	-0.19	-0.25	-0.35	-0.22	-0.36	-0.33	-0.25
Total check	ok	ok	ok	ok	ok	ok	ok	ok	ok	ok	ok	ok	ok	ok
Al#	0.00	0.00	0.00	0.00	0.00	0.00	0.00	0.00	0.00	0.00	0.00	0.00	0.00	0.00
Species	Mg-Hbl	Mg-Hbl	Mg-Hbl	Mg-Hbl	Mg-Hbl	Mg-Hbl	Mg-Hbl	Mg-Hbl	Mg-Hbl	Mg-Hbl	Mg-Hbl	Mg-Hbl	Mg-Hbl	Mg-Hbl
Physical-chemical Conditions														
T (°C)	812	803	816	804	794	789	797	781	799	808	791	798	795	804
Uncertainty (σ est)	22	22	22	22	22	22	22	22	22	22	22	22	22	22
P (MPa)	117	116	108	116	111	101	92	91	92	94	93	93	94	92
Uncertainty (max error)	13	13	12	13	12	11	10	10	10	10	10	10	10	10
oceanic depth (km)	4.1	4.1	3.8	4.1	3.9	3.6	3.3	3.2	3.3	3.3	3.3	3.3	3.3	3.2
continental depth (km)	4.4	4.4	4.1	4.4	4.2	3.8	3.5	3.4	3.5	3.5	3.5	3.5	3.5	3.5
ΔNNO	0.2	0.2	0.4	0.1	0.1	0.5	0.6	0.6	0.6	0.7	0.6	0.6	0.5	0.6
logfO2	-13.4	-13.6	-13.2	-13.6	-13.8	-13.6	-13.3	-13.7	-13.2	-13.0	-13.4	-13.3	-13.5	-13.2
uncertainty (σ est)	0.4	0.4	0.4	0.4	0.4	0.4	0.4	0.4	0.4	0.4	0.4	0.4	0.4	0.4
H2Omelt (wt.%)	4.7	4.8	4.7	4.8	4.8	4.9	4.9	4.7	5.0	5.0	4.9	4.9	5.0	5.1
uncertainty*	0.4	0.4	0.4	0.4	0.4	0.4	0.4	0.4	0.4	0.4	0.4	0.4	0.4	0.4

Thermobarometry calculations were performed using the Ridolfi et al. (2009) Amp-Tb spreadsheet. Fe^{2+} was calculated by determining the number of cation charges in a 15 atom sum amphibole configuration (Si + Al + Cr + Ti + Zr + Li + Fe + Mg + Mn + Ca = 15), if the sum of cations was less than 46 Fe^{3+} was determined as 46 minus the sum of cation charges. $Fe^{2+}$is then equal to the sum of iron charges minus the number of Fe^{3+} ions, with the caveat that the sum of Si +Ti + Al cations is less than 8 in an adjusted 13 atom sum amphibole (Si + Al + Cr + Ti + Zr + Li + Fe + Mg + Mn =13). Al# or aluminum number is defined as Al# = $^{[6]}Al/Al_T$. Total check ensures the formula calculated is charge balanced and the species was determined internally by the calculator on the basis of Al/ and $^{[4]}Al$ compositions and can be reported as: Mg-Hbl = magnesiohorblende, Mg-Hst = magnesiohastingsite, Tsch-Prg = tschermakitic pargasite, low-Ca = low calcium amphibole (i.e. BCa < 1.5; possibly cummingtonite) and Xenocryst = Al# > 0.21; invalid if Total check = wrong.

Table XV: Aluminum in hornblende barometry Cont.

Sample	15-CA-28													
Phenocryst #	Hbl1	Hbl1	Hbl1	Hbl1	Hbl1	Hbl1	Hbl2	Hbl2	Hbl2	Hbl2	Hbl2	Hbl3	Hbl3	Hbl3
Spot	1 / 6	2 / 6	3 / 6	4 / 6	5 / 6	6 / 6	1 / 5	2 / 5	3 / 5	4 / 5	5 / 5	1 / 3	2 / 3	3 / 3
SiO2 (wt. %)	41.80	41.55	41.83	41.96	42.09	41.74	41.69	41.98	41.79	41.32	41.59	41.62	41.82	41.59
TiO2 (wt. %)	3.32	3.30	3.38	3.41	3.39	3.46	3.23	3.32	3.28	3.34	3.46	3.53	3.50	3.81
Al2O3 (wt. %)	10.68	10.57	10.79	10.68	10.99	10.71	11.03	10.46	11.00	11.33	11.63	11.02	10.95	11.07
Cr2O3 (wt. %)	0.01	-	0.02	-	0.00	0.00	0.01	0.02	0.01	-	-	0.01	0.02	-
FeO (wt. %)	14.49	14.51	13.86	14.18	13.77	14.43	13.99	14.57	13.95	13.49	13.11	13.26	13.86	13.32
MnO (wt. %)	0.33	0.44	0.38	0.33	0.28	0.33	0.30	0.38	0.32	0.26	0.22	0.29	0.35	0.28
MgO (wt.%)	12.09	11.98	12.25	12.23	12.51	12.00	12.41	12.01	12.64	12.76	13.24	12.71	12.41	12.65
CaO (wt. %)	10.84	10.83	10.86	10.85	10.97	10.87	10.95	10.84	10.99	11.05	11.08	11.08	10.93	11.07
Na2O (wt. %)	2.23	2.26	2.27	2.25	2.31	2.29	2.28	2.32	2.41	2.44	2.41	2.27	2.38	2.31
K2O (wt. %)	1.04	1.01	1.04	1.03	1.01	1.02	1.03	1.06	0.96	0.88	0.85	0.92	1.01	1.08
F (wt. %)	0.26	0.31	0.30	0.25	0.20	0.10	0.17	0.24	0.21	0.44	0.19	0.26	0.14	0.31
Cl (wt. %)	0.06	0.04	0.05	0.05	0.04	0.05	0.04	0.05	0.03	0.03	0.03	0.03	0.05	0.03
Check composition and Classification														
H2Oamp (wt. %)	1.74	1.72	1.73	1.75	1.79	1.82	1.79	1.76	1.79	1.68	1.81	1.76	1.81	1.74
Fe2O3 (wt. %)	5.65	5.61	5.05	5.35	5.14	5.08	5.71	5.07	5.92	5.83	6.65	5.09	5.14	4.57
FeO (wt. %)	9.40	9.46	9.32	9.37	9.14	9.86	8.85	10.00	8.62	8.24	7.12	8.68	9.23	9.21
O=F,Cl (wt. %)	-0.12	-0.14	-0.14	-0.12	-0.09	-0.06	-0.08	-0.11	-0.09	-0.19	-0.09	-0.11	-0.07	-0.14
Total check	ok	ok	ok	ok	ok	ok	ok	ok	ok	ok	ok	ok	ok	ok
Al#	0.05	0.04	0.07	0.06	0.07	0.06	0.06	0.05	0.05	0.05	0.05	0.06	0.06	0.05
Species	Mg-Hst	Mg-Hst	Mg-Hst	Mg-Hst	Mg-Hst	Mg-Hst	Mg-Hst	Mg-Hst	Mg-Hst	Mg-Hst	Mg-Hst	Mg-Hst	Mg-Hst	Mg-Hst
Physical-chemical Conditions														
T (°C)	930	931	935	931	939	933	942	926	944	957	963	949	942	953
uncertainty (σ est)	22	22	22	22	22	22	22	22	22	22	22	22	22	22
P (MPa)	284	281	293	283	301	287	308	270	302	331	344	308	300	310
uncertainty (Max error)	31	31	32	31	33	32	34	30	33	36	38	34	33	34
oceanic depth (km)	10.0	9.9	10.3	10.0	10.6	10.1	10.9	9.5	10.6	11.7	12.1	10.9	10.6	10.9
continental depth (km)	10.7	10.6	11.1	10.7	11.4	10.9	11.6	10.2	11.4	12.5	13.0	11.6	11.3	11.7
ΔNNO	0.2	0.1	0.2	0.2	0.2	0.1	0.3	0.1	0.3	0.3	0.4	0.2	0.2	0.1
logfO2	-11.2	-11.2	-11.1	-11.1	-11.0	-11.2	-10.9	-11.3	-10.8	-10.6	-10.4	-10.8	-11.0	-10.8
Uncertainty (σ est)	0.4	0.4	0.4	0.4	0.4	0.4	0.4	0.4	0.4	0.4	0.4	0.4	0.4	0.4
H2Omelt (wt. %)	4.3	4.3	4.4	4.3	4.5	4.4	4.5	4.1	4.3	4.7	4.7	4.6	4.3	4.1
uncertainty*	0.7	0.7	0.7	0.6	0.7	0.7	0.7	0.6	0.7	0.7	0.7	0.7	0.6	0.6

Thermobarometry calculations were performed using the Ridolfi et al. (2009) Amp-Tb spreadsheet. Fe^{2+} was calculated by determining the number of cation charges in a 15 atom sum amphibole configuration (Si + Al + Cr + Ti + Zr + Li + Fe + Mg + Mn + Ca = 15), if the sum of cations was less than 46 Fe^{3+} was determined as 46 minus the sum of cation charges. $Fe^{2+}$is then equal to the sum of iron charges minus the number of Fe^{3+} ions, with the caveat that the sum of Si +Ti + Al cations is less than 8 in an adjusted 13 atom sum amphibole (Si + Al + Cr + Ti + Zr + Li + Fe + Mg + Mn =13). Al# or aluminum number is defined as Al# = $^{[6]}Al/Al_T$. Total check ensures the formula calculated is charge balanced and the species was determined internally by the calculator on the basis of Al/ and $^{[4]}Al$ compositions and can be reported as: Mg-Hbl = magnesiohorblende, Mg-Hst = magnesiohastingsite, Tsch-Prg = tschermakitic pargasite, low-Ca = low calcium amphibole (i.e. BCa < 1.5; possibly cummingtonite) and Xenocryst = Al# > 0.21; invalid if Total check = wrong.

Table XVI: Partition Coefficients

	Cs	Rb	K	Ba	Sr	Pb	Th	U	Zr	Hf	Ti	Ta	Y	Nb	Sc	Cr	Ni	Co	V	Ga	P	Zn	Cu
Felsic/Acidic Melts																							
Plagioclase	0.030	0.240	0.263	0.363	4.400	1.300	0.040	0.050	0.041	0.039	0.050	0.030	0.510	0.260	0.010	0.010	1.500	0.150		3.200		0.480	
K-Feldspar	0.110	0.610	1.490	7.200	4.500	0.120	0.022	0.040	0.010	0.020		0.001	0.017	0.010	0.023		1.100			0.450		0.042	0.240
Biotite	2.200	4.500	2.500	6.400	0.250	0.890	0.310	0.100	0.190	0.500		1.300	2.300	4.600	2.230	12.600	3.330	28.500		3.100		11.400	72.400
Apatite						0.030		43.700	0.500				40.000	0.100									
Zircon						7.500	22.100	254.000		2645		40.200	71.400		60.300	119.000		9.000					
Intermediate Melts																							
Plagioclase	0.030	0.130	0.151	0.500	2.600	0.610	0.015	0.010	0.030	0.030	0.050	0.025	0.060	0.025	0.010	0.010	0.010	0.010	0.010				
K-Feldspar	0.044	0.180		0.500	0.900	0.208	0.008	0.017	0.150			0.009	0.017										
Biotite	0.190	3.200		6.000	0.150	0.890	0.150	0.080	0.150			0.700	0.450	1.400			3.300						
Apatite	0.700	0.400		0.450	8.000		1.600	2.600	2.000	0.070		0.050			0.300			0.200					

	La	Ce	Pr	Nd	Sm	Eu	Gd	Tb	Dy	Ho	Er	Tm	Yb	Lu
Felsic/Acidic Melts														
Plagioclase	0.393	0.251	0.200	0.189	0.137	2.110	0.120	0.150	0.112	0.140	0.122	0.100	0.132	0.138
K-Feldspar	0.070	0.020	0.025	0.030	0.020	3.300	0.011	0.010	0.040	0.014	0.006	0.014	0.030	0.020
Biotite	0.318	0.377	0.300	0.339	0.390	0.328	0.442	0.393	0.500	0.750	0.400	0.660	0.450	0.450
Apatite		16.600	18.000	21.000	20.700	14.500	21.700		16.900		14.100		9.400	7.900
Zircon	1.300	2.040	2.540	3.350	3.790	0.450	9.210	24.800	38.800	74.500	99.800	150.000	194.000	264.000
Intermediate Melts														
Plagioclase	0.2300	0.1800	0.1300	0.1700	0.1500	0.9500	0.1300	0.0700	0.1000	0.1500	0.100	0.200	0.070	0.050
K-Feldspar		0.0170			0.0100	1.0000							0.003	0.002
Biotite	0.1500	0.1600		0.2000	0.1500	0.1700	0.1500	0.1300	0.1500		0.1000		0.150	0.130
Apatite	27.0000	31.0000			38.0000	30.0000		30.0000					10.000	7.000

References for Kd values

Partition coefficients were taken from FC-AFC-FCA and mixing modeler by Ersoy (2010), and aggregated from the GERM Partition Coefficient (Kd) database; specific references are shown below:

0.001	Ewart, A. and Griffin, W.L. (1994)
0.001	Higuchi, H. and Nagasawa, H. (1969).
0.001	Mahood, G.A. and Hildreth, E.W. (1983).
0.001	Villemant, B. (1988).
0.001	Matsui et al 1977
0.001	Schnetzler, C.C. and Philpotts, J.A. (1970).
0.001	Philpotts & Schnetzler (1970)
0.001	Nagasawa & Schnetzler (1971)
0.001	McKenzie and O'Nions (1991)
0.001	Brenan et al., (1995)
0.001	Mahood & Stimac (1990)

0.001	Rollinson (1993)
0.001	Bacon & Druitt (1988)
0.001	Stix & Gorton (1990)
0.001	Nash & Crecraft (1985)
0.001	Fujimaki et al., (1984)
0.001	Bea et al., (1994)
0.001	Larsen (1979)
0.001	Dunn & Sen (1994)
0.001	Schwandt & McKay (1998)
0.001	Estimated using an average of values found on GERM- partition coefficient database (GERM, last accessed June, 2017)